# Multi-contrast Optical Coherence Tomography for Brain Imaging and Mapping

A DISSERTATION
SUBMITTED TO THE FACULTY OF THE GRADUATE SCHOOL
OF THE UNIVERSITY OF MINNESOTA
BY

**HUI WANG**

IN PARTIAL FULFILLMENT OF THE REQUIREMENTS
FOR THE DEGREE OF
DOCTOR OF PHILOSOPHY

Adviser: Taner Akkin

August, 2014

August, 2014

# ABSTRACT

Although our knowledge of neuronal function and regional activity has been tremendously enriched in the past decades, coordination of these neurons to form the complex behaviors has yet to be understood. The neuronal pathways (also named connectome) form the structural foundation of the dynamic circuits in the brain. The recent interests in connectome and brainwide database have imposed a pressing need for high-resolution imaging techniques that allows large coverage. This dissertation develops a novel multi-contrast optical coherence tomography (MC-OCT) technique for the application of brainwide imaging and architectural mapping in 3D at high spatiotemporal resolution, with an emphasis on the connective tracts. The image contrasts originate from intrinsic optical properties of the brain tissues in which light propagates, back-scatters, attenuates, and changes its polarization state. Due to a birefringence property of the myelin sheath, MC-OCT specially targets the white matter, with qualitative architecture and quantitative orientation maps produced. The fiber tracts with diameters of a few tens of micrometers are visualized and tracked in 3D. As a further advance, a serial optical coherence scanner (SOCS) integrating the MC-OCT and a Vibratome slicer is realized for large-scale brain imaging and mapping at high resolution. The 3D fiber architecture and fiber orientation in rat brain are reconstructed at a resolution of 15 x 15 x 5.5 $\mu m^3$. SOCS enables systematic validations of diffusion magnetic resonance imaging (dMRI) at microscopic resolution. A cross-validation in a postmortem human medulla sample shows remarkably good agreement on fiber structures and orientations between the two techniques. In addition, SOCS resolves intricate fiber patterns that are not captured by the dMRI. Taken together, the serial MC-OCT technique has the potential to bridge cross-scale investigations for a hierarchical view of neuroanatomical connections, thus opening intriguing applications in brain mapping and neural disorders.

# ACKNOWLEDGEMENTS

I would like to express my earnest gratitude to my advisor Dr. Taner Akkin, who led me to the Biomedical Optics Lab and has been providing me continuous support throughout my way. The past years working under his guidance have been inspiring and productive. I could never forget the numerous time he spent with me in the lab and the millions of hands-on directions during my early exposures to the optics. Those systematic trainings have tremendously benefitted my later research. I am grateful to Taner for the many opportunities he directed on my way. His trust in my abilities has gone a long way towards my professional growth. I hope that the knowledge and skills he has passed to me continue to lead along my career path.

The same deepest thanks give to Dr. Gordon Legge, my mentor in the minor program of Psychology. His openness to every student and every possibility secured my lasting interests in brain and behavior sciences, broadened my sights and expanded my research fields. The ways he is doing research, supervising students and managing the lab profoundly influences me, towards my intellectual and personal growth. The experience being in his lab has been very stimulating and enjoyable.

I want to thank Dr. Tay Netoff in the Department of Biomedical Engineering. The collaboration with Tay and his lab initiated my endeavor in neuroimaging, to which I have devoted throughout the PhD and will be committed in the future. His enthusiasm has deeply influenced my attitude towards research. I thank to Dr. Aviva Abosch for her collaboration in clinical investigations. I am grateful to Dr. Shai Ashkenazi for serving on my preliminary oral exam and the rest of my dissertation committee Dr. Bin He and Dr. Kamil Ugurbil for their time and interest in my dissertation research.

I want to send my sincere acknowledgements to Dr. David Boas and Dr. Bruce Fischl, our collaborators at the Massachusetts General Hospital (MGH). David's insightfulness directs me to see more potentials of my research and his faith in my work encourages me to keep moving forward despite some hesitated times in front of challenges. Bruce exposed me to the field of MRI and has been always supportive to provide all possible resources. I had a joyful time interacting with Martin Reuter, Louis Vinke, Anastasia Yndiki, Caroline Magnain, and Allison Player at the MGH. The "validation" project could not have been accomplished without their helps.

I thank the faculty of the departments of Biomedical Engineering, Electrical Engineering, Neuroscience, and Psychology for instructing me to respective disciplines in and out of class. Specially, my gratitude gives to Prof. James Leger, a well-known expert in optics and wonderful teacher to deliver the knowledge in an inspiring and connected way. Without taking his class, I never imagined that I would fall in love with optics so much.

I like to thank all the Akkin lab members: Adam Black, Tina Yeh, and Chao Liu. The time with them though the ups and downs is a treasure in my life. I enjoyed the summers with Tina and Adam at the MBL, digging into cooking, programing, science and nature. The discussions with Chao keep me self-alert and critical-thinking. I owe a lot of thanks to Muhammad Al-Qaisi, our lab alumnus, who helped to step out for my initial research in the lab. The conversations I had with him always sped up my digestions in the mysterious problems. I appreciate the constructive interactions and discussions with Tyler Stigen, Rebecca Klank, Weihang Ji, Daphne Dong, Yunfeng Lu, Clay Sheaff, Mohammad Amin Tadayon, Qi Shao, Katia Morgounova, Oscar Miranda-Dominguez, my brilliant friends in the Department of Biomeidcal Engineering.

I am indebted to my husband Junfeng Zhu for his continuous backup in my strength and courage. For the past of times we have been striving days and nights, for the tears and laughs that we share and are only understood by us, thousands of thanks are never enough. I thank my family for their continuous encouragement, understanding and support.

# TABLE OF CONTENTS

# LIST OF FIGURES

# CHAPTER 1 INTRODUCTION

## 1.1 OVERVIEW

The nervous system is a network of billions of neurons and supporting cells communicating with each other through trillions of synapses. Groups of neurons reside in specific nodes, and construct intricate connections with others located near and far [1]. Since the pioneering work of Santiago Ramón y Cajal who began to describe the anatomical pathways that link different areas of the brain into functional networks, the endeavors on advanced neuroimaging techniques have never been stopped. Single-neuron recording [2] and molecular phenotyping in animal models have indicated that characteristic firing properties and biochemical markers are associated with neuronal functions. On the other hand, system-level functional brain imaging techniques such as electroencephalography [3], magnetoencephalography [4], positron emission tomography [5, 6], functional magnetic resonance imaging [7] and near-infrared spectroscopy [8] have been linking regional brain activity with a wide range of cognitive functions in humans. The recent focus on systematic generation of whole-brain datasets, for example, the Allen Mouse Brain Atlas for gene expression [9] and the ongoing Mouse Brain Architecture Project [10], has created a pressing need for the development of new instrumentation viable for high-throughput whole-brain imaging.

Parallel to the "node" studies within the network, the "path" explorations called neuronal connectivity or connectome have been attracting vast attentions more recently. A fundamentally unsolved question in neuroscience is how the neurons are coordinated and communicated with architectural pathways and dynamic circuits to form perception, thought, emotion and motion. To

reach these answers, understanding the neuronal connectivity becomes crucial, as the connectome forms the structural foundation underlying neural circuits, and bridges genotypes and behavioral phenotypes [11, 12].

Neuronal connectivity exists at multiple levels: macro-, meso- or micro-scale. At the macroscale, long-range, and regional connections can be inferred from imaging white matter fiber bundles through diffusion MRI [12] and computational techniques based on correlations in measured time series in living brain [14-16]. The Human Connectome Project has paved such a framework during the past five years [17, 18]. The regional-based connectivity revealed by diffusion MRI studies is relatively with low resolution (~mm) and necessarily require validation. At the microscale, connectivity is described in terms of individual synapses, primarily through electron microscopy with nanometer-scale resolution [19]. So far, C. elegans is the only species whose wiring diagram of the 302 neurons is completely reconstructed [20]. The enormous time and resources required for this approach makes it best suited for relatively small volumes of tissue (<1 $mm^3$).

The meso-scale is between the micro- and macro-scales, where both local connections and long-range projections can be established. Histological tracing studies have generated a rich yet scattered knowledge of brain architecture in a wide range of animal species. Neural tracers were injected into certain brain regions and the circuitry starting from or terminating at those neuronal populations were visualized in later dissected brains, each of which contribute to an extraordinarily sparse matrix of high dimensions. The Brain Architecture Management System database [21] and Collations of Connectivity data on the Macaque Brain database [22] are two examples of ongoing efforts in mapping mammal brains. To date, our knowledge of whole brain connectivity is fragmented, lacking of a comprehensive apprehension in any single vertebrate species. With recent advances in both computing power and optical imaging techniques, it is now feasible to systematically map connectivity throughout the entire brain [23]. However,

considering the time and resources the tracer studies take for a full reconstruction of brain connectivity in any single species, new techniques that allow dense sampling and reconstruction with reasonable computational costs are striking at the mesoscale.

Understanding human brain connectivity is extremely challenging at the meso- and micro-scale. Much of our theoretical knowledge stems from very old sources or gets inferred from other species. Burgel and colleagues [24] developed a probabilistic atlas localizing major fiber bundles based on myelin stain of postmortem human brains, but those maps are rather coarse. The neural tracers, on the other hand, cannot be injected to living human brains, which make this otherwise widely adopted approach exclusively inappropriate for human studies. New staining method permeable to postmortem human brains is required. From another perspective, innovative imaging techniques that do not require exogenous labeling to reconstruct the connective maps would be a great desire.

## 1.2 MOTIVATION

The goal of this dissertation is to build up a high-resolution optical imaging system that is viable for large-scale brain imaging with an emphasis on the neuroanatomical tracts and connectivity, and that could significantly contribute to the realizations of a full connectome in mammalian brains. Such an optical imaging system should preferably have the following attributes: 1) It probes diverse structures in the brain, while unveiling a signature characteristic of the fiber tracts at the same time; 2) It has a brainwide coverage, and the full reconstruction is approachable with a reasonable time frame. 3) The imaging and reconstruction procedures are reliably conducted with high throughputs and easily scalable for various species including human; 4) The technique can be validated and is compatible with established neuroanatomical methods.

The emergence of optical coherence tomography (OCT) [25] offers a viable solution for 3D reconstruction of biological tissues with high spatiotemporal resolution. OCT, analogous to ultrasound imaging, makes use of an optical interferometry technique to provide cross-sectional images of tissues up to a few millimeters. The signal is intrinsically generated by the light back-scattered from the sample, thus enabling non-invasive or minimally invasive *in-vivo* studies and also facilitating *ex-vivo* investigations with minimal requirements for sample preparations.

OCT has proved to be a useful tool in a wide range of applications in neuroscience and neuroimaging [26]. Since invention, OCT has been most widely established in the clinical applications of ophthalmology, especially for evaluating the conditions of age-related macular degeneration [27]. The capabilities of visualization and quantification of the multiple neuronal layers in retina have provided an easily accessible window for central nervous system diseases such as multiple sclerosis [28]. Early studies have made noticeable efforts on brain tumor detections. OCT has been used for differentiating normal cortex from experimentally induced cortical dysgenesis in the adult rat neocortex [29] and imaging a metastatic melanoma *in-vitro* human cortex [30]. Unlike conventional histology, OCT can perform *in-vivo* imaging on a single specimen over time. In developmental neurobiology, studies have been performed on a few animal models including Xenopus central nervous system [31] and zebra fish embryos and eggs [32]. More recently, feasibility of OCT probe guiding neurosurgical interventions such as deep brain stimulation has been discussed [33]. Capabilities of OCT in localizing nerves and blood vessels have been investigated in peripheral nerves on rabbit [34]. Catheter OCT has been reported and tested for *in-vitro* human brain [35] and *in-vivo* rat brains [36]. In functional studies, OCT combined with other optical imaging modalities has been successful in the studies of vasculature and hemodynamics of the brain in disease models, such as stroke and addiction [37-39]. Intrinsic optical signal changes in OCT have been found in isolated nerves during cellular physiological events, which have been directly correlated with changes in membrane potentials

[40]. Transient structure deformations have been suggested during nerve excitations by a phase sensitive optical low-coherence reflectometry [41].

Despite the diversity of applications, systematic investigation on brainwide neuroimaging and neuronal connectivity using OCT is in scarcity. During the past several years, we have made efforts to extend the OCT applications into the regime of brain imaging and mapping through technical innovations. The rationales to use OCT on brain imaging and mapping are based on the following facts: 1) OCT provides 3D imaging with high spatial-temporal resolution, thus provides a solution for microstructure delineation and also substantial spatial coverage with a tractable time period; 2) The signal of OCT originates from local optical properties in the tissue, thus produces dense sampling and reconstruction; 3) The application of OCT can be extended with contrast-enhancing methods such as nano-probe and incorporated with various microscopy techniques that allows molecular phenotyping.

However, the application of OCT in brainwide neuroimaging also faces great challenges that remain to be solved. These challenges cause uncertainties and concerns that may compromise the potentials the technique would possibly bring to neuroscience fields. For a brief summary of the most critical challenges in this regard, we ask the following questions: What are the optical signals within the brain that give rise to the delineation of microstructures and the global organizations? What are the contrasts available for visualization and quantification of connective tracts? How should we design the system that is suitable to reveal as much information as possible? How can the whole-brain imaging be realized in a reasonable time frame? How complex are the 3D reconstruction algorithms? Can this method be validated by standard histology approaches? Can this method be incorporated with other conncectivity studies and provide important perspectives?

This dissertation addresses the aforementioned questions in the context of a novel multi-contrast (MC) OCT system tailored for imaging large-scale complex brains. A central focus is given on neuroanatomical pathways and connectivity. Strategies on comprehensive imaging of rat brains and a portion of human brain are established in details. To the end, we show that an integrated framework of multi-modality imaging and cross-scale validation could potentially approach the complete wiring diagrams in complex brains in the future.

## 1.3 ORGANIZATION OF THE DISSERTATION

The organization of the thesis is described as follows.

Chapter 2 reviews the principle and basic operations of OCT. Varieties of optical setups are introduced with their pros and cons. The extensions of OCT techniques with particular applications are discussed at the end.

Chapter 3 presents the MC-OCT system based on the polarization-maintaining fiber technique. With a single acquisition, the system is able to generate different perspectives of tissue microstructure and function. The system performance is characterized and biological sample images are demonstrated.

Chapter 4 uses the MC-OCT system to image *ex-vivo* rat brains. The system is capable of differentiating the gray and white matter, and especially target the white matter with the polarization contrasts. Spatial organizations and quantitative orientations of fiber tracts are shown. Fiber maps at micrometer scale resolution are created from the 3D optical sections.

Chapter 5 develops a serial optical coherence scanner (SOCS) for large-scale brain imaging. SOCS integrates the MC-OCT that was developed in Chapter 3 with a vibratome slicer to achieve both high resolution and large spatial coverage of macroscopic brains. This technique enables 3D

reconstruction of whole-brain without necessity of complicated registration algorithms. Fiber maps of ex-vivo rat brain with a spatial resolution of 15 x 15 x 5.5 $\mu m^3$ are illustrated.

Chapter 6 develops a quantitative analysis on the optical images to realize 3D fiber orientation and tractography in the brain. A structure tensor algorithm is implemented on the SOCS images described in Chapter 5, which it is also applicable to conventional OCT images. The algorithm performance is evaluated by optical measures in SOCS. Tractography is readily achieved with the tools developed for diffusion MRI techniques. The computational model provides a complementary approach to optical measures to achieve quantitative investigations.

Chapter 7 conducts a cross-validation study of SOCS and diffusion MRI on a postmortem human brain tissue. A strategy to achieve co-registration between the two imaging modalities has been established. Images of SOCS and dMRI from the same sample illustrate remarkable agreements in fiber architectures and orientations. In addition, SOCS reveals complicated fiber patterns that are not resolved by dMRI. This study shows great potential for cross-modality investigation in normal and diseased brains.

Chapter 8 concludes the dissertation with an outlook.

# CHAPTER 2 OPTICAL COHERENCE TOMOGRAPHY

## 2.1 INTRODUCTION

This chapter reviews the basics of the optical coherence tomography (OCT) techniques. OCT was firstly introduced in 1991 [25] as a high-resolution imaging technique that supports non-invasive biomedical studies with 3D perspective. Distinguished from previous optical imaging techniques, several characteristics are outstanding in OCT. 1) The axial resolution is independent of the lateral resolution; therefore, high axial and lateral resolution can be simultaneously achieved in a system. The resolution of OCT approaches that of a histological image. 2) The interferometric technique supports high dynamic range and sensitivity (>100 dB); therefore, imaging of weakly scattered structures in a highly scattering medium is possible. 3) The non-contact property provides a solution for non-invasive or minimally-invasive imaging in *in-vivo* studies and clinical applications. Inspired by both technical enhancements and application demands, diversity of OCT systems that extends the morphological measures to more complex structural and functional aspects were developed later on, and have proved to convey important clinical and pre-clinical values. Among those, the polarization-sensitive (PS) OCT and Doppler OCT have been most widely used. In this chapter, the basic principles of OCT and its technical implementations are reviewed. The concept of multi-contrast OCT is paved at the end along with the introduction of various OCT systems.

## 2.2 PRINCIPLE OF OPTICAL COHERENCE TOMOGRAPHY (OCT)

OCT is built upon the technique of low temporal coherence interferometry (LCI). Majority of OCT setups recruit a Michelson interferometer based scheme (Figure 2.1). The light from low temporal coherence light source is split into a reference field $E_r$ and a sample field $E_s$. The sample field is focused to the inside of tissue (some point beneath the surface) through an objective lens. Light back scattered from the tissue enters into the interferometer and mixed with the reference field, which is acquired by the photodetector. The OCT signal is generated by single backscatters from the tissue. Although the multiple scattered light does not contribute to the OCT signal, it adds up the background noise, which causes the reduction of imaging contrast, resolution and penetration depth.

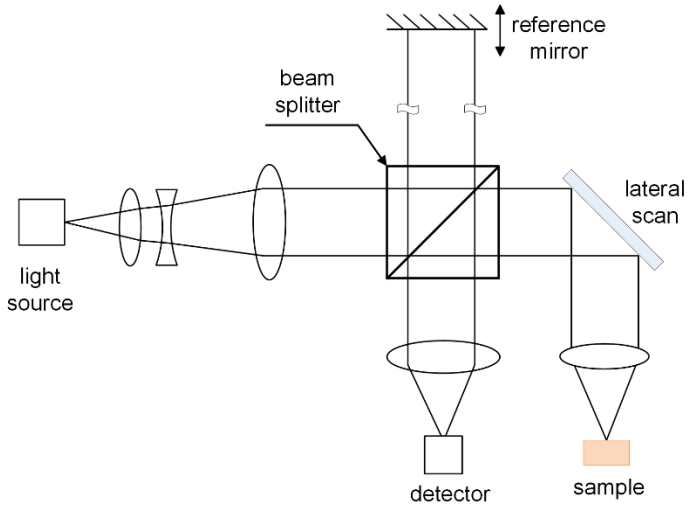


**Figure 2.1 Basic schematic of OCT setup.**

Constructive interference occurs when the mismatch between the optical path lengths of the sample and reference arms is within one coherence length. Otherwise, there is no interference fringe observed. The mutual coherence function of light waves from sample and reference arms are added up in the interferometer, and the interference of light waves is usually described as a second-order cross-correlation event. The averaged intensity exiting the interferometer is

$$\bar{I}_d(\tau) = 0.5(\langle I_s(t)\rangle + \langle I_r(t)\rangle) + G_{sr}(\tau) \quad \textbf{2.1}$$

$I_s$ and $I_r$ are the mean intensities reteruning from the reference and sample arms of the interferometer. They contribute to the dc signal at the detector. The third term, dependent on the time delay $\tau = \Delta z/c$ between the two beams, where where $\Delta z$ is the path difference between the beams and $c$ the speed of light, represents the amplitude of the interference fringes that carry the information about tissue structures. Assuming that the tissue behaves as an ideal mirror without altering the sample field, the correlation amplitude then depends on the temporal coherence of the source. The inteferogram $G_{sr}(\tau)$ is the real part of the cross-correlation of the two interfering beams, given by

$$G_{sr}(\tau) = Re\{\langle E_s^*(t+\tau)E_r(t)\rangle\} = |\Gamma(\tau)|cos[2\pi v_0\tau + \emptyset(\tau)] \quad \textbf{2.2}$$

$\gamma_{st}(\tau)$ is the complex temporal-coherence function of the source with argument $\emptyset(\tau)$, $2\pi v_0\tau$ is the phase delay between them, with $v_0 = c/\lambda_0$ being the central frequency of the source.

The complex cross-correlation function of $\Gamma(\tau)$ can be obtained from its real part by

$$\Gamma(\tau) = \frac{1}{2}G(\tau) + \frac{i}{2}HT\{G(\tau)\} \quad \textbf{2.3}$$

where HT denotes the Hilbert transform. The envelope of the coherence function in the form of $\Gamma_{sr}(\tau) = A_{sr}(\tau)e^{i\emptyset_{sr}(\tau)}$ is

$$A_{sr}(\tau) = \frac{1}{2}\sqrt{\left(G_{sr}(\tau)\right)^2 + (HT\{G_{sr}(\tau)\})^2} \quad \textbf{2.4}$$

And the phase is given by

$$\emptyset_{sr}(\tau) = arctan\left[\frac{HT\{G_{sr}(\tau)\}}{G_{sr}(\tau)}\right] \quad \textbf{2.5}$$

According to the Wiener-Khinchin theorem, the power spectral density $S(v)$ of the wave is related to the temporal correlation of the source $\Gamma(\tau)$ as a Fourier transform (FT),

$$\boldsymbol{S(\nu) = FT\{\Gamma(\tau)\}} \quad \textbf{2.6}$$

And the cross-spectral density function of the sample and reference beams is derived by the FT of the cross-correlation function. The following equation forms the basis of the Fourier domain OCT.

$$\boldsymbol{S_{sr}(\nu) = FT\{\Gamma_{sr}(\tau)\}} \quad \textbf{2.7}$$

A simple tissue scattering model treats the interference signal as a convolution of the sample response function or backscattering profile $h(\tau)$ with the temporal coherence of light source $\Gamma_{source}(\tau)$ [42]. By combining Eq. 2.2, the detected interference signal is given by

$$\boldsymbol{G_{sr}(\tau) = Re\{\Gamma_{sr}(\tau)) = Re\{\Gamma_{source}(\tau) * h(\tau)\}} \quad \textbf{2.8}$$

The Fresnel-reflecting interfaces sample model associates the amplitude reflectivity $\sqrt{R(\tau)}$ with the backscattering profile $h(\tau)$ [43]. When multiple scatters come from different layers in the sample, Eq. 2.8 can be rewritten as

$$\boldsymbol{I_d(\tau) = \sqrt{I_s I_r}\sqrt{R(\tau)} * |\Gamma_{source}(\tau)| \cos[2\pi\nu_0\tau]} \quad \textbf{2.9}$$

This convolution model has been used in many studies [44-47] to measure the locations and reflectivity of tissue layers in a manner analogous to pulse echo ultrasound, with $|I_d(\tau)|^2$ interpreted as a reflectivity profile analogous to an A-mode ultrasound scan.

## 2.3 OCT PARAMETERS

### 2.3.1. Resolution

The axial resolution of OCT is determined by the size of round trip coherence length ($l_c$).

$$\boldsymbol{l_c = \frac{2ln2}{\pi}\frac{\lambda_0^2}{\Delta\lambda} \approx 0.44\frac{\lambda_0^2}{\Delta\lambda}} \quad \textbf{2.10}$$

where $\lambda_0$ is the central wavelength and $\Delta\lambda$ is the bandwidth (full width at half maximum, FWHM) of the source.

As in conventional microscopy, the lateral resolution $\Delta x$ is related to the wavelength and the sample path optics that focuses the beam on a sample, and is given by

$$\Delta x = \frac{4\lambda_0}{\pi}\frac{f}{d} \tag{2.11}$$

where *d* is the spot size on the objective lens and *f* is its focal length.A specific problem in high-resolution OCT is the depth dependence of the lateral resolution. The depth of focus (DOF) is defined as the distance between the planes where the width of beam size becomes $\sqrt{2}\omega_0$ (Figure 2.2).

$$DOF = \frac{2\pi{\omega_0}^2}{\lambda_0} \tag{2.12}$$

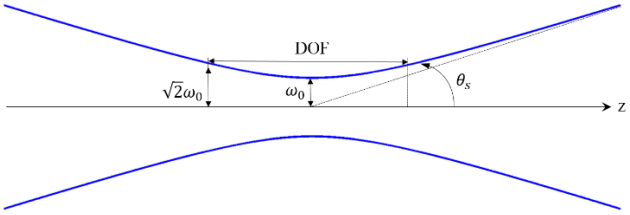


**Figure 2.2 Lateral resolution and depth of focus**

### 2.3.2. Depth

The typical light penetration of OCT is up to a few millimeters in tissue. With increasing depths, the number of photons detected by the photodetector contains more from multiple-scattering event. These photons can have their trajectories outside of the probing beam. The multiple scattering events will reduce time-coherence as well as space-coherence of these photons. Eventually, incoherent diffuse photons will dominate as light propagates through. The probing depth in OCT is defined as the depth at which double scattered photons begin to dominate.

The transition from single scattering to diffuse scattering has been experimentally studied [48, 49]. Gandjbakhche *et al* [50] showed that in the case of anisotropic random walks, the probability of a photon experiencing *n* scattering events and then returning to the surface is proportional to $n(1-g)/(1+g)$. Hence, the relative number of multi-scattering photons detected decreases with increasing scattering anisotropy $g$. On the other hand, increasing the NA causes detection of photons with a higher number of scattering events [48]. This dependence, however, is not as pronounced as the dependence on the optical anisotropy.

Since scattering and absorption in tissue monotonically diminishes with increasing wavelength at the near visible spectrum, the red end and the near-infrared (NIR) wavelength range is preferred in OCT. In this range, biological tissues have a scattering anisotropy around 0.9 [51], and hence the forward scattering photons dominate the detection.

Penetration depth is a critical parameter for *in-vivo* biomedical imaging studies. Since scattering is the major limitation of light penetration, there have been attempts to reduce that effect by matching the refractive indices of tissue with optical clearance. By applying anhydrous glycerol on the skin, a 50% increase of transmittance was achieved in OCT [52]. Tuchin *et al* [53] discussed index matching to enhance the optical penetration depth of blood.

### 2.3.3. Sensitivity

The sensitivity of OCT is referred to the weakest sample reflectivity $R_{S,min}$ yielding a signal power equal to the noise of the system. Sensitivity $S$ can be defined as the ratio of the signal power generated by a perfectly reflecting mirror ($R = 1$) and that generated by $R_{S,min}$. Since these signal powers are proportional to the corresponding reflectivitiy we have:

$$\boldsymbol{S = \frac{1}{R_{S,min}}} \qquad \textbf{2.13}$$

The dominating noise sources in OCT system are shot noise $\langle \Delta i_{sh}^2 \rangle$, excess intensity noise $\langle \Delta i_{ex}^2 \rangle$, and receiver noise $\langle \Delta i_{re}^2 \rangle$. The receiver noise can be calculated from manufacturer's specifications

or modeled as thermal noise. In the case of broadband light source the photocurrent noise comes from two factors: shot noise due to photocurrent variance and excess noise due to self-beating of the broadband light waves [54]. The signal-to-noise ratio (SNR) is the ratio of the mean signal power and the noise power:

$$\boldsymbol{SNR = \frac{2\alpha^2 P_s P_r}{\langle \Delta i_{sh}^2 \rangle + \langle \Delta i_{ex}^2 \rangle + \langle \Delta i_{re}^2 \rangle}} \qquad \textbf{2.14}$$

$\alpha$ is related to the quantum efficiency $\eta$ of the receiver with $\alpha = q_e \eta / E_v$.

In an optimized OCT system, the shot noise dominates the total noise power, and the sensitivity linearly depends on the source power. At lower power the receiver noise would limit the sensitivity, and at higher power no additional sensitivity could be gained due to the restraint of excess noise. In shot-noise limited regime, sensitivity of $S = 10^{11}$ and higher have been reported. Figure 2.3 illustrates the sensitivity of an OCT system as a function of reference reflectivity for different wavelength bandwidths. In a similar plot, Rollins and Izatt [55] applied the parameters of tissue scattering in OCT. Podoleanu [56] discussed the unbalanced versus balanced operation in OCT, indicating that the balanced OCT configuration has SNR benefit in high-speed OCT systems, in addition to the attenuation of mechanical noise and the avoidance of auto-correlation.

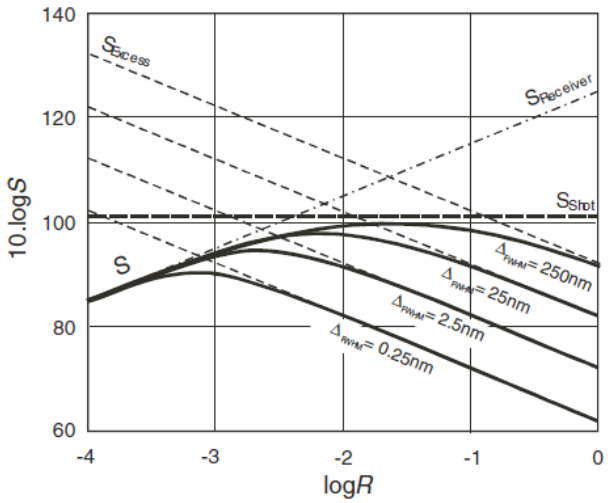


**Figure 2.3 Sensitivity curves of an OCT system as a function of logarithm reflectivity R from reference arm. Psource = 1.5 mW, mean wavelength $\lambda_0 = 830\ nm$; quantum efficiency $\eta = 0.8$. The corresponding sensitivity curves due to individual noise sources are shown as well. Reprinted from Fercher et al (2003) with permission.**

### 2.3.4. Phase noise

Noise on the phase of the interference pattern is related to the intensity SNR [57]. The phase noise, $\sigma_{\varphi}^{2}$, in radians is inversely proportional to the SNR in linear scale as follows

$$\boldsymbol{\sigma_{\varphi}^{2} = \frac{1}{2SNR}} \qquad \textbf{2.15}$$

Phase noise is largely influenced by mechanical and thermal vibrations too; Eq. 2.15 does not account for these environmental perturbations.

## 2.4 Implementations in time and Fourier domains

### 2.4.1. Time domain optical coherence tomography (TD-OCT)

The time domain (TD) OCT employs a depth-scan mechanism in the reference arm. It makes use of LCIs with different path length in the reference to detect depth localization of scatters where light re-emits in the sample. As the optical path in the reference arm cycles between shortest and longest possible lengths, a so-called depth profile or A-line is acquired. A broadband light source is used with an optical isolator that protects the source from back reflection of the interferometer. The light coupled into the interferometer is split between the sample and reference arms. The reference arm mainly consists of a mirror with an actuator that rapidly modulates the optical path length of the arm. It may also include a dispersion compensation mechanism, such as a rapid scanning delay line [58], or glass prisms with different indices of refraction [59]. The sample arm composes of a set of beam scanning component and a lens that focuses that the light on the tissue. By laterally scanning the position of the beam in the sample arm in 1D, a 2D cross-sectional or B-scan are realized. A second lateral axis in the sample arm can be used to construct a 3D volume. The returning light from the sample and reference arms interferes and the interference light is split at the beam splitter between source and detection arms. An optical detector is used in the

detection arm to acquire the signal from the interferometer. The acquired data is stored on a PC and can be analyzed in real time or with post-processing.

Figure 2.4 shows a sample of three reflectors and the corresponding A-line. The reflectivities of the three reflectors from left to right are 0.5, 0.5, and 0.8. Because $I_i \ \alpha\sqrt{R}$, and because light intensity after each reflector is attenuated, the maximum intensities measured at the same location of the reflectors are 0.25, 0.125, and 0.16.

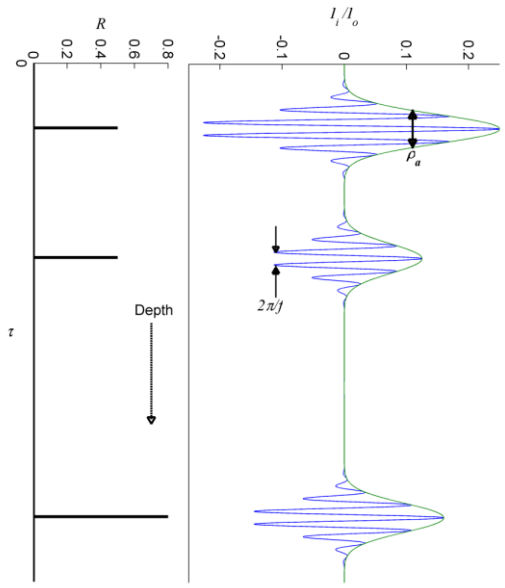


**Figure 2.4 (a) Simulation of a sample of three reflecting surfaces, where τ = 0 is at the top of the sample. (b) The TD OCT A-line of the sample. The A-line shows a coherence function corresponding to each reflector in the sample. The axial resolution, $\rho_a$, and the modulation interval $2\pi/f$ are indicated.**

The first OCT system uses a 50/50 splitter where 50% of the power is directed to the sample arm and the other 50% to the reference. As a result, only 25% of the source power is utilized in the detection. The efficiency of the imaging system can be improved by using a different splitting ratio. A 70/30 splitter which directs 30% of the light into the sample collects 70% of the light returning from the tissue in the detection arm improved the efficiency of light collected from the sample arm. The efficiency of OCT can be further improved in a fiber-based system. For

example, an optical circulator can be combined with a fiber coupler in the systems operating at 1300 nm [60].

Since the introduction of the first TD-OCT system, advanced mechanical scanning mechanisms were presented to increase imaging speed [58]. However, faster scanning also requires broader bandwidth of the modulation frequency [61]. The degraded sensitivity at higher acquisition speeds was observed [62].

### 2.4.2. Fourier domain optical coherence tomography (FD-OCT)

As opposed to TD-OCT which requires both axial and lateral scans in the system, the Fourier doman (FD) OCT only uses the lateral scan to construct a cross-sectional image. Spectral interference of light exiting the interferometer is acquired, and the depth information is encoded in such interference. FD-OCT is realized either by employing a spectrometer in the detection arm, called Spectral-Domain (SD) OCT [63-65], or by sweeping a wavelength-tuning light source, called Swept-Source (SS) OCT, or sometimes Optical Frequency Domain Imaging (OFDI) [66-68]. The speed of FD-OCT is limited by the acquisition rate of the spectrometer in SD-OCT, or by the source scanning speed in SS-OCT. Typical FD-OCT systems are an order of magnitude faster than the state of the art TD-OCT, and are more sensitive than TD-OCT systems [69-71]. Details about SD-OCT design will be discussed in Chapter 3.

As the Fourier components $A_s(K)$ of the scattering potential $F_s(z)$ cannot be measured directly, the FD-OCT derives a cross-correlation with acquired spectral power density function based on the Wiener-Khinchin theorem as described in Eq. 2.6. The measured spectral intensity $I(k)$ at the interferometer exit is the Fourier transform of the cross-correlation of the sample and reference waves, and is given by [72]

$$I(k) = I_r(k) + 2\sqrt{I_s(k)I_r(k)}\sum_n \sqrt{R_n}\cos kz_n + I_s(k) \quad \textbf{2.16}$$

with $k = 2\pi/\lambda$, the intensity in the sample arm $I_s(k)$ and reference arm $I_r(k)$. $R_n$ is the at different depths $z_n$ in the sample. A Fourier transformation links $z$ and $k$ space. Because of the nonlinear relation between k and λ, the spectra need to be interpolated first to create evenly spaced entities in the k-domain [65]. The middle term is superimposed by the spectral modulations of source at different frequencies. As a simplest case, a single mirror in the sample arm yields a modulation of the spectrum at one frequency. This frequency increases when the path length difference between sample and reference arms increases (Figure 2.5). Since additional surfaces will add more modulations, the so-called cross-spectral density function contains all spectral modulations caused by reflections from all the depths in the sample.

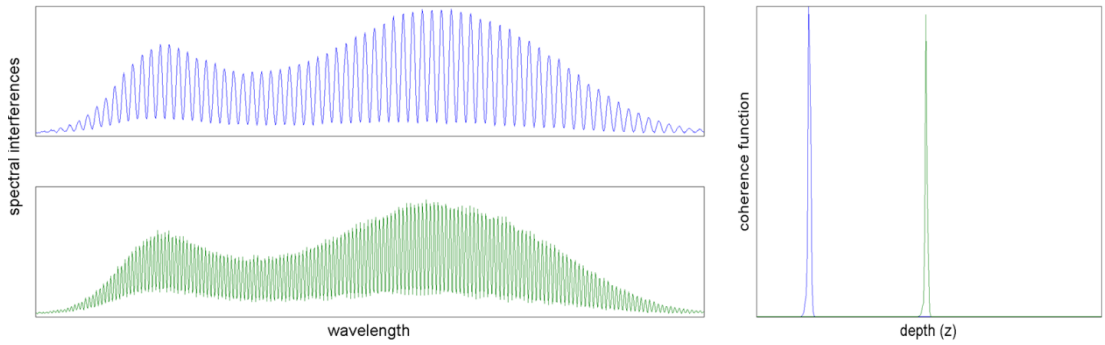


**Figure 2.5 Spectral modulations and the coherence functions (amplitude of depth profiles) in FD-OCT**

The depth profile is reconstructed by an inverse Fourier transform of the spectra, yielding the following convolution [72, 64]

$$FT^{-1}\big(I(k)\big) = \Gamma(z) \otimes (1 + \sum_n \alpha_n \delta(z - z_n) + \sum_n \alpha_n \delta(z + z_n) + O[I_s(k)]) \quad \textbf{2.17}$$

With the coherence function of the source is represented by $\Gamma(z)$; the second and the third terms yield conjugate pairs of sample scattering at different depth $z=z_n$. The last term represents the autocorrelation due to the interference of the sample centered at $z = 0$ and is usually ignored in

the representation of OCT images. After taking the absolute value of the Fourier transform, an A-line is created with reflected intensities encoded as a function of z.

## 2.5 POLARIZATION-SENSITIVE OCT

In this and the next section, we will focus on two specific types: polarization sensitive (PS) OCT and Doppler OCT, which will be jointly developed in later chapters of this thesis by using a novel fiber optics technique. Other specialized OCT techniques including spectral OCT, optical coherence elastography and thermal OCT have all proved to contribute to the pathological studies.

### 2.5.1. Light polarization

Light polarization describes the direction of wave oscillation. The light wave that propagates in the *z*-direction oscillates in the *x*-*y* plane; and the electric field of any polarization state can be described by the *x* and *y* components. For a low-coherence light wave with $\Delta v \ll v_o$, the electric field of the wave can be written as

$$\boldsymbol{E(t) = E_x(t)\hat{x} + E_y(t)\hat{y}} \qquad \textbf{2.18}$$

where $E_x(t) = E_{ox}(t)\cos[2\pi v_o t]$, $E_y(t) = E_{oy}(t)\cos[2\pi v_o t - \Delta\varphi]$, and $\Delta\varphi$ is the phase difference between of the electric field components in the *x* and *y* directions.

When either of $E_{ox}$ or $E_{oy}$ is equal to zero, light is said to be linearly polarized in the *y* or *x* direction, respectively. When $E_{ox}$ and $E_{oy}$ bear a phase difference of $n\pi$ ($n = 0, 1, 2\ldots$), the polarization is linear and oriented on *x*-*y* plane with an angle that depends on the ratio between $E_{ox}$ and $E_{oy}$. For other phase differences, the polarization state is elliptical. A special case is that

with $\Delta\varphi = \pm n\pi/2$ and $E_{ox} = E_{oy}$, the polarization state is circular. If an optical media alter the polarization state of propagating light, properties of the tissue may be inferred by the polarization alterations.

### 2.5.2. Birefringence

Birefringence is an optical property in tissue that can be caused by two mechanisms: intrinsic birefringence as a consequence of anisotropic properties of the molecules; and form birefringence originated from regularly arranged structures surrounded by another isotropic medium. When the period of the aligned molecules is shorter than the wavelength of the light, an electric field is induced across the structure. As a result, the speed of oscillating wave parallel to the axis of the structure is different from that perpendicular to the axis, resulting two orthogonal refractive indices (an ordinary refractive index $n_o$ and an extraoridinary refractive index $n_e$) in the medium (Figure 2.6). Birefringence ($\Delta n$) is defined as the difference between the two refractive indices.

$$\Delta n = n_e - n_o \qquad \textbf{2.19}$$

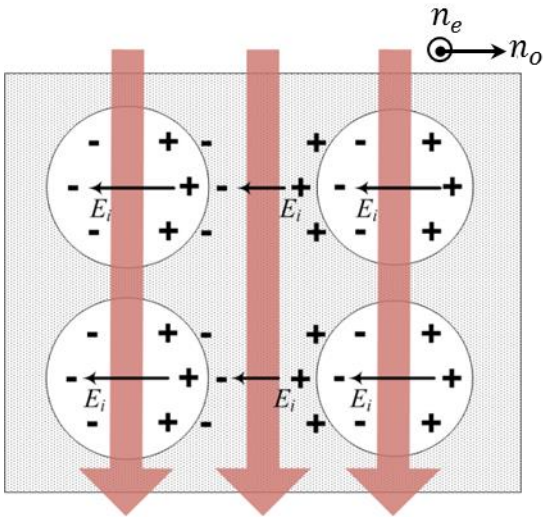


**Figure 2.6 Light propagation in a medium with aligned inclusions generates an induced electrical field $E_i$. The induced field alters the propagation speed of the polarization state parallel to it, resulting in form-birefringence.**

Birefringence also results in a single axis of optical anisotropy in the medium. Light passing through tissue with birefringence experiences a phase shift between the orthogonal oscillating waves parallel and perpendicular to the optic axis, called retardance ($\delta$), which linearly accumulates with propagating distance ($z$) (Figure 2.7).

$$\delta(z) = \frac{2\pi \cdot \Delta n \cdot z}{\lambda} \qquad \textbf{2.20}$$

Intrinsic birefringence can be found in dental enamel which consists of birefringent hydroxyapatite crystals. Form birefringence resulting from the spatial arrangement can be found in many tissues, such as collagen, muscle, tendon and nerve fibers.

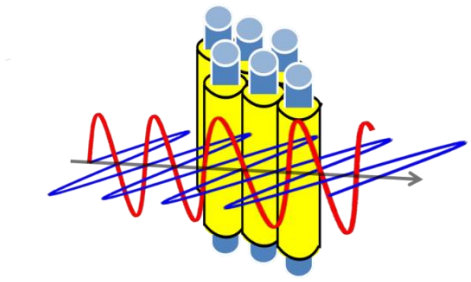

**Figure 2.7 Phase retardance linearly rises with depth as a result of birefringence.**

### 2.5.3. Polarization-sensitive OCT

The first polarization sensitive LCI technique was reported by Hee et al. [73], in which the phase retardance between orthogonal polarization modes backscattered from a birefringent sample was characterized. Later, de Boer et al. [74-75] developed a PS-OCT system for imaging thermally damaged tissue. Everett et al [76] and Schoenenberger et al [77] used PS-OCT to measure birefringence and generate birefringence maps of porcine myocardium. Hitzenberger et al. [78] reported PS-OCT images describing phase retardance and fast axis orientation in chicken myocardium. Since then, technical advances and biomedical applications of PS-OCT have been continuously developed.

The Jones formalism provides a convenient mathematical description of polarized light and

polarization effects [79] and has been commonly used in PS-OCT implementations. The first PS-LCI relies on the Jones formalism to measure the retardance independent of the sample axis orientation. The basic scheme based on a low-coherence Michelson interferometer is shown in Figure 2.8. A dual channel PS detection unit and polarization components are employed. A Jones matrix method has been proposed as well to describe the polarization properties of tissue [80].

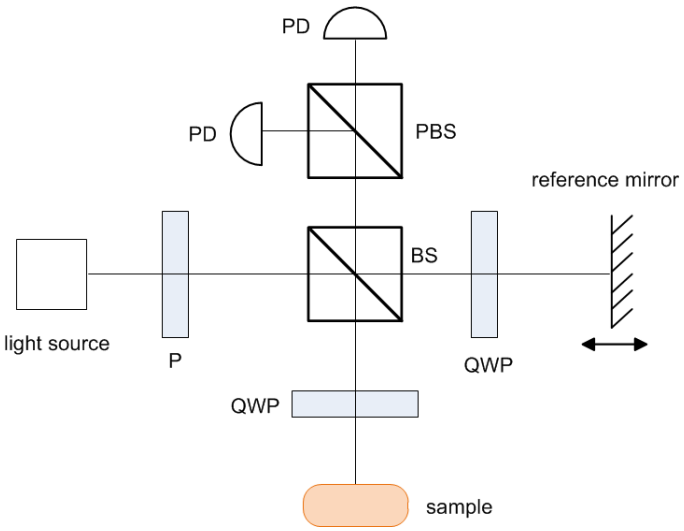


**Figure 2.8 Basic schematic of PS-OCT setup based on Hee et al (1992).**

The intensity at interferometer exit of each polarization channel can be described by a vector *I* as shown in Eq. 2.21, with the two elements representing the horizontal (h) and vertical (v) polarization states.

$$\langle \boldsymbol{I}(\Delta \boldsymbol{z})\rangle = \langle \boldsymbol{I_r}\rangle + \langle \boldsymbol{I_r}\rangle + \left\langle \begin{matrix} \boldsymbol{E^*_{r,h}E_{s,h}}(\Delta \boldsymbol{z}) \\ \boldsymbol{E^*_{r,v}E_{s,v}}(\Delta \boldsymbol{z}) \end{matrix} \right\rangle + \left\langle \begin{matrix} \boldsymbol{E_{r,h}E^*_{s,h}}(\Delta \boldsymbol{z}) \\ \boldsymbol{E_{r,h}E^*_{s,h}}(\Delta \boldsymbol{z}) \end{matrix} \right\rangle = \langle \boldsymbol{I_r}\rangle + \langle \boldsymbol{I_r}\rangle + \left\langle \begin{matrix} \boldsymbol{A_h}(\Delta \boldsymbol{z}) \\ \boldsymbol{A_v}(\Delta \boldsymbol{z}) \end{matrix} \right\rangle \quad \textbf{2.21}$$

Source light passing through the polarizer is horizontally polarized and described by the Jones vector as

$$\boldsymbol{E}(z) = E(z)\begin{pmatrix} 1 \\ 0 \end{pmatrix} \quad \textbf{2.22}$$

A 50/50 beam splitter splits the light into the reference and sample arms with equal amplitude, so the Jones vector representing light entering the sample and reference arms is expressed as

$$\boldsymbol{E}_{si}(z) = \boldsymbol{E}_{ri}(z) = \frac{E(z)}{\sqrt{2}}\begin{pmatrix}1\\0\end{pmatrix} \quad \textbf{2.23}$$

The polarization properties of any non-depolarizing optical components can be described by a Jones matrix $\boldsymbol{J}$, which transforms the incident polarization state $\boldsymbol{E}$ to a transmitted sate $\boldsymbol{E'}$, given by

$$\boldsymbol{E'} = \boldsymbol{J}\boldsymbol{E} \quad \textbf{2.24}$$

The Jones matrix for a birefringent material which induces a phase retardance $\delta$ between the electric field components parallel and orthogonal to a polarization state characterized by an orientation angle $\theta$ [81]

$$\boldsymbol{J}_b = \begin{bmatrix} e^{i\delta/2}cos_\theta^2 + e^{-i\delta/2}sin_\theta^2 & (e^{i\delta/2} - e^{-i\delta/2})cos\theta sin\theta \\ (e^{i\delta/2} - e^{-i\delta/2})cos\theta sin\theta & e^{i\delta/2}sin_\theta^2 + e^{-i\delta/2}cos_\theta^2 \end{bmatrix} \quad \textbf{2.25}$$

The polarization state of light returning from the reference arm is given by

$$\boldsymbol{E}_r(z_r) = \boldsymbol{J}_{QWP}(22.5)\cdot\boldsymbol{J}_{QWP}(22.5)\boldsymbol{E}_{ri} = \frac{1}{2}E(2z_r)\begin{pmatrix}1\\1\end{pmatrix} \quad \textbf{2.26}$$

The measurable Jones matrix for a linearly birefringent sample is $\boldsymbol{J}_s = \sqrt{R(z)}e^{-i2kz\bar{n}}\boldsymbol{J}_b(2kz\Delta n, \theta)$, with $R(z) and\ kz\bar{n}$ representing the reflectivity and average phase delay of a wave propagating to depth $z$, $\bar{n}$ being the average refractive index and $\Delta n$ the birefringence of the sample with an optic axis of $\theta$. The polarization state of light returning from the sample arm is given by

$$\begin{aligned}\boldsymbol{E}_s(z_s + z) &= \boldsymbol{J}_{QWP}(45)\cdot\boldsymbol{J}_s\cdot\boldsymbol{J}_{QWP}(45)\boldsymbol{E}_{si} \\ &\propto \sqrt{R(z)}\int \hat{e}(k)\, e^{-i2k(z_s+z\bar{n})}\begin{bmatrix}e^{i2\theta}\sin(kz\Delta n)\\ \cos(kz\Delta n)\end{bmatrix}dk\end{aligned} \quad \textbf{2.27}$$

where $z_s$ is the optical path length of the arm up to the sample surface. Using the Wiener-Kintchine theorem [Eq. 2.6], the interference terms in the horizontal and vertical polarization channels are given by

$$A_h(z,\Delta z) \propto \sqrt{R(z)} \int \sin(kz\Delta n)\cos(2k\Delta z + 2\theta)\, S(k)dk$$
$$A_v(z,\Delta z) \propto \sqrt{R(z)} \int \cos(kz\Delta n)\cos(2k\Delta z)\, S(k)dk \quad \textbf{2.28}$$

where $z$ is the depth of the light propagating in the tissue and $\Delta z$ is the optical path length difference between the sample and reference arms. Under the assumption of Gaussian power spectral density for the source

$$S(k) \propto exp\left[-(\frac{k-k_0}{\kappa})^2\right] \quad \textbf{2.29}$$

Where the FWHM spectral bandwidth of the source is $\kappa 2\sqrt{ln2}$. The intensity on the two polarization channels can be simplified as follows, with the FWHM of the interference fringe envelope given by $\Delta l 2\sqrt{ln2}$.

$$A_h(z,\Delta z) \propto \sqrt{R(z)}\sin(kz\Delta n)\cos(2k\Delta z + 2\theta)\, e^{-(\Delta z/\Delta l)^2}$$
$$A_v(z,\Delta z) \propto \sqrt{R(z)}\cos(kz\Delta n)\cos(2k\Delta z)\, e^{-(\Delta z/\Delta l)^2} \quad \textbf{2.30}$$

It should be noticed that layered samples yield depth cumulated retardance and optic axis orientation, so that the measured information may not be accurate for deeper layers without the depth-dependent correction.

The Stokes parameters and Mueller matrices provide a more complete description of the polarization properties of light passing through a turbid media. As both birefringence and scattering change the polarization state of light, the degree of polarization may degenerate during light propagation. In addition, the optic axis is typically variable in complex tissues. The Stokes parameters can be written as a real 4-vector $\boldsymbol{S = [I, Q, U, V]^T}$. The Mueller matrix $\boldsymbol{M}$ is a 4 by 4 matrix which linearly relates the Stokes vector of the backscattered light $\boldsymbol{S'}$ with the Stokes vector $\boldsymbol{S}$ of the illuminating light [82] $\boldsymbol{S' = MS}$.

The PS-OCT systems capable of yielding the full 4 x 4 Mueller matrix images have been presented [83, 84]. de Boer et al [85] presented an approach to realize depth resolved Stokes

parameters. The events of multiple scattering and speckle also affect the polarization measurement [86]. As polarization states in single-mode fibers alters due to the imperfect symmetry of the fiber core, translation of PS-OCT in fiber optics techniques demands more hardware components. Multiple polarization states and rapid modulations were introduced in single-mode fiber based PS-OCT system to achieve the immunity to the polarization variations in the fibers [87, 88].

## 2.6 DOPPLER OCT

Optical Doppler techniques describe a frequency shift arising from the motion in a sample relative to a reference, are based on interferometry technique when the light scattered by the moving particles interferes with a reference beam. The success of laser optical Doppler techniques has led to vast clinical applications in disease screening and diagnosis. The development of LCI and OCT further extends the optical Doppler techniques, by virtue of their depth localization capability. Doppler OCT provides quantitative information on 3D flow rates in vivo [89-94].

Wang et al [95] first demonstrated the velocity data in a LCI experiment. The power spectrum of the interference intensity was acquired with a spectrum analyzer, and a velocity profile of microspheres suspended in the fluid was derived using the centroid of the Doppler-shifted spectrum at each position in the conduit [96, 89]. Another approach to obtain the Doppler shift is to use a phase-sensitive measurement [97]. The phase change ($\Delta\emptyset$) calculated from multiple A-lines collected at the same position of the sample is related to the flow velocity ($v$) with a refractive index $n$, a collection time $T$ and the angle of incidence of the probe beam relative to the moving scatter $\alpha$.

$$v = \frac{\Delta\emptyset \cdot \lambda_0}{4\pi \cdot T \cdot n \cdot cos\alpha} \quad \textbf{2.31}$$

Chen et al [98] applied sequential lateral scans to detect the flow information. Zhao et al [99] applied a short-time fast Fourier transform algorithm to reconstruct the structure and the depth localized Doppler signal with demodulated depth-scan of interference. Depth resolution of the velocity estimate is related to the STFT window length by the Fourier uncertainty relation. Figure 2.9 presents an example obtained by a color DOCT technique in which the detected velocity is color coded to indicate the magnitude and the direction of flow. Such imaging can be used for studying the pathogenesis of vascular diseases in ophthalmology and cardiology. In contrast to angiography, Doppler OCT is non-invasive.

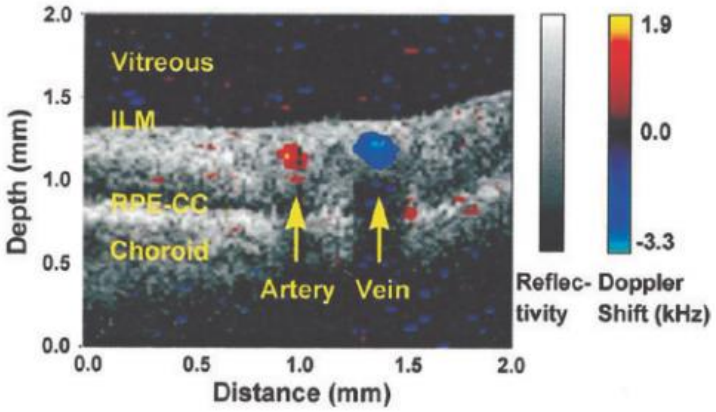


**Figure 2.9 Doppler OCT images of bidirectional blood flow in retina. Reprinted from Yazdanfar et al (2000) with permission.**

In FD-OCT, the depth distribution of the Doppler frequency can be obtained from two spectral records of the scattered spectrum laterally. An important advantage of Doppler OCT in Fourier domain is the high phase stability and the speed [100]. Leitgeb et al [101] have shown that longitudinal velocity components from ~10 μm/s to 2 mm/s can be measured at a rate of 104 A-lines per second without readjusting the instrumental parameters. Continuous hardware and algorithm developments for more sensitive and more robust Doppler OCT techniques have been seen in recent years [102-108].

# CHAPTER 3 POLARIZATION-MAINTAINING FIBER BASED MULTI-CONTRAST OPTICAL COHERENCE TOMOGRAPHY

## 3.1 INTRODUCTION

The multi-contrast (MC) OCT incorporates multiple functional variations of OCT into a single system that enables multi-parametric acquisition at the same time, including conventional, phase-sensitive, polarization-sensitive and Doppler OCT imaging. As opposed to individual OCT setups that may obtain the multi-angle information through separate sessions, the MC-OCT provides unique opportunities in several aspects. From temporal perspective, it can provide the interaction of different signals revealing physiological processes through simultaneous data collection. From spatial perspective, it allows for interrogation of structural architectures probed by different contrasts through automatically aligned framework. Those merits are particularly beneficial for answering some important neuroscience questions such as neurovascular coupling, brain mapping, and brain-wide wiring diagram and their topological relationship with cell types. In addition, the integrated system is more time efficient in data acquisition and potentially cost efficient as multiple OCT setups commonly share essential hardware components. Previous studies have built up multi-functional OCT using single mode fibers, where PS and Doppler signals are obtained in a single set of measurements.

There are several reasons for incorporating PS and Doppler measures in a MC-OCT. Among the functional variations of OCT techniques, which provides additional information relevant to physical or physiological parameters of biological tissues, PS-OCT and Doppler flow OCT are

two of the most commonly used. On the other hand, the analysis of light polarization in PS-OCT often requires the phase information of the optical signals, which naturally supports the feasibility of the Doppler measures as well.

PS-OCT focuses on tissue birefringence, and characterizes the structural anisotropy and the angle of axis. Two approaches have been parallel seen in PS-COT setups (see examples in Figure 3.1). The bulk system [74, 76, 109, 110] operates the polarized light in free space. It has the advantages of simple optics and computational inexpensive algorithms, and the polarization states are stably kept in air. However, the stability of the interferometer may not be guaranteed when the system is transferred from bench-top to bed-side, and it's not easy to be incorporated into endoscopy. The single-mode fiber setup [87, 88, 111], on the other hand, has more flexibility in clinics. However, sophisticated polarization manipulation such as polarization modulator has to been employed to ensure the polarization states immune from external disturbance, and multiple measurements are usually required. Those complications results in highly demanding computations, and may lead to compromised reliability of transient polarization measures.

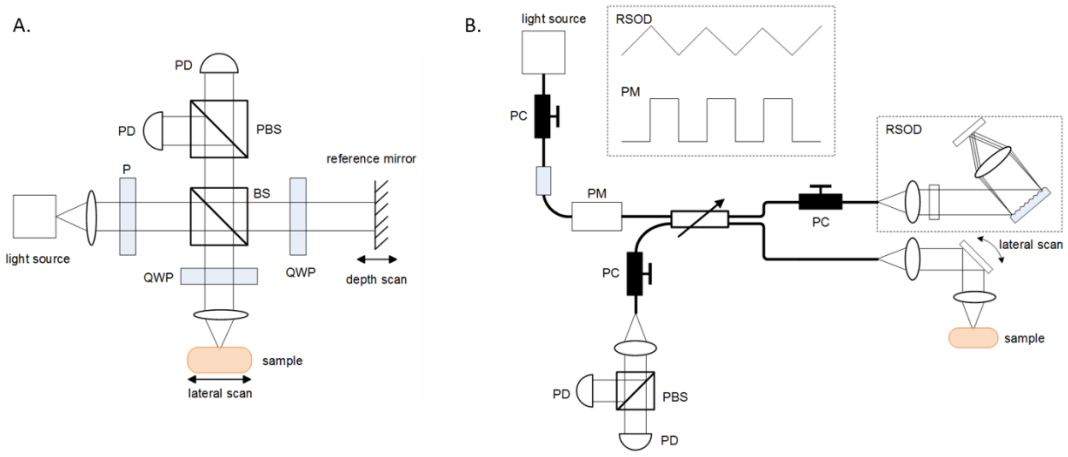


**Figure 3.1 Two illustrative schematics of bulk (A) and single-mode fiber based (B) PS-OCT systems.**

The introduction of polarization-maintaining fiber (PMF) based technique into PS-OCT has made efforts in untangling the complications in PS-OCT setups and shown promises for vast

biomedical applications [112, 113]. The PMF technique is able to maintain the orthogonal linear-polarization states in a specially designed single-mode fiber core, and thus combines the advantage of flexibility in fiber-based system, and design and computation efficiency in bulk system, thus provides a viable solution for clinical translations. As earlier discussed, the Fourier domain OCT is superior in sensitivity and acquisition speed, the goal of this chapter is to design a PMF based OCT system in spectral domain. Because the phase information is simultaneously available with the spectral domain design, this PMF based PS-OCT system supports the phase-sensitive and Doppler flow measurements as well. To this end, a PMF based MC-OCT system is constructed for high-resolution tissue imaging and characterization. The major challenges are to design a spectrometer that allows simultaneous acquisition of two polarization channels with equally high performance, and to eliminate any ghost lines and ghost images. This chapter will discuss the optical design and implementation of PMF based multi-contrast OCT system. System characterization is provided and several biological applications are demonstrated at the end.

## 3.2 SYSTEM DESCRIPTION

### 3.2.1. Polarization-maintaining fiber

Polarization-maintaining fiber is a special type of single-mode fiber that preserves the polarization states during light propagation within the fiber. The polarization-maintaining fibers have been successfully demonstrated with bow-tie fibers [114], flat depressed-cladding fibers [115], and PANDA fibers [116], by a stress effect to induce differed refractive indices between the orthogonal modes. In this type of design, stress-applying parts were applied to the fiber core through a buffer layer in between. The PMF can also be fabricated using the geometrical effect of core and stress around the core, such as elliptical core fibers [117-122], a dumbbell core fiber [123], a four-section fiber [124], a side pit fiber [125], and a side tunnel fiber [126]. However, this type of PM fibers generally bears high optical loss.

In PM fiber selection, there are two parameters that are taken consideration, the mode-coupling parameter and transmission loss. The first parameter characterizes the polarization-maintaining ability and crosstalk as follows:

$$\boldsymbol{CT = 10log\frac{P_y}{P_x}} \qquad \textbf{3.1}$$

where $P_x$ and $P_y$ are the powers of the input mode and the coupled mode in an ensemble of fiber length.

A PANDA PM fiber with a PM coupler is selected for the MC-OCT design. Figure 3.2 shows a diagram of the cross section of the PMF. The stress rods yield a fast axis and a slow axis on the orthogonal channels. Light in the fast axis experience a lower index of refraction and propagates faster than the slow axis. PMF maintains the orthogonal linear polarization states despite external perturbations. Typical polarization isolation in PMF is 40 dB per 4 m for PANDA fibers[1].

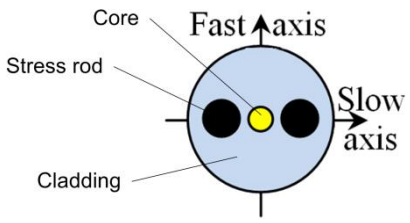


**Figure 3.2 Cross section of the PMF. The two stress elements create a uniaxial stress on the core and generate constant birefringence in the fiber.**

### 3.2.2. Optical setup

The light source is a 25 mW superluminescent diode centered at 840 nm with a full-width-half-maximum bandwidth of 50 nm. Light from the source is linearly polarized by a polarizer in a fiber bench, and coupled into one of the orthogonal channels of the PMF. A 2x2 PM coupler splits the light into the reference (70%) and sample (30%) arms. In the reference arm, collimated

[1] From Corning datasheet

light travels through a quarter-wave plate (QWP) oriented at 22.5° with respect to the incoming polarization state, and is reflected by a mirror. After passing the QWP twice, the linear polarization state is oriented at 45°; thus, light returning from the reference arm is coupled back into the fast and slow channels of the PMF with equal power. In the sample arm, light passes through a QWP oriented at 45°, which ensures circularly polarized light incident on a sample. Since tissue birefringence alters the polarization state, the back-scattered light couples into the PMF channels after passing through the QWP again. An OCT scan lens (focal length: 36 mm) is mounted in the sample arm to ensure high quality over large scan area. During imaging, the light beam is scanned by xy-galvo mirrors over the tissue.

In the detection arm, a custom-built polarization-sensitive spectrometer records the spectra for interferences. The spectrometer contains a collimating lens, a grating to split the wavelength of light source, a prism to divide the polarization channels, focusing lens and a camera to acquire the spectra. The specifications of each component need to be design complying with the available products and the performance requirements.

a) Imaging depth

The camera is a 2048-pixel line scan camera (Basler, Germany). Each polarization channel occupies 1024 pixels (*N*). Given a light source with the bandwidth $\Delta\lambda = \lambda_{max} - \lambda_{min}$, the spectral resolution $\delta\lambda$ is given by

$$\boldsymbol{\delta\lambda = \frac{\Delta\lambda}{N}} \quad \textbf{3.2}$$

The imaging depth $z_{max}$ is inversely proportional the spectral resolution and expressed as

$$\boldsymbol{z_{max} = \frac{\lambda_0^2}{4n\delta\lambda}} \quad \textbf{3.3}$$

where $\lambda_0$ is the central wavelength of the light source, n is the refractive index. With a central wavelength of 840 nm, $\lambda_{max}$ of 876.83 nm and $\lambda_{min}$ of 805.79 nm, the imaging depth is 2.54 mm in air.

b) The focal length of the collimator in the detection

Resolvance ($R$) of the grating is defined by $R = \frac{\lambda_0}{\delta\lambda}$, where $\lambda_0$ is the central wavelength and $\delta\lambda$ is the spectral resolution. Then the spot size ($A$) on the grating is calculated to be A=R/1200 (line/mm).

As the NA of the fiber is 0.13, NA = n·sinα, where n is the refractive index, the focal length ($f_2$) is given by

$$\boldsymbol{f_2 = \frac{A}{tan\alpha}} \qquad \textbf{3.4}$$

c) The focal length of the focusing lens in front of the camera

Dispersion of the source with bandwidth $\Delta\lambda$ is given by $s = \frac{\Delta\lambda}{D}$. As the total length ($L$) of the sensor on the camera is $L = N \times \Delta l$, given the individual sensor size ($\Delta l$) to be 10 μm, the focal length of the lens ($f_1$) is given by

$$\boldsymbol{f_1 = \frac{L}{tan\, s}} \qquad \textbf{3.5}$$

d) Split angle of the prism

The split angle of the prism is customized so that the spectra on the two polarization channels are completely separated side by side and occupy the full pixels on the camera. Figure 3.3 gives an illustrative schematic of the optical path.

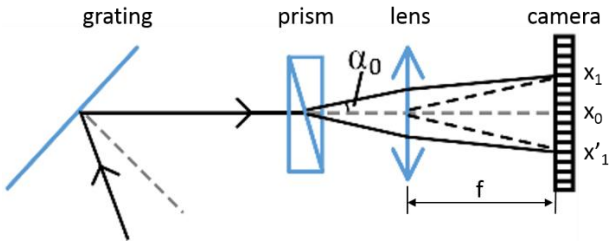


**Figure 3.3 Design of the prism split angle ($\alpha_0$) optimized for the spectrometer in the MC-OCT.**

Assuming the central wavelength of the light source is directed to the middle of left and right half of the camera pixels for each polarization state, given individual sensor size $\Delta l$, the number of

pixels ($N$) each polarization channel occupies, and the focal length of the lens $f$, the split angle $\alpha_0$ is expressed as

$$\boldsymbol{\alpha_0 = 2atan\left(\frac{x_1 - x_0}{f}\right) = 2atan(\frac{N\Delta l}{2f})} \quad \textbf{3.6}$$

Based on the desired parameters discussed above, the spectrometer implementation includes a 50 mm achromatic collimating lens directs the light exiting the interferometer to a 1200 lines/mm transmission grating. A Wollaston prism with splitting angle of 6° separates the orthogonal polarization channels. Then, a 200 mm achromatic lens focuses the optical spectra from two channels onto a single line scan camera (*Basler sprint 140k*) which contains 2048 pixels (1024 pixels for each channel). The schematic of the optical setup is shown in Figure 3.4.

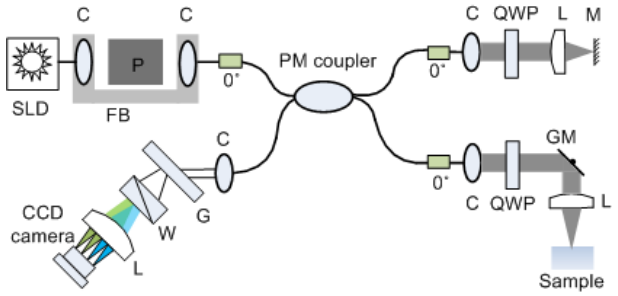


**Figure 3.4 (a) Schematic of multi-contrast OCT. SLD: superluminscent diode, C: collimator, P: polarizer, QWP: quarter-wave plate, L: lens, M: mirror, GM: galvo mirror, G: grating, W: Wollaston prism, LSC: line scan camera.**

When the path difference between the reference and sample arms is within the imaging depth, spectral modulations related to depth information occur. Images are reconstructed by following steps: data in wavelength-space are remapped and interpolated in *k*-space [127], dispersion imbalance is compensated [128], the background from reference arm is subtracted [69], and an inverse Fourier transform algorithm is applied. The algorithms for individual steps are discussed in the following sub-sessions. Figure 3.5 illustrates the spectral modulations on the orthogonal polarization channels (a), and corresponding coherence functions (b).

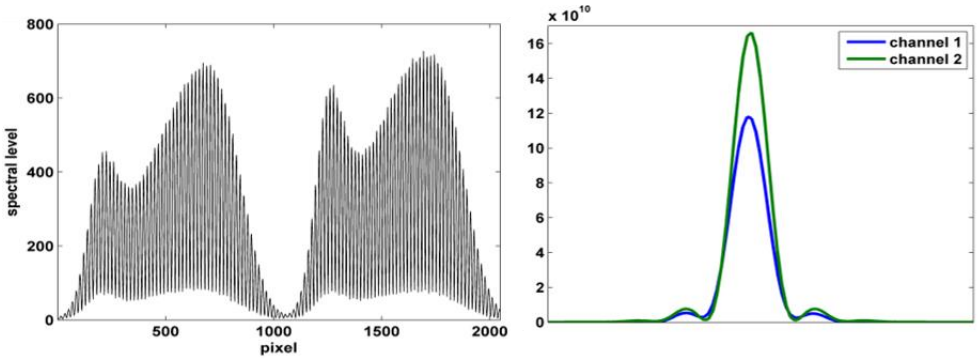


**Figure 3.5 Data acquisition and reconstruction in the spectral domain MC-OCT. Left: spectral modulations on the two polarization channels; Right: their corresponding coherence functions.**

The system has an axial resolution of 7.7 μm in air, and 5.5 μm in tissue (refractive index: 1.4). The lateral resolution estimates to be ~15 μm.

### 3.2.3. Spectrometer characterization

The spectrometer needs to be calibrated to obtain the pixel-wavelength correspondence of the two polarization channels on the camera. This relationship can be deduced theoretically by grating equations.

$$\boldsymbol{d(sin\vartheta_i + sin\vartheta_d) = \lambda} \quad \textbf{3.7}$$

where $\vartheta_i$ and $\vartheta_d$ are the incident angle and the diffracted angle with respect to the grating's normal vector, $\lambda$ is the wavelength, and $d$ is the slit width of the grating.

For a light source with central wavelength $\lambda_c$, we would like to direct it to the center of the camera sensor without polarization splitting. Therefore, the grating equation is given by

$$\boldsymbol{d(sin\vartheta_i + sin\,\vartheta_c) = \lambda_c} \quad \textbf{3.8}$$

thus

$$\boldsymbol{\vartheta_c = sin^{-1}(\lambda_c/d - sin\vartheta_i)} \quad \textbf{3.9}$$

For other wavelengths diffracted with an angle α with respect to the optical axis of the lens,

$$\boldsymbol{\vartheta_d = \vartheta_c - \alpha} \quad \textbf{3.10}$$

And

$$\boldsymbol{tan\alpha = \frac{x - x_0}{f}} \quad \textbf{3.11}$$

We get the wavelength corresponding to the pixel index *i* on the camera

$$\boldsymbol{\lambda_i = d\{sin\vartheta_i + \sin\left[\sin^{-1}(\frac{\lambda_c}{d} - sin\vartheta_i) - \tan^{-1}\left(\frac{x_i - x_0}{f}\right)\right]\}} \quad \textbf{3.12}$$

Considering an extra small angle $\alpha_0$ due to polarization separation by the Wollaston prism, the wavelength correspondence is modified as

$$\boldsymbol{\lambda_i = d\{sin\vartheta_i + \sin\left[\sin^{-1}\left(\frac{\lambda_c}{d} - sin\vartheta_i\right) - \tan^{-1}\left(\frac{x_i - x_0}{f}\right) \pm \alpha_0/2\right]\}} \quad \textbf{3.13}$$

As the practical spectra alignments may be slightly off from the theoretical design, the calibration was conducted experimentally. Two approaches are proposed here. In the first method, a wavelength tunable Ti-Sapph laser is included. The laser replaces the SLD and a commercial spectrometer was used with the customized spectrometer together. The laser was tuned to specific wavelengths that can be accurately read by the commercial spectrometer. At the same time, the pixel numbers on the camera were recorded. The pixel numbers on the camera for 14 wavelengths were identified, and second-order interpolation was applied to find wavelengths of all pixels for both polarization channels (Figure 3.6A). In the second method, a grating is included to selectively direct the wavelength of SLD to the OCT spectrometer and a calibration spectrometer. The grating is placed in the reference arm. The spectral component, whose optical axis is orthogonal to an end mirror, is coupled back into the PMF; hence, selection of a single wavelength is realized by adjusting the mirror. The pixel numbers on the camera are identified. At the same time, the zero-order component of the transmission grating from the detection arm of the MC-OCT is coupled to the multimode fiber of the commercial spectrometer for actual reading of the wavelength (Figure 3.6B).

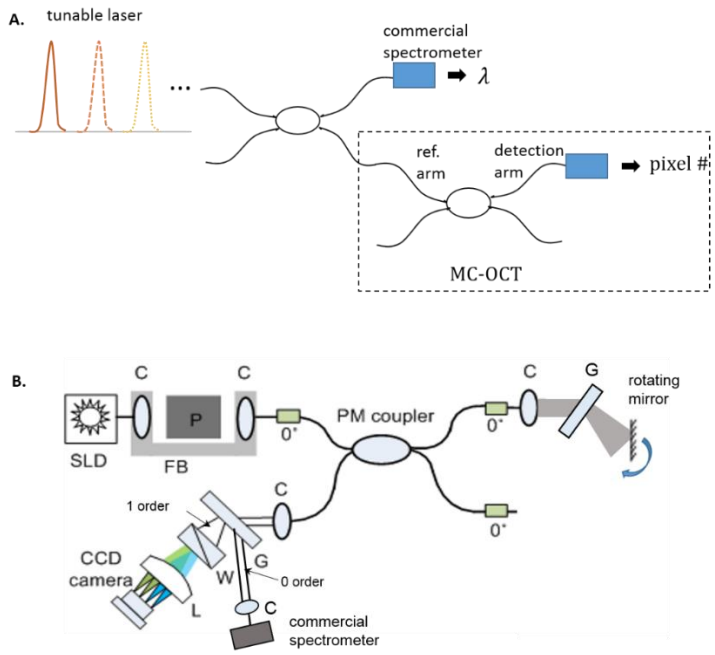


**Figure 3.6 Two setups for spectrometer calibration (wavelength v.s. pixel number on the camera) in the MC-OCT. SLD: superluminscent diode, C: collimator, P: polarizer, QWP: quarter-wave plate, L: lens, M: mirror, GM: galvo mirror, G: grating, W: Wollaston prism, LSC: line scan camera.**

## 3.3 IMAGE RECONSTRUCTION

### 3.3.1. Dispersion compensation

Chronic dispersion occurs when broadband light passes through multiple optics components. The refractive index differs between the spectral components of light passing through a medium, and thus influences the speed of achromatic light with different impacts. When the optical path lengths of reference and sample arms are different, the dispersion mismatch could significantly broaden the width of coherence function in OCT [130]. Dispersion can be compensated by hardware such as using a rapid scanning optical delay [58] in the reference arm, or adding glass or fused silica prism with adjustable thickness [59]. However, software based compensation algorithms would be more convenient to implement [132].

A dispersion mismatch introduces a phase shift $e^{i(k)}$ in the complex cross-spectral density *I(k)* as a function of wave vector *k*. The relation between the phase *θ(k)* and the dispersions can best be described by a Taylor series expansion [133]:

$$\boldsymbol{\theta(k) = \theta(k_0) + \theta^{(1)}(k_0)(k - k_0) + \frac{1}{2}\theta^{(2)}(k_0)(k - k_0)^2 + \cdots + \frac{1}{n!}\theta^{(n)}(k_0)(k - k_0)^n} \quad \textbf{3.14}$$

where $k_0$ is the wave number corresponding to the central wavelength $\lambda_0$ ($k_0 = 2\pi/\lambda_0$). Dispersion can be compensated by multiplying the dispersed cross-spectral density function *I(k)* with a phase term $e^{-i\theta(k)}$ [128]. To determine the phase term, the spectrum with respect to k-space is Fourier transformed to z-space, and the coherence function is shifted to the origin. Then a complex spectrum *I'(k)* is obtained with an inverse Fourier transform. The phase *θ(k)* is obtained from the real and imaginary components of *I'(k)* by

$$\boldsymbol{\theta(k) = \tan^{-1}\frac{imag(I'(k))}{real(I'(k))}} \quad \textbf{3.15}$$

The curve of *θ(k)* was fit to a 9th order polynomial function, yielding a set of coefficients. The last seven coefficients are used for compensation.

### 3.3.2. Contrasts

Polarized light and optical components can be described by Jones calculus. Interferometric signals on the orthogonal polarization channels are expressed as:

$$\tilde{A}_{1,2}(z) \propto A_{1,2}(z)\exp\left[i\Phi_{1,2}(z)\right] \quad \textbf{3.16}$$

where *A* and *Φ* denote the amplitude and phase of the interference signal, respectively along the depth z, and subscripts *1* and *2* correspond to the cross-coupled and main polarization channels. In SD-OCT, an inverse Fourier transform is applied to the measured spectral intensities to obtain

the depth profiles of the sample as shown in Eq. 3.16 [64]. The reflectivity $R(z)$ and phase retardance $\delta(z)$ information are extracted from the magnitudes of the complex signals on each channel as [134]

$$R(z) \propto A_1(z)^2 + A_2(z)^2 \quad \textbf{3.17}$$

$$\delta(z) = \arctan(A_1(z)/A_2(z)) \quad \textbf{3.18}$$

The optic axis orientation is derived from the phase information of the complex depth profiles and expressed as below [134]. Due to an arbitrary phase delay between the PM-fiber channels, our system yields a relative optic axis orientation $\theta'(z)$ across lateral scans.

$$\theta'(z) = \frac{\pi - (\Phi_1(z) - \Phi_2(z))}{2} \quad \textbf{3.19}$$

However, the absolute axis orientation can be realized by using a reference retarder with a known axis. The calibration procedure and the signal reconstruction is discussed in Chapter 4.4.

Sequential processing approach is implemented to get the flow information, in which the phase difference between successive depth scans is used to determine flow velocity [99]. Bi-directional flow ($\omega$) under PS-OCT configurations can be calculated as [127]:

$$\omega(z) = \frac{1}{T} \frac{A_1^2(z)\Delta\Phi_1(z) + A_2^2(z)\Delta\Phi_2(z)}{A_1^2(z) + A_2^2(z)} \quad \textbf{3.20}$$

where $\Delta\Phi_{1,2}(z) = \Phi^{(n)}_{1,2}(z) - \Phi^{(n-1)}_{n-1}(z)$, *n* and *n-1* denoting sequential A-lines, and *T* is the time interval between two A-lines.

## 3.4 SYSTEM CHARACTERIZATION

### 3.4.1. Noise

The photon collection in the spectrometer of spectral domain OCT is obtained by a charge-coupled device (CCD) of a line array. To facilitate the noise analysis in the case of CCD

detections, the signal and noise terms will be expressed in charge squared ($q_e^2$). As only the real part of the complex cross-spectral density is detected in spectral domain PS-OCT, the resulting signal S is given by

$$\boldsymbol{S = \frac{2\eta^2 q_e^2 P_{ref} P_{sample} \tau_i^2}{E_v^2}} \quad \textbf{3.21}$$

Where $q_e$ is the electron charge, $P_{ref}$ and $P_{sample}$, respectively, are the reference and sample power per detector element at the detection arm fiber tip, $\tau_i$ is the integration time, and $E_v$ is the photon energy.

The read out and dark noise $\sigma_{r+d}^2$, shot noise $\sigma_{sh}^2$ and relative intensity noise (RIN) $\sigma_{RIN}^2$ contribute to the overall noise per read out cycle and per detector elements, and the overall noise is given by

$$\boldsymbol{N = \sigma_{r+d}^2 + \sigma_{sh}^2 + \sigma_{RIN}^2 = \sigma_{r+d}^2 + \frac{2\eta q_e^2 P_{ref} \tau_i}{E_v} + \frac{2\eta^2 q_e^2 {P_{ref}}^2 \tau_i \tau_{coh}}{E_v^2}} \quad \textbf{3.22}$$

Where $\tau_{coh}$ is the coherence time given by $\tau_{coh} = \sqrt{2lin2/\pi\, \lambda_0^2/c\Delta\lambda}$, and c is the speed of light. The optimal signal to noise performance is achieved when shot noise dominates the read-out noise and the RIN. The optimal reference power is found when read-out noise and dark noise are equal to the RIN. Thus, the optimal reference power is found to be

$$\boldsymbol{P_{ref} = \frac{\sigma_{r+d} E_v}{\eta q_e \sqrt{2\tau_i \tau_{coh}}}} \quad \textbf{3.23}$$

For a shot noise dominated system, we have $\sigma_{sh}^2 > \sigma_{RIN}^2$ and $\sigma_{sh}^2 > \sigma_{r+d}^2$, resulting a prerequisite for the reference power of $P_{ref} < 12.7\mu W$ directed to the camera.

We characterize the noises of the MC-OCT system as shown in Figure 3.7. The readout and dark noises are recorded by the CCD sensors without incident light, and the measured noise is the variance of the light source spectrum. The measured noise is significantly greater than the readout and dark noises, and the reference power to the detection arm as discussed in the later section of sensitivity analysis is significantly less the maximum requirement for shot-noise dominance.

Therefore, we conclude that the MC-OCT system is shot-noise dominant. Treating the shot noise as a Poisson process, the theoretical noise is calculated by

$$\boldsymbol{\sigma^2 = \langle \left( I_e(\lambda) - \overline{I_e(\lambda)} \right)^2 \rangle = \frac{\overline{I_e(\lambda)}}{\Delta n_e}} \qquad \textbf{3.24}$$

where $\Delta n_e$ is the number of electrons required for 1 unit of intensity increment on the CCD sensors.

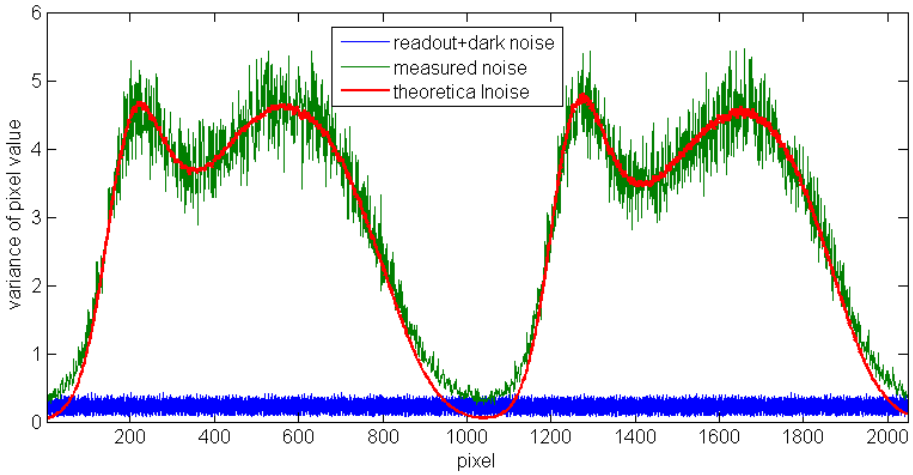


**Figure 3.7 Noise characterization of the MC-OCT system. The green curve shows the noise of the source spectrum. The curve in red is the simulated theoretical noise. The blue line indicates the noise from the detecting device without incident light on the camera.**

### 3.4.2. Sensitivity

In the shot-noise limit, the signal to noise ratio (SNR) in the spectral domain system is

$$\boldsymbol{SNR = \frac{\eta P_{sample} \tau_i}{E_v}} \qquad \textbf{3.25}$$

To test the system sensitivity for reflectivity measurement as a function of ranging depth, a mirror with an attenuator (neutral density filter) in the path was used as a sample. With a power of 2 mW coupled to the sample arm, the reflected power from the sample ($P_s$) was 110 nW (1.12 μW for the reference light), measured at the fiber tip of the detection arm. Spectra were acquired at a rate of 25 kHz (40 μs/A-line) for 8 different locations of the sample separated from each other by 250 μm. Dispersion imbalance between the interferometer arms was compensated in software as

described in the previous section. In Figure 3.8, the reflectivity signals {*10 log(R(z))*} are shown for 8 locations. The ratio of the peak at the depth of 250 μm and the noise level resulted in a dynamic range of 59.8 dB. Without attenuation in the sample arm, the measured power returning to the detection arm ($P'_s$) was 827 μW. Therefore, sum of the dynamic range and the attenuation contribution {$10\ log(P'_s/P_s)$=38.8 dB} yields a sensitivity of 98.6 dB. The peak at zero is due to the autocorrelation of the source spectrum. The peak drops by 16.1 dB at a depth of 2 mm because of the finite size of the CCD pixels. Small peaks at 1.3 to 1.5 mm indicate a fixed noise pattern that can be removed by subtraction of the reference arm signal. Cross coupling in the PM coupler and imperfect splicing of the PM fiber segments if axes are not aligned carefully may cause ghost lines. However, these are displaced from the imaging depth by using longer PMF segments (~15 m) in the reference and sample arms. The leakage between the PMF channels, on the other hand, may contribute to the noise floor. With a quantum efficiency $\eta$ of 28%, the sample-arm power directed to the detection of 110nW, and an integration time $\tau_i$ of 40μs, the theoretical SNR is 67.2 dB.

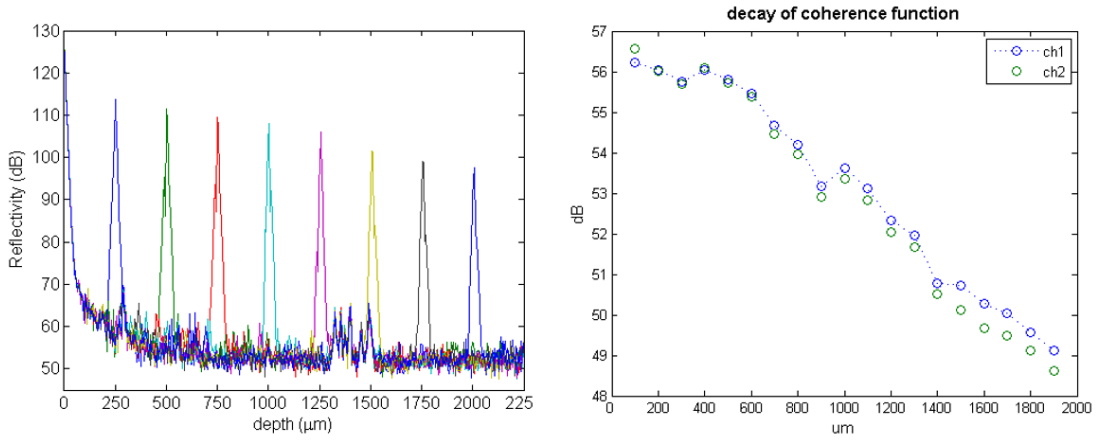


**Figure 3.8 Dynamic range and depth-dependent decay in reflectivity. (A) The coherence functions (in dB) at eight different depths. (B) The decay of the SNR with depth up to 2 mm.**

The phase sensitivity determines the minimal phase change that can be measured in a phase-sensitive OCT system. Since the optic axis orientation and Doppler flow contrasts in MC-OCT

are obtained from the phase information, and differential phase quantity is often used in functional measurement [41], the phase sensitivity is a critical factor in MC-OCT. We characterize the phase sensitivity in two polarization setups. In the first setup, 45° linearly polarized light is launched into the input arm of the MC-OCT, and no wave-plate is used elsewhere. A reflector is placed under the sample arm for the characterization. In the second setup, 0° linearly polarized light is launched, the setup is the same as that used for PS imaging (see Section 3.2). A quarter-wave plate is placed under the sample arm and used as a birefringent sample for the characterization. The phase sensitivity is defined as the standard deviation of the differential phase from two polarization channels in 1000 A-lines. Figure 3.11 shows the phase sensitivity at different depths along with the variation from single polarization channels. The differential phase measurements demonstrate a significant superiority, with a sensitivity less than $10^{-4}$ degree. The performance is comparable in the two setups.

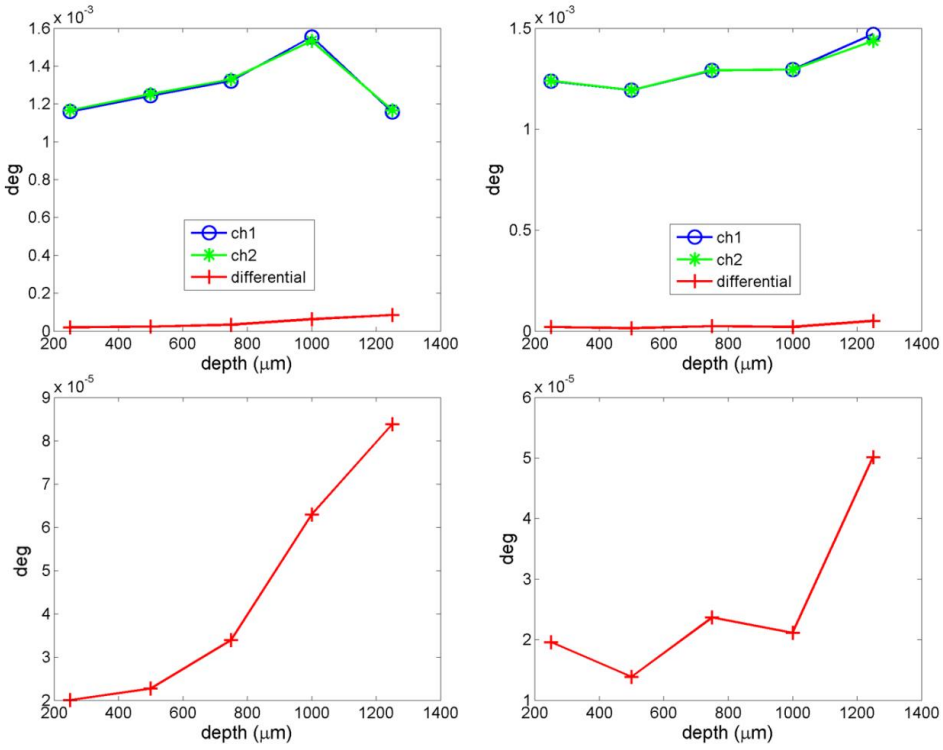


**Figure 3.9 Phase sensitivity curves of the MC-OCT in two polarization setups. Blue: standard deviation of phase measurement on polarization channel 1, green: standard deviation of phase measurement on polarization**

**channel 2, red: standard deviation of the differential phase between two channels. The differential phase sensitivity (red) on top panels are zoomed in on the bottom.**

### 3.4.3. Retardance and optic axis orientation

To characterize the retardance measurement, a voltage-controlled liquid crystal variable retarder (LCVR) was inserted into the sample arm between the QWP and the back reflector. Data were recorded when voltage applied to the LCVR was changed from 0 to 10 V stepping by 10 mV (Figure 3.9A). Figure 3.9B shows the retardance measurement as a function of voltage (solid line) together with the manufacturer's test data (dashed line). The two curves are in good agreement. Small deviations may result from misalignments, mismatch between our (840 nm) and manufacturer's test (848.7 nm) wavelengths, and temperature dependence of the LCVR.

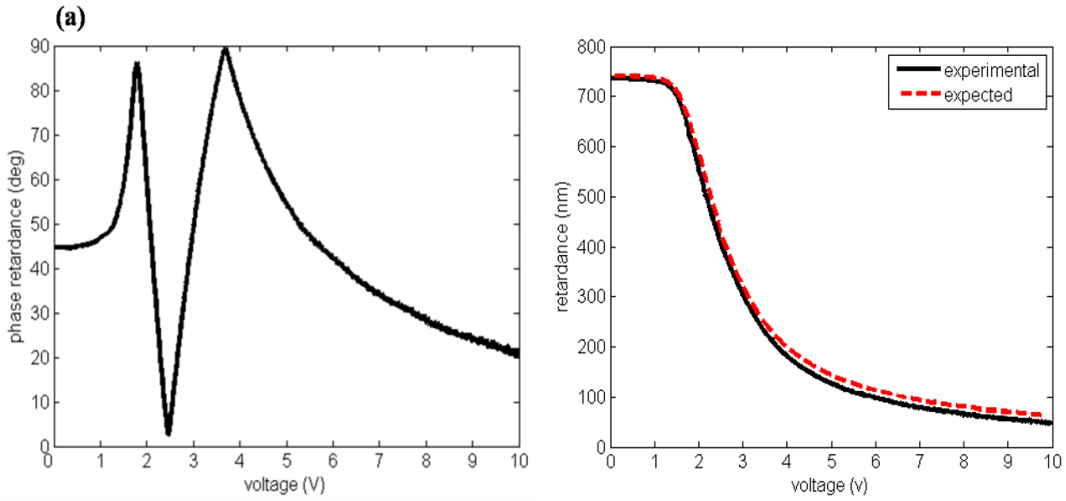


**Figure 3.10 (A) Phase retardance measurement using a voltage driven LCVR; (B) Retardance after correcting the phase anomaly and the manufacturer's test data.**

Measurement of relative optical axis orientation was examined by using a known retarder (QWP at 633 nm) as the sample. Data were recorded in steps of 10° rotation of the retarder, over a range of 180°. Figure 3.10A shows the relative axis orientation measurements (circles) with the expectation (solid line). The mean value of the error is 2.64°. Figure 3.10B shows the phase

retardance measurements (square) with a mean value of 68.38°, and a standard deviation of 0.83°. Errors, which are negligible, may arise from misalignments and imperfect polarization components.

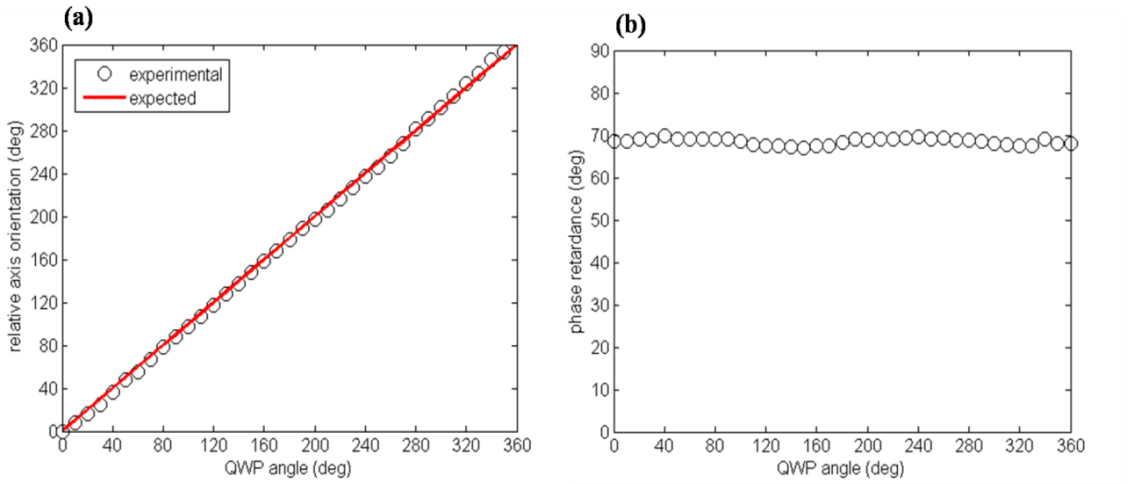


**Figure 3.11 (A) Relative optical axis orientation measurement (circle) for a known retarder with expected slope (line), (B) and the corresponding phase retardance.**

## 3.5 MULTI-CONTRAST IMAGING

### 3.5.1. In-vivo human finger imaging

Imaging performance of our SDPS-OCT system was demonstrated by stacking multiple A-lines while a galvanometer-controlled mirror scanned the beam (~2.5 mW) over a human finger nail and skin. Cross-sectional images containing 1000 A-lines were acquired and saved at 20 fps (50 μs/A-line). The real-time display for the reflectivity and retardance images was about 1.5 fps. Figure 3.12 show the reflectivity, phase retardance and relative axis orientation images, reflectively. The measured axial resolution is about 5.5 μm in tissue. The reflectivity image, which has a dynamic range of 30 dB, is relatively uniform across the tissue. High-contrast banding patterns can be seen in the retardance image. The banding patterns are not the same for the nail plate and the skin, because birefringence values for these tissues are different. More iterations of banding pattern indicate that the nail in this sample is more birefringent than the

skin. The relative axis orientation image is fairly uniform across the transverse direction of nail; however, different orientations indicated by red, yellow and light green spots are observed in the skin portion.

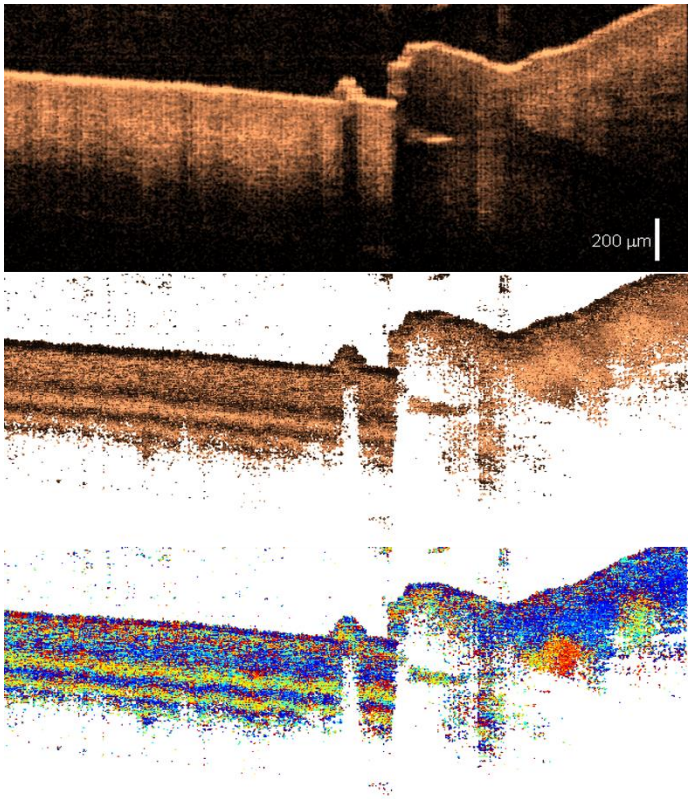


**Figure 3.12 SDPS-OCT's reflectivity, phase retardance (dark: 0°; light: 90°) and relative axis orientation (blue: -90°; red: 90°) images of the nail and skin of a human finger.**

### 3.5.2. In-vitro flow imaging

Here, we also demonstrate the feasibility of MC-OCT for flow imaging using a U-shaped tube with an Intralipid solution flowing inside (Figure 3.13). These findings suggest that MC-OCT can detect bi-directional blood flow, allowing for the localization of blood vessels in living brain, which could minimize the risk of intracranial hemorrhage— a significant risk in neurosurgical

procedures. Thus, development of an endoscopic MC-OCT technology could provide real-time intraoperative visualization and monitoring, making it potentially useful in clinical applications.

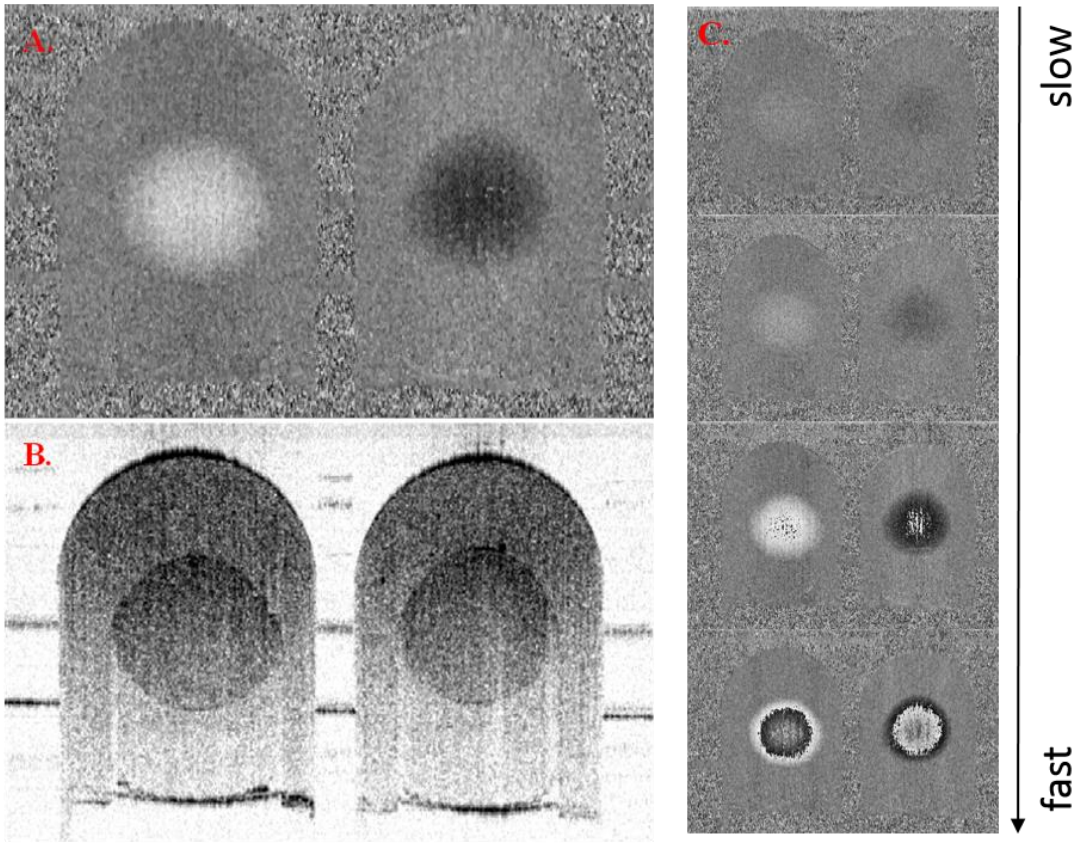


**Figure 3.13 Doppler flow images of a U-shaped tube with Intralipid perfusion. A. Bi-directional flow is demonstrated as the white and black circles, and the gray shells surrounding them are the tube. B. The corresponding reflectivity image. C. Multiple flow images are shown with different velocities. Flow speed is increasing from top to bottom. The external diameter of the tube is 1 mm.**

### 3.5.3. Multi-contrast images of *in-vivo* human retina

To evaluate the system capability of multi-contrast imaging, a healthy human's retina is imaged. Experimental setup is similar to that used for finger imaging, except that an additional lens was employed in the sample arm to allow pivoting the collimated beam at the pupil. Since the cornea and lens focus the beam onto the retina, imaging retinal layers and blood vessels is achieved. Cross-sectional images of reflectivity, Doppler flow, retardance and optic axis orientation

contrasts were generated from a single optical scan (Figure 3.14). The black and white clusters in (b) suggesting the flows at different depths can be visualized using the Doppler image, which can be used to indicate blood vessels in tissue. The range of the lateral scan is about 6 mm, starting from the fovea and covering the optic nerve head. If a smaller region of tissue is scanned, flow in small blood vessels may be visualized.

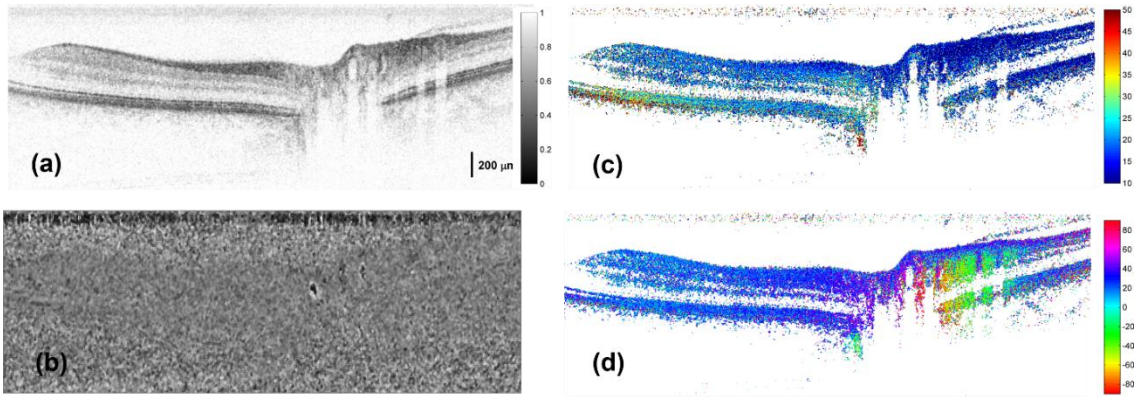


**Figure 3.14 MC-OCT images of a health human's retina in-vivo: (a) reflectivity, (b) Doppler flow, (c) retardance, and (d) optic axis orientation.**

## 3.6 DISCUSSIONS AND CONCLUSION

In conclusion, we demonstrated a high-speed MC-OCT system for imaging tissue reflectivity, birefringence, relative axis orientation and Doppler flow with a single optical scan. This PMF based approach is unique in the fiber based PS-OCT implementations because it is capable of generating birefringence information along a depth profile with a single measurement. The retardance measurement does not require compensation for polarization transformations known in non-PM single-mode fibers. The axis orientation image, which is calculated from the phase difference, is sensitive to external perturbations. As a result, most of the PM fiber-based components of the MC-OCT are kept in polystyrene enclosure. By virtue of the high speed in spectral domain OCT system, the phase disturbances were not observed on axis orientation and Doppler flow images (Figure 3.12-3.14) within one optical scan. Although PMF setups require

careful implementation, simple design and operation of the PMF-based system make it attractive for real time physiological studies and clinical applications.

Another concern in PMF is the unequal transmission loss of the orthogonal modes in the PMF, which might be due to even transmission efficiencies of the polarization splitter/combiner or caused by splicing. This is not observed in the current PMF system. However, for more sophisticated fiber based design, this uneven transmission loss may manifest which can be corrected by rescaling the intensity of polarization channels in software [113].

Birefringence of the PMF yields a phase lag between the polarization states in the slow and fast axes. If the phase difference is matched in reference and sample arms, the coherence functions of the two polarization channels will exactly overlap in depth. Otherwise, an axial shift between the coherence functions of the two channels is observed, which causes a degradation in the axial resolution. We ensure the spatial overlap of the coherence functions by precisely matching the fiber lengths in the sample and reference arms. A length mismatch of one beat length leads to a $\lambda_0$ shift between the coherence functions on the two channels, an order of magnitude smaller than the axial resolution. However, if not taken care of, a mismatch of several beat lengths can easily induce a noticeable spatial shift between the coherence functions. Phases of the coherence functions, on the other hand, cannot be matched using this method. Hence, as opposed to the bulk PS-OCT which yields absolute axis orientation [134], the optical axis orientation images in PMF based system are relative due to a phase offset. Absolute orientation images can be obtained by removing the offset using a retarder with known axis. In case of unmatched fiber lengths in sample and reference arms, a numerical compensation based on Fourier analysis can be applied to realign the two channels [135].

Polarization-maintaining fiber has high isolation between its orthogonal channels. However, any small amount of leakage between the polarization channels could lead to interferences with the sample or reference light, and the problem is not negligible due to the extremely high sensitivity of OCT. The cross-coupling in the PM coupler and the PM fiber splices, for example, can

generate considerable ghost images. The separation between the ghost and main images is attributed to the length of the PMF segment after the leaking point. Therefore, this problem can be fixed by extending the length of PMF in the interferometer (or adding other birefringent materials) to displace the ghost images beyond the imaging range. In this MC-OCT, we used 15 meters PMF in the sample and reference arms to remove the artifacts. For a beat length $B$, and PMF length $l$, the displacement is given by $l \times \lambda_0/2B$ considering the double pass length. With $B$ = 1 to 2 mm for the Corning's PM fiber, the ghost line due to leakage in the PM coupler should be displaced by an amount of 6.3 to 12.6 mm away from the main line; we measured a displacement of about 8.5 mm. Leakage in either of the detection or input portions of the interferometer gives rise to fixed lines. These lines are minimized by optimizing the optical. Residuals, if any, can be eliminated by software algorithms of reference subtraction.

Light in the orthogonal PMF axes travel different optical paths. As a result, the dispersion imbalances between the reference and sample arms may not be identical for the two polarization channels. With the superluminescent diode with a bandwidth of 50 nm, we computed that coherence lengths deviate 0.8 μm from the theoretical value. Therefore, the effect was negligible. However, for ultra-resolution design with broader bandwidth light source, the system needs to be implemented with additional care. Numerical dispersion compensation may not be sufficient alone and combination of hardware compensation may be more appropriate.

# CHAPTER 4 MULTI-CONTRAST OPTICAL COHERENCE TOMOGRAPHY FOR BRAIN IMAGING AND OPTICAL TRACTOGRAPHY

## 4.1 INTRODUCTION

The brain is composed of roughly 100 billion neurons that contain trillions of connective tracts. Despite the progress in understanding operations of single neurons and their functions at the system level, the communicative and cooperative pathways in the axonal networks of the brain remains elusive. Considerable research has been directed toward identifying the pathways of axonal connections between nuclei and cortical layers in recent years. Histological methods have contributed in the microscopic anatomy and local tracing of myelinated nerve fibers [136-138]; however, majority of those studies are limited on 2D plane [167]. Diffusion magnetic resonance imaging (MRI) techniques such as diffusion tensor imaging and high angular resolution diffusion imaging utilizing the anisotropic diffusion of water molecules along the fiber tracts have been developed recently to noninvasively study brain connectivity [139-141]. However, the diffusion imaging approach suffers from relatively low spatial resolution (in millimeters), and the nature of probability-based analysis may lead to spurious interpretations of rel fiber structures in the brain [142]. Comprehensive understanding of structural connections in the brain requires 3D visualization of fiber tracts with high spatial resolution.

The capability of OCT in depth-resolved imaging with micrometer scale resolution of [25] provides a perspective to look into the question. The feasibility of using OCT to image the brain has already been demonstrated [35]. Traditional OCT utilizes the scattering properties of light

from the white and gray matter. However, there is an optical property of the myelin sheath of nerve fibers, known as birefringence ($\Delta n$), which may be probed by PS-OCT and provide additional benefit to determine the spatial organization and orientations of fiber tracts. Birefringence, which is a consequence of the alignment of macromolecular arrays of lipids and proteins contained in myelin [143] results in a single axis of optical anisotropy in each fiber. Birefringence can be quantified by a phase shift, known as phase retardance, between the orthogonal polarization states of polarized light passing through the tissue, and the axis of optical anisotropy which is parallel to the fiber axis can be obtained as well. Birefringence images of neuronal architectures have been reported by polarized light microscopy [144]. Fiber tract maps in human postmortem brains have also been constructed using polarized light imaging [145]. In this method, spatial resolution was defined by the pixel size of the imaging camera and the section thickness of the brain slice. Nakaji et al. [146] reported a free-space PS-OCT with multiple measurements to differentiate white and gray matter and determine fiber orientations in brain slices.

To date, systematical studies of OCT in brain imaging and mapping are still sparse. The big challenge is how to make use of the high resolution (both axial and lateral) of OCT to construct the 3D brain maps with interpretable anatomy and structure-specific information. In this chapter, we use the PMF based MC-OCT system developed in the previous chapter to realize 3D imaging and fiber tractography in *ex-vivo* rat brain. The capability of the reflectivity, retardance and optic axis orientation contrasts in revealing brain microstructures and especially depicting the white matter tracts will be systematically investigated. The strategies of constructing 3D fiber maps within one optical section will be established using these MC-OCT contrasts. We will show that the micrometer scale resolution of MC-OCT enables visualization of fiber tract architecture with an unprecedented level of detail.

## 4.2 EXPERIMENTAL PROCEDURES

### 4.2.1. MC-OCT data acquisition

The MC-OCT developed in Chapter 3 is used for brain imaging in this Chapter. The experimental setup is illustrated in Figure 4.1. Briefly, light from the source (a near-infrared superluminescent diode, $\lambda_0 = 840\ nm$, $\Delta\lambda = 50\ nm$) is linearly polarized and coupled into one of the orthogonal channels of the PMF. Then, a PMF-based 2 × 2 coupler splits the light into the reference and sample arms of the interferometer. In the reference arm, 45° linearly polarized light is coupled back into PMF. In the sample arm, circularly polarized light is incident on the sample. Light interacts with anisotropic tissues and the polarization state is altered to an elliptical state due to tissue birefringence. The light back scattered from the sample is coupled into the PMF channels. The waves from the sample and reference arms are then combined in the 2 × 2 coupler and their interference is acquired in the detection arm of the interferometer. Oscillations on the spectra yield information along the depth (z-axis) profile. During the experiment, the incident beam is laterally scanned over the sample in two dimensions (xy plane) allowing for 3D reconstruction of the tissue sample. The depth resolution is about 5.4 µm in tissue (with a refractive index of 1.4), and the lateral resolution is about 15 µm.

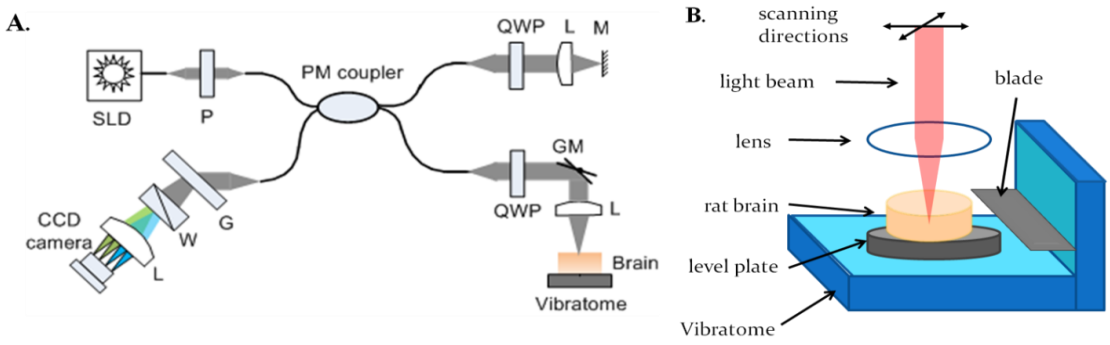


**Figure 4.1 MC-OCT setup for brain imaging. (A) System schematic diagram. SLD, superluminscent diode; FB, fiber bench; P, polarizer; C, collimator; QWP, quarter-wave plate; L, lens; M: mirror; GM, galvo mirror; G, grating; W, Wollaston prism. (B) Experimental configuration under sample arm. The brain sample is mounted on a Vibratome slicer, which is placed under the sample arm optics that scans the beam over the tissue.**

Two healthy adult rat brains were obtained from the Tissue Sharing Program after approval by the Research Animal Resources at the University of Minnesota. One brain was fixed in 10% buffered formalin for 48 hours prior to imaging. Myelin sheath integrity in postmortem brain tissue is not affected by proper fixation [143]. Another brain was immediately translated to the imaging stage after dissection. During the imaging, one hemisphere of the brain was glued to a metal plate with the sagittal plane (xy plane) facing upward, and submerged in saline. The preparation was then mounted on a Vibratome (Leica Microsystems, Bannockburn, IL), which was placed under the sample arm of MC-OCT for imaging (Figure 4.1B). The incident power on the sample was 3.9 mW. With an optical scanning angle of ±6°, the imaging area covered a field of view of 6.25 × 6.25 $mm^2$. Each cross-sectional image contained 1000 A-lines, and 250 cross-sections (frames) were acquired at 20 fps for 3D imaging. Each A-line contained 512 points with 3.4 μm spacing. Therefore, each voxel spanned a tissue volume of 6.25 x 25 x 3.4 $\mu m^3$. After one volume scan, a 500-μm brain section was removed using the Vibratome, allowing deeper regions to be imaged for a new section. A total of twelve scans were performed over the hemisphere. Afterwards, the brain slices were imaged using a conventional microscope for comparison.

### 4.2.2. Image reconstruction

The contrasts of reflectivity $\boldsymbol{R(z)}$, phase retardance $\delta(z)$ and optic axis orientation $\theta(z)$ are used in ex-vivo brain imaging and are extracted by the amplitude and the phase information of the complex depth profiles on the two polarization channels (Eq. 3.17 - 3.19). Reflectivity represents the scattering properties of the brain. Phase retardance indicates the presence of anisotropic tissue with an optic axis. Optic axis orientation, also called in-plane orientation, represents the angle of the axis of tissue anisotropy on the oscillation plane of the incident wave with respect to a reference axis. Due to an arbitrary phase delay between the PMF channels, our system determines a relative optic axis orientation across lateral scans. Cross-sectional images are generated by stacking 1000 A-lines acquired during lateral scanning (x-axis).

Phase retardance is a cumulative phase shift between the orthogonal polarization states when polarized propagates in a tissue with birefringence $\Delta n$, and is given by

$$\boldsymbol{\delta(z) = \int 2\pi/\lambda \cdot \Delta n(z) dz} \qquad \textbf{4.1}$$

Birefringence $\Delta n$ can be characterized by the derivative of retardance along the axial ($z$) direction as

$$\Delta n(z) = (\lambda/2\pi) \cdot \frac{d\delta(z)}{dz} \qquad \textbf{4.2}$$

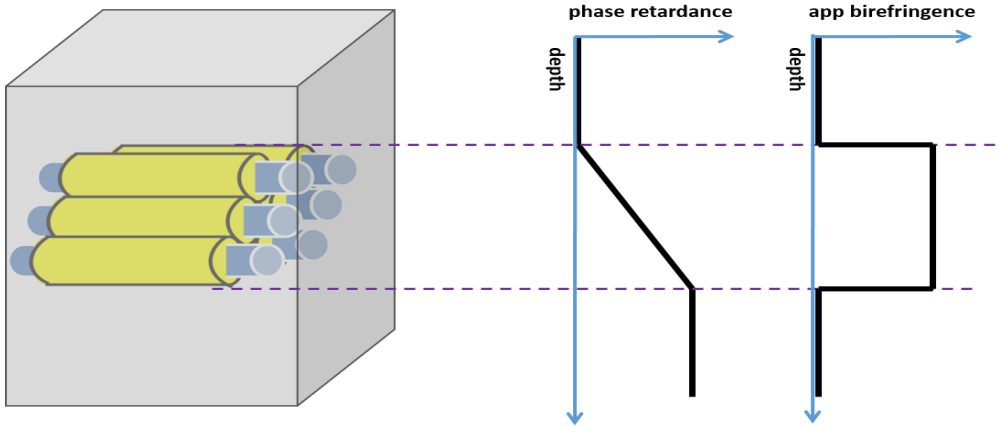


**Figure 4.2 Relationship between phase retardance and birefringence.**

The relationship of phase retardance and birefringence is illustrated in Figure 4.2. A fiber bundle is located inside an isotropic medium. The retardance accumulates linearly with depth where light passes through the fiber. It should be noted that the measured retardance is also dependent on the inclination angle between the tissue axis and the wave oscillation plane [147]. The measured birefringence is

$$\Delta n = n_1 - (n_1^{-2} sin^2\alpha + n_2^{-2} cos^2\alpha)^{-1/2} \quad \textbf{4.3}$$

where $\alpha$ is the angle between the fiber axis and the projection of the axis onto the section plane, called the inclination angle. With approximation, the simpler form can be expressed as

$$\Delta n \approx (n_1 - n_1)\, cos^2\alpha \quad \textbf{4.4}$$

Therefore, the value calculated from Eq. 4.2 is apparent birefringence.

## 4.3 GRAY MATTER AND WHITE MATTER DIFFERENTIATION

White matter and gray matter exhibit distinct optical properties on the images. In this section, we examine the capability of MC-OCT in structure distinction. To differentiate the white matter and gray matter in the brain, features were extracted from the MC-OCT images first. Then a classifier was run on the features to assess the differentiability performance of the MC-OCT contrasts.

### 4.3.1. Boundary detection of the tissue-air interface

The cross sectional images typically contains data that is air-tissue interface at the top. As a result, prior to parameter extraction, the data must be automatically parsed to determine the segment of the top surface of tissue reflectivity. Since the signal decays exponentially with depth, it is necessary to exclude the data from the bottom part with low SNR. And there might be extra noise peaks or ghost lines that need to be eliminated as well. Here, we use cluster algorithm to extract the tissue boundaries in each cross sectional image. First, all data points with a SNR below 6 dB are set to floor value. Next, we apply an algorithm that detects the maximum cluster whose signals are significantly above the floor value, and assigned the starting and ending points as the boundaries of the tissue. By doing this, patterns of non-tissue artifacts such as water surface were removed. To avoid error from specular reflection at the air-sample interface, the starting point was shifted 4 pixels (~20 μm) beyond the first peak. After that, a classical edge detection

algorithm was applied to further remove the small disturbance on the surface. These routines were automatically applied to all the scans to determine the data range over which to compute the feature parameters. The average depth over which the signal was analyzed was about 600 μm.

### 4.3.2. Feature extraction

Signal parameters were extracted for each A-line, and the mean value of each parameter was used to represent the sample. Each parameter was calculated using an automated MATLAB script. Noise reduction was implemented for preprocessing. Each parameter is listed as $\mu \pm \sigma$, where $\mu$ is the mean, and $\sigma$ is the standard deviation. The *p*-values were calculated using a two-sided unpaired *t*-test to determine if the difference in sample means between parameters representing the white matter and gray matter were statistically significant.

*Attenuation coefficient*

Collimated light attenuates exponentially with depth according to the Beer-Lambert law. The light attenuation in tissue can be quantified by the slope of the logarithmic reflectivity in the axial direction (A-line), provided that the beam is not tightly focused. A high slope indicates more attenuation and a larger attenuation coefficient, whereas, a low slope indicates a smaller attenuation coefficient. The slope was calculated by a first-order polynomial fit over the region of interest.

*Reflective variation*

The variation of scattering within one A-line depth profile can be used as another parameter for classifying tissue type. One way to assess the scattering variance is to measure the slope-subtracted standard deviation of the axial depth profile. If the scattering fluctuates significantly, the reflection profile will have high scattering peaks interspersed with low signal, and the standard deviation will be high. Conversely, if the scattering is relatively homogeneous, the signal

will be more uniform, and the standard deviation will be low. To remove the effect of the bulk averaged scattering coefficient, the residual of the linear fit was used to compute the standard deviation.

*Birefringence*

Anisotropic tissue with single optics axis will display the property of birefringence when the light passes through the tissue. Birefringence is defined as refractive indices difference between two polarization states parallel and perpendicular to optics axis respectively, and can be calculated from phase retardance between the two channels. The slope of the phase retardance is proportional to birefringence. A slope of zero means the tissue is isotropic, and there's no birefringence for the tissue. On the contrary, a high slope indicates the tissue is highly birefringent. The slope was calculated by a first-order polynomial fit over the region of interest.

### 4.3.3. Classification

A multivariate Gaussian model was used for classification. Three out of four scan sessions were used as the training set for feature extraction and the remaining was used for validation. A pooled estimate of the covariance matrix was used for the training set. The Bayesian detection method was applied to test the probabilities of white matters versus gray matter, and a threshold was adjusted to achieve the best performance. The accuracy of the algorithm for brain tissue classification was assessed by comparing the results to other standard method.

### 4.3.4. Results

Figure 4.3A illustrates a microscopy sagittal section of the right hemisphere, in which white matter appears bright white. The dashed red lines indicate two B-lines (i and ii), where cross-sections are displayed by MC-OCT contrasts in Figure 4.3B-D. The reflectivity images in Figure 4.3B suggest that white matter, in general, has a higher peak scattering signal (bright colors) than

gray matter, and a sharp decay with depth due to increased attenuation of light. On the other hand, the gray color regions indicate that gray matter has a deeper penetration and slower attenuation. The left side of the cross-section (i) with highly scattering spots in the reflectivity image represents small fiber branches running perpendicular to the viewing plane, which can also be seen in the corresponding microscopy image. The phase retardance images in Figure 4.3C indicate that retardance dramatically increases with depth in the white matter, whereas retardance remains low in gray matter. This distinction is more evident in large fiber bundles as shown on the right side of the cross-section (ii), where banding patterns start to appear due to phase wrapping. From visual inspection, the location of peak reflectivity and the position where retardance starts to rise are roughly matched on the same A-line. Figure 4.3D illustrates the axis orientation images that provide additional information to locate the fiber tracts and distinguish fiber directions in the white matter. Note that phase wrapping in the large fiber tract also alters the axis orientation color in the deeper region, which can be corrected by the software.

The identification of white matter can be more complicated due to its axis-dependent optical characteristics [148]. Figure 4.3E demonstrates a comparison of reflectivity profiles for three distinct neighboring brain regions (left), which are marked by the color-coded arrows on the cross-sectional images. The internal capsule, indicated by the blue arrow, exhibits the strongest signal in the superficial layer due to the parallel alignment of its component nerve fibers with respect to the viewing plane. On the other hand, the reflectivity profile of the optic tract, in green, is even smaller than that of the gray matter (in red). Therefore, determination of whether a structure is gray or white matter based on the reflectivity information alone from conventional OCT can be misleading. The retardance information provided by the MC-OCT provides a more robust differentiation of the white matter from the gray matter on the corresponding retardance curves for these three regions (left). It is clear that the slope of retardance curves representing the birefringence can be a main indicator of the myelinated nerve fiber tracts.

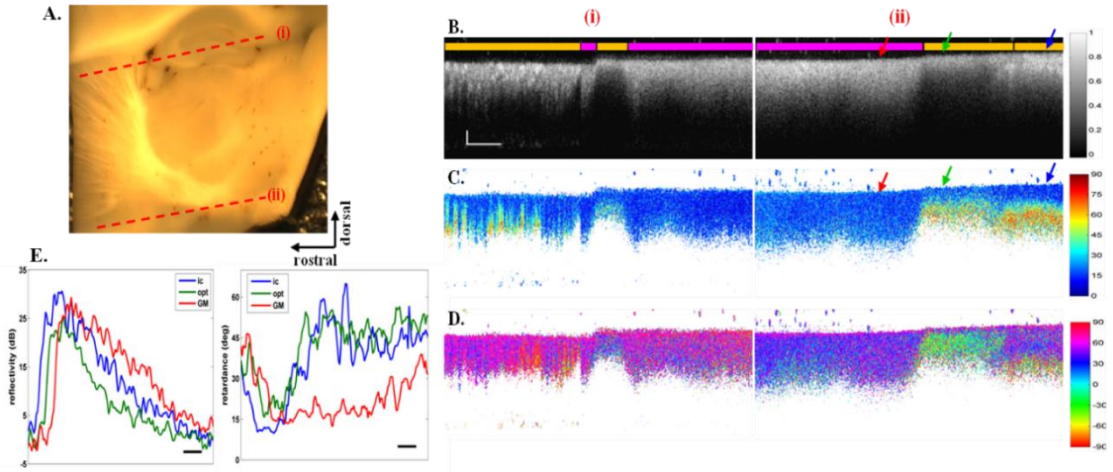


**Figure 4.3 Microscopy and cross-sectional MC-OCT images of an ex-vivo rat brain. Microscopy image (A) demonstrates a sagittal section of the right hemisphere. Cross-sectional MC-OCT images of reflectivity, phase retardance and optic axis orientation are shown in panel B, C and D, respectively, for two cross-sections (i and ii) indicated by the dashed lines on A (scale bars: 100 µm axial, 500 µm lateral). White and gray matter regions are marked by orange and pink bars on top of the reflectivity images. Color-coded arrows on cross-section ii indicate white matter regions with small (blue) and large (green) inclination angles, and the adjacent gray matter region (red). Reflectivity and phase retardance profiles of six A-line averages for these regions are shown in E (scale bar: 50 µm).**

Figure 4.4A shows a zoomed-in region of white matter (left) and gray matter (right) on the cross-sectional image. Representative A-lines of reflectivity and retardance with their 1$^{st}$ order polynomial fitting were shown on Figure 4.4B.

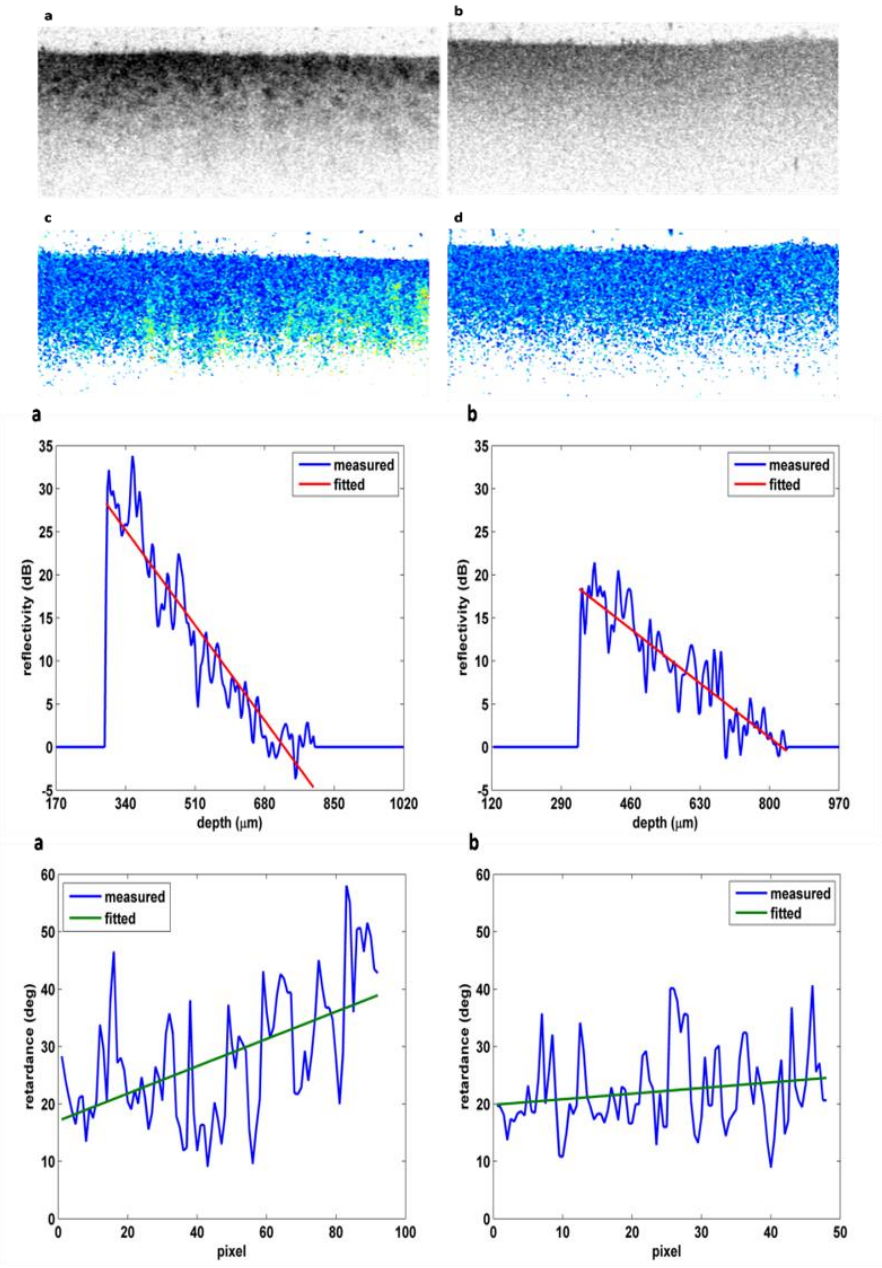


**Figure 4.4 (A) A zoomed-in region of white matter and gray matter on the cross-sectional image. Gray scaled images on top are logarithmic reflectivity, and dark indicates higher reflectivity; Color scaled images at bottom are phase retardance, and light color indicates higher value of retardance. (B) Reflectivity (top) and phase retardance (bottom) of one A-line along depth, a: white matter, b: gray matter.**

The attenuation and birefringence are extracted from each A-line for white matter and gray matter regions, and the statistical results are provided in Figure 4.5. The reflectivity signal attenuates at $(8.48 \pm 1.46) \times 10^{-2}$ dB/μm in white matter, and $(6.14 \pm 0.88) \times 10^{-2}$ dB/μm in gray matter.

Therefore, for conventional OCT images, attenuation may be a better indicator to differentiate the white and gray matter than the peak reflectivity discussed above. The slopes of phase retardance were found to be 0.33 ± 0.10°/μm for white matter and 0.03 ± 0.01 °/μm for gray matter, representing the birefringence of $(7.78 \pm 0.61) \times 10^{-4}$ and $(0.21 \pm 0.068) \times 10^{-4}$, respectively. The values for attenuation and birefringence features are significantly higher for white matter compared to gray matter. However, the differentiation is more pronounced in the birefringence contrast. Thus, birefringence provides a more reliable means of distinguishing myelinated fiber tracts in the brain.

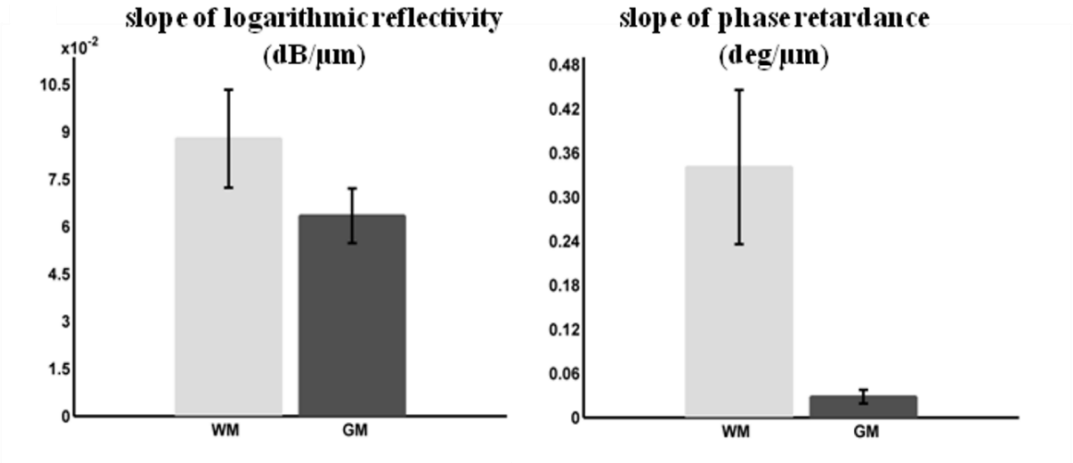


**Figure 4.5 Mean and standard deviations of attenuation and birefringence for white and gray matter.**

Using three features, the comparisons between white and gray matter from the training set are listed in Table 4.1. Each parameter has a significant *p*-value. The average magnitude of the reflectivity slope was higher for white matter, which indicates a higher scattering coefficient compared with gray matter in the brain. White matter has a higher reflective variation because of high scattering nerve bundles of white matter tracks. The birefringence of white matter is significantly greater than zero. However there's no detectable birefringence in gray matter.

Table 4.1 Statistics of features (with arbitrary units) from training set.

| Parameter | White matter | Gray matter | *p* |
|---|---|---|---|
| Scattering coefficient | 3.64 ± 0.66 | 2.84 ± 0.59 | < 0.0001 |
| Reflective variation | -0.18 ± 0.03 | -0.12 ± 0.03 | < 0.0001 |
| Birefringence | 0.22 ± 0.11 | 0.04 ± 0.06 | < 0.0001 |

A region of interest (ROI) chosen from the enface image of the scan session was used for validation. The result from the detection algorithm was compared to other identification method for the accuracy evaluation. Classification results using all three parameters are listed in Table 4.2. The goal was set to detect the white matter in the brain. Therefore, the correct classification of white matter is a true positive (*TP*), and the correct classification of gray matter can be viewed as a true negative (*TN*). In this way, the sensitivity, as defined by *TP/(TP+FN)* (*FN* = false negative) is equivalent to the accuracy of detecting white matter. The specificity, as defined by *TN/(TN+FP)* (*FP* = false positive) is equivalent to the accuracy of detecting gray matter. The sensitivity and specificity of the validation set are 82.8% and 76.3%, respectively.

Table 4.2 Classification of white and gray matter using two-parameter and three-parameter models.

| | Three-parameter model | Two-parameter model |
|---|---|---|
| Sensitivity | 82.8% | 86.3% |
| Specificity | 76.3% | 55.5% |

In order to compare the classification performance acquired from PS-OCT system with that got from conventional OCT (polarization-insensitive OCT) and evaluate the significance of parameter of polarization information (birefringence), classification results only using the first

two parameters listed in Table 4.1 (scattering coefficient and reflective variation) are also listed in Table 4.2. The results indicate that sensitivities to detect white matter based on three parameters (82.8%) and two parameters (86.3%) are both good in this detection algorithm. However, specificity is much higher from the three parameter based detection (76.3%) than that tested by two parameters (55.5%). Overall, detection performance is better in the three-parameter system including polarization information. Therefore, PS-OCT provides important tissue features that improve the system capability in classification of white matter and gray matter for brain imaging.

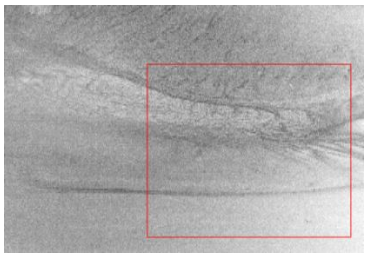

**Figure 4.6 A region of interest for detection from an enface image of the rat brain, the dataset used for validation are labeled by the rectangle in red.**

## 4.4 MULTI-CONTRAST *EN-FACE* IMAGES

### 4.4.1. Reconstruction methods

To resemble the view of block-face microscopy, the volumetric data from an optical scan were projected onto the xy-plane for each optical section, forming the *en-face* images. In such a way, surface and subsurface features are unveiled on the images. We reconstructed *en-face* images for each MC-OCT contrast, and correlated the results with the bright field images of the brain slice from the microscope. Four pre-processing steps are performed on each cross-sectional image to improve the image quality. First, the reflectivity image is used to exclude the low signal-to-noise ratio (SNR) (< 6) areas. Then, a median filter is applied to reduce the speckle noise. Next, segmentation is used to identify the tissue region. This enables removal of artifacts (e.g. water-air interface and auto-correlation terms) located outside the imaging area. Finally, an edge detector

[149] is used to determine the tissue surface. The pixel intensity $\bar{I}(i, j)$ of the *en-face* images is calculated from these processed/masked images by taking the mean value on each A-line, and is expressed as

$$\bar{I}(i, j) = \frac{1}{N_{i,j}} \sum_{k=1}^{N_{i,j}} S(i, j, k) \quad \textbf{4.5}$$

where $S(i, j, k)$ represents a 3D data set for reflectivity, retardance or axis orientation, $i$ and $j$ are the indices for lateral coordinates and $k$ is the index for axial direction, and $N_{i,j}$ is the number of unmasked (non-zero) elements along depth at the specified $(i, j)$ location. Data was interpolated along the y-axis to maintain the aspect ratio of the 2D image. As a result, *en-face* images of reflectivity, phase retardance and optic axis orientation are reconstructed to facilitate the structure identification and perform comparisons with standard microscope images. Finally, 2D tractography is built up by combining the *en-face* phase retardance and the axis orientation maps, and is displayed in HSV color space. Orientation and retardance maps are encoded as hue and brightness, respectively, as seen in the color scheme given in Figure 4J.

### 4.4.2. *En-face* images of reflectivity, retardance and optic axis orientation

*En-face* images of a rat brain were reconstructed to produce the sagittal view. Figure 4.7A shows the microscopy image with labeled structures and the reconstructed MC-OCT images. The *en-face* maps of reflectivity, phase retardance and optic axis orientation reveal various features, some of which are apparent only in one map. In addition, sub-surface structures, are visible in *en-face* MC-OCT images, and if desired, the specific structures can be localized in depth using the cross-sectional images. The *en-face* reflectivity map (in Figure 4.7B) provides clear contour delineation and differentiation of gross structures in the brain which correlate well with the microscope image. In general, the white matter appears brighter than the gray. The dark appearance of the fimbria and the optic tract may be due to the large inclination angle of the fiber axis at the

specific location against the viewing plane as discussed in the previous section. As shown in Figure 4.7C, the phase retardance map highlights the fiber tracts further because the presence of gray matter is suppressed due to a lack of birefringence. The brightness of the tracts qualitatively provides a sense of axis alignment to the plane. In the internal capsule, small fiber tracts, measuring tens of micrometers in diameter, are clearly visible. Inclined fibers, which might be misinterpreted in the reflectivity map due to their dark appearance, can also be identified. Multiple fiber tracts in the midbrain are visible, and the structural feature of the white matter embedded in the thalamus emerges.

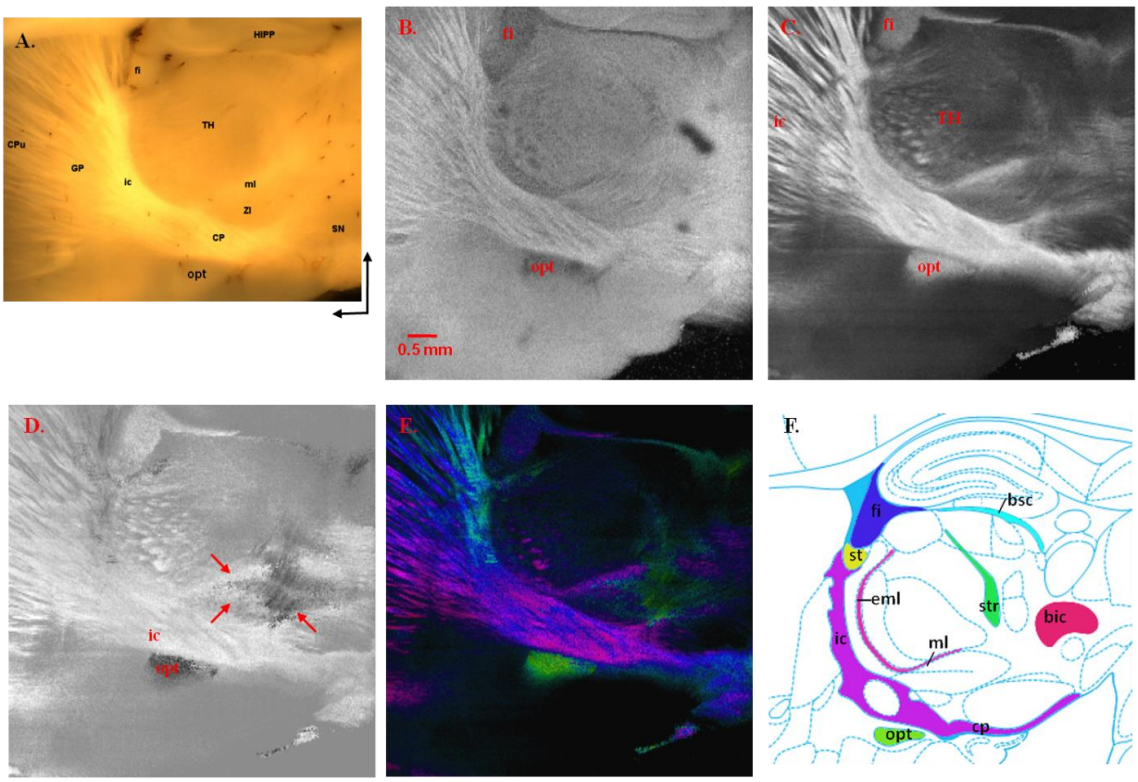


**Figure 4.7 Microscopy image (A) and reconstructed MC-OCT en-face images (B-D) of a sagittal rat brain section, with comparison of anatomy (F). Structures are labeled on the microscope image (A): cp- cerebral peduncle; CPu- caudate putamen; fi- fimbria; GP- globus pallidus; HIPP- hippocampus; ic- internal capsule; ml- medial lemniscus; opt- optic tract; SN- substania nigra; TH- thalamus; ZI- zona incerta. Leftward arrow: cranial; upward arrow: dorsal. Reconstructed brain maps of reflectivity (B), phase retardance (C), optic axis orientation (D) and combined image for tractography (E) are shown. The color map of (E) is illustrated in Figure 4J. The arrows in (D) indicate three groups of fiber bundles with different orientations. The image in (F) is modified from The Rat Brain in Stereotaxic Coordinates [164] with permission. Abbreviations of structures:**

**bic- brachium of the inferior colliculus; bsc- brachium of the superior colliculus; cp- cerebral peduncle; eml- external medullary lamina; fi- fimbria; ic- internal capsule; ml- medial lemniscus; opt- optic tract; st- stria terminalis; str- superior thalamic radiation.**

The optic axis orientation map in Figure 4.7D provides further information about the in-plane angle and alignment of the fiber axes. The arrows indicate three groups of fiber tracts with different orientations around the zona incerta. Such detail is not distinguishable in reflectivity and phase retardance maps and is barely detectable using bright-field microscopy. The use of axis orientation information enhances the identification of intermingled fiber tracts running across the viewing plane. An excellent illustration of this feature is the differentiation of internal capsule and optic tract, seen in Figure 4.7D. Moreover, the MC-OCT contrasts can be combined in order to facilitate better tractography. Figure 4.7E shows the implementation of 2D tractography by utilizing phase retardance and orientation maps. The axis orientation and the retardance of fibers are encoded by color and brightness of the colors, respectively. The detailed color scheme is illustrated Figure 4.7J. The spatial organization of the fibers in tractgraphy is in good agreement with the anatomy (4.7F). Based on the brightness and the color of the *en-face* maps, the spatial orientation vector of fibers in the brain may be interpreted.

Multiple sagittal sections illustrating the course of fiber tracts on 2D tractography (top panels) and microscopy images of the corresponding slices (bottom panels) were shown in Figure 4.8. The HSV color scheme for 2D tractography images is shown in Figure 4.7J. The *en-face* orientation ($\bar{\theta}$) and retardance ($\bar{\delta}$) images were used to determine colors and brightness of the colors, respectively. The cyan color represents a reference direction (0°) for fiber orientations. Since $\bar{\theta}$ is average axis-orientation along depth, its value may not reach the actual value due to noise and filtering effects. For instance, the maximum deviation ($\bar{\theta}_{max}$) from the reference direction was calculated to be 68°, instead of reaching 90°. Therefore, the colors on the wheel are scaled accordingly. We used en-face retardance $\bar{\delta}$ images to adjust the brightness of colors. As seen along the radial direction of the color wheel, the minimum retardance ($\bar{\delta}$ = 0°) yields black

and the maximum retardance ($\bar{\delta}$ = 60°) represents the full color. For each row panel, the positions of the imaging sections from left to right are indicated by the dashed lines (1-4) on the rat brain (I). The details of fiber tracts are well appreciated in these MC-OCT images. By incorporating optical slices of all sections, white matter distribution and orientation from the lateral to medial sections of the brain may be continuously tracked. More importantly, it is possible to use depth-resolved images to localize the nerve fibers precisely, and track the fibers in 3D.

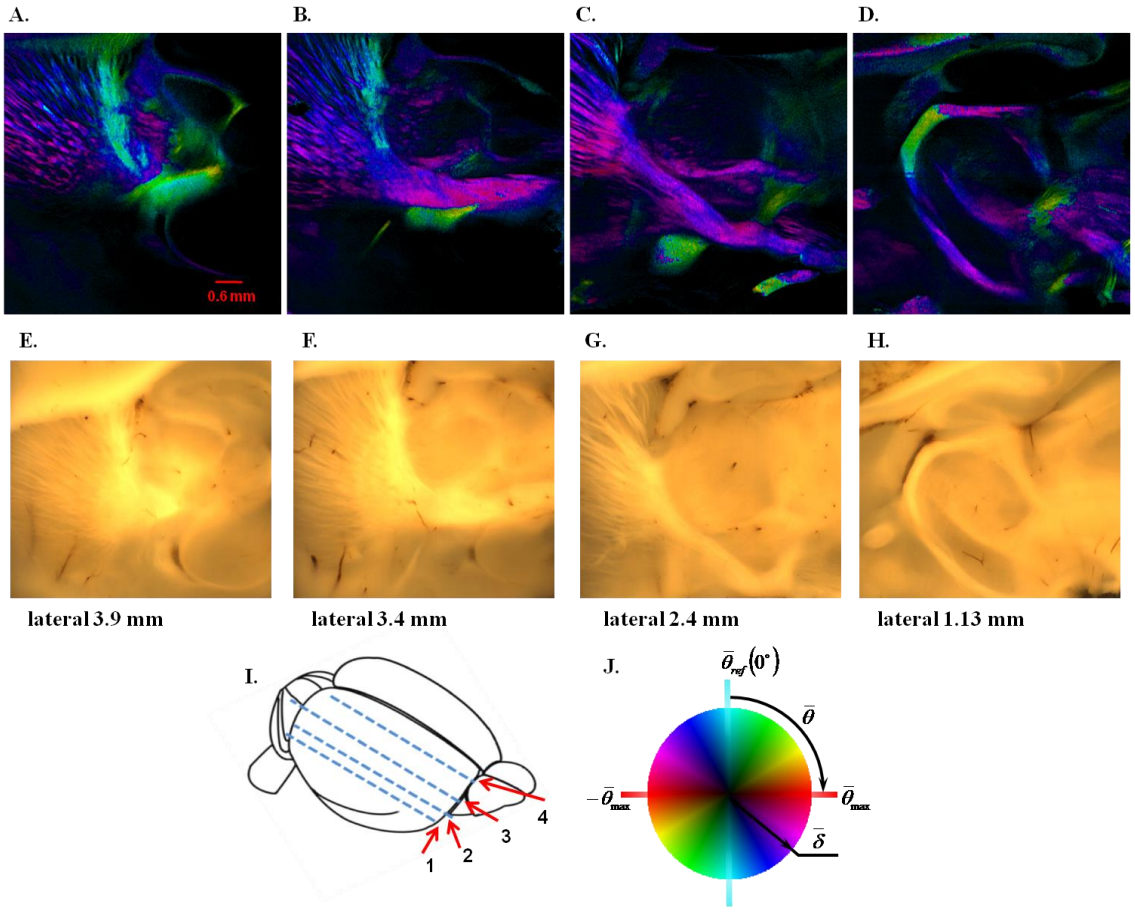


**Figure 4.8 2D tractography of the right hemisphere of the rat brain for four sagittal sections (A, B, C, D) and corresponding microscope images (E, F, G, H). The four locations of the images from left to right are lateral 3.9 mm, 3.4 mm, 2.4 mm and 1.13 mm, which are indicated by the dashed lines (1-4) on the right hemisphere of rat brain (I), respectively. The color scheme of tractography images is shown in (J). The en-face orientation $\bar{\theta}$ and retardance $\bar{\delta}$ of fiber tracts determine the color and brightness of the images, respectively.**

Using fresh rat brain, the MC-OCT is also able to produce high-quality images. Figure 4.9 demonstrates the *en-face* reflectivity, retardance and axis orientation images of a sagittal view close to the midline of the brain. The hippocampus, thalamus, callosum and midbrain portion were shown. The optical contrasts from fresh brain and fixed brain (Figure 4.7) are comparable, indicating that fixation does not influence the images created by MC-OCT. The major problem of using fresh tissue is that the vibratome cannot cut an ultra-flat surface especially in the white matter fibers with high myelination, thus inducing artifact on the *en-face* images (see the arrow indication on the reflectivity map). As OCT is a depth-resolved technique with high axial resolution, the surface flatness is an essential factor in undistorted 3D reconstruction. Therefore, in the following sections and chapters, we all use fixed brain tissue for imaging. However, with technical advance in microtome slicer, reconstruction of fresh brain by MC-OCT is possible and preferential.

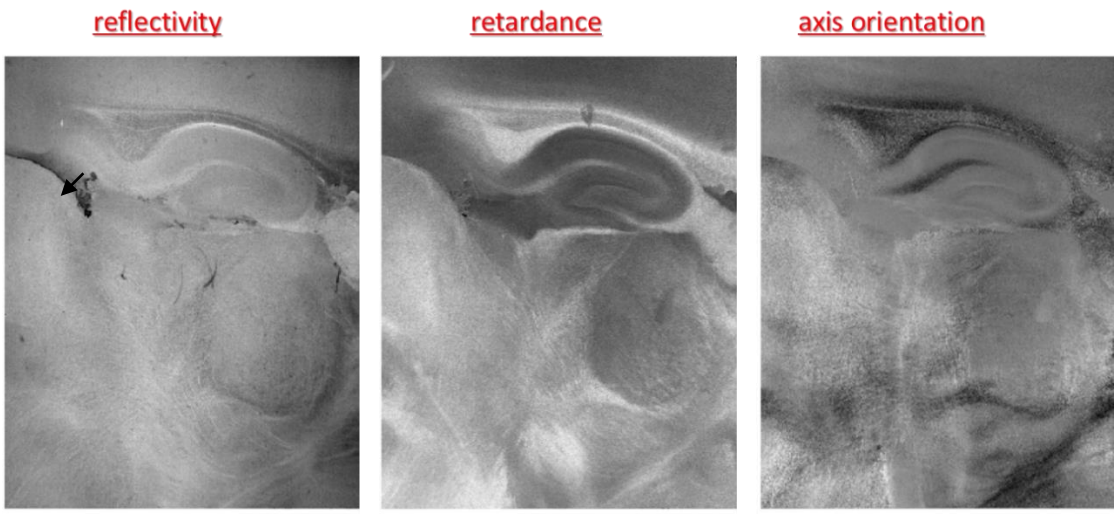


**Figure 4.9 En-face images of unfixed rat brain (sagittal view). A, reflectivity; B, retardance; C, axis orientation.**

## 4.5 OPTICAL TRACTOGRAPHY

The 3D localization of fiber bundles is obtained by utilizing the cross-sectional phase retardance images. The presence of fibers is revealed by an accumulative phase retardance, which increases

with depth when light passes through the white matter, compared with no detectable or negligible change in the gray matter. Therefore, the depth localization of the nerve fibers can be achieved by using the birefringence contrast. The local slope of phase retardance is quantified by taking the numerical difference between two neighboring retardance values along depth [150]. Since speckle noise significantly affects the differential calculation, we eliminated the speckle through three steps. First, a 4 × 4 moving average filter is applied over the lateral (xy) plane. Then an adaptive nonlinear diffusion filter [151, 152] was performed on cross-sectional images. The purpose of the nonlinear diffusion filter is to further reduce the speckle noise while preserving the edge of the features. Finally, a "spline" smoothing algorithm was applied to eliminate the local fluctuations on the A-lines. After the speckle de-noising, the numerical difference of retardance along the depth profile was computed, and a birefringence threshold was set to mask the gray matter areas. In addition, we used histogram equilibrium and binary conversion algorithm on the *en-face* phase retardance image to identify A-lines that do not exhibit birefringence. Masking those A-lines further improved the result. We combined the birefringence and axis orientation information for locating and tracking fibers in 3D space. The 3D tractography is constructed in HSV color space, where axis orientation and birefringence of the fiber tracts are used.

### 4.5.1. Birefringence image

Three dimensional tractography is created from a single section dataset for a 3D brain volume. Two types of information are encoded in the reconstructed tractography: fiber localization implied by birefringence, and its axis orientation. Figure 4.10 demonstrates depth localization of fiber tracts in the internal capsule region. The cross-sectional images in A and B show phase retardance image before and after elimination of speckle noise. The birefringence is derived by taking the pixel-wise slope of the phase retardance. As shown in Fig. 4.10C, the birefringence image allows depth localization of individual fiber bundles within the internal capsule. Considering the discrepancy of the slope values, which may be due primarily to diversity of the

fiber inclinations, the fiber bundles are identified as highlighted dots and bands in red, yellow, cyan and light blue. Gray matter is masked in the dark blue background due to the lack of birefringence.

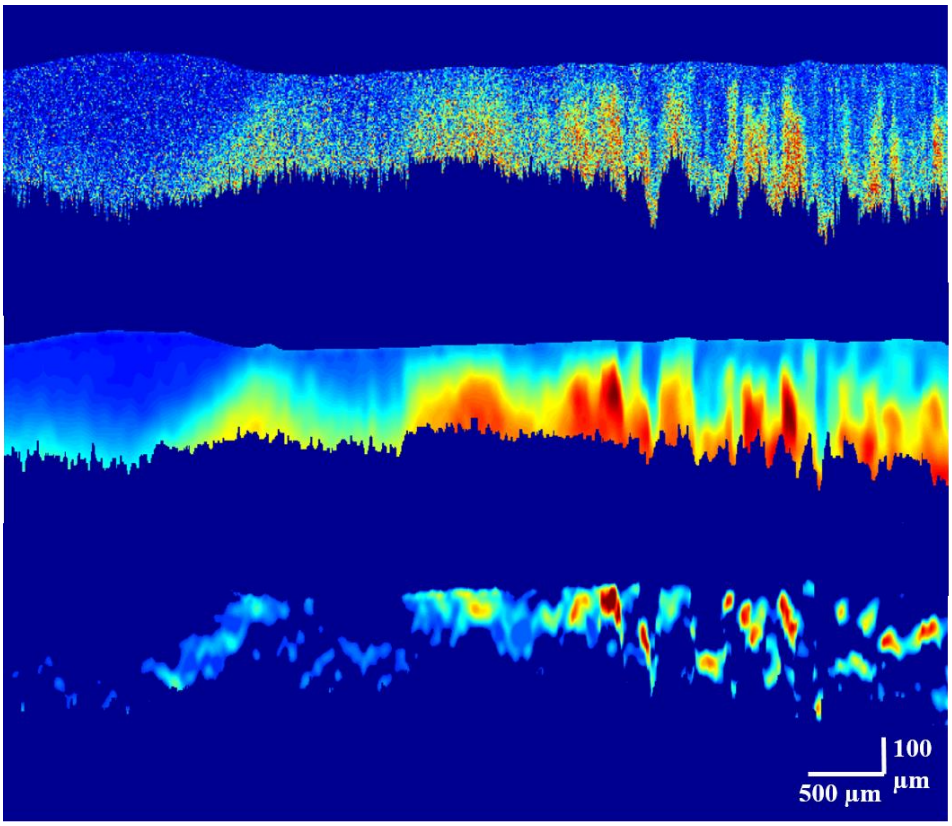


**Figure 4.10 Depth localization of fiber tracts in the internal capsule of the rat brain. A. Original phase retardance image. B. Cross-sectional phase retardance image after speckle reduction. The image in B is used to obtain the birefringence image (C) that shows nerve fibers at particular depths. White matter is illustrated in red, yellow, cyan and light blue in C, and gray matter is masked in the dark blue background due to the lack of birefringence.**

### 4.5.2. 3D fiber maps and tractography

By combining multiple cross-sections, visualization of nerve fibers is achieved in 3D. Volume rendering of the 3D dataset is constructed by the software V3D [153]. Figure 6 shows optical tractography for a brain volume of $6 \times 6 \times 0.45$ mm$^3$. HSV color scheme for 3D tractography is shown on the lower right corner of Figure 4.11. The axis orientation ($\theta$) and birefringence ($\Delta n$) of

fiber tracts are encoded by colors and brightness of the colors, respectively. Due to noise and filtering effects, the maximum orientation angle ($\theta_{max}$) with respect to the reference direction was 80°, and the $\theta$ values on the wheel were scaled accordingly. The brightness of the colors, from black to full color, is controlled by the value of $\Delta n$. A white background is selected for better visualization. The nerve fiber tracts are identified by their spatial connections and color.

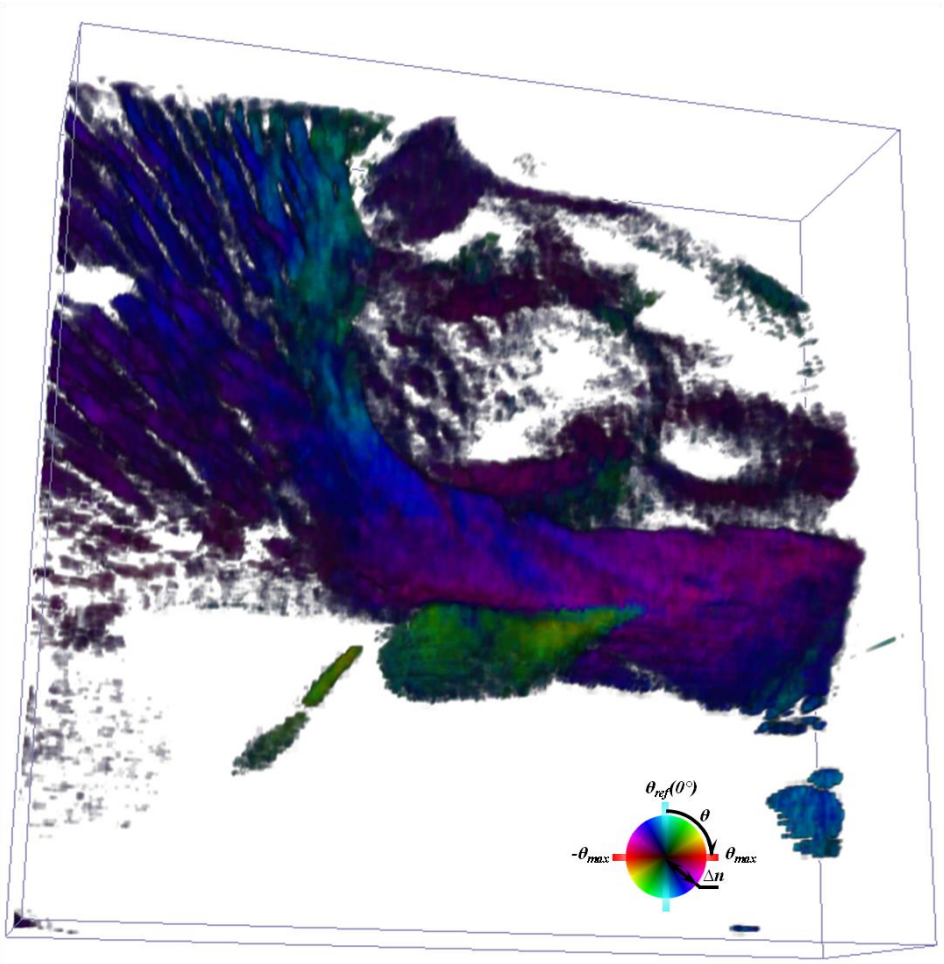


**Figure 4.11 3D optical tractography of a rat brain section (brain volume: 6 × 6 × 0.45 mm3). The color scheme is given on the lower right corner. Nerve fibers are continuously tracked and presented in different colors which indicate their axis orientations θ, and the brightness of colors is controlled by the birefringence Δn (See also a movie in the supplemental material).**

The architecture of tightly packed fiber bundles and the diverse directions of small fiber branches in the internal capsule are visible. The course of small fibers of the commissural stria terminalis

are accurately tracked throughout the slice. In addition, some fiber tracts are visible in the deeper regions within the thalamus. The color for a single tract may vary spatially due to change in axis orientation. The color also helps to distinguish neighboring tracts. For example, the oval-shaped optic tract rising from the inferior-posterior brain is clearly differentiated by the color-coded orientation. The fragmented patterns located in the deeper, low SNR regions will likely be visualized better by using more advanced signal processing approaches or a MC-OCT operating at longer wavelength.

Figure 4.12 shows three sagittal sections of optical tractography images from medial to lateral. The continuity and spatial extension of large fiber bundles are indicated, and small features are uniquely visualized in particular sections. By stacking the optical sections together, whole-brain tractography can be realized with micrometer scale resolution.

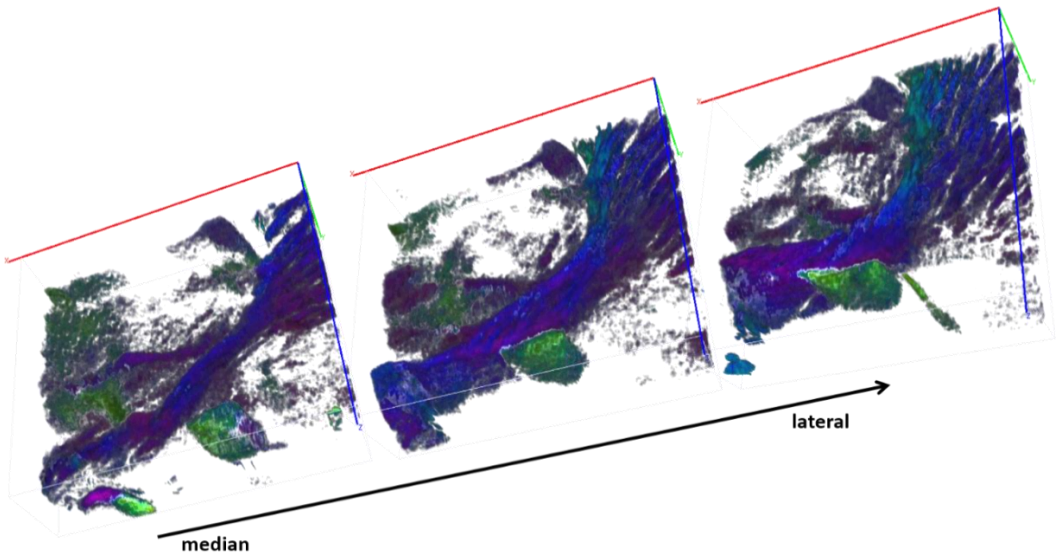


**Figure 4.12 Optical tractography of three sagittal sections from median to lateral positions. The color space is coded the same as in Figure 4.11.**

## 4.6 DISCUSSION AND CONCLUSION

We used a PMF-based MC-OCT to generate high-resolution 3D images of microstructures and nerve fiber tracking in *ex-vivo* rat brain. We have demonstrated here that MC-OCT imaging with retardance and optic axis orientation contrasts, is a valuable method for distinguishing between white and gray matter, based on the birefringence property of myelinated axons. This technology enables visualization of nerve fiber tracts that are as small as a few tens of micrometers, and provides comprehensive 3D optical tractography in which unprecedented detail of brain spatial architecture is clearly visible.

MC-OCT exhibits a distinctive ability to differentiate the white and gray matter. The feasibility of using OCT to distinguish the two structures has been shown by Jeon et al. [35] with parameters of penetration and scattering peaks. However, we showed that the scatter peaks may cause miss identification of white matter due to a fiber orientation dependency of the light intensity. Attenuation coefficient is a more reliable parameter in the differentiation. Taking advantage of the PS-OCT technology, birefringence supports the unique probe on the white matter tracts. We compare the classification with and without polarization information, and indicate improvement of the algorithm performance with PS information available. Other qualitative and quantitative features have been identified in OCT images [154]. Texture analysis using speckle properties has been proposed. Classification algorithms such as Mahalanobis distance, ANOVA and decision tree have been investigated for distinguish different tissues. Recently, feature grouping and machine learning based approaches have been investigated. Those quantifications are especially important in pathological detections. Two types of skin cancers have been classified with reasonable accuracies (81%, and 73%) using Support Vector Machine (SVM) model [155]; and breast tumor has been identified using clustering and correlation model [156]. The development of computational analysis, which provide automatic and objective measures, and real-time or post-acquisition classifications, will eventually benefit scientist and physicians in basic research and clinical diagnosis.

Speckle noise, the dominant noise in coherence imaging, needs to be carefully removed in order to enhance image quality. The spatial average of A-lines was commonly adopted in conventional OCT based retinal imaging for speckle reduction. In addition, various digital signal processing algorithms have been demonstrated, including enhanced Lee filter, median filter, symmetric nearest neighbor filter and adaptive Wiener filter [157]. More sophisticated approaches have been proposed for performing filtering in a transform domain, such as wavelet [158] and curvelet [159]. In polarization-sensitive OCT, the effect of speckle noise can be more severe in the retardance and birefringence images. The phase retardance information is typically illustrated in the image; whereas, depth resolved birefringence images which may provide better localization and delineation of anisotropic tissues were rarely utilized, in spite of the fact that it can be calculated from the derivative of retardance. The result, based on the differential operation, is severely degraded by speckle noise. Recently, a coherence-enhancing diffusion filter has been applied to reduce speckle noise in phase retardance images with multiple banding patterns to obtain a stress-induced birefringence distribution [150]. Here we used a modified nonlinear diffusion filter to minimize speckle effect in the phase retardance images for localizing nerve fibers in the reconstructed birefringence images. The goal of the nonlinear diffusion filter is to preserve the critical edges of features in the image while reducing speckle noise. As our results indicated, fiber localization in unprecedented detail is realized in 3D, with significantly suppressed speckle effect. One potential problem in the 3D visualization presented here is that some fragmented patches at deeper locations are unrecognized, which might be small fibers running into the gray matter structures. Advanced signal processing approaches may show these low SNR regions better. Moreover, a swept source based imaging system operating at 1300 *nm* wavelength [160] may allow for improved imaging due to better depth penetration in turbid tissues.

A limitation of MC-OCT is that currently axis orientation of fibers beneath fibers with different orientations is not quantitatively available and phase retardance would not be accurate where multiple layers of fibers are crossing in diverse directions. As discussed in Chapter 2.5, using Jones calculus layered samples yield depth cumulated retardance and optic axis orientation, so the measured information may not be accurate for deeper layers without the depth-dependent correction. Figure 4.13 shows a simulation of orientation quantification using Eq. 3.19 in the two-layer fiber architecture. Relative orientation in the second layer with respect to the first was set between 0° and 75° with a 15° increment in the six panels. The x-axis is the retardance in the second layer representing retardance accumulation with depth. In each panel, the measured orientation of the second layer with respect to the first were shown for different retardance for the first layer representing low to high birefringent medium. It is indicated that the relative orientation monotonically changes with depth. At the surface of the second layer, the relative orientation is always zero. Along with depth, the orientation approaches the set value, but never reaches the true orientation. This problem is especially severe when the first layer is highly birefringent and the relative orientation between the two layers is large. Considering the complex scenario in the brain with multi-fiber crossing along depth, this problem needs to be fixed for depth-resolved orientation quantification. A quaternion based algorithm has been proposed to distinguish multi-layered local birefringence and optic axis orientations in PS-OCT [161]. Quantification of depth-resolved axis orientation and birefringence has also been demonstrated in a bulk PS-OCT setup [162]. Using the PMF-based MC-OCT technology, more sophisticated models need to be established to achieve better visualization and quantification of depth-dependent axis orientation and phase retardance of fiber tracts in the brain.

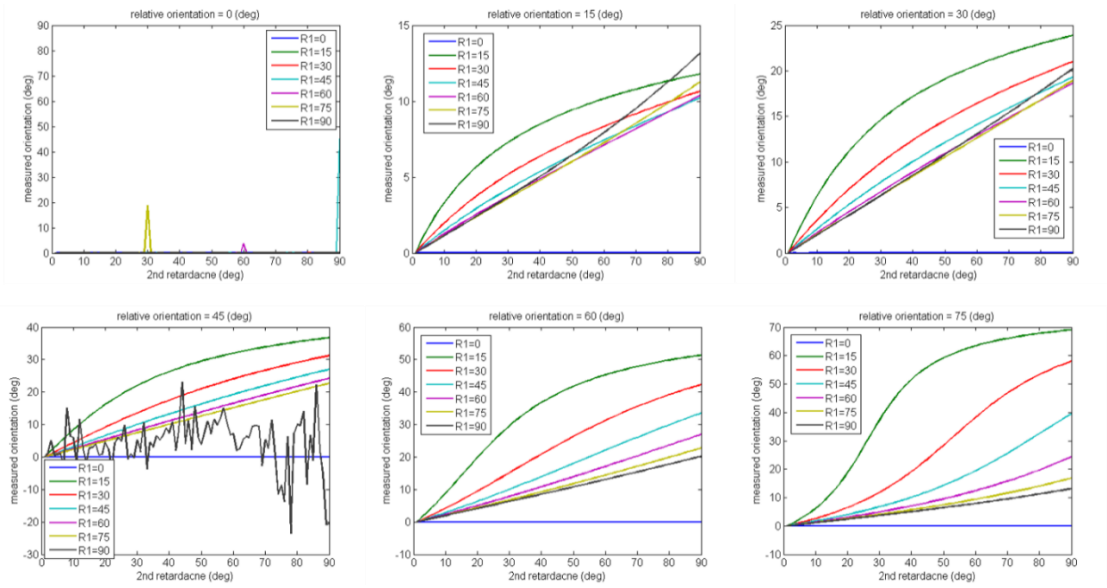


**Figure 4.13 Simulation of fiber orientation in two layer architecture. The relative orientation between the two layers was set 0°, 15°, 30°, 45°, 60° and 75°, respectively in the six panels. The x-axis is the retardance in the second layer. From left to right, the retardance is linearly increasing, representing the increasing path light passes through. The y-axis is the simulated orientation value between the two layers. In each panel, the seven curves describe the scinerios with different retardance values by the end of layer one.**

As a measure of MC-OCT technique, birefringence can potentially be used as an early indication of pathological changes [163, 164] in white matter disease, allowing for the detection of fiber atrophy or myelin loss before any morphological deformation is detectable on diffusion MRI. Quantification of birefringence can be obtained from phase retardance acquired by the MC-OCT. However, it should be noted that the influence of inclination angle on phase retardance may confound the interpretation of birefringence changes in the current measures, resulting in an apparent birefringence. A possible solution was proposed using a variable incident angle based polarization-sensitive OCT approach [165], in which both tissue birefringence and 3D optic axis orientation can be quantitatively evaluated with series measurements. MC-OCT technology, by providing accurate birefringence data, might be useful for the analysis of neuropathological processes.

The development of technology that can distinguish white matter, gray matter, and blood vessels via an endoscope would be of significant utility to the neurosurgeon. An endoscopic OCT setup has been proposed for neurosurgical guidance where conventional contrast of scattering was used to differentiate white matter and gray matter [33, 36]. In spite of some successful identification, it was suggested that the subthalamic nucleus, a primary target for deep brain stimulation (DBS) surgery, was difficult to differentiate from adjacent structures. This difficulty might be overcome by multiple contrasts provided by an endoscopic MC-OCT. Preliminary findings suggest that MC-OCT can detect bi-directional blood flow (data not shown), allowing for the localization of blood vessels in living brain, which could minimize the risk of intracranial hemorrhage— a significant risk in neurosurgical procedures. Thus, development of an endoscopic MC-OCT technology could provide real-time intraoperative visualization and monitoring, making it potentially useful in clinical applications.

# CHAPTER 5 SERIAL OPTICAL COHERENCE SCANNER FOR LARGE-SCALE BRAIN IMAGING AND MAPPING

## 5.1 INTRODUCTION

Light microscopy has made tremendous contributions to our knowledge in neuroanatomy including conformation and function of neural cells in the brain over the past century. In recent years, more consensuses arise to realize the role communication pathways play in brain disorders such as autism and schizophrenia. Comprehensive navigation of the white matter routes imposes great challenges to current imaging technologies. Histology bears serious limitation as single axonal tract can extend up to centimeters long, and the structures of the axonal networks are extremely complicated. Inevitable distortion caused by tissue processing and embedding makes the alignment of sequential microscopy images extremely difficult and laborious [168, 169]. To overcome the problem, plane illumination microscopy [170] and ultramicroscopy in combination with optical clearance technique [171, 172] eliminate mechanical sectioning and produce entire brain imaging of young mice with comparable resolution. Nevertheless, better optical clearance has yet to be developed for large scale reconstruction of the axonal networks in adult brain [173, 174]. Neural tracers in combination with fluorescent microscopy contribute to sensitive identification of local neural circuits. However, the timeline imposes a formidable obstacle to establish the full connection map in a brain template, considering systematic characterization of hundreds of injection sites on multiple samples [10, 23].

Firstly introduced in light microscopy [175], block-face imaging with electron microscopy [19], confocal microscopy [176] and two-photon microscopy [177, 178] targets large scale synaptic

connections or axonal networks in 3D space. The entire tissue block was mounted on a slicer and thin slices were removed between consecutive scans, the procedure of which yields automatically aligned image stacks in 3D. However, due to the high density of slicing and the point-scan scheme, complete reconstruction of complicated mammalian brains remains challenging.

The OCT technique with its 3D capability shines a light to overcome with the difficulties. The development of Fourier domain OCT [63] has dramatically improved the imaging speed by capturing the information at all imaging depths with a single measurement. Since invention, its application in peripheral nervous system such as retina has been rapidly translated to clinical studies with continuous support of technical advances [179, 180]. In contrast, the applications of OCT in central nervous system have been sparsely reported until very recently (see early review by Boppart [26]) [146, 181, 201, 202]. After demonstrating the feasibility to differentiate the gray and white matter in the brain [203, 35], development of OCT probes to guide neurosurgical interventions has been presented [33, 36, 183]. However, the utilization on large-scale brain structures and white matter organizations have not been reported.

As a step forward, based on the brain imaging described in the previous chapter, we develop a serial optical coherence scanner (SOCS) for large-scale volumetric imaging of *ex-vivo* brain in this chapter. The objective is to reconstruct the comprehensive neuronal pathways in 3D brain space. The optical system is the PMF based MC-OCT described in Chapter 3 and 4 [184, 185]. We have shown that the multiple contrasts provide the anatomical information, the differentiation between the gray and the white matter, and the fiber architectures. In this chapter, we will add the information of light attenuation and cross-polarization, and compare the contrast images of brain structure and fiber delineation. In addition, we correct the relative measurement problem of optic axis orientation introduced in Chapter 3 and 4, and achieve quantification of absolute fiber orientations in the brain. With integrated tissue sectioning between serial scans, to this end we

show that SOCS reconstructs a rat brain with axial resolution of 5.5 μm and transverse resolution of ~15 μm. The axonal networks are visualized and fiber tracts can be traced at various scales.

## 5.2 SERIAL OPTICAL COHERENCE SCANNER

### 5.2.1. Serial optical coherence scanner

SOCS integrates a tissue slicer into a MC-OCT system for reconstructing large-scale biological tissues in 3D. Schematic diagram of SOCS is demonstrated in Figure 5.1. The MC-OCT combines a PMF technique [113] and the spectral domain measurement to provide morphological and polarization sensitive imaging with high spatial-temporal resolution [184]. The light source is a broadband superluminescent diode operating at the center wavelength of 840 nm with a 50 nm bandwidth, yielding an axial resolution ($z$) of 5.5 μm in tissue (refractive index: ~1.4). Polarized light is directed through PMF coupler into the sample and reference arms. A scan lens ($f$ = 36 mm) in the sample arm ensures consistent imaging quality over a large area. The lateral resolution estimates ~15 μm ($xy$). Interferometric signals carrying the optical delay gate between reference light and back-scattered light from sample are detected by a customized spectrometer, which consists of a grating to disperse spectral components, a Wollaston prism to separate the PMF channels, and a lens to focus the spectra on a 2 x 4096 pixel line-scan camera (*Basler sprint 140k*). Vertical and horizontal binning was applied on the camera to enhance photon collection. The spectra on the two polarization channels are acquired simultaneously at a rate of 25 kHz. An inverse Fourier transform of the spectral modulations (in k-space) produces a complex depth profile (A-line) for each channel $A_{1,2}(z)exp\{i\Phi_{1,2}(z)\}$, where $A$ and $\Phi$ denote the amplitude and phase, respectively, along the depth $z$, and *1* and *2* correspond to the cross-coupled and main polarization channels. The imaging contrasts are derived from amplitudes and phases of the depth profiles: reflectivity (Eq. 3.17), the traditional OCT contrast, is the addition of intensity on the two channels; cross polarization ($C(z) \propto A_1(z)^2$) only takes the intensity of the cross-coupled

channel; retardance (Eq. 3.18) and optic axis orientation (Eq. 3.19) are computed based on the Jones analysis [109].

A volumetric scan (optical section) contains 300 cross-sectional frames (B-line) with 1000 A-lines in each frame, covering a field of view of 7x7x1.78 $mm^3$ in *xyz*. The voxel size is 7x23x3.47 $\mu m^3$, correspondingly. The pixel anisotropy in *xy*-plane is caused by the limitation of maximum B-lines that the current system can save in one optical scan.

A vibratome (Leica Microsystems, Bannockburn, IL) is mounted under the sample path optics. The brain is glued on the slicer and immersed in water. After imaging one optical section, a slice is removed by the vibratome, allowing deeper regions to be imaged. The procedure is repeated until the whole block is imaged. The thickness of the slice is less than the penetration depth of light, and it is optimally selected to ensure satisfactory SNR for high-quality 3D reconstruction of the entire sample (see Figure 5.4B). The water level and the imaging surface are controlled at constant heights during the scans.

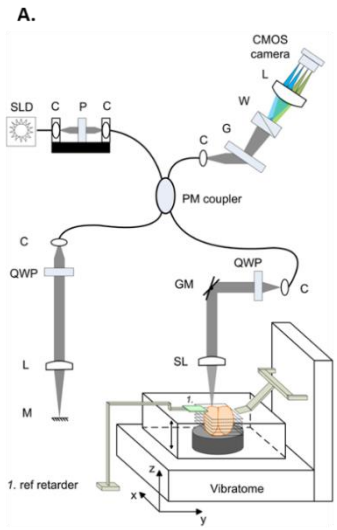


**Figure 5.1 SOCS schematic diagram. SLD, superluminscent diode; P, polarizer; C, collimator; QWP, quarter-wave plate; L, lens; M: mirror; GM, galvo mirror; SL, scan lens; G, grating; W, Wollaston prism; LSC, line scan camera.**

### 5.2.2. Imaging procedures

Euthanized adult rats were obtained from the tissue sharing program with approval by the Research Animal Resources at the University of Minnesota. Brain was dissected and kept in 10% buffered formalin for 72 h before imaging.

Three brains were imaged in the current study, one sectioned in sagittal planes and two in coronal planes. The sagittal sections consist of 28 slices of 200 μm each, and compose the left hemisphere of the brain. The coronal sections in one brain consist of 66 100-μm slices, and cover the regions between frontal cortex and the middle portion of thalamus in the left hemisphere. To achieve reconstruction of entire coronal sections, for the third brain, two scans are performed between sequential slices. The optical scan head is laterally translated between the two scans. A 15% overlap is reserved for image registration.

### 5.2.3. Calibration of axis orientation

The optic axis orientation quantifies the in-plane orientation of neuronal tracts as a relative measure, because it bears a time-variant offset induced by environmental factors such as temperature change and movement of the optical fiber [184]. To resolve this issue and obtain an absolute axis orientation measure, a retarder film was included as an active calibrating reference. The film was placed next to the brain and imaged together with the brain sections. The offset in the orientation measurement is hence determined as the optic axis of the retarder is known (Figure 5.2). Another issue is that large-scale lateral scans may affect the orientation measure by inducing polarization effects. By scanning a retarder at the same field of view as used for brain imaging, trends of the axis orientation in *xy*-plane are extracted prior to brain imaging and removed afterwards.

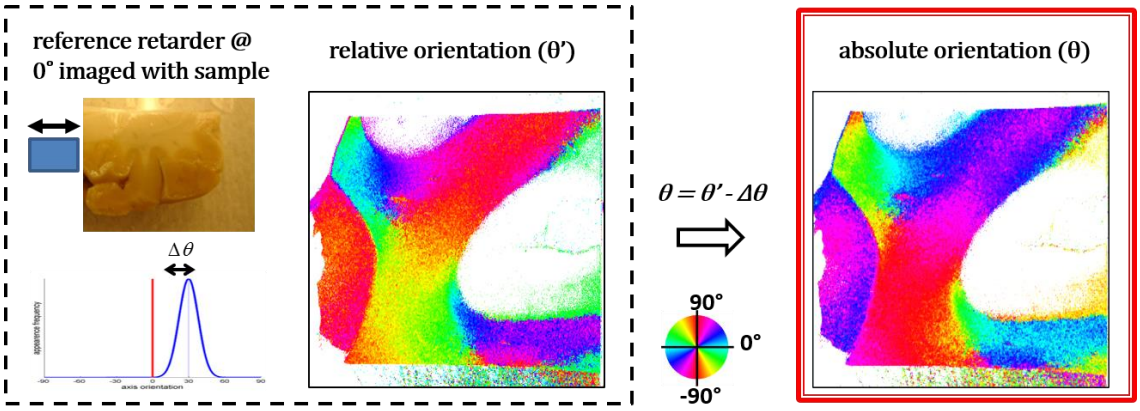


**Figure 5.2 Correction of relative optic axis orientation. A reference retarder is placed next to the sample and imaged with it together. The orientation offset is obtained from the measured orientation of the retarder and used to derive the absolute orientation.**

## 5.3 RECONSTRUCTION METHODOLOGY

With the depth profiles computed and saved from the raw spectra, the processing routines work as follows. Top surface of the tissue in cross sections is extracted from reflectivity contrast by an edge detection algorithm. The inclusion of viable data starts 35 µm below the surface to avoid a potential distortion caused by mechanical slicing. A tissue mask was created with a threshold of SNR > 6 dB. Image creation and quantitative analysis are conducted in the next based on the pre-processed frames. Unless otherwise stated, image processing and quantification algorithms were implemented in Matlab.

### 5.3.1. Reconstruction from en-face images

*En-face* image is the 2D projection of a 3D dataset on the *xy*-plane. The pixel values represent characteristic of the depth profiles. The contrast specific algorithms for image creation are described below.

***Reflectivity.*** A 2x2 median filter was applied to the cross-sectional reflectivity images. The pixel values on the *en-face* were derived by the mean of the depth profiles. The depth range included in the computation matches the physical thickness of the slice.

***Attenuation.*** Due to scatter and absorption, the intensity of light propagating in tissues exponentially decays with a medium-specific attenuation coefficient. We performed least-squares first-order polynomial fit on logarithmic reflectivity profiles, which present linear decreases along the axial direction. The slope of the linear function was used to form the *en-face* attenuation image. Data points up to 200 μm below surface were included in the fitting. The thickness was selected to minimize the effect of noise on the fit while keeping an optimal illustration of the microstructures.

***Retardance.*** A 2x2 median filter was applied to the cross-sectional retardance images. Then, the e*n-face* value was calculated by taking the mean of the retardance profile. The depth range used in calculation matches the physical slice thickness.

***Axis orientation.*** A histogram based approach was developed to compute the *en-face* orientation. Histogram of the axis orientation for each A-line was computed at $5^0$ intervals and fitted by a Gaussian function. The mean of the Gaussian function was used for the *en-face* orientation. When histogram presented two peaks centering at about $\pm 90^0$, the lower and upper limits of measurement, circular shift was applied to form a continuous distribution before fitting. The depth range used in the histogram matches the physical slice thickness. Unless otherwise stated, representative orientation along a line or in a region of interest (ROI) was computed this way.

The *en-face* images generated from serial scans are stacked to form the 3D space of rat brain, without the necessity of additional registration between slices. The resolution along *z*-axis in this case is determined by the depth range used in the image calculation, and it matches the thickness of physical sections. Such constructions facilitate quick identification and global assessment of

large-scale brain structures at a mesoscopic resolution. The volumetric data was visualized in Vaa3D [153]. The process of reconstruction at this meso-scale resolution is illustrated in Figure 5.3. The 3D reconstruction can be accomplished at higher resolution by z-stacking the cross sections as well, which is discussed in the following section.

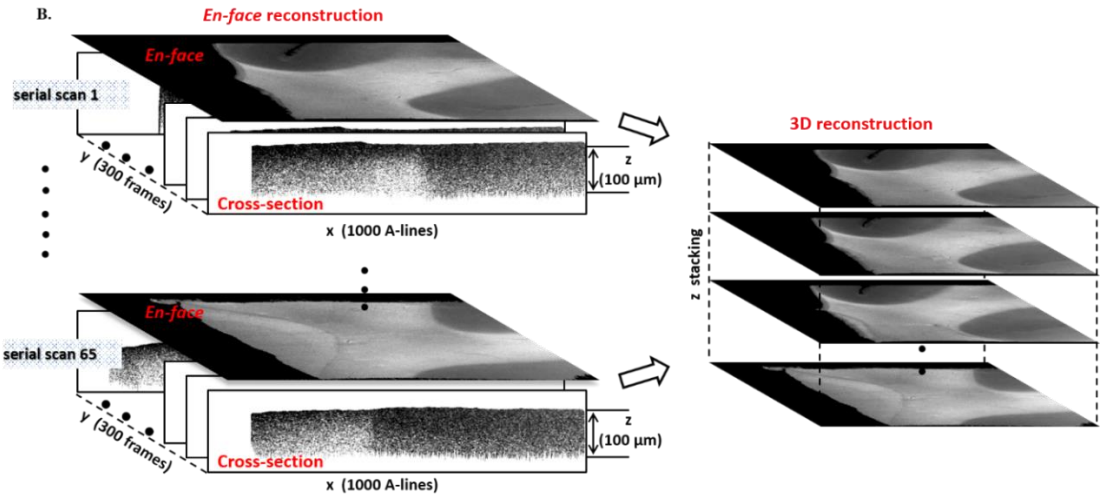


**Figure 5.3 3D reconstruction at meso-scale resolution by stacking the en-face images.**

To construct a complete coronal plane from two lateral scans in the third brain, we applied a pairwise stitching algorithm [186] on *en-face* reflectivity images using Fiji software. The algorithm computed the overlap between the scans which was then linearly blended to compose a full section. The registration parameters were saved and applied to all other contrast images of the same brain section. Orientation offset of the first scan (left hemisphere) was corrected with the reference retarder; however, the second scan (right hemisphere) utilized the white matter, typically the commissural fibers, in the overlapping region as a reference to compute and correct for the orientation offset. Another reference retarder could have been added for the second scan, but we decided to develop the serial correction method that uses internal references in the overlap between adjacent scans. More importantly, the method allows for reconstruction of larger samples, in which multi-grid scans are required and inclusion of external references in the center zone is problematic.

### 5.3.2. Reconstruction at the natural resolution of SOCS

Successful fusion of serial volumetric scans forms the basis of 3D reconstruction of the entire brain at the natural resolution of SOCS (15 x 15 x 5.5 $um^3$). Cross polarization was utilized for this purpose. Carrying the properties of reflectivity and birefringence, the cross polarized light describes the nerve fibers and preserves decent signal intensity in deeper regions. The depth range of the optical section matches the physical slice thickness, but the starting point along depth is adjustable for optimal fusing outcome.

To achieve smooth transition between serial scans, trends along depth direction *z* were minimized by multiplying each A-line with a regularization function *L(z)*,

$$L(z) = \begin{cases} \exp\left(-\frac{2z-N}{N}\ln\left(\frac{a_i + b_{i-1}}{2a_i}\right)\right), & z \le N/2 \\ \exp\left(\frac{2z-N}{N}\ln\left(\frac{a_{i+1} + b_i}{2b_i}\right)\right), & z > N/2 \end{cases} \quad \textbf{5.1}$$

where *N* is the number of points in each A-line, *i* is the slice index, $a_i$ and $b_i$ are local averages of intensities for the start and the end of A-lines in slice *i*. The operation minimizes the intensity mismatch across stitching borders, while maintaining the intensity at the central locations. Residual trends may be removed by advanced image processing algorithms. The 3D reconstruction process by SOCS is summarized in Figure 5.4.

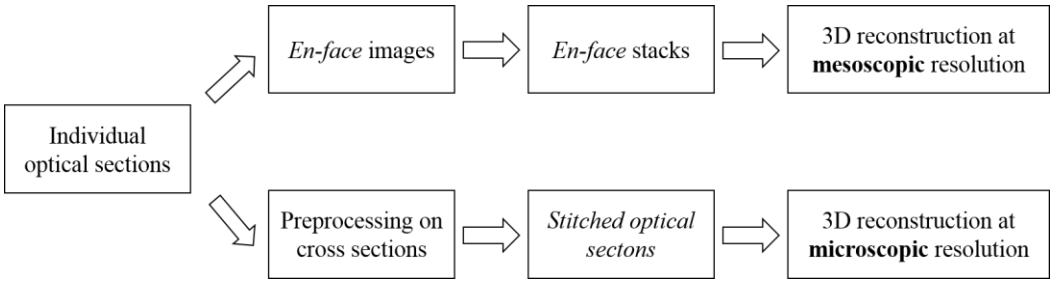


**Figure 5.4 Flow chart of large-scale reconstruction process by SOCS.**

### 5.3.3. Histology of brain slices

Brain slices were sent for histological validation after OCT imaging. Cresyl violet and Weil's myelin stains were performed on selective coronal slices for labeling cell bodies and fiber tracts, respectively. We didn't stain the sagittal sections because 200 μm slices are too thick for histological processing.

## 5.4 RESULTS

The following sections demonstrate the results of SOCS imaging from three rat brains. Serial scans of coronal sections, and those of sagittal sections are presented.

### 5.4.1. SOCS based brain atlas

SOCS provides morphology of tissue structures in a volumetric scan. As a representative optical section in Figure 5.5A shows, the most visible nerve fibers manifest as bright spots or strips followed by fast attenuation in axial (*z*) direction. The transverse (*xy*) plane resembles a coronal section resolving the microscopic anatomy. The top ~35 μm section is not included in the image. To evaluate the light penetration in brain tissues, an ROI (black box in Figure 5.5C) containing the hippocampus and the corpus callosum (cc) is selected, and the averaged reflectivity profiles in the ROI are plotted for the two structures (circles in Figure 5.5B). Light propagating through cc undergoes faster decay with shallower penetration comparing to that through hippocampus. With a polynomial fit (solid curves) and a 6 dB intensity threshold, the imaging depths in the hippocampus and the cc are estimated as 330 μm and 298 μm, respectively. The physical slice thickness can be determined by a criterion that ensures sufficient SNR (e.g. 12 dB) for successful stitching of optical sections, while minimizing the load of slicing. Indicated by the gray lines in the plot, a thickness of 100-200 μm was favorable as described in the Method section.

The *en-face* reflectivity image generated from the optical section is presented in Figure 5.5C. By stacking sequential *en-face* images, the left hemisphere of a rat brain is assembled in Figure 5.5D. The coronal section representing the *en-face* plane starts at Bregma -2.2 mm in front, and reaches

Bregma 4.3 mm towards anterior direction. The dimension of the reconstructed brain in *z*-direction is currently limited by the maximum elevating distance of the mounting stage on the vibratome. Complete coverage can be achieved with a longer traveling distance of the stage. The *en-face* (*xy*) plane with a resolution of ~15 µm delineates the anatomy and preserves decent features of nerve fibers which exhibit intricate organizations. The resolution on *z*-axis is 100 µm for this sample. For smooth visualization, data was interpolated five times yielding a sampling pitch comparable to the resolution on *xy*-plane. Trajectories of long axonal tracts are visible on orthogonal planes (Figure 5.5D). The size and the geometry of brain structures are better apprehended in 3D. The continuity and smoothness of fiber bundles on *xz*- and *yz*-planes confirms the quality of automatic alignment, which relieves the load of inter-slice registration and remarkably accelerates the reconstruction speed compared to conventional histology. Comprehensive 3D atlas of the brain supports high-level structural identification and quantifications such as segmentation, and also forms the basis for further investigations on the progress of neurological and psychiatric diseases.

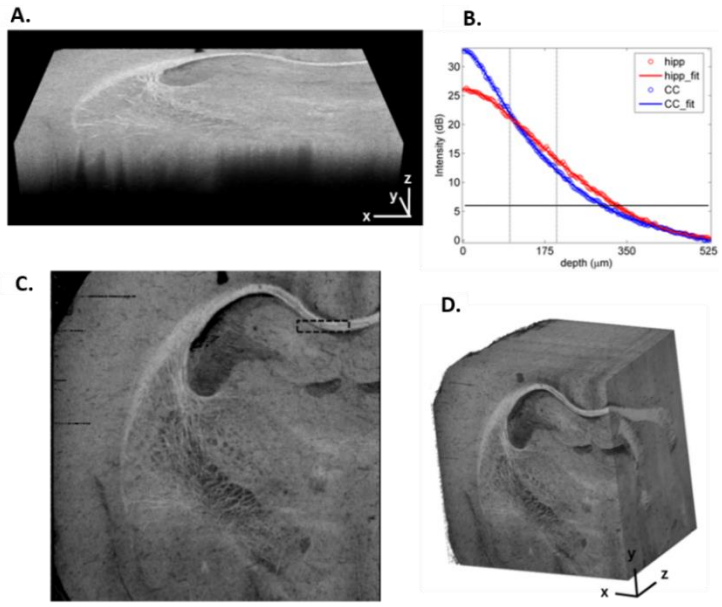


**Figure 5.5 SOCS reconstruction of rat brain images. (A) Volumetric scan of an optical section. xz-plane represents the cross section, and xy-plane assembles the coronal section. (B) Depth profiles of reflectivity in**

**hippocampus (red circles) and corpus callosum (blue circles). The plots present an average of 400 A-lines for each structure within the ROI in (C). Fifth-order polynomial fits were applied for the estimates of light penetration (solid lines). The horizontal line sets the intensity threshold at SNR > 6 dB for the estimation. The vertical lines indicate the slice thickness used in the current studies. (C) En-face image created from the optical section in (A) resembles the coronal view. The black rectangular box indicates the ROI used for the plots in (B). Scale bar: 500 µm. (D) Large scale brain imaging (7 x 7 x 5.5 mm3) is presented by stacking sequential en-face images (see also supplemental video 1). xy: coronal plane; yz: sagittal plane; xz: axial plane.**

### 5.4.2. Brain maps by *en-face* images at mesoresolution

Extracted from single dataset, the contrasts of SOCS provide multidimensional depiction of brain anatomy from different perspectives. *En-face* reflectivity distinguishes the gross structures with altered intensity, and keeps track of the small features by virtue of the superior sensitivity and dynamic range (Figure 5.6A, D). Small features might not be easily recognized on global images due to the high dynamic range. For better visualization, local contrast enhancement was applied to selected ROIs with Fiji (Figure 5.6, i, ii and iv). Retardance map targets the white matter and yields an integral delineation of the fiber routes (Figure 5.6B, E). Attenuation image enriches the anatomical information by sustaining subdivision of a local structure with clear borders (Figure 5.6C, F).

It is known that the reflective intensity of the white matter relies on the orientation of fiber tracts with respect to the illumination plane [148, 185]. For coronal sections, the brightest regions on the reflectivity images are seen among the inter-hemispheric bundles such as cc when the fiber tracts travel parallel to the plane (Figure 5.6D); and the intensity becomes minimum for the fibers running perpendicularly through the plane, observed as dark dots in the striatum (Figure 5.6A, D). The variation of reflectivity brightness exposes the complexity of fiber organization in 3D space, but also reflects detailed in-plane architectures of the white matter. For example, within cc, irregular fiber patterns are visible against a dim medium (upper ROI in Figure 5.6A, and i), indicating sharp turn and cross between the *en-face* plane and the orthogonal direction. Another demonstration is in the lower ROI that reflects interweaving fiber patterns at the lower border of

anterior commissure (ac) (Figure 5.6A, and ii). The regular pattern and direction of fibers in the fimbria of the hippocampus (fi) (ROI in Figure 5.6D, and iv) is verified by myelin staining at higher magnification (x40) (Figure 5.6D, v).

*En-face* retardance images clearly identify the fiber bundles and delineate the fiber paths. The intricacy of white matter in reflectivity images was released by retardance, where white matter consistently presents a positive contrast over gray matter regardless of the orientation (Figure 5.6B, E). For example, fibers in the striatum which are dark in the reflective images are highlighted across coronal sections. The only exception would occur for fibers running about 90° throughout the *en-face* plane. In contrast to reflectivity, the consistent expression of birefringence leads to a more uniform portrait of the cc as shown in the ROI of Figure 5.6B.

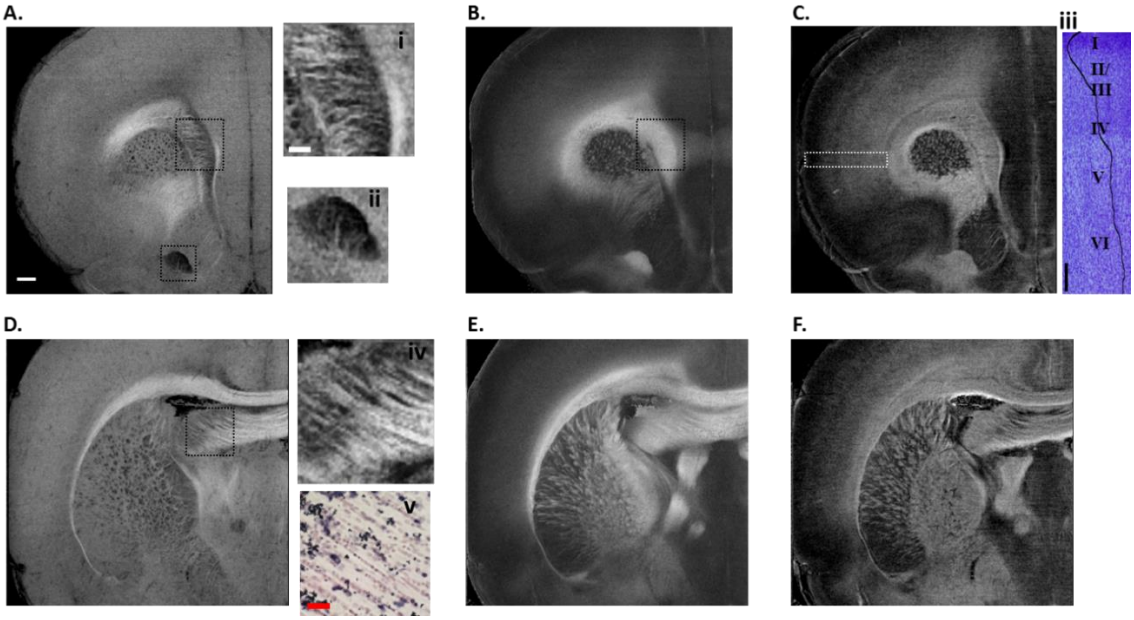


**Figure 5.6 En-face images of reflectivity (A, D), retardance (B, E) and attenuation (C, F) for two coronal sections. Details of the ROIs in the reflectivity images manifest in i, ii and iv with local contrast enhancement implemented in Fiji. The spatial patterns of small fiber tracts are clearly visible. Fiber directions in iv demonstrate consistent result with the myelin stain in v (objective: 40x). The attenuation maps own a different signature. The cortical layers in somatosensory cortex are visible in the ROI on C. The attenuation values in the ROI were averaged along the vertical direction, the plot is then rotated clockwise by 90° (trace in iii), and displayed on top of the cresyl violet stain in the ROI (objective: 10x). Scale bars: 500 µm for coronal sections (A-F), 200 µm for ROIs (i, ii, iii and iv), and 30 µm for histology (v).**

Attenuation maps favor the subdivision of local structures, facilitating the comprehension of spatial organizations and functional implications of fiber pathways (Figure 5.6C & F). The layers of somatosensory cortex are distinguishable with alternating brightness (ROI in Figure 5.6C), and the alternations are well correlated with the results from cresyl violet stain (Figure 5.6C, iii). The morphology changes in the insular cortex below. In addition, the boundary between globus pallidus and striatum is clearly visible (Figure 5.6F). The attenuation image also provides the capability to identify the white matter, most of which highly correlates with the retardance.

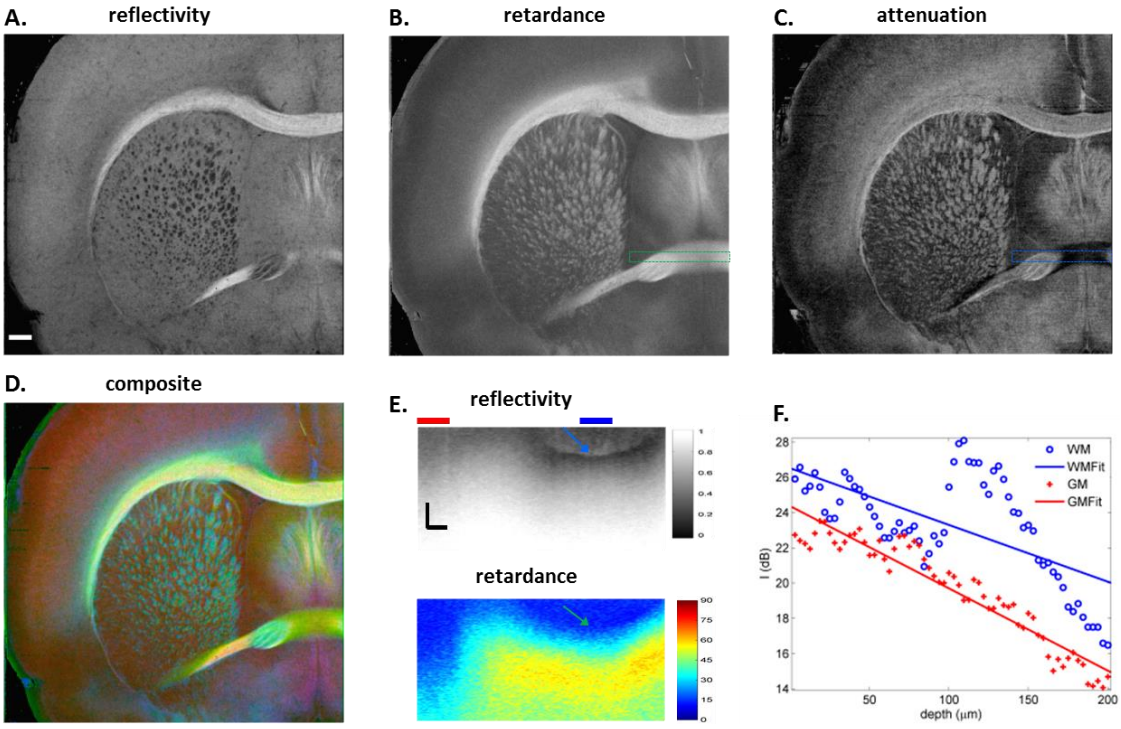


**Figure 5.7 Correlation and comparison between contrasts. Reflectivity (A), retardance (B), and attenuation (C) are color coded (A, red; B, green; C, blue), and merged in a composite image (D). Scale bar: 500 μm. Cross sectional images in E demonstrate the case that for deeply embedded fiber bundles (blue and green arrows), en-face attenuation might miss the identification (dark region of ROI in C); the bundle is positively detected by retardance. Scale bars: horizontal, 200 μm; vertical, 100 μm. Averaged depth profiles for the regions under the horizontal bars (blue and red) on E are plotted in F (blue circles and red dots) together with the linear fits (solid lines). The slope in the embedded bundle region (>100 μm) is large, but the overall slope appears smaller than that of the gray matter region.**

To correlate and compare the contrasts, we used color channels to fuse *en-face* images (Figure 5.7A-C) of reflectivity (red), retardance (green), and attenuation (blue) into a composite image (Figure 5.7D). The brightest region represents the fiber bundles lying parallel to the plane, while the fibers with large inclination angle are shown in blue-green color with missing identity of reflectivity. The myelinated fibers in layer V/VI of cortex extended from the cc are implied by the attenuation contrast in blue. The attenuation map could miss fiber routes highlighted by retardance (ROI in Figure 5.7B & C). Cross sectional image indicates that those fibers are deeply located in the optical section (blue arrow in Figure 5.7E), hence resulting in an irregular depth profile and a lower attenuation from a linear fit comparing with the adjacent gray matter (Figure 5.7F). In contrast, retardance reliably captures the existence of the fiber bundle on the cross section (green arrow in Figure 5.7E).

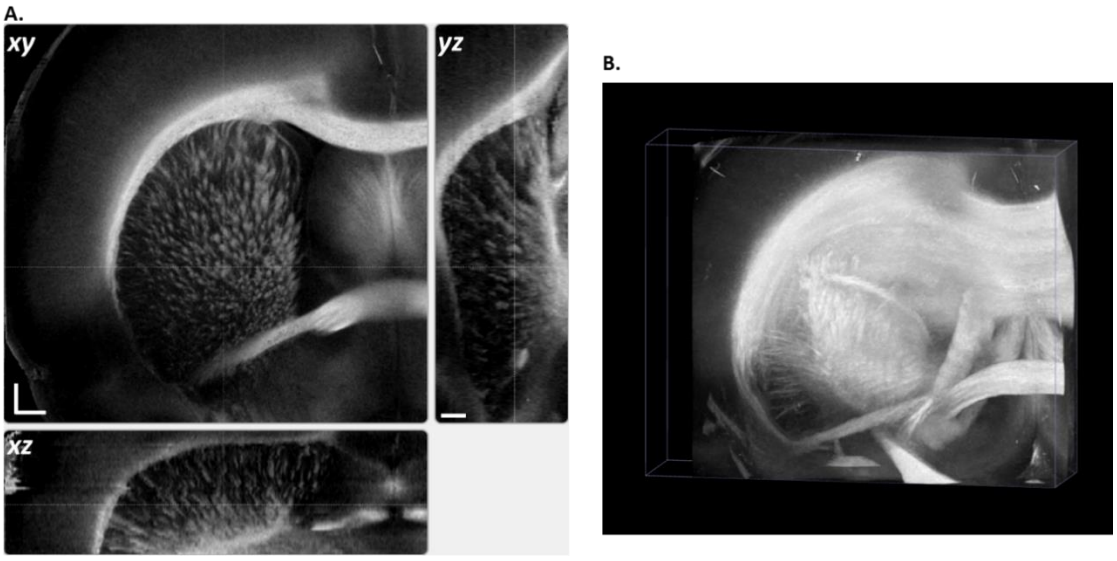


**Figure 5.8 Global identity of 3D neuronal roadmaps in rat brain at the mesoscopic resolution (15 x 15 x 100 µm) is achieved by stacking en-face retardance images of the entire sample. (A) Orthogonal viewing planes: xy, coronal view; xz, axial view; yz, sagittal view. Scale bars: xy, 500 µm; z, 1 mm. (B) Volume rendering of the 3D dataset (7 x 7 x 5.5 mm$^3$, see also supplemental video 2). Maximum projection illustrates the spatial organization of major fiber tracts in the brain.**

Taken all the aspects together, *en-face* retardance offers the most robust detection for global description of the neuronal fibers at mesoscopic resolution. We use stacks of *en-face* retardance

to portray the major fiber roadmap in 3D. Geometry and spatial organizations of neural pathways are captured on the orthogonal viewing planes (Figure 5.8A). Maximum intensity projection of volume rendering provides a perspective view and discloses the complex configurations of the white matter in the brain (Figure 5.8B).

Optic axis orientation offers quantitative assessment of fiber orientations in the illumination plane. Figure 5.9A demonstrates the *en-face* orientation map (left) of a sagittal section around the midline of the brain along with the anatomical (*en-face* reflectivity) image on the right. The orientations of neuronal tracts generally agree with the geometry and directional features as revealed by the anatomical image. Gradually changing directions in the stria medullaris of thalamus are expressed as smooth color transitions according to the color wheel. The fibers of outer layer of cc align parallel to the plane, and the orientation change at the tail of genu of the cc (rectangular ROI in Figure 5.9A) is clearly shown in the magnified image. The orientation map is also capable of uncovering groups of axonal bundles by differentiated directions such as fiber clusters within the thalamic area (round ROI in Figure 5.9A), whereas the fiber tracts are hardly distinguishable in the anatomical image. The quantification of fiber orientation is better visualized by a vector field. Figure 5.9B shows a similar brain slice with the orientation vectors superimposed on the retardance image. The direction of the vectors is well aligned with the geometry of fiber bundles where the fiber architecture is clearly depicted with bright retardance (black arrows), indicating the accuracy of orientation measurement is high there. However, more noise is observed in the regions where retardance is relatively low probably due to the large inclination of the fibers such as in the region of cc and fornix (white arrows).

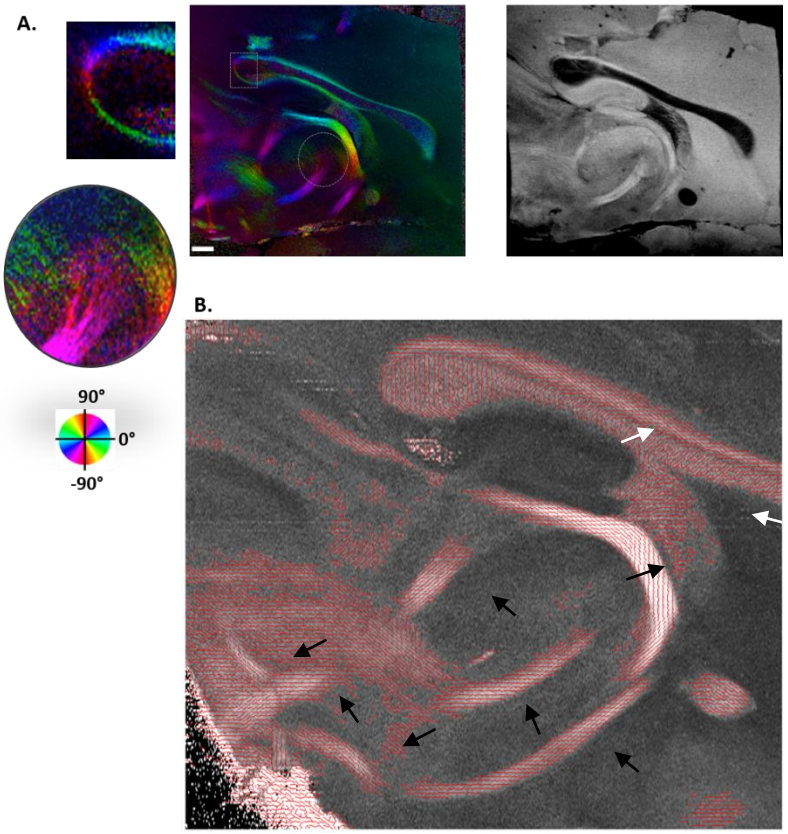


**Figure 5.9** ***En-face*** **orientation maps of sagittal sections show the in-plane orientation of fiber tracts. (A) Orientation image of a sagittal section around the midline is shown on the left with the magnified images of two ROIs. The anterior side is on the right, and the posterior is on the left. The value of orientation is color coded in HSV space according to the color wheel, and the brightness is controlled by the retardance which masks the gray matter. The associated anatomy (reflectivity image) is shown on the right. (B) The vector map of fiber orientations in a similar slice. The red lines indicating the fiber orientations obtained by the optic axis orientation are superimposed on the retardance image. The arrows in black indicate the fibers where orientation vector high higher accuracy, while those in white indicate the regions where more noise is observed.**

The orientation map of an entire coronal section is achieved by stitching the images of two scans (Figure 5.10). The orientation offset of the second scan with respect to the first was estimated in the overlap region: the difference in the commissural fibers (i - ii) was plotted in histogram and fitted by a Gaussian function, the mean of which represents the estimate of the offset. After stitching, the orientation map of the entire coronal section was demonstrated with the anatomy (bottom panels). As expected, orientations of cc, fi and fornix on contralateral sides exhibit symmetric colors with respect to the vertical line on the color wheel. The consistency of colors on

the commissural fibers (cc and ac) at the inter-hemispheric region indicates a good match between the two scans. With this successful fusion, investigation of fiber orientations in large samples is plausible.

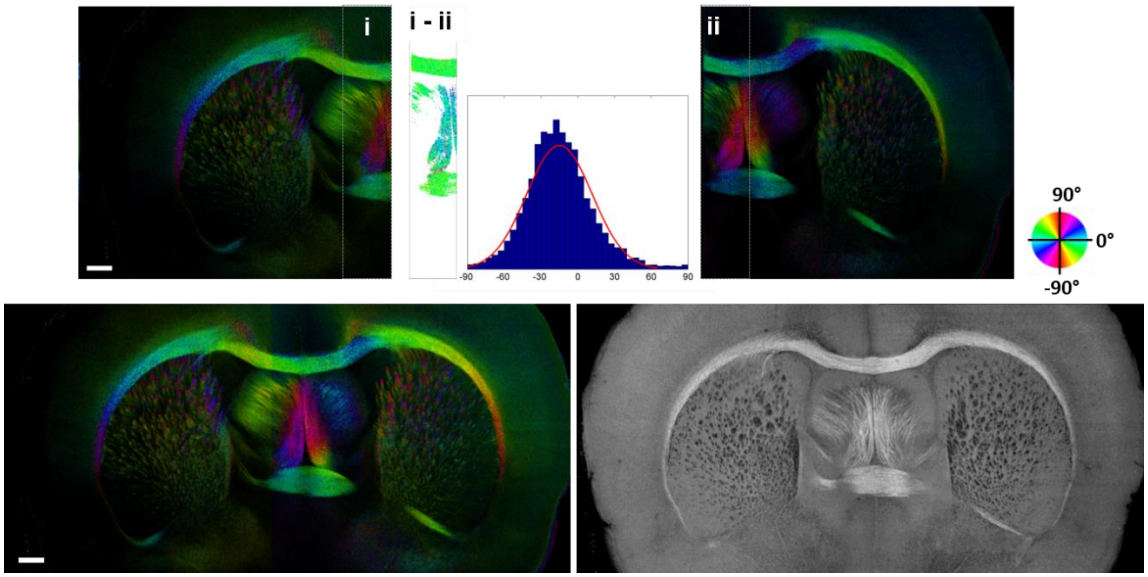


**Figure 5.10 Reconstruction of an entire coronal section. Overlap of the left and right scans is used to estimate the orientation offset of the second scan. Histogram and Gaussian fitting of the orientation difference are demonstrated. Stitching results for the entire coronal section are shown in the orientation and anatomy maps at the bottom. Scale bars: 500 µm.**

### 5.4.3. High resolution reconstruction by serial optical sections

3D reconstruction of fiber maps in rat brain

Cross sectional images take advantage of depth resolved capability of the system (5.5 µm) to unveil microstructures that are not exhibited by *en-face* stacks. To achieve 3D reconstruction at the natural resolution of the SOCS, it is ideal to stack depth-resolved optical sections of the sequential scans. Three types of contrasts are viable to depict localized fiber tracts. These are reflectivity, cross polarization and birefringence as illustrated in Figure 5.11A. The blended image of cross polarization (red) and reflectivity (green) shows that reflectivity loses the strength to elucidate fibers in deeper regions (red domination), and is inferior in suppressing the gray

matter (green in non-fiber regions), albeit the equivalent expression of the fiber tracts in yellow at shallower locations. Color merged image of cross polarization (red) and birefringence (blue) exhibits co-identification of large fibers in magenta. However, the advantage of depth-localized identification by birefringence is compromised for small fibers. This is due to the extensive noise-reduction processing on retardance image for birefringence calculation, which smoothes the sharp features, leads to lower birefringence values and worsens the effective spatial resolution. Based on these comparisons, we utilized cross polarization to conduct inter-section stitching. We also examined cross polarization images on *xy*-plane at various depths. As shown in Figure 5.11B, deterioration of image quality was not observed within the depth of consideration.

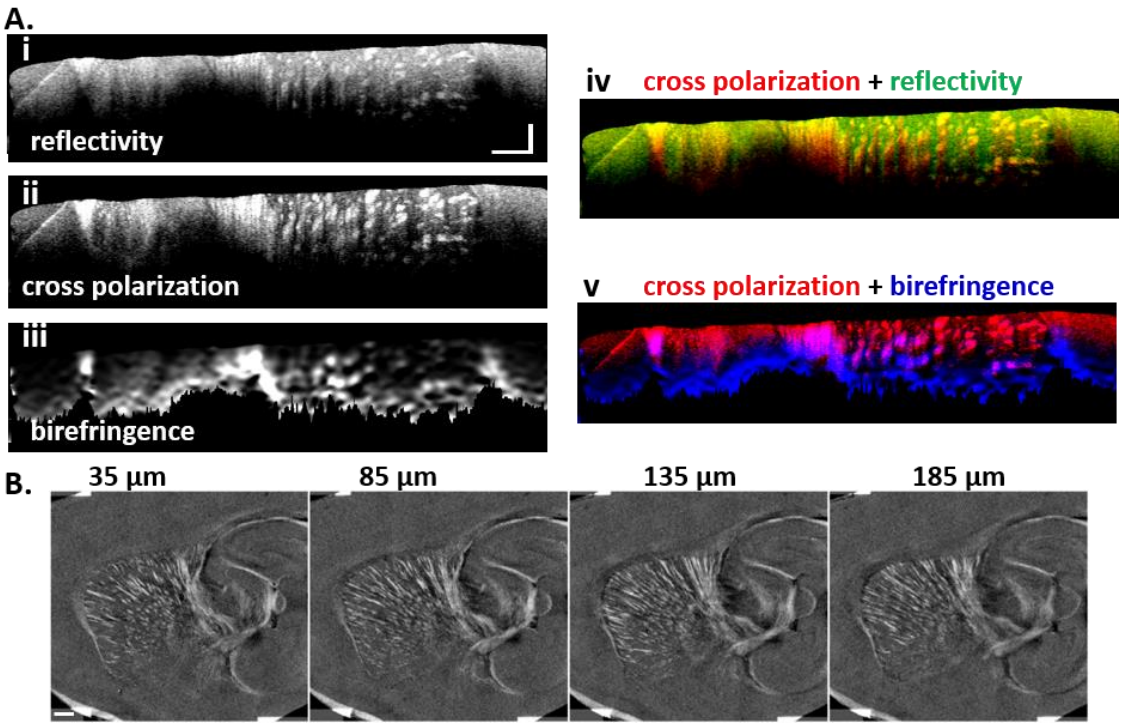


**Figure 5.11 (A) Reflectivity, cross polarization and birefringence images are available to reveal localized fiber tracts on cross sections. For contrast comparison, color blended images are shown on the right. The co-expression of cross-polarization (red) and reflectivity (green) is illustrated in yellow, and that of cross-polarization (red) and birefringence (blue) is in magenta. Scale bars: horizontal, 500 µm; vertical, 150 µm. (B) En-face cross polarization images are reconstructed at various depths (35, 85, 135 and 185 µm) to demonstrate consistent image quality within an optical section (a volume scan). Scale bar: 500 µm.**

Stitching consecutive volume scans requires careful alignment. Figure 5.12A shows two cross-sections from consecutive volume scans (section 13 and 14). The rectangular boxes indicate the same region, whose landmarks are used to examine the stitching quality. After connected along *z*-axis, the color blended image of the two scans demonstrates a decent overlap of the small and large fiber tracts. Moreover, the fused image after removing the trend of depth-dependent intensity exhibits a smooth transition. These images suggest that mechanical distortion due to slicing is negligible and additional registration is not in need for the preservation of lateral coordinates. For further confirmation, we constructed *en-face* images from the overlap region of the adjacent scans. For scan 13, data is located between 200 μm and 250 μm below surface; while for scan 14, data is selected from the top 50 μm. Figure 5.12B shows that the two images are highly alike, despite the slight difference in lateral resolutions due to depth dependence of beam width within the depth of focus. Cross-correlation of the images peaks at the origin, indicating that no lateral displacement was induced by slicing. These results demonstrate that the sequential images produced by serial scans can be successfully connected to reconstruct large tissues at high spatial resolution. Specifically, continuity of fiber tracts across the stitching border demonstrates the feasibility of tracing long axonal fiber bundles in the brain.

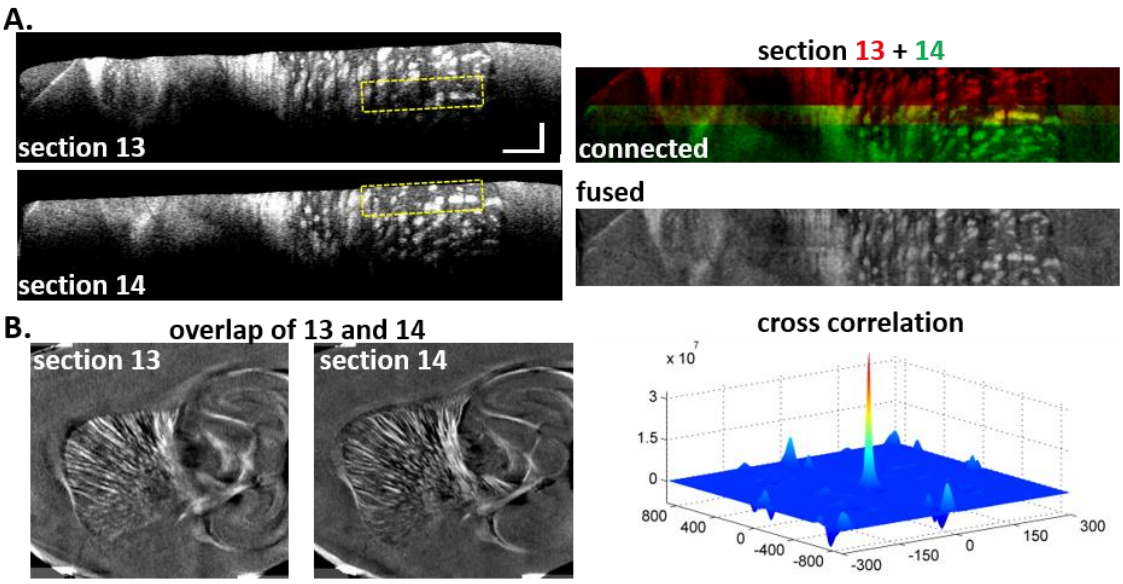


**Figure 5.12 Stitching cross sections of consecutive volume scans (13 and 14). Same regions are covered in both scans, as exampled by the yellow boxes. The connected image is color coded (13 in red, and 14 in green), and fused image, after removal of depth-dependent trend, is in gray scale. Scale bars: horizontal, 500 µm; vertical, 150 µm. (D) En-face cross polarization images from the overlap region for each scan. Scale bar: 500 µm. The cross-correlation peaks at the origin.**

The results of stitched cross-section from all the serial scans are shown in Figure 5.13. Images on the horizontal planes sensitively catch the fiber tracts (Figure 5.13A, D), although residual stitching effect is still visible due to imperfect compensation of the depth-dependent trend. The tiny dots in the rectangular ROI (Figure 5.13A) are intersected fiber tracts on the sagittal view in the midbrain region (arrow in Figure 5.13E). The dots are better visualized by a 3D surface plot (Figure 5.13B) and intensity profile of a representative line (Figure 5.13C). Estimated from full width at half maxima, the mean size of the tracts in the ROI is found to be about 23 µm. Trajectories of small fibers are recognized on the high resolution images as well. In Figure 5.13F, fiber tracts emerging from the border of globus pallidus and running through striatum to cc are shown on sequential horizontal planes from ventral to dorsal direction. The images are separated by 25 µm and presented in two groups. The first group (0-100 µm) starts with the square ROI of Figure 5.13D, and the second group is 500 µm away from the ROI.

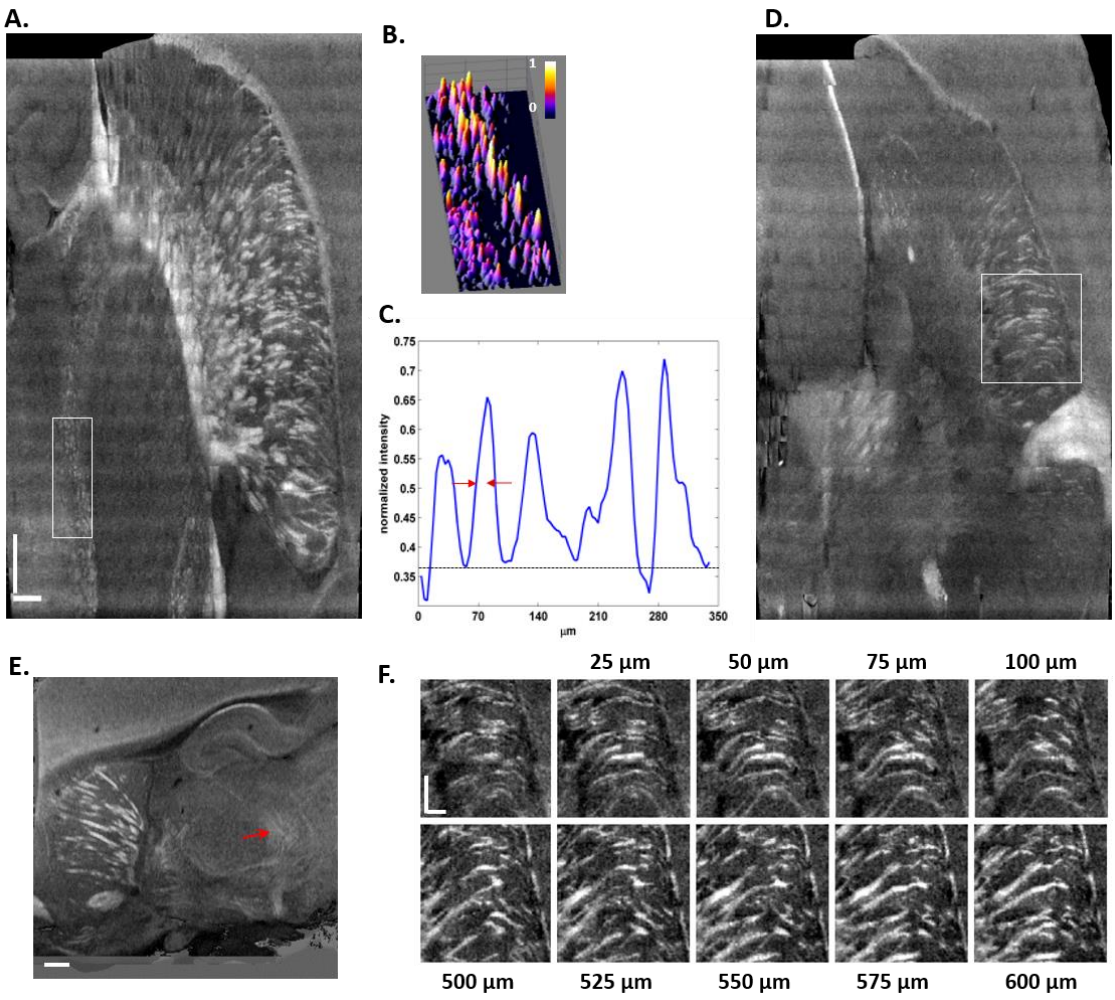


**Figure 5.13 Stitched optical sections. (A) and (D) are two representative horizontal planes constructed by stitching the cross sectional images of serial scans. Most of the neuronal tracts appear bright, whereas the fibers oriented perpendicular to the illumination plane may appear rather dim. The rectangular ROI in (A) represents crossing fibers in the midbrain region which are visualized on the sagittal plane in C (indicated by the arrow). Surface plot (B) and intensity profile along a vertical line (C) clearly illustrate individual fiber tracts. (F) Trajectories of small fibers are shown on sequential sections along y-axis towards superior direction. The first image specifies the square ROI of B. Pixel sizes: 7 x 3.47 μm2 for B and F, and 7 x 7 μm2 (interpolated) for C. Scale bars: 500 μm in A and E, and 250 μm in F.**

Full reconstruction of the rat brain in 3D at the natural resolution of SOCS is visualized in orthogonal planes by using the cross-polarization contrast (Figure 5.14). The sagittal view denotes the *en-face* plane with an isotropic resolution of 15 μm, and horizontal and coronal sections compose of stacks of cross-sectional images owning the resolution of 5.5 x 15 $\mu m^2$.

Although features in the commissural fibers like cc are not distinctive owing to the fiber orientation dependence of light intensity, geometry of the fiber bundles can be predicted. Overall, the integration of serial volumetric scans enables the multi-perspective and multi-scale inspections of the intricate neuronal roadmaps in the brain.

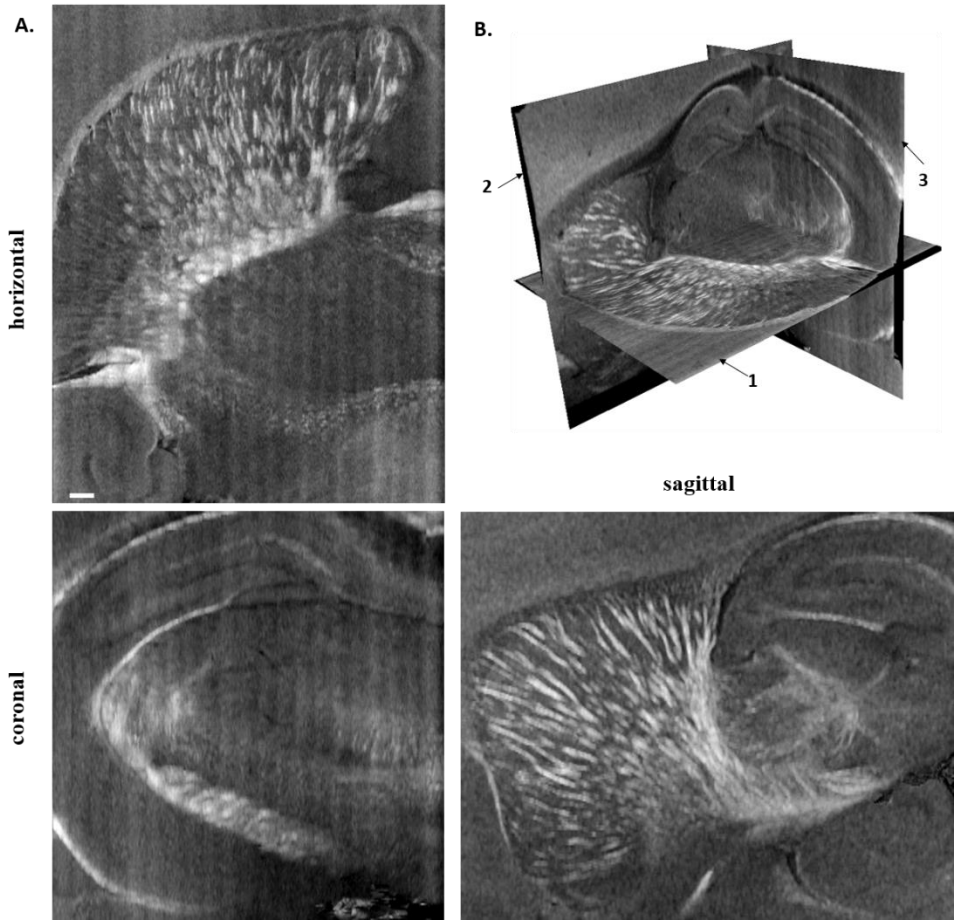


**Figure 5.14 Reconstruction of rat brain at natural resolution of SOCS. (A) orthogonal views with 3 representative planes. (B) Visualization of 3D reconstruction, 1: horizontal, 2: sagittal, 3: coronal.**

## 5.5 DISCUSSION

We demonstrated a novel approach of SOCS to reconstruct large-scale neuroanatomical circuitry of brain at microscopic scale resolution. The imaging modality takes advantage of intrinsic optical properties of tissues to depict the anatomy of brain, especially the architectures of white

matter within and between local structures, and the orientation of constituting fiber tracts. We described global fiber organizations by *en-face* image stacks, and inspected fiber tracts of various sizes at the natural resolution of SOCS by stacking serial scans.

The multiple contrasts generated from a single measurement of SOCS enlighten the exploration of neural pathways from different perspectives. The reflectivity highlights different types of scatters and their interface; hence, it unveils the fine features in a fiber bundle which are typically reported in histological images [187]. On the other hand, the reflectivity contrast loses the depiction of fibers with large inclination angle. The attenuation contrast holds the general property of photon propagation in tissue. The characteristic is affected by cell type, density and alignment. Therefore, the attenuation images reveal the structures in gray matter such as cortex and subcortical regions in addition to fiber delineation. For white matter identification, the attenuation has a weaker dependence on the direction of fiber axis. Due to the limitation of first order fit on logarithmic depth profile, attenuation does not reflect the structure change in depth, resulting in miss identification of fiber tracts that occupy the lower portion of the imaging depth. Local attenuation image can be generated based on the derivative of depth profiles, but considerable noise-reduction procedures needs to be investigated in the future. Retardance provides a reliable identification of fiber tracts due to the birefringence property of myelination. Unlike histological images which merely describe the superficial features of a tissue slice, the retardance contrast enables deep fiber tracts emerge on the en-face images as well. Quantification of fiber orientation has been obtained through texture analysis on digital images [187, 188]. The optic axis orientation contrast of SOCS offers a direct access to in-plane fiber orientations, and 3D orientation could be realized with geometrical analysis on volumetric data. Owing to the unique merit of each contrast, an important future work is to translate and integrate the multi-contrast images into quantitative representations for the physical properties of neuronal networks

such as fiber density and anisotropy, which will enable comparisons across various imaging modalities.

Complete reconstruction of neuronal connectivity maps has been prohibited in conventional histology because of the failure to track long fibers throughout the brain. Currently, diffusion magnetic resonance imaging [139] serves as the unique approach to sketch the fiber maps of *in-vivo* human brains at a resolution of ~2 mm. While pushing the resolution to submillimeter regime for distinguishing crossing fibers [189], the scanning time greatly increases up to tens of hours making it only available for *ex-vivo* studies [190]. In addition, the technique needs to be validated which turns out to be another challenge [191].

To address the issue of full-scale brain imaging at microscopic resolution, speed of SOCS becomes a most appealing attribute. By adopting serial block-face design, SOCS automatically enables spatial alignment of the optical sections. Comparing to serial confocal [176] and two photon microscopy [178], SOCS is superior in light penetration, which alleviates the slicing load. Besides, SOCS acquires features along a depth profile simultaneously without requiring a mechanical scan, which shortens the imaging time further. Currently, the total time required for serial scans is limited by manual operations and speed of the vibratome. However, time for data acquisition alone for an entire rat brain is estimated to be ~1.5 hours with a voxel size of 6 x 6 x3.5$\mu m^3$ and the sectioning thickness of 200 μm. Future enhancement of optical resolution will necessitate finer grids and longer acquisition, but the speed of acquisition can be improved by a shorter integration time of the camera. Alternatively, imaging can be performed with swept-source technology, which can enhance the acquisition speed up to 50 times using a VCSEL source [192, 193]. We envision that implementation of an automated serial scanner and development of post-processing tools will eventually lead comprehensive reconstruction of primate and human brains in a manageable time.

There are technical issues to be resolved for drawing comprehensive wiring diagrams in the brain. First of all, the dependence of reflectivity on fiber orientations causes missing identity of fiber tracts with large inclination angles. Similar observations have been reported in collagen networks with reflective confocal microscopy [194]. To have a full viewing angle of the fiber tracts, multi-directional illuminative beams are appealing [195, 196]. Another related issue is to measure the inclination angle, which will allow quantification of the 3D orientation of fiber tracts and the true birefringence. Variable-incidence angle has been incorporated to polarization-sensitive OCT to quantify the 3D axis orientation of a tendon sample [165, 197]. In addition, current computations of retardance and axis orientation assume that in-plane axis does not change along depth in one optical section; however, this condition would not be satisfied in the regions where fiber crossing is widely observed. Quantification of depth-resolved true birefringence and 3D axis orientation is indispensible. Local birefringence and axis orientation in layered structures have been obtained by modified polarization-sensitive OCT setups and numerical analysis [161, 162, 198]. However, the capability to unveil more complex and heterogeneous patterns of the white matter in the brain has yet to be investigated.

The big challenge of obtaining comprehensive connectivity in the complex brain would be whether intrinsic contrasts are sufficient to visualize trajectory of distinctive fiber tracts within large bundles, including the commissural fibers, the association fibers and crossing fiber regions. The features on the fiber maps demonstrated the ability of SOCS to visualize interweaving fibers (Fig. 7C); however, the resolution must be improved to visualize individual axonal tracts at a fiber scale. Electron microscopy of corpus callosum reveals a dense package of axons with separations of 1-2 um [199]. The axial and lateral resolutions of SOCS can be improved by incorporating a broader bandwidth light source and a high numerical aperture lens, respectively. Using an optical coherence microscopy (OCM) system at 1300 nm wavelength, neurons and axonal fibers in different cortical layers were characterized [200], and myofibers are visualized in

different tissues [188]. The progressive development of plaques was observed in a mouse model of Alzheimer's diseases using an extended-focus OCM setup [201]. With a full-field OCT setup, myelinated fiber tracts were visualized in central and peripheral nervous systems [181]. However, systematic characterizations of white matter in the brain using ultrahigh resolution OCT have not been reported. The contrasts of SOCS can be utilized and investigated for brain imaging at the OCM resolution.

SOCS and its future advances open up intriguing applications in neurological and psychiatric disorders. As a new tool that offers multi-scale images and multi-parametric quantitative analysis, SOCS may lead to unprecedented discoveries of anatomical changes in population neurons and fiber networks of pathological brains, building up our current knowledge in multiple sclerosis, Parkinson's, Alzheimer's, autism and schizophrenia.

# CHAPTER 6 STRUCTURE TENSOR ANALYSIS FOR FIBER ORIENTATION AND TRACTOGRAPHY

## 6.1 INTRODUCTION

Quantitative neuronal imaging and connectome (human connectome project) in the nervous system are important both in basic neuroscience research and clinical diagnosis. It is believed now that many brain diseases are associated with abnormity in the white matter, including changes in fiber architecture, orientation and connections within or between distinct regions [202, 203]. Despite of the crucial role of the communication pathways in brain function, the knowledge we possess on the wiring system is in great scarcity.

Diffusion magnetic resonance imaging (dMRI) [139] technique provides a unique solution to non-invasively target the white matter in living human brain at millimeter scale resolution. Clinical applications have indicated changes in white matter organization in patients with traumatic and ischemic brain injury and brain tumor, and abnormal connectivity patterns are accompanied in addition to volume change of gray matter in patients with autism or schizophrenia [204, 205]. Based on those observations, it is reasonable to hypothesize that alteration in fiber orientations would be a sensitive indicator of brain conditions, but it has not been under finer scrutiny due to limitations of current imaging techniques. Advances in dMRI, such as high resolution diffusion tensor imaging (DTI), high angular resolution diffusion imaging (HARDI) [141] or diffusion spectrum imaging (DSI) [207], enable investigations at submillimeter resolution and/or with over hundred directions.

At a finer spatial scale, light microscopy enlightens single axon visualization. Quantification of fiber orientations and tract tracing have been obtained by digital signal processing on the images. For example, Bock et al. [208] and Jespersen et al. [209] performed digital reconstructions of stained neurons and conducted fiber tracking based on reconstructed binary images. Budde *et al*. [210] applied a Fourier transform algorithm to obtain fiber orientation maps in normal and tumor induced rat brains. Choe et al. [211] recruited a filter matching algorithm to compare the fiber orientations computed from light microscopy images with diffusion tensor MRI. So far, majority of studies have been performed on 2D space or restricted to a small spatial coverage of the tissue. Global explorations on fiber orientation maps remain exclusively unsolved and thus leave a gap with the system-level reconstruction by dMRI.

The serial optical coherence scanner (SOCS) developed in Chapter 5 could potentially bridge the gap due to its capability of multi-scale and high-resolution in brain imaging with particular target of the white matter. However, one of the remaining issues is that the axis orientation measure is restricted on 2D plane, thus 3D tractography is prohibited under the current setup. This could be resolved with enhanced optical setups as discussed at the end of Chapter 5. The alternative approach is to achieve the orientation quantification on 3D structural images by computational analysis.

In this chapter, we use a structure tensor (ST) analysis on SOCS images to construct quantitative fiber orientation maps in 2D and 3D space. ST is a computational analysis to extract features on digital images or volumetric data. It takes the neighboring gradients of a pixel into account and describes the anisotropy and directionality of local textures on the images [212]. The approach has been widely used in image or video processing for edge detection and motion tracking [213, 214]. Biomedical applications of ST include quantitative analysis of anisotropic elements, such as collagen networks [215], myocardial fibers [216] and human brain cortex [217, 218]. Budde and Frank [187] applied ST on histological slices of rat brain to examine the fiber orientation in 2D. Our work extends the previous studies to interrogate 3D fiber orientations in rat brain. We will

evaluate the accuracy and the reliability of ST based orientation by comparing the computational results with the optical measures in SOCS. In addition, because of the analogy of ST with the tensor matrices in DTI, we can implement the tractography and the connectivity analysis using the software tools developed for dMRI techniques. The pipeline of this computational model to be developed in this chapter is shown in Figure 6.1.

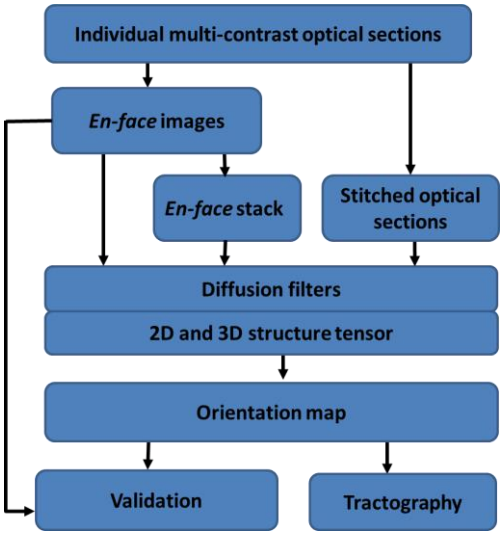


**Figure 6.1 Processing pipeline of structure tensor analysis in SOCS. The volumetric data of multiple contrasts are generated for each optical scan. En-face images of reflectivity, attenuation, retardance and cross-polarization are created for 2D ST computation. En-face stack of retardance and cross-sectional stitch of cross-polarization are obtained for 3D ST computation. Structure tensor metrics are constructed, and the structure and orientation maps of fibers are derived from the eigenvalues and eigenvectors, respectively. The ST-orientation maps are validated by the en-face optic axis orientation measures. Tractography is conducted based on the structure tensor.**

## 6.2 METHODOLOGY OF STRUCTURE TENSOR ANALYSIS

Structure tensor describes the features of the dataset by taking the neighboring profiles into account. The features of the white matter in the brain are mainly line or tube like structures in SOCS images because of the advantageous resolution. Densely packed fibers such as corpus callosum may present a sheet-like geometry in 3D space. As we are especially interested in fiber delineation and orientation quantification, the anisotropy and directionality related information

from the structure tensor is the major focus. The computational processes are described as follows.

1. The gradient ($\nabla I_\sigma$) of the image data ($I$) is computed. To avoid the singularity in discrete digital images, we use theconvolution of the first-order derivative Gaussian kernel with the original image to compute the partial derivatives of the image data.

$$\boldsymbol{\nabla I_\sigma = \nabla K_\sigma * I} \quad \textbf{6.1}$$

2. The structure tensor ($J$) is constructed by the outer product of the gradient vectors as follows.

$$\boldsymbol{J = \nabla I_\sigma \nabla I_\sigma{}^T} = \begin{cases} \begin{pmatrix} I^2_{\sigma_x} & I_{\sigma_{xy}} \\ I_{\sigma_{yx}} & I^2_{\sigma_y} \end{pmatrix} & \textbf{for 2D data} \\ \begin{pmatrix} I^2_{\sigma_x} & I_{\sigma_{xy}} & I_{\sigma_{xz}} \\ I_{\sigma_{yx}} & I^2_{\sigma_y} & I_{\sigma_{yz}} \\ I_{\sigma_{zx}} & I_{\sigma_{zy}} & I^2_{\sigma_z} \end{pmatrix} & \textbf{for 3D data} \end{cases} \quad \textbf{6.2}$$

3. The components of the tensor matrix are smoothed through a convolution with a Gaussian kernel $K_{n,\rho}$., where $n$ represents the number of neighboring points included, and $\rho$ –standard deviation of the Gaussian kernel – controls the weights of the neighbors take in smoothing.

$$\boldsymbol{J_{n,\rho} = K_{n,\rho} * J} \quad \textbf{6.3}$$

4. Eigen-decomposition is performed on the tensor matrices, and the eigenvalues and eigenvectors are extracted. The fiber orientation is represented by the eigenvector corresponding to the smallest eigenvalue.

Noise especially speckle is a non-trivial problem in SOCS imaging. Because of the high-contrast property of the speckle pattern, it is sensitively captured by the ST and treated as image features. Therefore, appropriate filter is important for ST computation. We adopted a nonlinear anisotropic diffusion filter described by Kroon and Slump [219]

(http://www.mathworks.com/matlabcentral/fileexchange/25449-image-edge-enhancing-coherence-filter-toolbox) on SOCS data and for ST calculation. The filter has been applied in a ST incorporated model of MRI and diffusion weighted imaging for tractography construction [220]. We will evaluate the effectiveness of filtering in Results.

## 6.3 FIBER ORIENTATIONS BY STRUCTURE TENSOR AND VERIFICATIONS

The structure tensor analysis is applied on the fiber architecture maps that are established in the previous chapter. The data acquisition and reconstruction algorithms are described in Chapter 5.2 and 5.3. ST-orientation is verified by the optic axis orientation measurement. The 2D ST-orientation map is directly correlated with the *en-face* optic axis orientation image. Quantitative comparisons are performed in selected ROIs. The orientation difference (in degree) between computation and measurement in a specific ROI is presented in histogram. The mean difference estimates as the angle with highest appearance frequency, and the width of the difference distribution is counted by FWHM of the histogram.

Direct validation of 3D ST-orientation is not available with the current SOCS setup. Instead, we constructed an *en-face* ST-orientation map and correlate it with the *en-face* optic axis orientation on the xy-plane. The *en-face* ST-orientation is derived as follows: the 3D orientation vector is projected onto the xy-plane, and a depth integrated orientation map is obtained for each optical scan by applying a histogram approach that has been used for the *en-face* optic axis orientation. The ST-orientation on z-axis can be linked with prior knowledge of anatomy and diffusion MRI techniques. Future improvement of the optical setup in the imaging system could support direct comparisons as described in the Discussion.

### 6.3.1. 2D structure tensor on en-face images and verification

*Structure tensor on multi-contrast SOCS images*

SOCS produces multi-contrast *en-face* images which reveal the anatomical information from different perspectives (Figure 6.2A).The reflectivity describes gross structures, but the white matter can be either brighter or darker than the gray matter depending on the fiber orientation with respect to the illumination beam. The attenuation not only distinguishes local structures but also preserves fiber identification given that big fiber bundles are not deeply embedded below the sectioning surface. The cross-polarization and the retardance especially target on the white matter where birefringence is present.

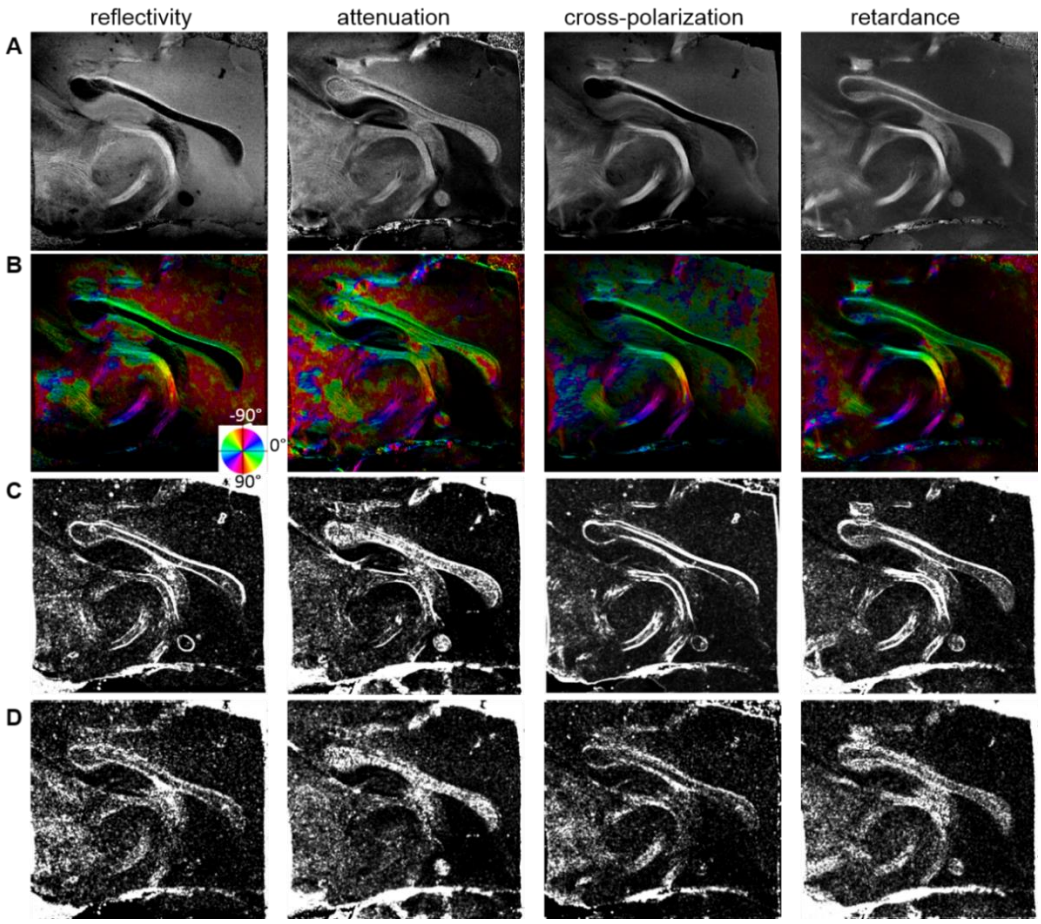


**Figure 6.2 Structure tensor on the multi-contrast en-face images of SOCS. (A) Structure tensors are applied on the en-face images of multiple contrasts in SOCS, including reflectivity, attenuation, cross-polarization and retardance. The images are normalized in each contrast for a desirable dynamic range. (B) The ST-orientation maps corresponding to individual contrast images are shown. The orientation values are color coded by the color wheel, and the brightness comes from the intensity of each en-face image. The larger (C) and smaller (D)**

**eigenvalue images of the structure tensor represent fiber identification and are shown for each contrast. The eigenvalues are normalized in each image for an optimized visualization.**

We applied the structure tensor on each contrast and evaluate the performance of fiber identification and orientation quantification. The ST-orientation maps are shown in Figure 6.2B. The orientation of the four images shares the same color-coding based on the color wheel, but image brightness is determined by the individual contrast. The ST-orientation exhibits great similarity in the white matter among the multiple contrasts. Best agreements are found in the bundles aligned parallel to the plane where fiber identities are highlighted on all the contrasts, such as the fiber groups around the medial thalamus region. In the fiber clusters caudal to the thalamus, some discrepancies are seen depending on the characteristics of each contrast. The eigenvalues of the structure tensor represent feature identification in the images (Figure 6.2C & 6.2D). The greater eigenvalue (Figure 6.2C) catches the edges of the major features, and depicts the skeleton of fiber architectures. The smaller eigenvalue (Figure 6.2D) provides secondary identification in the fibers, whereas it bears more noise. The overall capability of fiber delineation by eigenvalues is inferior to the optical contrasts, due to degraded resolution and background noise contamination. We will use the ST-orientation and the optical contrast for fiber-map delineation hereafter. As the retardance provides the most robust identification of the white matter on the *en-face* plane, 2D ST-orientation maps shown later are computed based on this contrast otherwise stated.

*Filter effect on the structure tensor*

Filtering plays a significant role in obtaining smooth orientation agreeable with the physical alignment of fiber bundles, as structure tensor is sensitive to abrupt changes in image intensity. The noise in SOCS, especially the speckle with high contrast, severely influences the orientation estimation of true features. We tested the structure tensor on original data and data smoothed by nonlinear anisotropic diffusion filters with varied sizes of Gaussian kernel. Figure 6.3A displays the ST-orientation maps accompanied by the histograms of fiber orientation in a selected ROI.

Two kernel sizes are used on the structure tensor metrics: $K_{10,2}$ (top) and $K_{20,4}$ (bottom). In general, increasing the size of Gaussian kernel enhances the consistency of orientation representation; however, without filtering, the orientation image is hardly immune from noise even when more neighboring points are involved and given higher weights during smoothing (left column). The nonlinear anisotropic diffusion filter dramatically diminishes the noise (middle and right columns). The filter applied on the tensor data (right column) is more advantageous than on the SOCS image (middle column), as it allows less contaminated orientation description with smaller size of smooth kernel, and hence impairing the averaging effect. The standard deviations of the ROI orientations are plotted in Figure 6.3B.

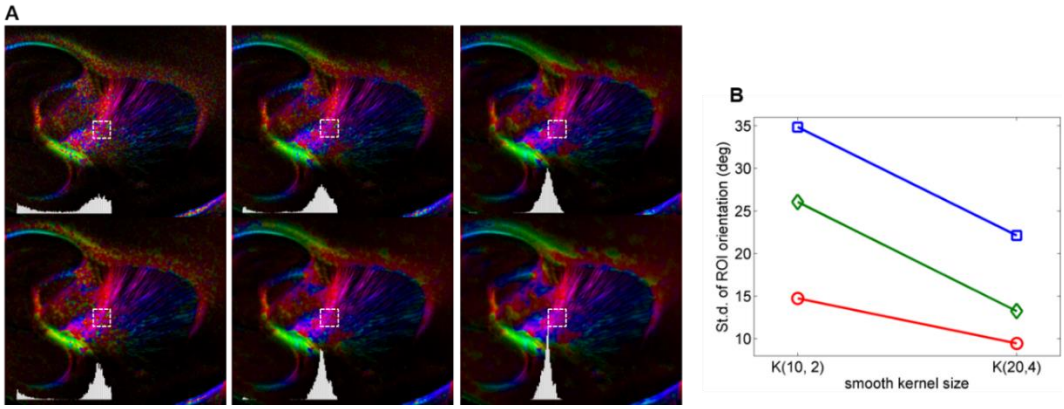


**Figure 6.3 Evaluation of the effectiveness of filtering during ST computation. (A) The ST-orientation maps are compared in three filtering conditions: left – no filtering, middle – with nonlinear anisotropic diffusion filter on the SOCS image, right – with nonlinear anisotropic diffusion filter on the structure tensor; and the structure tensors are smoothed with two sizes of Gaussian kernels: top – $K_{10,2}$, bottom – $K_{20,4}$. The images use the same color space as described by Figure 6.2B. The histogram represents the distribution of fiber orientations in the ROI. The range of the distribution (x-axis) is between -90° and 90°, and the range of the appearance frequency is set the same for all the six histograms. (B) The standard deviations of fiber orientations within each ROI are plotted with two Gaussian kernels: $K_{10,2}$ and $K_{20,4}$. Blue: no filtering; green: with nonlinear anisotropic diffusion filter on the intensity image; red: with nonlinear anisotropic diffusion filter on the structure tensor.**

*Verification by optic axis orientation*

To verify the accuracy and the robustness of the structure tensor approach, we correlate the ST-orientation with the optical contrast of optic axis orientation. Figure 6.4 compares the orientation

maps in two sagittal sections. The computed (left column) and measured (middle column) orientations use the same color coding according to the color wheel at the bottom, and the brightness is uniquely controlled by the *en-face* retardance. The absolute difference of the two orientation maps (in degree) is shown on the right. The ST-orientation and optic axis orientation reach a remarkable agreement with less than 10° difference in well delineated fibers where higher brightness is usually seen, such as, the internal capsule (top), the stria medullaris thalamus (sm), the cingulum (bottom), and the fiber tracts in caudate putamen (top and bottom).More deviations are seen in the white matter regions where intensity becomes dimmer, such as the corpus callosum and the fimbria of the hippocampus (top and bottom). This observation may be attributed to two factors: 1) less effective features are seen on the *en-face* plane where the intensity is weaker, and 2) the geometry on the *en-face* plane may mislead the computation of fiber orientation which would be different in 3D space, such as a sheet-like structure running through the plane. Histogram of the pixel-wise orientation difference in the white matter (with a en-face retardance threshold > 25°) indicate that the computational approach and the optical measure have a difference (mean ± 0.5 x FWHM) of A and B, respectively, on the two sections.

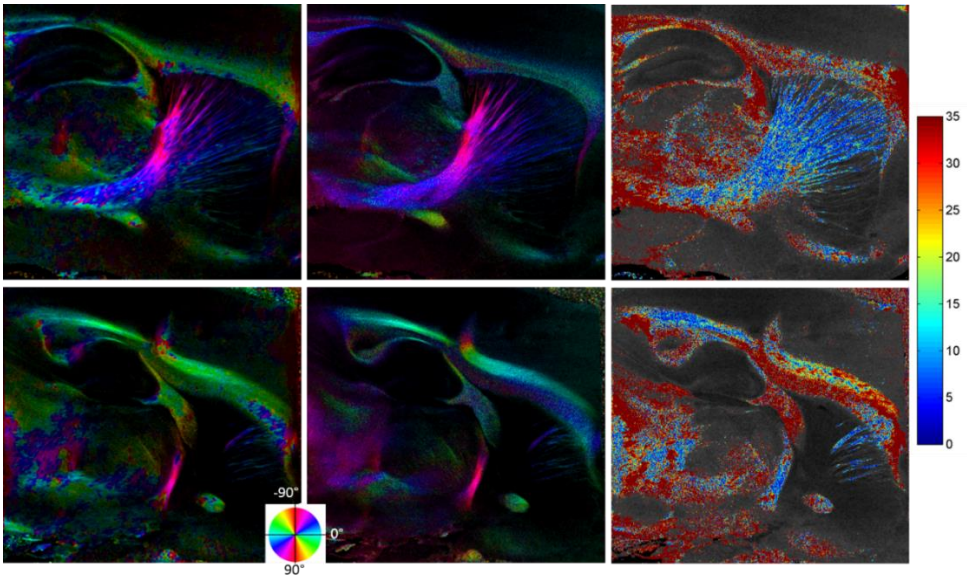


**Figure 6.4 Comparison of 2D ST-orientation and en-face optic axis orientation. The ST-orientation (left) and the optic axis orientation (middle) are shown in HSV color space, where the orientation is coded according to the**

**color wheel, and the brightness is controlled by the en-face retardance. The ST-orientation is constructed based on the retardance image. The absolute orientation difference in the white matter (with a retardance threshold of 25°) is shown on the right. The color-coded difference image is overlaid on the en-face retardance image for a better presentation of the anatomy. Scale of the colorbar: 0 – 35; unit: degree.**

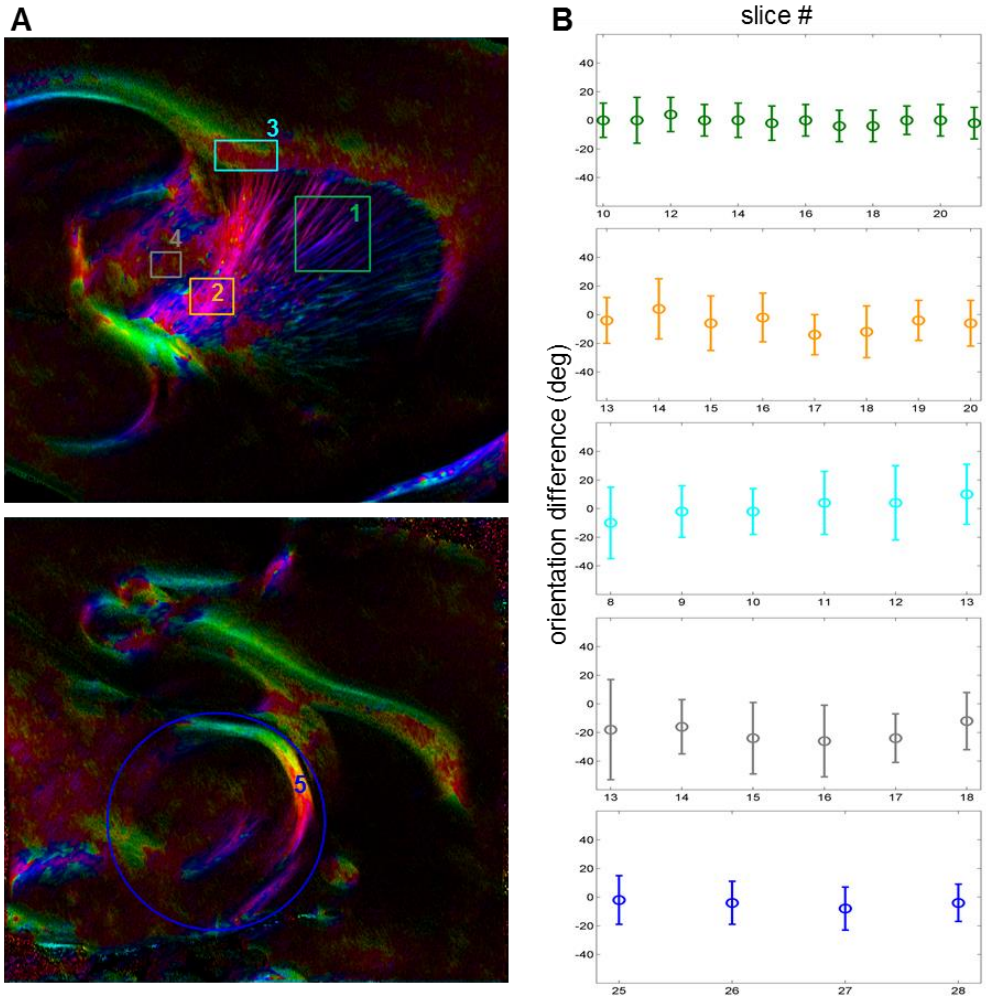


**Figure 6.5 Quantitative comparison between 2D ST-orientation and optic axis orientation in selected ROIs. (A) The ROIs are located on fibers or fiber groups with diversity of architectures, and across multiple slices (x-axis in B). (B) Fiber orientation difference (with the retardance threshold of 25°) between computation and measurement in each ROI is calculated, and the mean ±0.5 x FWHM of the histograms are plotted from top to bottom for ROI groups 1 – 5, respectively. The x-axis represents the index of the slice in SOCS, and the y-axis represents the orientation difference in degree.**

We then interrogate the robustness of the ST-orientation in specific architectures of the white matter. Five ROIs are selected to compare with the optical measurements. The four ROIs on Figure 6.5A (left) include small fiber tracts in the caudate putamen, dense fiber package in the

internal capsule, extension of fibers from dorsal putamen into corpus callosum, and local fiber tracts in the lateral thalamus. The fifth ROI (Figure 6.5A, right) contains multiple fiber bundles around the medialthalamic region, including the stria medullaris thalamus (sm), the fornix, the mammillothalamic tract (mt), and the fasciculus retroflexus (fr). The ROIs are across multiple slices where the selected architectures are clearly visible.

The difference between the computed and the measured fiber orientations are examined. Figure 6.5B shows the mean and the FWHM of the histogram of the difference in all the ROIs. The differences between computations and measurements are fairly small (<10°) across various fiber architectures and consistent among multiple slices in ROI 1-3 and 5. Consistent with Figure 6.4, the ST- and optic axis orientations have the best match in ROI 1 and 5, with smallest mean differences and narrowest FWHMs, where individual fiber tracts are clearly identified. In addition, the ST-orientation is viable in the dense white matter pack where small features inside can be captured (ROI 2 and 3). The orientations are less comparable with more variations observed in the lateral thalamus (ROI 4) where the intensity becomes significantly weaker.

### 6.3.2. 3D structure tensor on fiber maps

The ST analysis are further extended to compute the fiber orientations in 3D. The datasets of 3D fiber maps can be generated by stacking the *en-face* images or stitching the optical sections from sequential slices. Figure 6.6 demonstrates the 3D structure tensor based on the *en-face* retardance stack of the coronal sections. One advantage of using this mesoscopic resolution dataset is that it provides a global view of fiber organization with multi-angular information, as the retardance reliably identifies the white matter with less dependency on the fiber orientation comparing to other SOCS contrasts. Therefore, neural fibers running through the xy-plane with an inclination angle can be captured by the structure tensor. Figure 6.6A demonstrates the 3D orientation maps from the orthogonal views. The direction of fiber orientation are indicated by the color-coded

axes, and the brightness of the map is controlled by the retardance value. The orientations on the coronal section are clearly distinguished into three groups: the anterior commissure (ac) connecting the two hemispheres is going left-right, the fornix is aligned in superior-inferior direction, and the fibers in the putamen are running in rostral-caudal direction through the coronal section. Color transitions are seen in the fimbria of the hippocampus and the posterior branch of the ac which are tilted with respect to the xyz-axes. Fiber orientations consistent with the geometry and the anatomy are seen on the sagittal and horizontal sections as well. The orientation in the large white matter regions such as corpus callosum exhibits less coherence. Two reasons may explain this observation: first, the orientations of small fibers in the dense white matter package are not uniform from microscopic view; second, the noise may contaminate the consistency on the intensity images. The anatomical maps of the retardance and the eigenvalues of ST are shown on the coronal section in Figure 6.6B. The greatest eigenvalue catches the most appealing features including the edges of large bundles, the small tracts in the putamen, and the trends of fibers in the fimbria. The second eigenvalue provides a similar identification of small fibers and edges with some indicative information inside the fiber, but suffers from greater noise. The smallest eigenvalue preserves the gross contrast of the white matter, but loses the detailed structures of fiber architecture.

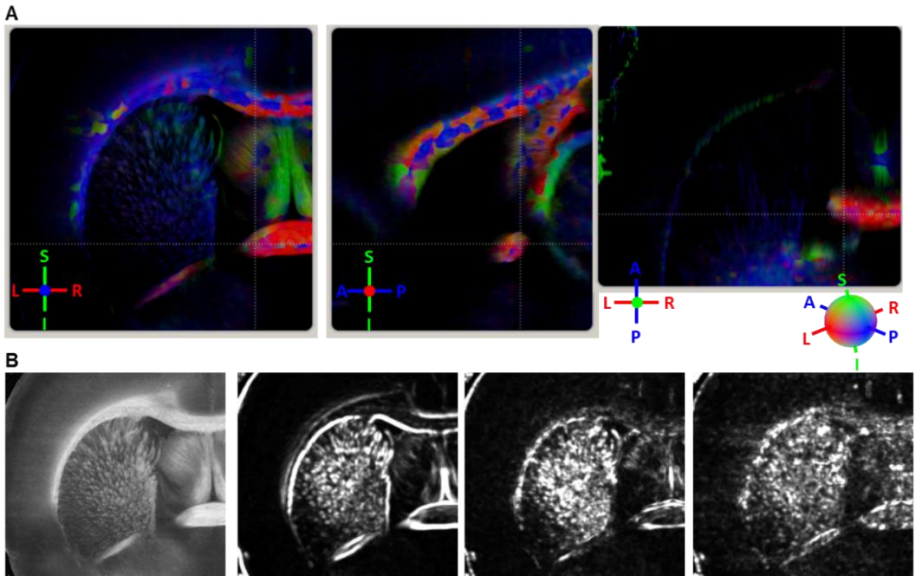

**Figure 6.6 3D ST computation at mesoscopic resolution provides a global quantification of neural fiber maps. The structure tensor is applied on the en-face stack of retardance, and eigen-decomposition is performed. (A) The orthogonal views of 3D ST-orientation map. The color represents fiber orientation indicated by the color sphere at the bottom (red: left-right, green: superior-inferior, blue: anterior-posterior), and the image intensity is masked by the retardance value which highlights the white matter. Directions are labeled on the orthogonal planes as well. (B) The original retardance image and the eigenvalue images (from largest to smallest) of the coronal section in A are shown respectively. The eigenvalue images are normalized separately to get an optimized visualization.**

Structure tensor applied on 3D optical sections of SOCS provides a favorable solution for large-scale orientation quantification and comprehensive connectivity investigations. Figure 6.7 shows a 3D ST-orientation map of the right hemisphere of a rat brain. The structure tensor is computed on the optical sections of cross-polarization contrast in SOCS, which are fused from the serial scans of saggital sections. The colors represent the orientation in 3D (red: rostral-caudal, green: left-right, blue: superior-inferior), and the brightness represents the cross-polarization contrast of SOCS. Orthogonal views of the 3D maps demonstrate fiber tracts with varieties of preferable directions (Figure 6.7A). Fiber orientation in left-right direction is less visible, because the SOCS signal barely picks up the fibers parallel to the illumination beam. Therefore, the intensity masks suppressed the expression of those fibers. However, directional changes of small fiber tracts can still be sensitively apprehended. On the coronal plane, the neural tracts through the putamen are tilted more horizontally in the lateral region (ROI 1) and vertically in the upper region (ROI 2). Similar color transitions are also shown on the horizontal and sagittal planes. 3D ST-orientation clarifies the ambiguity of fiber alignments on 2D images. For example, the orientation map on the horizontal plane elucidates that the fiber bundles in the internal capsule are along the superior-inferior direction rather than the left-right which would be the apparent intuition on the 2D plane. Volume rendering of the 3D orientation map is implemented in V33D [153] and shown in Figure 6.7B.

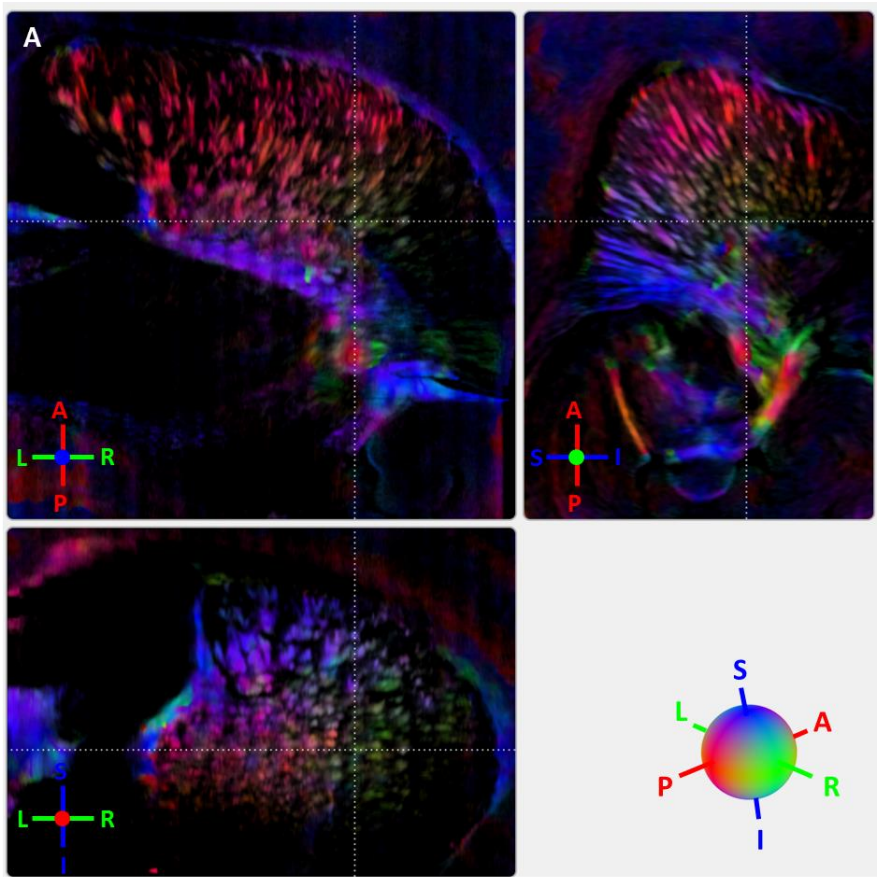
A
A
L
R
P
A
S
I
P
S
L
R
S
L
A
P
R
I

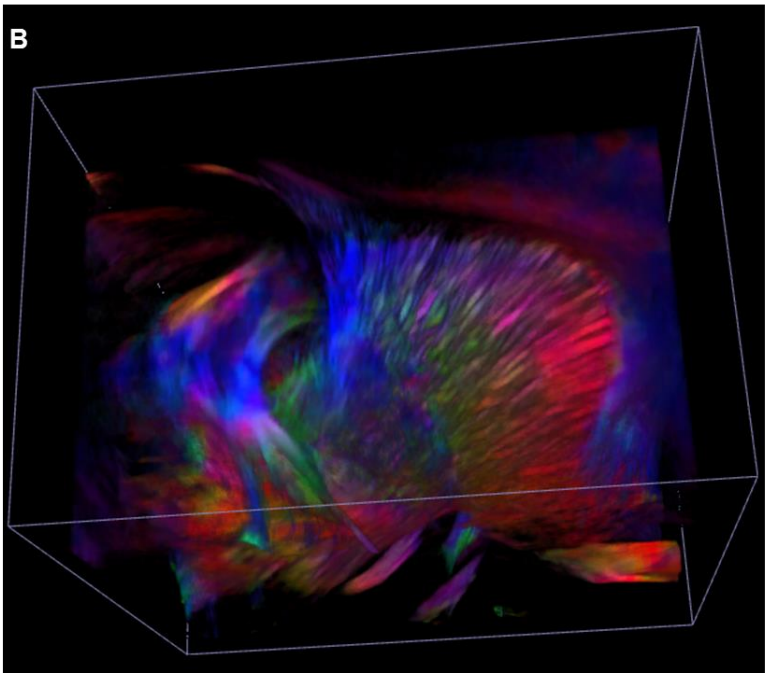
B

**Figure 6.7 3D ST-orientation constructed from comprehensive optical sections of SOCS. (A) Orthogonal views of the fiber orientation map. The orientation is color-coded as indicated by the color sphere at the bottom (red: anterior-posterior, green: left-right, blue: superior-inferior), and the brightness is manipulated by the cross-polarization contrast of the SOCS data. Directions are labeled on the orthogonal planes as well. Some of the fiber bundles going in left-right direction (parallel to the illumination beam of SOCS) are masked out on the images, because of the lower signal intensity compared to the surrounding gray matter. The fibers in the putamen on the coronal section are separated into three groups with different preferable directions. (B) Volume rending of the 3D orientation map provides a perspective view.**

The 3D ST-orientation is difficult to validate in current SOCS setup, as the optical measure of fiber orientation is restricted to 2D. Instead we project the 3D ST-orientation vectors onto the xy-plane, obtain an *en-face* ST-orientation image and compare with the *en-face* optic axis orientation. The sagittal sections of *en-face* ST- and optic axis orientation maps are shown in Figure 6.8 (left and middle panels, respectively).The computation and the measurement are well correlated in most of the white matter. The absolute difference between the two images is shown on the right. Fiber orientations obtained by the two approaches closely match with the differences less than 10° in most regions where the image intensity is high and neural fibers are clearly traceable, such as the internal capsule, the tracts in the putamen, the optic tract, the superior thalamic radiation, and the local fibers within thamalus. More deviations are seen in the fiber bundles going through the plane, including the corpus callosum and the fimbria, and the stria terminalis, where the intensity on the image becomes weaker. The histogram of the pixelwise difference in the white matter peaks around 0° with 0.5 x FWHM of 15°.

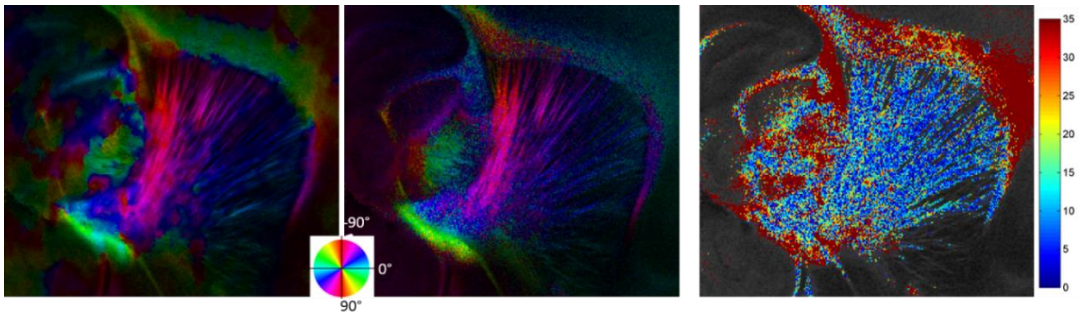


**Figure 6.8 Verification of 3D ST-orientation on the en-face plane. The 3D ST-orientation is projected onto the xy-plane, transformed into an en-face ST-orientation by using a histogram approach within one optical scan**

**(left), and correlated with the en-face optic axis orientation (middle). The color represents fiber orientation as indicated by the color wheel, and the brightness is manipulated by the en-face retardance. The absolute orientation difference of computation and measurement in the white matter (with a retardance threshold of 25°) is shown on the right. The en-face retardance image is overlaid for a better understanding of the anatomy. Scale of the colorbar: 0 – 35; unit: degree.**

## 6.4 TRACTOGRAPHY

As the structure tensor metric holds the same pattern as the tensor data in diffusion tensor imaging (DTI), tractography that has been developed for the diffusion MRI technique can be easily applied. The ST and SOCS metrics are transformed into NIFTI format using an open source tool of FreeSurfer [221]. Tractography is performed on 3D structure tensor using a deterministic tracking algorithm in Diffusion Toolkit [222], with normalized SOCS data as the intensity mask. The tracks are visualized in TrackVis [222]. For detailed exploration, ROIs are selected and fibers passing through the nodes are examined.

Tractography with high resolution is desired for connectivity studies. The ST applied on stitched optical sections preserves the natural resolution of SOCS thus bearing the most enriched information of fiber traces. Figure 6.9 shows the tractography of rat brain on 3D ST described in Figure 6.7. The tracks are color-coded by their orientations in each segment, with the direction indicated by the tube on the bottom-right corner. Primarily the sagittal view shows the dense fiber bundles extending from the cerebral peduncle to the frontal cortex. Other fiber tracts around the thalamus and in the midbrain region are visualized as well. The Fiber Assignment by Continuous Tracking (FACT) algorithm [223] was used to conduct tracking shown in Figure 6.9. However, we don’t find substantial differences using variety of other tracking algorithms including streamline, Runge-Kutta second order [224] and tensor deflection method [225] with the ST matrices.

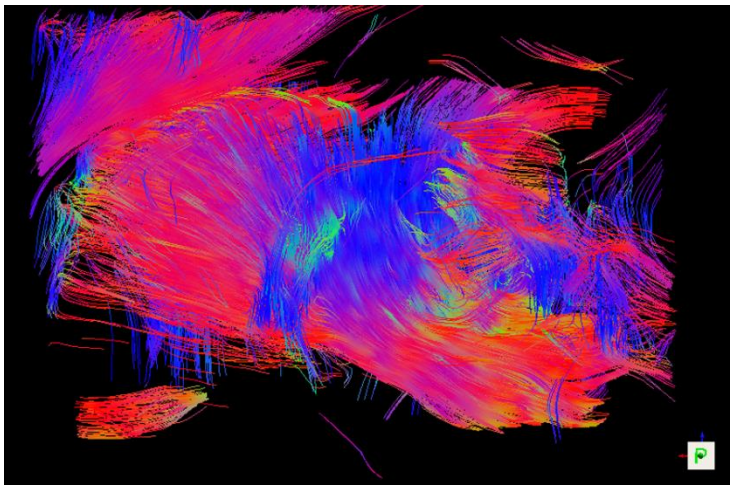

**Figure 6.9 Tractography of 3D SOCS images. The tracks are computed from the structure tensor applied on the stitched optical sections of the whole sample. The directional information of the tracks is color-coded in every segment according to the cube at the right-bottom corner. For a better visualization purpose, only 2% of the tracks are presented.**

Figure 6.10 shows a representative tractography of the *en-face* stack of retardance. The tracks are color-coded by their orientations in each segment, with the direction indicated by the tube on the bottom-right corner. The intensity images are overlaid for a better interpretation of the anatomy. Figure 6.10A illustrates the tracks beneath the corpus callosum (14%). Major directions of the tracks are consistent with the prior knowledge of brain anatomy and complies with DTI results.Tracks of corpus callosum are excluded here for two reasons: 1) the cc forms like a shell on the image which blocks the visualization of most structures inside, and 2) features of individual fiber tracts may not be captured because of the high density in the fiber packs, therefore, the tractography may not reveal the true alignment of the fiber components. To explore the fibers passing through a specific region, a sphere ROI (indicated by the black arrow on Figure 6.10B) is placed at the conjunction of fornix and anterior commissure. The tracks on Figure 6.10B indicate that the fibers passing through this region primarily include fornix, fimbria of the hippocampus (fi), and ac. The ac is further branched in anterior and posterior directions (aca and acp).Tracking of the ac is better visualized when the ROI is moved more laterally (Figure 6.10C).

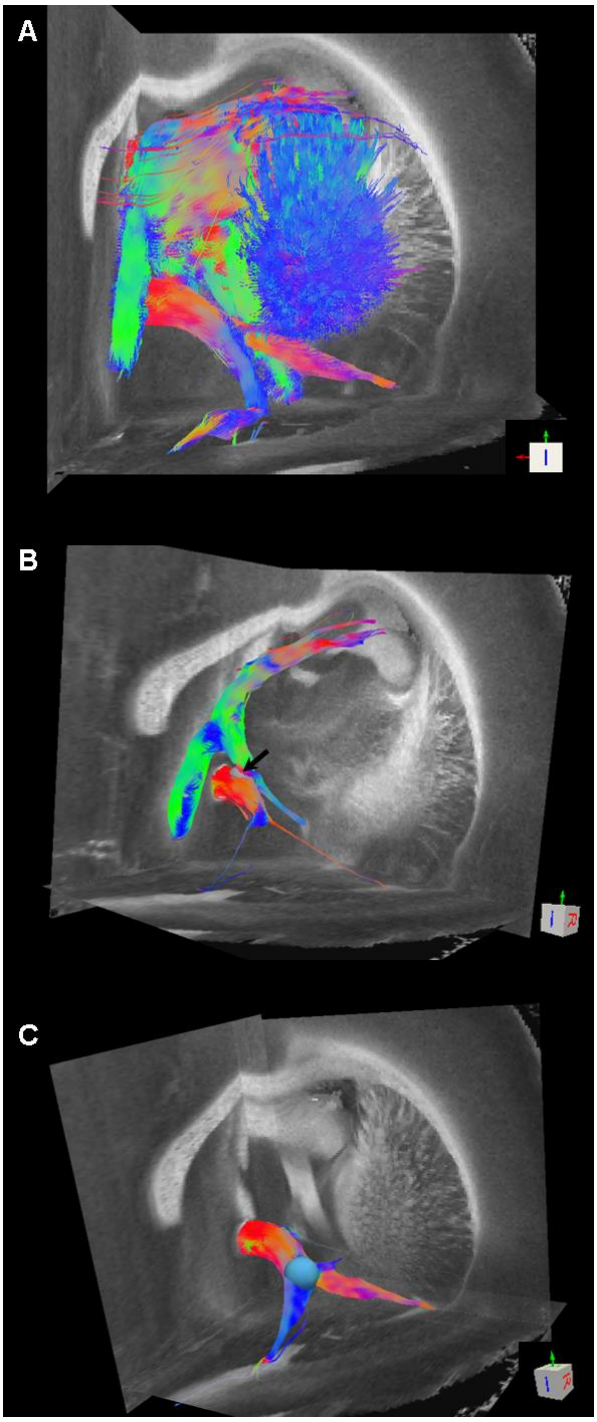


**Figure 6.10 Tractography of SOCS en-face stack of retardance. The directional information of the tracks is color-coded in every segment according to the cube at the right-bottom corner. The intensity images (en-face stack of retardance) are overlaid on the tracks. The tracks of the entire sample excluding the corpus callosum are shown in A. For a better visualization purpose, only 14% of the tracks are presented. Fibers passing through specific ROIs are shown in B and C. (B)The ROI is placed at the junction between the ac and the fornix (gray sphere, indicated by the black arrow). (C) The ROI is placed on the ac (blue sphere).**

## 6.5 DISCUSSION

Abnormalities of structure, orientation and connectivity in the white matter have been linked to many brain diseases; however the capability of current techniques to explore those factors is either limited by the spatial resolution, or prohibited by 2D information with a restricted spatial coverage. In this paper, we proposed a structure tensor approach to establish comprehensive fiber orientation maps and the structural connectivity in rat brain based on 3D SOCS imaging. This data-driven model offers a viable solution for 3D quantification of fiber orientation at high resolution in complex brain which can be linked to the diffusion MRI, and can also serve as a complement to the microscopy imaging where quantitative orientation measurement is not available. Especially, the SOCS based ST analysis builds up the dimensions of the imaging capability, leading to a cross-scale investigation on brain structure and its connections to functionality.

The eigenvectors of the structure tensor sensitively catches the directionality of image features. Structure tensor can be applied to multiple contrasts of the *en-face* images in SOCS and generate similar results in the orientation assessment. In this study, we use the retardance image for 2D ST computation because the contrast provides a robust identification in the white matter [185, 226]. However, the approach is easily extended to other modalities such as conventional OCT to facilitate quantitative evaluation where direct access is not supported. Moreover, it is worthwhile exploring the quantities on various contrasts where image characteristics may reveal certain perspectives of the microstructures. The structure tensor has been applied on histological sections of rat brains to reveal 2D fiber orientation, and fiber identity has been correlated with DTI images [187].

In our work, we directly validate the computation approach by SOCS measurement of the fiber orientation. The ST-orientation maps have decent concordance with the optic axis orientation on the *en-face* plane of SOCS. Quantitative comparisons between computation and measurement

discloses that precise agreements (with angular difference between 0° and 10°) arise in the well delineated fiber tracts regardless of the size and the surrounding medium, including the internal capsule, the striamedullaris thalamus (sm), the fornix, the mammillothalamic tract (mt), and the fasciculus retroflexus (fr) on the sagittal plane. Verification of 3D ST-orientation on the *en-face* plane declares similar observation as well. With the evidences shown in accuracy and consistency, the ST method is capable of offering an objective assessment in disease models where microstructure changes on the image may occur [202].

The binding of 3D ST-orientation on SOCS imaging distinctly strengthens the capability of optical neuroimaging. Quantification of fiber orientation in complex brain has imposed tremendous challenges in light microscopy. The polarized light imaging (PLI) technique has been developed for 3D characterization of fiber orientations in histological slices [145]; however, registration of histological sections in 3D proves to be extremely difficult, and thereby fiber tracking in comprehensive brain space is prohibited. Recently, the PS-OCT technique has been advanced to support 3D orientation estimation [197] which has potential to achieve the whole brain mapping; however, the intricate crossing fibers at microscopic scale induces great complications and the differentiability of depth-resolved orientation measures in the complex wiring system needs to be evaluated. SOCS makes use of the multi-contrast OCT techniques to unveil 3D microstructures especially fiber architectures in the brain. By integrating a serial-scan scheme, SOCS establishes a descriptive neural roadmap of the entire brain sample with high resolution. This comprehensive dataset sets the basis for the quantitative formation of the 3D orientation map. The 3D ST-orientation based on comprehensive optical sections of cross-polarization contrast provides unprecedented details on the directions of fiber alignments, especially benefitting the orientation quantification in small fibers with a resolution that conventional diffusion MRI technique cannot achieve. The computation analysis also provides a viable tool for validating the micro-MRI technique, in which improved spatial resolution has been achieved by using large 3D arrays with high magnetic field [227].

The formation of the structure tensor establishes a seamless connection to the tractography tools developed in diffusion MRI to investigate fiber tracking and structural connectivity. For proof of principle purpose, we construct a tractography based on the *en-face* stack of retardance images. The data albeit bearing a compromised resolution on z-axis, presents a robust detection of the fiber tracts with diversity of alignments in brain coordinates, and hence supports a full-angle perspective of the fiber maps. The tracks comply with the prior knowledge of anatomy and demonstrate a high resemblance with the results from DTI technique. Although a simple deterministic approach was used here for the tractography construction, the ST formation can be easily extended by a probabilistic model like fiber orientation distribution analysis to examine multi-fiber crossing within a local neighborhood, provided that the features support the distinction. In such case, the structure tensor can be recruited to validate more sophisticated diffusion MRI techniques such as high angular resolution diffusion imaging (HARDI) [141] or diffusion spectrum imaging (DSI) [207]. It is also noticed that we could use the data of comprehensive optical sections with higher isotropic resolution to create the tractography as well, but considering the weaker identification of fibers along z-axis, the track map could miss certain directionality and induce a biased connectivity analysis. The full-angle feature expression needs to be investigated in the imaging system for a more comprehensive texture analysis.

There are several limitations in the current structure tensor analysis. First of all, the eigenvalues of the structure tensor, which are expected to represent image features, have overall inferior capabilities in fiber architecture description, comparing to the optical contrasts of SOCS. The greatest eigenvalue is mostly immune from the noise influence and decently preserves the identity of small tracts and the edges of big bundles, but the subtle features with dimmer intensity inside the white matter regions were not captured; on the other hand, smaller eigenvalues keeps the gross identification, whereas bears more severe background noise contamination. Because of the characterisitcs of SOCS imaging, the noise inevitably coming from every undesired intensity mismatch in local neighborhood – uneliminated speckles, small creatures or contaminators on

tissue surface and the vessels passing through brain sections – may also present considerable contrast. The nonlinear anisotropic diffusion filter, which improves the directional representation of orientation, does not appreciably benefit the effective feature identification by the eigenvalues. The edge-preservation characteristic of the filter rather underlines the unwanted patterns in the background which influences overall image quality. As a result, we did not use filtering for the eigenvalue representation. The concept of fractional anisotropy in DTI [206] and coherence index in ST [215] could be introduced for anisotropic characterization; however, regularization has to be taken care of to eliminate the noise in the background.

We also found greater discrepancies of orientation between computation and measurements in the white matter where the retardance signal on SOCS image becomes weaker and the architectures are less visible. The low retardance typically implies the presence of fibers with low birefriengence, running through the plane or crossing with each other. In either scenario, the optic axis orientation bears more noise, and the computation is prone to error due to lack of effective features. Strategies to enhance feature visibility are the key but also have substantial complications. Improving spatial resolution increases feature discrimination [228], but sufficient photon collection has to be guaranteed which imposes another challenge in anisotropic microstructure imaging by using intrinsic optical properties [185]. As a result, angle-resolved imaging technique needs to be developed for a realization of full-angle description of fiber maps in the complex brain [229, 230].

In summary, the incorporation of the structure tensor analysis and the SOCS imaging provides an insight of brain-wide orientation mapping and connectome exploration. In future work, continuous advances of SOCS technique will be parallel to the evolvement of computational models for a better understanding of the wiring system and an objective assessment in pathological conditions. We anticipate that the convergence of computational analysis on SOCS and other modalities, including histology and MRI will lead to multi-scale investigations in comprehensive brain mapping.

# CHAPTER 7 CROSS-VALIDATION OF SERIAL OPTICAL COHERENCE SCANNING AND DIFFUSION MRI

## 7.1 INTRODUCTION

Diffusion magnetic resonance imaging (dMRI) has revolutionized our understanding of structural connections in humans. The technique provides a unique solution to noninvasively visualize white matter fiber bundles over macroscopic distances in the living brain. dMRI captures the anisotropic diffusion of water molecules in the brain which run preferentially along the direction parallel to the axonal axes, and can be used to infer fiber organization and orientation. Recent technical developments have improved the spatial resolution to sub-millimeter scale and enabled high angular resolution imaging which describes the human brain with unprecedented details. dMRI has been proven to be valuable in clinical neuroscience [202, 203], with studies showing that an array of disorders may have corresponding connectional components, including Alzheimer's disease [231, 232], schizophrenia [233-236], autism spectrum disorders [237, 238], major depression [239], and dyslexia [240-242].

While there have been a number of neuroscientific and clinical applications of dMRI, the systematic validation of the dMRI technique for evaluating microstructural properties and connectivity in the human brain remains incomplete. Although light microscopy is able to visualize single axons, axonal tracking is extremely labor intensive, and cannot realistically be carried out for multiple fascicles traversing many centimeters of brain tissue through the white matter. Traditional validations by histology are divided into two realms: 1) neural tract tracers have been injected into local regions, and compared with selected tracks by dMRI tractography

[243-245]; and 2) quantitative information have been derived by digital signal processing of myelin stained images and compared with dMRI orientation [210, 211, 246, 247]. Those studies are predominantly performed on 2D slices. Early three-dimensional (3D) histological validation has proven to be difficult and has resulted in a relatively low correlation with dMRI tracks [248]. Using multi-step registrations, Jbabdi et al. [249] reported both agreements and dissociations between neural tracing trajectories and dMRI tractography on the organizations of ventral prefrontal fibers in macaque monkey. Polarized light imaging [145] has recently been proposed as an alternative technique for imaging fiber orientation, as it provides 3D orientation information with a voxel size of approximately 100 μm isotropic. However, the technique requires tissue slicing before the imaging, which makes inter-slice tracking of fiber bundles difficult and is prone to registration errors due to distortions intrinsic to cutting and mounting of large tissue sections.

The development of optical coherence tomography (OCT) has shown promises to depict the fiber tracts in central and peripheral nervous system [181, 185]. OCT is a depth-resolved imaging technique that generates cross-sectional images of tissue microstructures with micrometer-scale resolution [25]. By integrating a tissue slicer with a multi-contrast OCT, serial optical coherence scanner (SOCS) provides an insight into large-scale brain imaging with microscopic resolution [226]. SOCS enables a comprehensive 3D reconstruction of the brain and supports quantitative assessments of fiber architecture and orientation with optical contrasts. The fast acquisition speed becomes an appeal factor for macroscopic tissue imaging such as primate and human brains. With 3D visualization of fiber connection and orientation available, optical tractography has the potential to provide the assessment of diffusion MR images.

In this chapter, we present cross-validation of SOCS and diffusion tensor imaging (DTI), which is a dMRI technique, on a postmortem human medulla sample. This validation process includes data acquisition and image reconstruction by individual imaging modalities, two-step co-registrations and comparison between DTI and SOCS (see Figure 7.1 for a flow chart), and discussed step-by-

step in the following sections. To the end, we establish a strategy that allows registration between 3D datasets of DTI and SOCS at high resolution. The white matter structures in the medulla are correlated on co-registered images. The fiber orientation maps produced by these modalities are compared. The results indicate a successful cross-validation. This co-validation process paves a path for a cross-modality investigation on structure connectivity and brain mapping in normal and pathological conditions.

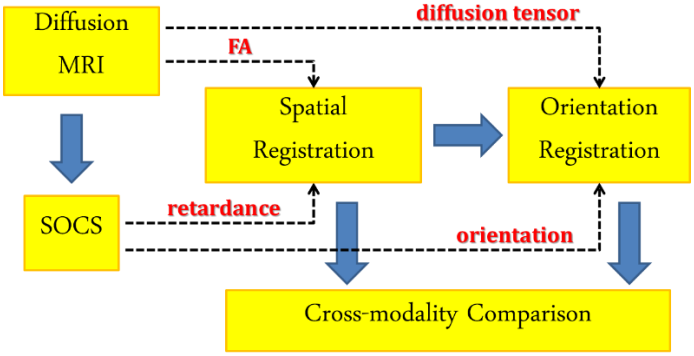


**Figure 7.1 Flow chart of cross-validation between dMRI and SOCS. A brain sample is scanned by dMRI and then by SOCS. Spatial co-registration between the two modalities are completed first, and then the orientation vectors are re-oriented accordingly. With the success of 3D co-registration, the fiber architectures and orientations are compared between dMRI and SOCS.**

## 7.2 DATA ACQUISITION AND POST-PROCESSING

### 7.2.1. Tissue

Tissue sample was taken from the right hemisphere of a 60 year old male initially fixed in 10 % buffered formalin beginning 14 hours postmortem for 2 months, and then subsequently stored in 4% periodate-lysine-paraformaldehyde (PLP) prior to and during data collection. Brain tissue was obtained from the Neuropathology Department at the Massachusetts General Hospital and is considered to be cognitively normal. A block of tissue, with an approximate size of

11x15x30mm, containing the medula oblongata was removed from the right brainstem which fit within a 28mm inner diameter (ID) plastic cylinder. MRI human brain tissue experiments were approved by an Institutional Review Board at Massachusetts General Hospital. After scanned by diffusion MRI, the sample is transferred to University of Minnesota for optical imaging.

### 7.2.2. DTI data acquisition and post-processing

Diffusion Tensor imaging (DTI) data was acquired using a Bruker Biospec Avance system (4.7T/40 magnet, 12cm bore, 40 G/cm gradients) at a 300 μm isotropic spatial resolution. The acquisition employed a 3D spin-echo sequence (TR/TE = 320/28, $\delta$ = 7 ms, $\Delta$ = 10.4 ms, matrix size = 256x96x96) with a maximum b-value of 4032 s/mm^2 for 20 non-collinear directions plus two additional scans with a b-value of 0. Total scan time was 18 hours.

*Radio Frequency coil*

A custom-built transmit/receive solenoid coil was designed to minimize the distance between the blocked sample in the plastic cylinder container and the surrounding coil, with an inner diameter of 30 mm and active length of 70 mm resulting in 5 turns of the copper coil element.

*Diffusion MRI post-processing*

Diffusion tensor estimation and data reconstruction was performed using Diffusion Toolkit (Ruopeng Wang, Van J. Wedeen, TrackVis.org, Martinos Center for Biomedical Imaging, Massachusetts General Hospital) using the Fiber Assignment by Continuous Tracking (FACT) algorithm [223] and an angle threshold of 35 degrees. The tensor maps were used to estimate the apparent diffusion coefficient, fractional anisotropy (FA), and fiber orientations.

### 7.2.3. SOCS data acquisition and post-processing

SOCS integrates a multi-contrast (MC) OCT and a Vibratome tissue slicer [226]. The MC-OCT is a spectral-domain polarization-maintaining-fiber (PMF) based technique [184] that is capable of making intensity, phase and polarization sensitive measurements. In addition to the conventional reflectivity contrast, polarization-sensitive OCT imaging [74] has been shown to be useful for characterizing anisotropic/birefringent tissues. The applications in brain include differentiation of white matter and gray matter, and delineation of myelinated axons [185].

The light source was a super-luminescence diode (central wavelength: 840 nm; bandwidth: 50 nm) yielding an axial (z-axis) resolution of 5.5 μm in tissue. A scan lens (focal length: ~36 mm) providing an estimated lateral (x/y- axis) resolution of ~15 μm was employed in the sample arm for consistent imaging quality over a large area. The acquisition speed for a depth profile (A-line) was 25 kHz. This is determined by a line scan camera recording interference related spectral oscillations on the orthogonal PMF channels. Inverse Fourier transform of the spectra in k (wave number) space yields the complex depth profiles, where the subscripts represent the polarization channels. The reflectivity, phase retardance and relative axis orientation along depth *z* are extracted from the magnitudes and phases of the complex depth profiles (Eq. 3.17 – 3.19). Constructional and operational details of the imaging system can be found in Chapter 3 and 5.

The medulla sample was cropped into a 2 x 1 x 0.7 $cm^3$ block (in *xyz*) and mounted on a vibratome slicer (Leica Microsystems, Bannockburn, IL) positioned under the scanner. One volumetric scan (optical section) contained 300 cross-sectional frames with 1000 A-lines in each frame. Each scan covered a 3D volume of 7 x 7 x 1.78 $mm^3$ and produced images with a voxel size of 7 x 23 x 3.47 $\mu m^3$. Eight scans were performed to cover the entire sample surface. The scan head was repositioned between the adjacent sections, which had a 15% overlap to aid post-processing. One of these scans was also used for calibrating the axis orientation contrast, since a retarder with a known axis was placed next to and imaged together with the medulla sample (Figure 7.2A). After imaging the superficial region, a 150 μm thick tissue slice was removed

from the top surface, allowing for deeper regions to be exposed to light. The physical slice thickness was less than the useful imaging depth to ensure 3D reconstruction of the whole sample with satisfactory signal-to-noise ratio (SNR) at all depths. The sections of consecutive slices were imaged in reverse order to minimize the lateral repositioning of the scan head, which also facilitates successful stacking of the slices (Figure 7.2B). The imaging and then slicing procedure was repeated 45 times until the entire tissue block was scanned. Correspondingly, a total of 360 optical sections were recorded.

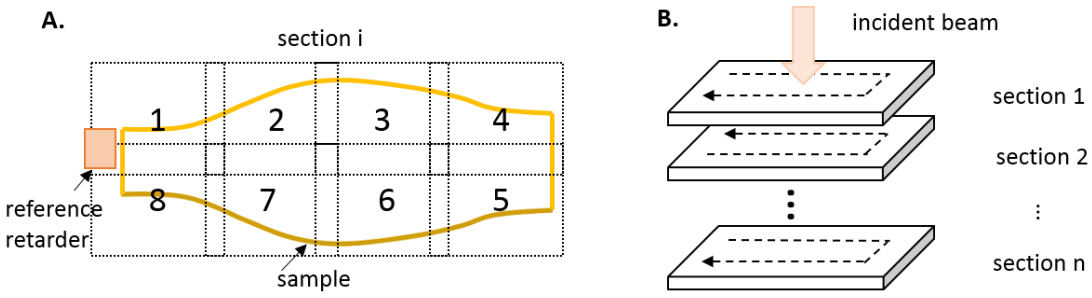


**Figure 7.2 SOCS scan schemes. A. Eight optical scans covering the whole surface were applied for each slices. A reference retarder was imaged with the tissue for scan 1 and 8. B. Serial slices were imaged in reversed order.**

*SOCS image reconstruction and post-processing*

*En-face* images are created by projecting the volumetric data onto the xy-plane. The pixel intensity in *en-face* reflectivity and retardance images was computed by taking the corresponding mean value along the depth direction. The pixel intensity in *en-face* orientation images was determined by the peak of a histogram formed by binning the orientation values along depth into 2° intervals.

*En-face* views of eight optical sections were stitched to construct a slice. The *en-face* retardance images were chosen as those display the most remarkable features in the medulla with high contrast. An algorithm based on Fourier shift theorem computed the translations between all image pairs, found the best overlaps and produced a globally optimized configuration for the

whole image [186]. The operation was performed by Fiji software (http://pacific.mpi-cbg.de/). The same registration was then applied to stitch the *en-face* reflectivity and axis orientation images.

The 3D reconstruction of the medulla sample was achieved by stacking the *en-face* images of the slices. The imaging procedure allows for precise alignment of the slices without further registration. However, lateral positions of the slices can be fine-tuned by referencing the sections that were imaged without the lateral repositioning of the scan head.

The optic axis orientation represents the axis of anisotropy in the plane perpendicular to the illuminative beam. This measure indicates the in-plane orientation of nerve fibers; however, it bears an offset that needs to be removed to achieve physical fiber orientation. The offset originates from an arbitrary delay between the optical paths of the two PMF channels, which varies with environmental factors such as movement of reference or sample arm fibers and temperature change. To obtain the absolute orientation of nerve fibers, a retarder film was placed next to the tissue, and a small portion of it was covered in one of the eight scans. The offset was derived by subtracting the measured and set orientations of the film axis, and removed from the measured axis orientation of the tissue in that section. Other sections of the slice were corrected serially by matching the fiber orientations within the overlap regions.

## 7.3 Co-registration between SOCS and DTI

### 7.3.1. Co-registration methods

As the coordinate space of SOCS imaging was determined independent of DTI coordinate system, coregistration between the two imaging modalities is crucial, especially for the accuracy of orientation comparison. We used two registration phases in the study: (1) spatial (scalar)

registration that ensures alignment of the anatomical images, and (2) orientation (vector) registration for direct comparison of fiber orientations.

The spatial registration was performed by using DTI FA and SOCS retardance images, as most features including the gray and white matter boundary and the architectures of the white matter fiber tracts are captured in the two contrasts. The DTI dataset was mapped into the SOCS space and interpolated to match the voxel size of SOCS. After an initial manual rotation and cropping on the 3D dataset of FA, first a rigid transformation (translation and rotation) followed by an affine alignment (translation, rotation, scaling and shearing) was estimated and applied to the FA block. The rigid registration allows rotation and translation and has 6 degrees of freedom (DOF). For a small rotation angle, the displacement $\vec{d}_6$ for a location $\vec{x}$ is expressed as

$$\vec{\boldsymbol{d}}_{\boldsymbol{6}} = \begin{pmatrix} \boldsymbol{p_1} \\ \boldsymbol{p_2} \\ \boldsymbol{p_3} \end{pmatrix} + \begin{pmatrix} \boldsymbol{p_4} \\ \boldsymbol{p_5} \\ \boldsymbol{p_6} \end{pmatrix} \times \vec{\boldsymbol{x}} \qquad \textbf{7.1}$$

The affine registration has 12 DOF, and the displacement $\vec{d}_{12}$ is a combination of a translation and a 3 x 3 matrix:

$$\vec{\boldsymbol{d}}_{\boldsymbol{12}} = \begin{pmatrix} \boldsymbol{p_1} \\ \boldsymbol{p_2} \\ \boldsymbol{p_3} \end{pmatrix} + \begin{pmatrix} \boldsymbol{p_4} & \boldsymbol{p_5} & \boldsymbol{p_6} \\ \boldsymbol{p_7} & \boldsymbol{p_8} & \boldsymbol{p_9} \\ \boldsymbol{p_{10}} & \boldsymbol{p_{11}} & \boldsymbol{p_{12}} \end{pmatrix} \vec{\boldsymbol{x}} \qquad \textbf{7.2}$$

The registration algorithm is based on a symmetric registration procedure described in Reuter et al. [249]. The symmetric registration constructs a robust simultaneous alignment of two set of images into an unbiased common space. Therefore, instead of understanding the registration as a local shift of intensity values at specific locations from the source to the target space, both sets of images are transformed: the source $I^S$ half way to the target $I^T$ and the target half way in the opposite direction to the source with symmetric transformations. The residual at each voxel is

$$r(\vec{p}) \coloneqq I^T\left(\vec{x} - \frac{1}{2}\vec{d}(\vec{p})\right) - I^S\left(\vec{x} + \frac{1}{2}\vec{d}(\vec{p})\right) \quad \textbf{7.3}$$

The objective is minimize the residual with normalized mutual information as the cost function. The registration process is implemented under the FreeSurfer [221] platform.

Vector registration is built upon the spatial registration. First, the same registration as done in FA was applied to the tensor images to achieve spatial alignment with SOCS orientation images. Second, tensor matrix was rotated accordingly by a rotation matrix extracted from the registration transform. The orientation vector was extracted from registered diffusion tensor and projected onto the en-face plane of SOCS. The unique advantage of this registration strategy is that it enables a voxelwise co-evaluation of the entire sample with high resolution.

### 7.3.2. Evaluation of co-registration results

DTI images

The diffusion tensor provides quantification of 3D fiber orientation with the strength of diffusion anisotropy. As water molecules diffuse along the axonal tracts, the anisotropy is high in the white matter, and the eigenvector corresponding to the greatest eigenvalue indicates the primary fiber orientation within that voxel. In contrast, the diffusion is more isotropic in the gray matter which leads to a weak FA signal. Figure 7.3 shows the DTI images of the human medulla with a photograph of the sample on the upper left corner. The colors represent the orientation vector in 3D (red: left-right, green: anterior-posterior, blue: superior-inferior) and the brightness is coded by the FA values. There are relatively uniform color patches in local regions, as well as complex color patterns both on the 3D view and the orthogonal planes, which indicate the presence of sophisticated fiber architectures in the human medulla. Due the resolution limit, the DTI is not able to catch the detailed features in the fiber bundles. Figure 7.3 also shows that the sample orientation in the scanner is arbitrary and not aligned with the RAS coordinates; therefore, spatial co-registration with SOCS needs more attention.

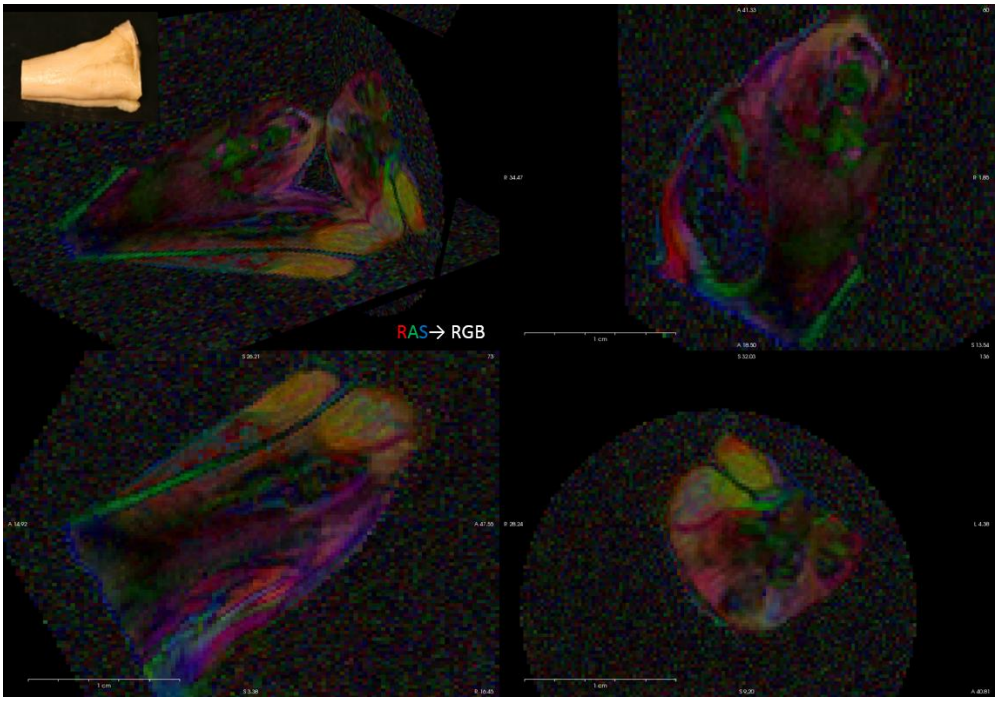


**Figure 7.3 DTI images of the human medulla sample showing fiber orientations in 3D. The colors represent the orientation vectors, and the brightness is controlled by the FA signal. A photograph of the sample is shown on the upper left corner of the first panel.**

*En-face SOCS images*

Figure 7.4 displays the *en-face* SOCS images of a medulla slice composed of eight (2x4) laterally scanned optical sections roughly parallel to the coronal plane. The *en-face* reflectivity image emphasizes the layer of inferior olivary nucleus with high scatters, which may contain high-density of cell bodies. The accessory olivary nuclei are also recognized. Those nuclei appear dark on the retardance images with no indicative birefringence. The intensity of the white matter varies on the reflectivity images, depending on the fiber orientation with respect to the direction of the illuminative beam. However, textures within gross white matter are distinguishable, which are highlighted in the magnified region on right. The *en-face* retardance image emphasizes the white matter fiber bundles with detectable birefringence. The brightest regions are seen where fiber tracts are densely packed in a uniform direction and aligned parallel to the *en-face* plane. Crossing fibers are identifiable with lower retardance values yet distinct features, such as the

reticularis alba and fiber clusters at the pyramid decussation. Fiber tracts running through the plane with an inclined angle also appear dim, but the orientation effect is less severe than that on the reflectivity image. Small fibers traversing the olivary nuclei (pointed by the arrows) are observed on the magnified region on right. The size of the individual tracts estimates about 20 – 30 μm. By using color-coded channels, reflectivity and retardance images are overlaid for a better visualization of the structure layout and spatial interactions. The stacking order is reversed in the zoomed-in region to unveil the pattern of fiber tracts crossing with each other and running through the nuclei region. The retardance images are selected for spatial registration with the DTI data, because of its advantageous capability of targeting the white matter tracts and revealing decent features in their architecture.

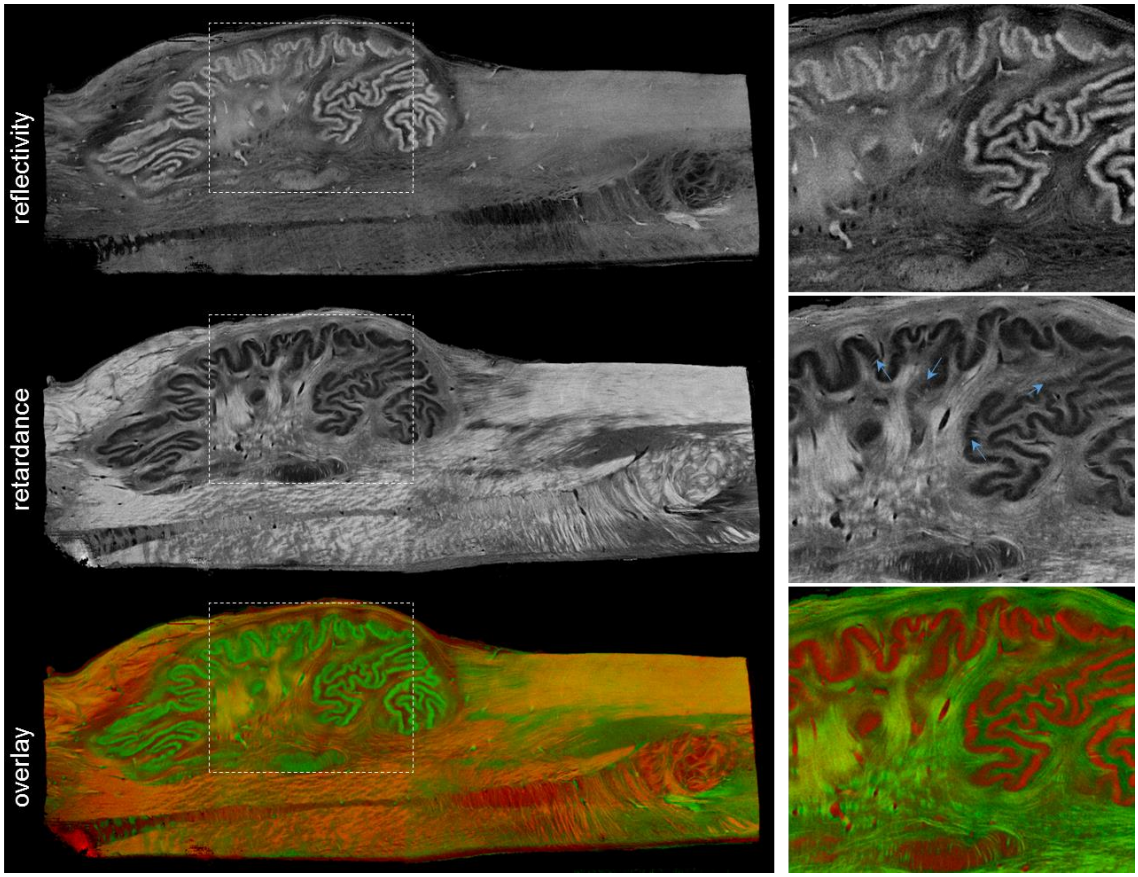


**Figure 7.4 En-face reflectivity and retardance images of the medulla oblongata. Left: A slice composed of eight (2x4) lateral scans. Reflectivity highlights the inferior olivary nucleus layer and the accessory olivary nuclei.**

**Retardance probes the white matter region. The overlay is merged by color channels (red: retardance; green: reflectivity). Right: Images elaborate the details in the dotted box. Arrows on the retardance image indicate small fiber tracts transverse the inferior olive nucleus. The colors of the overlay are switched to underscore the spatial interactions within fiber tracts and between the tracts and the nuclei.**

The *en-face* optic axis orientation maps in Figure 7.5 show fiber orientations on the coronal plane. The colors represent the fiber directions as shown on the color wheel. The brightness of colors is determined by the *en-face* retardance values. As expected from anatomy, the majority of white matter bundles in the maps are aligned along the superior-inferior direction. However, there are greater complications at the pyramid decussations and in the inferior olive. Small fiber groups with vast diversity of orientations are seen spatially interacting with each other (top row, Figure 7.5). The optic axis orientation accurately traces the directional trajectory of small tracts of tens of micrometers, and detects the individual directions of the intricate networks. The high-resolution quantitative assessment sets the basis for a direct correlation with the DTI contrasts.

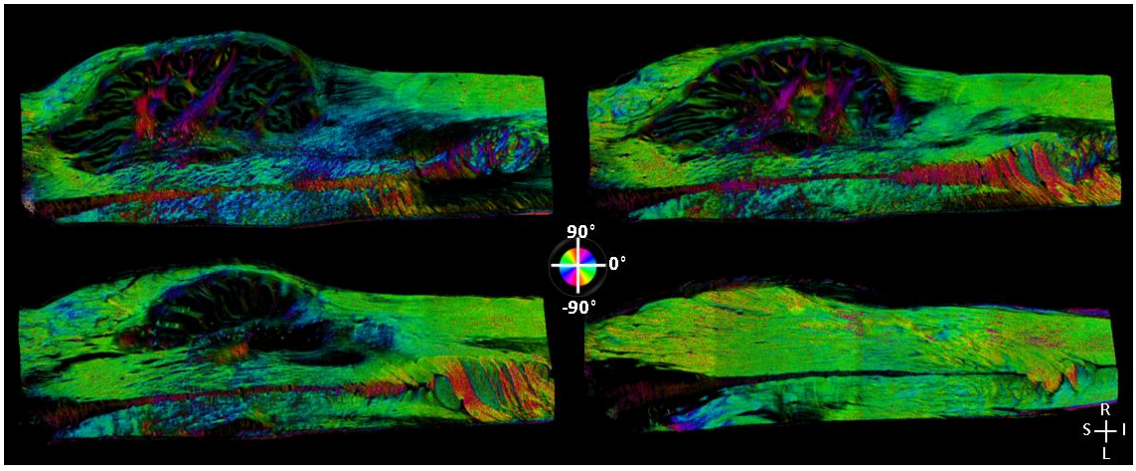


**Figure 7.5 En-face optic axis orientation maps produced by SOCS quantitatively depict in-plane fiber orientations in the medulla. Each map is composed of eight (2x4) serial scans. The color wheal shows the orientation values ranging between -90° and 90°. The brightness of colors in the images is determined by the en-face retardance values.**

*Co-registration of DTI and SOCS images*

Spatial alignment between the images of the two modalities was performed by transforming the DTI data into the SOCS coordinate space. The co-registered retardance and FA images of the medulla sample are shown in Supplemental Video 1 on the xy-plane. Figure 7.6 demonstrates a representative co-registration result on orthogonal views. Both FA and retardance images highlight the white matter with greater brightness. The registered images exhibit appreciated affinity on all the orthogonal planes. The fiber structures in the inferior olive are less distinctive on FA images (top) due to a limited spatial resolution of DTI. These fiber tracts, as estimated from the retardance images, are less than 500 μm in diameter, which is comparable to the DTI voxel size. Figure 7.6 also shows color-merged binary images that are obtained by applying thresholds on retardance (22.5°) and FA (0.15) images. Tissue boundaries on the blended images present a close match, attesting minimal distortion due to serial sectioning of SOCS. Small misalignments are seen on the inferior and superior edges, which might be attributed to an excessive shear transformation during registration. These images also indicate a general agreement between the white matter borders. Discrepancies exist in detailed structures (e.g. the inferior olive), which might originate from slicing artifacts, registration errors and a mismatch in the spatial resolutions.

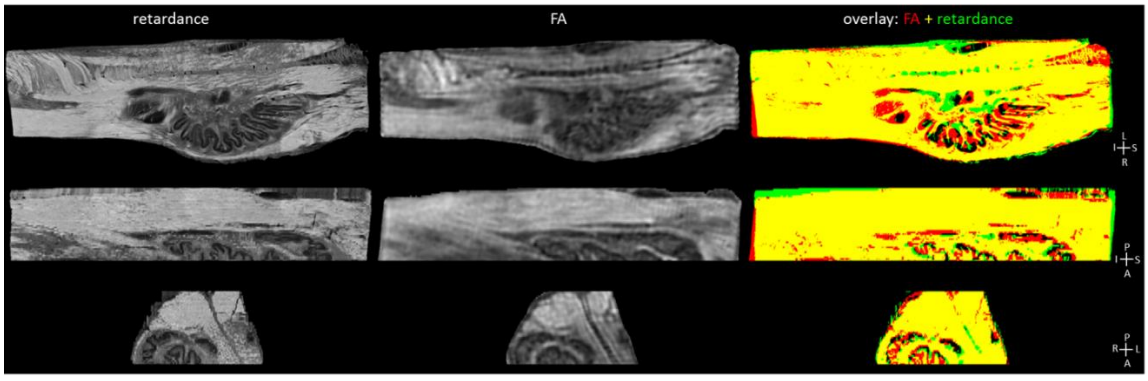


**Figure 7.6 Spatial co-registration of SOCS and DTI images. Retardance (left column) and FA (middle column) images are shown on axial (top row), sagittal (middle row) and coronal (bottom row) views. Color-coded binary images of the white matter regions indicate the quality of registration (green: retardance; red: FA; yellow: the overlap).**

To assess the quality of co-registration, we computed the correlations of the 3D datasets of FA and retardance using three measures: Pearson's correlation coefficient, Dice's coefficient of the tissue masks, and Dice's coefficient of the white matter masks. All three measures suggest successful co-registration of the images from the two modalities. The Dice's coefficient on tissue mask was 0.96, indicating a nearly perfect overlap of the co-registered datasets. Dice's coefficient of the white matter masks and Pearson's coefficient were both 0.90, signifying appreciable agreements in the co-registered white matter structures. Because the voxel size of SOCS *en-face* stack is anisotropic, we further examined whether this anisotropy along lateral and axial axes could unevenly affect the registration quality. We calculated the Pearson's correlation coefficients in every section on individual viewing planes across the whole sample. Figure 7.7 shows that the average correlation coefficients all range between 0.8 and 0.9 and are comparable on xy-, xz- and yz-planes despite the anisotropy in voxel size.

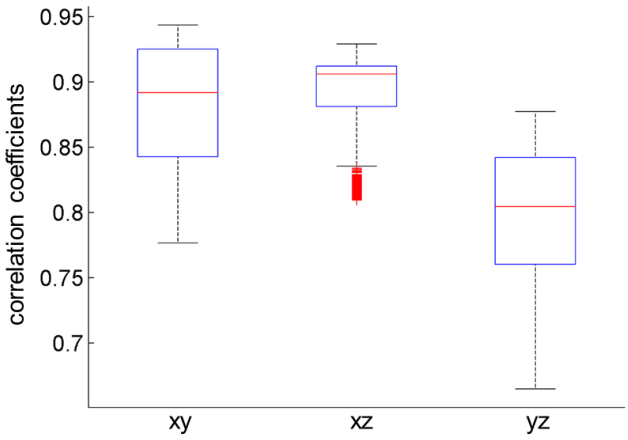


**Figure 7.7 Pearson's correlation coefficients between co-registered FA and retardance data on the orthogonal planes. The average values are 0.89 (n = 45), 0.91 (n = 1690), and 0.81 (n = 610) for xy, xz and yz planes, respectively.**

## 7.4 STRUCTURE CORRELATION BETWEEN SOCS AND DTI

Although both FA and retardance highlight the white matter, the underlying physics of the signals are different: FA represents the anisotropy of water diffusion in tissue, while retardance originates from the birefringence (anisotropy of refractive index). As the nerve fiber tracts influence both measures greatly, further comparison of the FA and retardance images is of interest. Figure 7.8A shows the co-registered retardance and FA images in four slices. We selected five regions of interest (ROIs) within the white matter regions, and compared the features across the two imaging contrasts. ROI-1 is located in dense fiber bundles of pyramid which owns high brightness albeit lack of detailed features. ROI-2 is placed in the reticularis alba with meshing patterns visible on the retardance. ROI-3 is on the fiber tracts beside the olive with less density. ROI-4 contains small fibers in the inferior olive with complicated interacting orientations. ROI-5 is located at the median fissures between the left and right medulla. The ROIs are included in multiple slices where individual structures are clearly visible.

The mean values of retardance and FA are plotted against each other for all selected ROIs in Figure 7.8B. The data follow a linear trend in general with a positive slope for ROIs 1-4. This indicates that greater anisotropy in DTI correlates with higher birefringence due to nerve fibers running parallel with each other. The lower anisotropy might be explained by less density, fiber crossing or intricately spatial interactions within fiber networks or with surrounding nuclei. The correspondence discloses a deviation in ROI5, where FA is significantly brighter than the retardance. Therefore, the anisotropy of water diffusion can be outstanding without the necessity of running along myelinated fiber bundles. It should also be mentioned that, the inclination angle of fibers with respect to xy-plane could reduce the apparent birefringence and measured retardance, which is not an issue for FA relying on multi-angular scans.

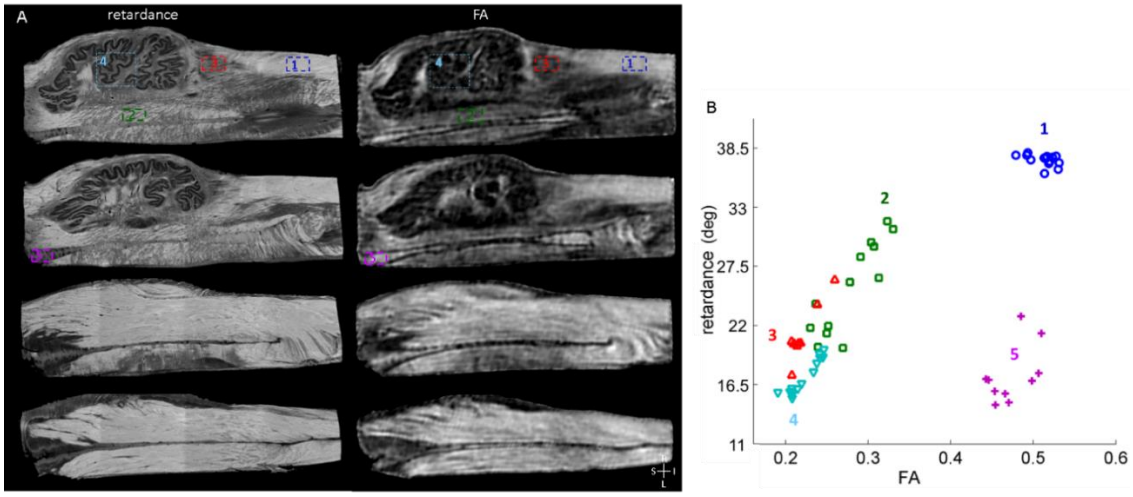


**Figure 7.8 Correlation between retardance and FA images. A. Representative retardance (left) and FA (right) images on the xy-plane are shown. Five ROIs are selected on varied structures. The ROIs are across multiple slices where specific structures are clearly visible. B. The scatter plot relates the mean values of retardance and FA in the ROIs. ROI 1 – 4 exhibit a similar linear relationship between the retardance and FA values. The correspondence in ROI 5 is deviated. The ROIs and the corresponding data points are color coded.**

## 7.5 Fiber orientation correlation between SOCS and DTI

### 7.5.1. Fiber orientations for cross-validation of DTI and SOCS

The quantitative assessment of fiber orientation in SOCS enables a direct comparison with DTI orientation. The DTI orientation vectors were interpolated, mapped onto SOCS coordinates, and projected onto the *en-face* plane. Figure 7.9 demonstrates the co-registered orientation maps for four representative medulla slices. The orientation maps share the same color coding given in the color wheel. The brightness of colors on SOCS and DTI images was controlled by the retardance and FA values, respectively. The color patterns hold substantial similarity between the co-registered images. This also suggests successful registration. Precise matches are seen in gross white matter regions bearing uniform directions, regularly grouped fiber bundles in the pyramid running at the decussation, and large fiber tracts located in the inferior olive. In contrast, discrepancy is observed where small fiber bundle regions introduce noisy patterns on DTI maps.

This is apparent in the olive region where the size of fiber bundles is comparable to the DTI resolution.

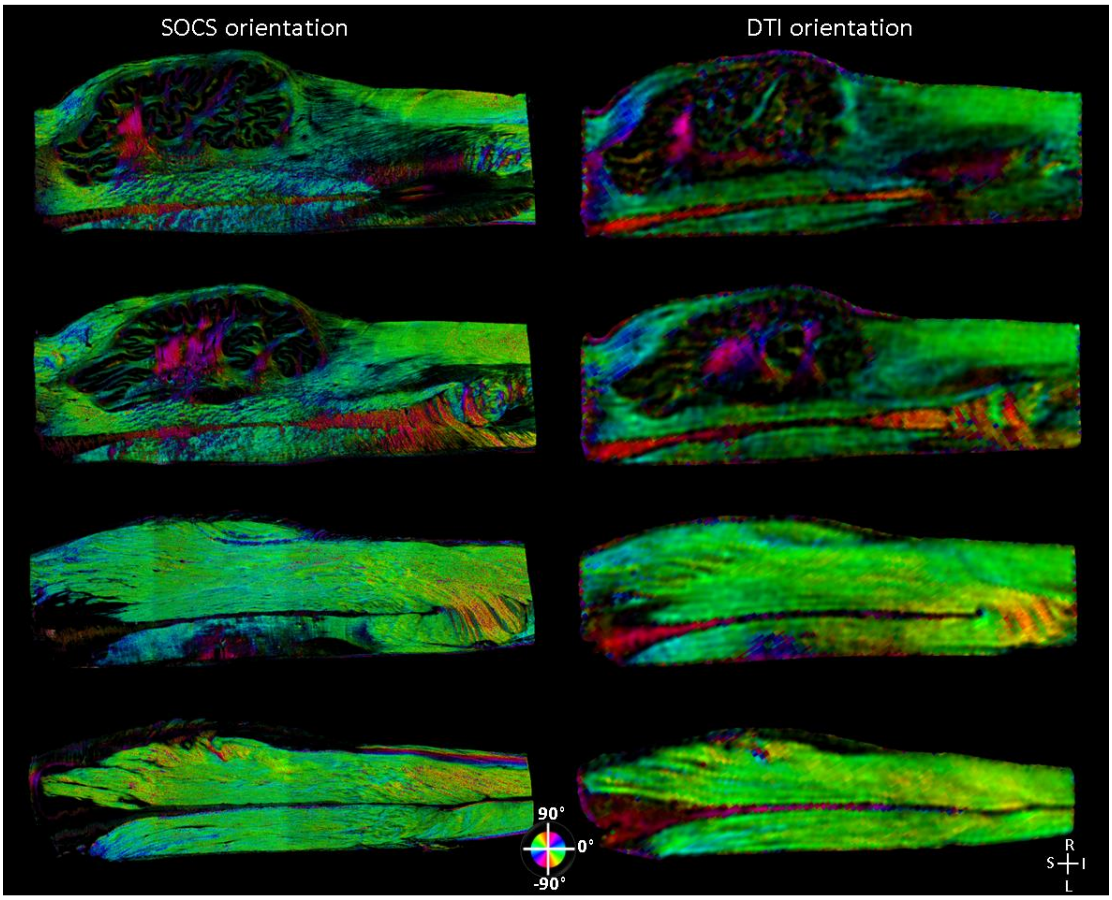


**Figure 7.9 Co-registered SOCS (left) and DTI (right) fiber orientation maps on the xy-plane. The color wheel indicates the orientations of fiber tracts. The brightness on SOCS and DTI maps is controlled by retardance and FA values, respectively.**

### 7.5.2. Fiber orientations comparison

Pixel-wise subtraction of the DTI and SOCS orientation maps yields the mismatch between the measurements of these imaging modalities. Three sets of FA and retardance thresholds were applied to select the white matter regions for comparisons. Figure 7.10A shows the orientation mismatches on two representative sections of the medulla sample, whose structure is given by gray-scale retardance images. In general, convergence of co-registered orientations is seen in

majority of areas, indicating a concordance between DTI and OCT measures. The lowest threshold pair (FA > 0.15 and retardance > 22.5°) covers almost all white matter in the medulla, and exposes areas with discrepancy in the orientation with distributed patches of hot colors. This includes borders of the white matter where registration errors may play an important role. Discrepancies gradually diminish with increasing thresholds, as the DTI and SOCS better describe the white matter regions better and their orientation measurements become closer. The highest threshold pair (FA > 0.35; retardance > 35°) tends to select unidirectional fiber bundles that are aligned parallel to the SOCS *en-face* plane. As shown, this reveals the smallest difference between the orientation maps.

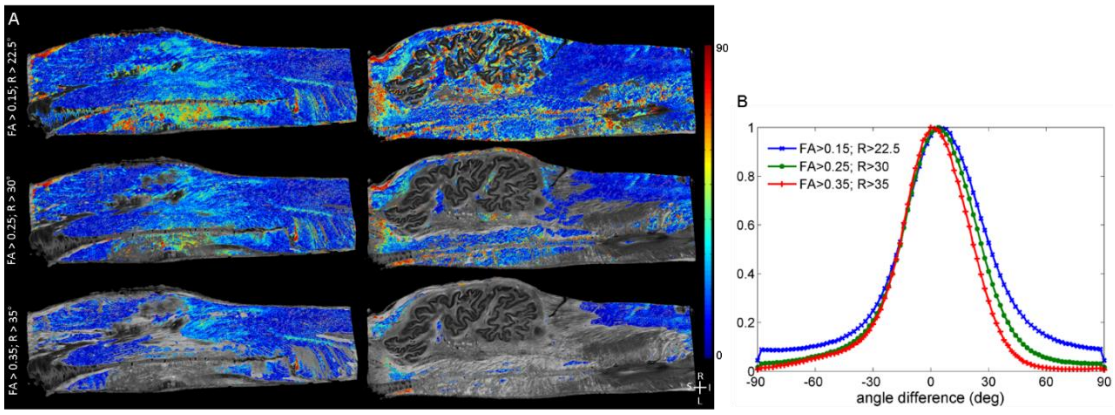


**Figure 7.10 Pixel-wise comparison of the DTI and SOCS orientation maps. A. The orientation mismatch (absolute values) is overlaid on gray-scale retardance images for two representative slices. Fiber bundles in white matter regions are selected by three sets of thresholds (top: FA > 0.15, retardance > 22.5°; middle: FA > 0.25, retardance > 30°; bottom: FA > 0.35, retardance > 35°). Color bar: 0° – 90°. B. Normalized histograms of the pixel-wise orientation difference (bin width: 2°). The pixels are selected from all slides by applying the thresholds. The mean differences are at 5.4°, 3.3° and 0.1°, and the standard deviations are 32.5°, 26.3° and 22.6°, for increasing thresholds, respectively.**

Figure 7.10B shows the normalized histograms of the pixel-wise orientation differences, which were obtained from all slices for each threshold pair. The bin-width was 2°. The mean values of the orientation difference are small for the three threshold pairs (5.4°, 3.3° and 0.1° from low to

high thresholds°). Similarly, the standard deviations of the distributions are decreased with the threshold increase (32.5°, 26.3° and 22.6°) as the width of distributions becomes narrower.

Fiber orientations are further compared in selected ROIs with varied architectures. Figure 7.11A shows four ROIs on the co-registered orientation maps. ROI 1 contains densely packed fibers exhibiting high FA and retardance values. ROI 2 is a transition area where small fiber tracts with lower density are visible on retardance image and FA image bears lower intensity. ROI 3 is above the inferior olive where FA indicates greater anisotropy and retardance image shows clustered fiber bundles aligned along a preferred direction on xy-plane. ROI 4 is in the pyramid at the decussation where two groups of fiber bundles with differed orientations are found. The ROIs are across multiple slices where specific structures are recognizable. Figure 7.11B shows histograms of fiber orientations measured by SOCS and DTI (bin width: 5°). Fiber orientations in ROI 1 present highest affinity, where SOCS orientation peaks at -35° and DTI orientation peaks at -30°. The histograms also have the narrowest width, indicating that the fiber bundles are aligned parallel with each other. Although fiber density gets lower in ROI 2, the comparison still supports a good concordance, with SOCS peaking at -10°and DTI at -15°. DTI and SOCS mismatch becomes greater on the histograms of ROI 3 and ROI 4, yet fairly comparable with a difference within 20°. Broader distributions may suggest complex patterns within the ROIs. For instance, ROI 4 exhibits a bimodal distribution that arises from distinct fiber bundles in a larger volume. The distribution of SOCS orientation is generally broader than the DTI in selected ROIs. This might be due to high resolution enabling SOCS to reveal subtle orientation variations.

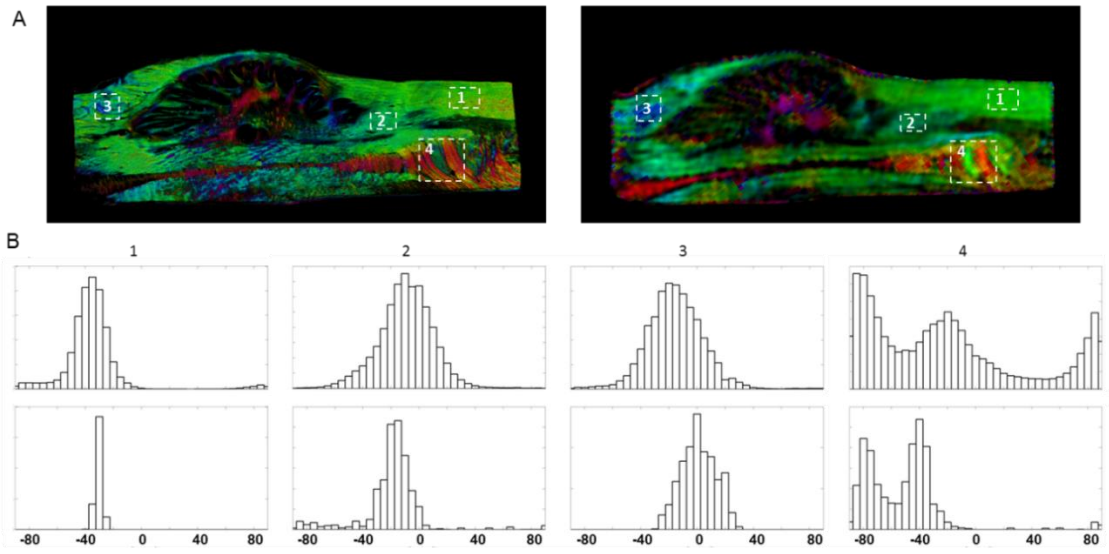


**Figure 7.11 Fiber orientations in ROIs. A. Four ROIs are shown on SOCS (left) and DTI (right) images. The color chart is the same as in Figure 7.9. The ROIs are across multiple slices containing the specific features. B. Histograms of the orientations in the ROIs for SOCS (top) and DTI (bottom). Bin width is 5°.**

Despite the affirmative correlations between DTI and SOCS measures, there are yet complicated fiber patterns that the DTI techniques cannot resolve. Figure 7.12A provides two examples which are magnified ROIs marked on Figure 7.12B. The top panels on Figure 7.12A (ROI 1 in B) contains small fiber tracts less than 100 μm in diameter. The superior resolution of SOCS supports the description of individual fiber traces accompanied by altered orientations, whereas pixelated color patches are observed on DTI orientation image without interpretable structures. For example, SOCS orientation in ROI 1-1 demonstrates three major groups present at the intersections, centered at 30°, -60° and 90°; whereas, the DTI orientation loses the differentiation of the crossing fibers. Moreover, delicate patterns of fiber crossing are visible by SOCS at the lower-right corner of ROI 1-2, where the anisotropy on DTI gets low and suppresses the expression of orientation. Fiber-crossing problem in DTI is more apparent on the bottom panels of Figure 7.12A (ROI 2 in B) which composed of fibers in the pyramid decussation. Although the low-resolution estimation preserves the parallel orientation in small fibers (yellow-orange patterns), it completely loses the indication of crossing features with multiple angles in the round

shaped fiber groups, which are captured on SOCS orientation image. Figure 7.12 (ROI 3 in B) shows another example of inter-weaving fibers in SOCS orientation, a branch of which might be an extension from the vertical tracts in the upper region. In order to achieve a quantitative evaluation, fiber orientations in the crossing region (ROI 3-1) are analyzed by histograms. Supporting the crossing pattern on SOCS, the histogram shows a side lobe at an angle of 70° intersecting with the primary peak. In contrast, the distribution of fiber orientation on DTI only specifies a single peak.

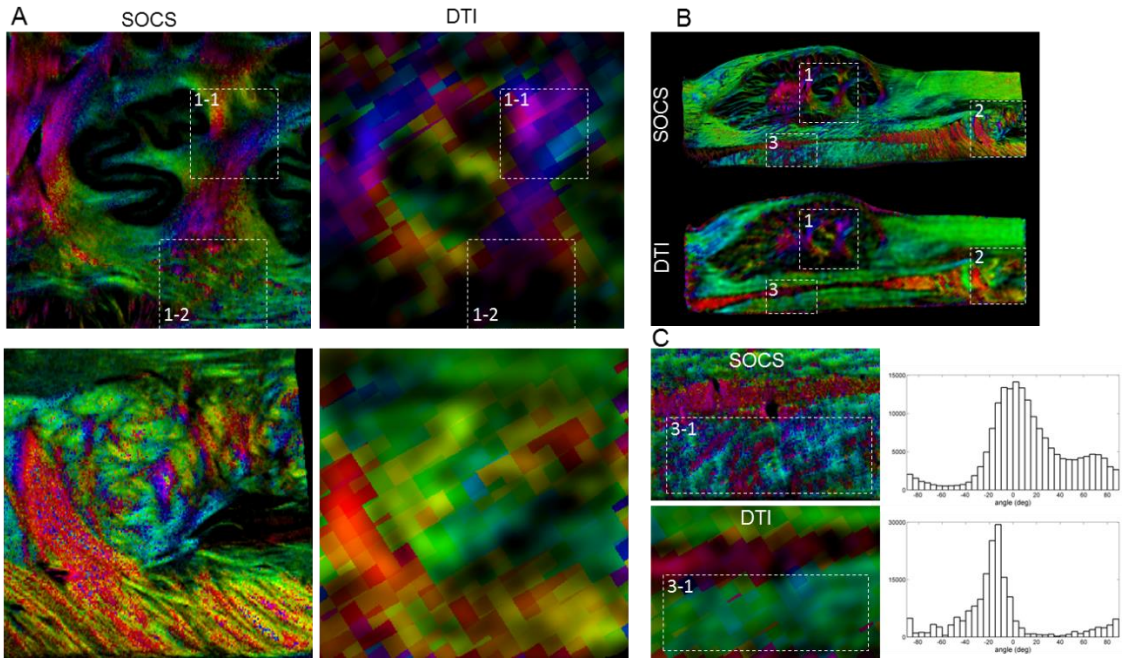


**Figure 7.12 Crossing fibers on SOCS and DTI orientation maps. A. Two magnified ROIs (ROI 1 and 2 in B) demonstrate complicated crossing patterns of fiber networks. SOCS images (left) clearly delineate individual fiber bundles with altered colors, while pixelated DTI images (right) lose track of subtle variations. B. SOCS and DTI orientation maps of the medulla slice showing the ROIs. C. Reticular patterns of crossing fibers by SOCS, and more homogeneous DTI representation. Histograms of orientations in ROI 3-1 (top: SOCS, bottom: DTI, bin width: 5°).**

## 7.6 DISCUSSION

This work presents covalidation of SOCS and DTI measurements using neural fiber pathways on a postmortem human medulla oblongata sample. We established a registration strategy that supports precise alignments of the 3D data from the two modalities, and accomplished direct comparison of white matter structures and fiber orientations at high resolution.

The multiple contrasts of SOCS describe the fiber tracts and the nuclei in the medulla from different perspectives. The polarization measures especially target at the white matter fiber tracts due to the birefringence property of axons. The *en-face* retardance stack delineates the architecture of fiber networks, which forms an analogy with the FA in DTI and sets the basis for cross-modality registration. 3D construction of macroscopic sample is accomplished by stitching and stacking multiple optical scans. Unlike validation with histology that requires complicated tissue processing and inter-slice registration, the registration procedure is rather straightforward and mechanical distortions are not observed. The quality of co-registration between 3D datasets of FA and retardance was remarkable as indicated by Dice's coefficients of 0.96 and 0.90 for tissue and white matter masks, respectively. As a result, SOCS shows a prominent merit in comprehensive studies on macroscopic brains.

Although underlying origins of FA and retardance signals are different, the co-registered images of the entire sample exhibit remarkable similarities with a Pearson's correlation coefficient of 0.90. The microscopic resolution of SOCS enables a closer inspection on the neuro-anatomical factors affecting the FA values. We found that high FA corresponds to high retardance where parallel fibers are densely packed (Figure 7.8). Reduction in FA could be due to lower fiber density, reticular formations, and small fiber tracts crossing with each other or interacting with nuclei. These factors as well as the lack of myelination and inclination angles of fibers with respect to the *xy* plane could reduce the measured retardance. We noticed high diffusion anisotropy (FA) and low retardance in median fissure (Figure 7.8, ROI 5). This might be contributed to high anisotropy of water diffusion in fibrous structures and low birefringence.

The optic axis orientation contrast yields the axis of tissue anisotropy in the plane perpendicular to the illumination beam. By projecting the DTI orientations onto the *en-face* (xy) plane, we obtained a good agreement between the orientation measurements of SOCS and DTI. Pixel-wise orientation mismatch in the white matter estimates 5.4° with a standard deviation of 32.5°. The mismatch is further reduced to 0.1° with a standard deviation of 22.6° when the thresholds of FA and retardance are elevated to include only the densely packed parallel fibers in the analysis. The ROI analyses reveal a fair comparability in multiple sites where unambiguous fiber axes are defined by DTI (Figure 7.11). The results are in consistency with previous reports in which the accuracy of local fiber orientations in DTI was examined by histological images. Leergaard et al. [246] performed manual trace on myelin stained mouse brain slices to validate DTI and q-space diffusion imaging (QSI) orientations, and found a correlation greater than 0.9 in parallel fiber tracts with DTI and an average of 5 – 6 degree deviation from QSI in crossing regions. Using a Fourier analysis, Choe et al. [211] declared a within 10 degree difference between DTI orientations and the axonal directions revealed on microscopy images. Similar agreements of fiber orientations were also discovered between histology images and DT microscopy on human spinal cord slices [247].

The orientation validation reported here has two distinct merits that were not paralleled in previous studies. Compared to validation with myelin stained histology that quantifies ROI based orientation using image processing [210, 211, 246, 247], the axis orientation contrast of SOCS allows for direct and pixel-wise correlation to DTI orientation. Compared to neural tracer labeled connective tracts [208, 243, 245, 248], the orientation verification by SOCS sets a more fundamental evaluation of dMRI results, a step preceding connectivity tracking that relies on orientation vectors and reconstruction algorithms [251].

Apart from the positive correlations discussed above, complications stand out for crossing fiber regions. SOCS is capable of catching the orientation variations in smaller fiber tracts in the

pyramid decussation and inferior olive; however, DTI orientation loses the track of those intricate fibers, left with a noise pattern or an average effect (Figure 7.12). Spatial resolution is a major factor limiting the distinction in DTI. Orientation comparability becomes less reliable for fiber tracts smaller than ~500 μm. The partial volume sampling effect and the incapability to resolve intra-voxel multi-directions increase the deviations of orientation estimation in DTI [252]. The latter issue is untangled in more sophisticated techniques of dMRI, such as high angular resolution diffusion imaging [141], q-ball imaging [253] and diffusion spectrum imaging [207]. The optic axis orientation contrast of SOCS is currently not able to resolve multiple axes within a depth of an optical section, thus *en-face* orientation values may have a bias towards the orientation of superficial fibers. Although the optic axis orientation is restricted on the *xy*-plane, information about the orientation in third dimension is implied in the retardance measure [147]. Further discussion on retardance and orientation measurements can be found in Chapter 4 and 5. Overall, SOCS serves as an appealing tool for validating DTI orientations and can be readily applied to interrogate other dMRI techniques resolving complex orientations within a voxel by borrowing the established strategies in present study.

In this study, we targeted the myelinated fibers. However, the method can be adapted to visualize the unmyelinated fibers, dendrites and cell bodies by increasing the lateral resolution to the level of optical coherence microscopy (OCM). The OCM was used to image individual axons and unveil the myeloarchitecture in the cortex [200, 254]. Previous studies on brain and peripheral nerves using OCM have reported close correlations with histology [181, 201, 228]. Therefore, the method we propose (SOCS) has potential to bridge multi-modality investigations on the central and peripheral nervous systems to construct a hierarchal view of neuro-anatomical connections from molecular to system levels, thus opening vast opportunities for systematic studies on brain mapping and neural disorders.

# CHAPTER 8 CONCLUSION AND OUTLOOK

## 8.1 CONCLUSION

This dissertation is written at a time coincide with the Brain Research through Advancing Innovative Neurotechnologies (BRAIN) Initiative project newly launched [257], that the new technologies for understanding of the human brain is so eagerly to be revolutionized than ever before. Under the current focus of systematic mapping of brainwide architectures and circuits, development of large-scale brain imaging at microscopic resolution with emphasis on the connective tracts is in great need.

The work makes progresses in overcoming this challenge by proposing a novel technique of serial multi-contrast OCT. To the end, several critical issues have been addressed through the developed chapters: 1) With a novel MC-OCT technique, the intrinsic optical contrasts based on back-scattering, light attenuation, and light polarization serve as reliable and multi-perspective views of brain. 2) Among these, the retardance, cross-polarization and optic axis orientation have been shown to be useful for quantitatively mapping its neural pathways. 3) Using a serial optical coherence scanner, 3D reconstruction can be accomplished to a spatial extent of brainwide coverage at a level of microscopic details. 4) This technique is well correlated with histological methods and can be used to cross-validate the diffusion MRI techniques, with which a hierarchical and cross-modality framework for systematic investigations of brain connectomics may be achieved.

Birefringence of the white matter tracts is the key property that supports delineation and quantification of the brain maps with MC-OCT. For white matter tracing, the PMF based system can be changed to other PS-OCT setups that are capable of retardance and optic axis orientation measurements. The bulk PS-OCT system which operates in the absence of optic fibers and fiber couplers, is able to produce the absolute optic axis orientation without extra calibrations as did for the PMF based system. For future standardization of serial PS-OCT in brain imaging, portability and translatability between varieties of experimental platforms needs more caution. In addition to PMF based system, PS-OCT generating the Stokes parameters in free space or with single-mode fibers and a polarization modulator [84, 111] also provides polarization information, and other contrasts derived from polarization alone or in combination, might be useful in characterization and classification of specific groups of neurons. This could include alternation in degree of polarization uniformity, which has been found useful for delineation of the eye's retinal pigment epithelium layer [255].

Current limitations of MC-OCT techniques in revealing full-angle neuronal networks require dedicated theoretical work as well as technical innovations. As discussed in Chapter 4 and 5, scattering directionality from the fiber bundles blocks the visibility of a range of viewing angles when the fibers are tilted through the plane with large inclination. This inclination angle not only in itself is a parameter of interest in 3D orientation, but also is related to the concern of a true birefringence derivation from the measured retardance. To solve these problems, multi-angular illumination and detection could be introduced, and a mathematical model to isolate the inclination angle from the true birefringence needs to be established. Another issue is that depth localized quantification in complex neuronal netoworks such as crossing fiber patterns and orientations which require additional computations and modified optics needs to be built.

With MC-OCT, the intrinsic contrasts are well correlated with histological methods as discussed in Chapter 5. The cortical layers shown on the en-face attenuation maps are quantitatively linked

to those observed by the Nissl stain images. The fiber organizations portrayed by the retardance have high affinity to the myelin stain results. With the thriving of OCT in high-resolution brain imaging in recent years, such validation and correlation work have been more frequently reported in normal and pathological brains, consolidating the evidences of its validity and reliability in neuroscience studies. Magnain et al. [228] systematically studied the characteristics of OCT and Nissl stain in delineating the cortical layers with human brain slices. Assayag and colleagues compared the capability of ultrahigh-resolution OCT in brain tumor diagnosis with histology [256]. Using a living transgenic mouse model of Alzheimer's disease, Bolmont and colleagues observed the cerebral A$\beta$ amyloidosis with OCT that have been verified by immunohistochemical staining and well co-localized with fluorescence imaging [201].

Apart from the histological validation, we also established a strategy for cross-validation with diffusion MRI techniques in Chapter 7, with the aim to bridge the gap between microscopic scrutiny and system-level views of connectomics, especially in human brains. Together with histological links, the efforts we have made here sets an anchor for future cross-modality investigations that have not been possible with such a comprehensive and coherent scale-span in the past.

## 8.2 OUTLOOK

The MC-OCT has pronounced advantage of creating dense reconstruction through intrinsic properties of diverse structures, but a fundamental miss is cellular specificity. This cellular specificity or molecular pheonotyping are usually achieved by bio-marker encoded fluorescence proteins, the detection of which is essentially incoherent that cannot be directly adopted by OCT. For example, immunohistochemistry has been widely used in targeting specific neuron populations. The neural tracers that express green fluorescent protein in either a pan-neuronal or cell-type-specific manner are commonly used to determine connective pathways with

directionality and terminal zones. This deficiency can be compensated with a combinational mode using multi-modality imaging. Ultrahigh-resolution OCT or OCM has been combined with confocal microscopy for various applications [258-260]. This combined system is relatively easy to implement because the two techniques typically operate at different wavelength band, which results in fairly separable subunits except for the common optical path on the sample [259, 260]. The OCT/OCM has also been combined with multiphoton microscopy to achieve more comparable probing depths. Although optimized light sources can be employed separately in individual units [261], a common Ti:Sapphire pulsed laser can serve as a common light source for both OCT/OCM and multiphoton imaging [262, 263]. This implementation improves the efficiency of hardware, but requires customized optical design and more careful alignment. After the proof-of-principle demonstration, the clinical applications of integrated OCM-multiphoton has come to horizons especially in dermatology [264]. Those combined cellular imaging systems bear similar resolution to that of single-photon or multiphoton microscopy; however, speckle noise that is inevitable in coherence imaging may significantly reduce the contrast information and thus hamper the interpretation of OCT/OCM images.

The feasibility of OCM in cytoarchitecture and myeloarchitecture has been demonstrated [254]; however, the capability of systematically mapping of neuronal types and axonal connectivity need further investigation. The quantities of connectivity and connective strength have to be defined in an analytical way that is interpretable under other neuroanatomical contexts. We think a combined multi-contrast OCT/OCM and multiphoton imaging technique with genetically engineered cell-type-specific neural tracers could potentially be appealing for drawing the mesoscale circuitry in mammal brains. The OCT/OCM images may serve as a framework that the neural tracers refer to when the local circuitry is registered to a global template.

The link of MC-OCT and diffusion MRI has great potentials as the birefringence measure in MC-OCT has direct access to the white matter tracts, and moreover, the microscopic resolution of

OCT provides abounding architecture details that are prohibited in dMRI. As the spatial coverage of serial scanning is improved with acquisition speed, comprehensive studies by dMRI and MC-OCT on the same sample can be conducted. This collaborative investigation is crucial in discovering the pathological pathways. The missing details of the altered diffusion-related parameters commonly found in brain disorders by dMRI may be uncovered optically.

The brain imaging by MC-OCT requires minimal histological preparation of tissues. Therefore, the same sample scanned by MC-OCT may be reused for higher resolution imaging with targeted regions, such as the synaptic junctions revealed by electron microscopy. To this end, we envision that hierarchical architecture maps could be linked together to form a cross-scale wiring diagram.

The MC-OCT favors the description of global fiber networks without pre-selecting neuronal types or spatial locations. This capability facilitates the acceleration of the whole-brain reconstruction process. The scalability of the SOCS technique to human and non-human primate brains will be dramatically enhanced by automated actuating procedures and post-processing tools. Mainly due to time needed for physical slicing and manual manipulations, SOCS currently takes 1~2 days for the entire data collection of a sample of 1-2 $cm^3$. An automated scanner with programmable scanning and sectioning parameters will tremendously facilitate the image acquisition of both smaller and larger brains. Comparing to data acquisition, post-processing of big data takes even longer time. Stitching multiple *en-face* images can readily borrow the tools developed for microscopy; whereas, stitching serial optical sections with signal decay along depth would require more pre-processing steps and customized algorithms. In addition, objective assessment in brain architecture and connectomics would require automated feature selection, classification, segmentation and tracing. Therefore, dedicated package with routine pipelines and quantitative tools will greatly speed up the application of SOCS in neuroscience research. We envision that with an automated serial MC-OCT scanner and routine processing engines, data acquisition of a mouse or rat brain can be done in a few hours and reconstruction of its entire

neuronal pathways achieved in several days. Full reconstruction of primate and human brains is more challenging; however, it is not impossible with standardized procedures in the future.

# REFERENCES


1. Swanson, L. W. *Brain Architecture: Understanding the Basic Plan* 331 (Oxford Univ. Press, 2012)
2. Schmidt EM. 1980. Single neuron recording from motor cortex as a possible source of signals for control of external devices. Ann Biomed Eng 8: 339–349.
3. Berger H. 1929. Über das Elektroenkephalogram des Menschen. Arch. f. Psychiat. 87: 527-70.
4. Cohen D. 1968. Magnetoencephalography: evidence of magnetic fields produced by alpha-rhythm currents. Science. 161: 784-786.
5. Fox PT, Raichle ME. 1986. Focal physiological uncoupling of cerebral blood flow and oxidative metabolism during somatosensory stimulation in human subjects. Proc. Natl. Acad. Sci. USA. 83: 1140-1144.
6. Fox PT, Raichle ME, Mintun MA, Dence C. 1988. Nonoxidative Glucose consumption during focal physiologic neural activity. Science 241: 462-464.
7. Ogawa S, Lee TM, Kay AR and Tank DW. 1990. Brain magnetic resonance imaging with contrast dependent on blood oxygenation. Proc. Natl. Acad. Sci. USA. 87(24): 9868-9872.
8. Jobsis FF. 1977. Noninvasive infrared monitoring of cerebral and myocardial oxygen sufficiency and circulatory parameters. Science 198: 1264-1267.
9. Lein, E.S. et al. 2007, Nature 445, 168–176.
10. Bohland, J.W., Wu, C., Barbas, H., Bokil, H., Bota, M., et al., 2009. A proposal for a coordinated effort for the determination of brainwide neuroanatomical connectivity in model organisms at a mesoscopic scale. PLoS Comput. Biol. 5, e1000334.
11. Seung, S. *Connectome: How The Brain's Wiring Makes Us Who We Are* 359 (Houghton Mifflin Harcourt, 2012)
12. Sporns, O. *Networks of the Brain* 412 (The MIT Press, 2011)
13. Moseley ME, Cohen Y, Mintorovitch J. 1990. Early detection of regional cerebral ischemic injury in cats: evaluation of diffusion and T2-weighted MRI and spectroscopy. Magn Reson Med 14*:* 330–346.
14. Horwitz B. 2003. The elusive concept of brain connectivity. NeuroImage. 19(2): 466-470.
15. David O, Cosmelli D, Friston KJ. 2004. Evaluation of different measures of functional connectivity using a neural mass model. NeuroImage, 21(2): 659-673.

16. Ioannides AA. 2007. Dynamic functional connectivity. Curr. Opin. Neurobiol. 17: 161-170.
17. Van Essen, D.C., et al., 2012. The Human Connectome Project: A data acquisition perspective. Neuroimage 62: 2222-2231.
18. Van Essen, D. C. et al. The WU-Minn Human Connectome Project: an overview. NeuroImage 80, 62–79 (2013)
19. Denk, W. & Horstmann, H. 2004. Serial block-face scanning electron microscopy to reconstruct three-dimensional tissue nanostructure. PLoS Biol. 2, e329.
20. White, J. G., Southgate, E., Thomson, J. N. & Brenner, S. 1986. The structure of the nervous system of the nematode Caenorhabditis elegans. Phil. Trans. R. Soc. Lond. B 314, 1–340.
21. Bota, M., Dong, H. W. & Swanson, L. W. 2005. Brain architecture management system. Neuroinformatics 3, 15–48.
22. Stephan KE, Kamper L, Bozkurt A, Burns GA, Young MP, et al. 2001. Advanced database methodology for the collation of the connectivity data on the macaque brain (CoCoMac). Philos Trans R Soc Lond B Biol Sci 356: 1159–1186.
23. Oh SW, Harris JA, Ng L, Winslow B, Cain N, Mihalas S, Wang Q, Lau C, Kuan L, Henry A, Mortrud M, Ouellette B, Nguyen TN, Sorensen SA, Slaughterbeck CR, Wakeman W, Li Y, Feng D, Ho A, Nicholas E, Hirokawa K, Bohn P, Joines K, Peng H, Hawrylycz HJ, Philips JW, Hohmann JG, Wohnoutka P, Gerfen CR, Koch C, Bernard A, Dang C, Jones AR, Zeng H. 2014. A mesoscale connectome of the mouse brain. Nature 508, 207 – 214.
24. Bürgel, U., Amunts, K., Hoemke, L., Mohlberg, H., Gilsbach, J. M., and Zilles, K. 2006. White matter fiber tracts of the human brain: three-dimensional mapping at microscopic resolution, topography and intersubject variability. Neuroimage 29, 1092–1105.
25. Huang, D., Swanson, E.A., Lin, C.P., Schuman, J.S., Stinson, W.G., Chang, W., Hee, M.R., Flotte, T., Gregory, K., Pufialito, C.A., Fujimoto, J.G., 1991. Optical coherence tomography. Science 254, 1178-1181.
26. Boppart S. A., Optical coherence tomography: technology and applications for neuroimaging, Psychophysiology 40, 529-541, 2003
27. Hee M. R., , Baumal C. R., , Puliafito C. A., , Duker J. S., , Reichel E., , Wilkins J. R., , Coker J. G., , Schuman J. S., , Swanson E. A., , and Fujimoto J. G., " Optical coherence tomography of age-related macular degeneration and choroidal neovascularization. ," Ophthalmology 103, 1260–1270 (1996).
28. de Bruin D M, Burnes D L, Loewenstein J, Chen Y, Chang S, Chen T C, Esmaili D D, de Boer J F. "In vivo three-dimensional imaging of neovascular age-related macular

degeneration using optical frequency domain imaging at 1050 nm." Invest Ophthalmol Vis Sci 49, 4545-4552 (2008).

29. Roper S N, Moores M D, Gelikonov G V, Feldchtein F I, Beach N M, King M A, Gelikonov V M, Sergeev A M, and Reitze D H. “In vivo detection of experimentally induced cortical dysgenesis in the adult rat neocortex using optical coherence tomography.” Journal of Neuroscience Methods 80, 91–98 (1998).
30. Boppart S A, Brezinski M E, Pitris C, and Fujimoto J G. “Optical coherence tomography for neurosurgical imaging of intracortical melanoma.” Neurosurgery 43, 834–841 (1998).
31. Boppart S A, Brezinski M E, Bouma B E, Tearney G J, and Fujimoto J G. “Investigation of developing embryonic morphology using optical coherence tomography.” Developmental Biology 177, 54–63 (1996).
32. Boppart S A, Brezinski M E, Tearney G J, Bouma B E, and Fujimoto J G. “Imaging developing neuralmorphology using optical coherence tomography.” Journal of Neuroscience Methods 2112, 65–72 (1996).
33. Jafri M S, Farhang S, Tang R S, Desai N, Fishman P S, Rohwer R G, Tang C M, and Schmitt J M. “Optical coherence tomography in the diagnosis and treatment of neurological disorders.” J Biomed Opt 10, 051603 (2005).
34. Boppart S A, Bouma B E, Pitris C, Tearney G J, Southern J F, Brezinski M E, and Fujimoto J G. “Intraoperative assessment of microsurgery with three-dimensional optical coherence tomography.” Radiology 208, 81–86 (1998).
35. Jeon S W, Shure M A, Baker K B, Huang D, Rollins A M, Chahlavi A, and Rezai A R. “A feasibility study of optical coherence tomography for guiding deep brain probes.” J Neurosci Methods154, 96–101 (2006).
36. Jafri M S, Tang R, Tang C -M. “Optical coherence tomography guided neurosurgical procedures in small rodents.” J Neurosci Methods 176, 85-95 (2009).
37. J. Lee, H. Radhakrishnan, W. Wu, A. Daneshmand, M. Climov, C. Ayata, and D. A. Boas 2013. Quantitative imaging of cerebral blood flow velocity and intracellular motility using dynamic light scattering-optical coherence tomography. J. Cereb. Blood Flow Metab. 33(6), 819–825.
38. Wicks RT, Huang Y, Zhang K, Zhao M, Tyler BM, Suk I, Hwang L, Ruzevick J, Jallo G, Brem H, Pradilla G, Kang JU 2014. Extravascular optical coherence tomography: evaluation of carotid atherosclerosis and pravastatin therapy. Stroke 45: 1123-1130.
39. Ren H, Du C, Yuan Z, Park K, Volkow ND, et al. 2012. Cocaine-induced cortical microischemia in the rodent brain: clinical implications. Mol Psychiatry. 17: 1017-1025.

40. Stepnoski R A, LaPorta A, Raccuia-Behling F, Blonder G E, Slusher R E, and Kleinfeld D. “Noninvasive detection of changes in membrane potential in cultured neurons by light scattering.” Proceedings of the National Academy of Sciences 88, 9382–9386 (1991).
41. Akkin T, Davé D, Milner T, and Rylander III H. "Detection of neural activity using phase-sensitive optical low-coherence reflectometry." Opt. Express 12, 2377-2386 (2004).
42. Fuji T, Miyata M, Kawato S, Hattori T and Nakatsuka H 1997 J. Opt. Soc. Am. B 14 1074–8
43. Pan Y, Birngruber R, Rosperich J and Engelhardt R 1995 Appl. Opt. 34 6564–74
44. C. K. Hitzenberger, W. Drexler, and A. F. Fercher, “Measurement of corneal thickness by laser doppler interferometry,” Invest. Ophthalmol. Vis. Sci., vol. 33, pp. 98–103, 1992.
45. J. M. Schmitt, A. Kn¨uttel, and R. F. Bonner, “Measurement of optical properties of biological tissues by low-coherence reflectometry,” Appl. Opt., vol. 32, pp. 6032–6042, 1993.
46. D. Huang, J. P. Wang, C. P. Lin, C. A. Puliafito, and J. G. Fujimoto, “Micron-resolution ranging of the cornea anterior chamber by optical reflectometry,” Lasers Surg. Med., vol. 11, pp. 419–425, 1991.
47. M. D. Kulkarni, C. W. Thomas, and J. A. Izatt, “Image enhancement in optical coherence tomography using deconvolution,” Electron. Lett., vol. 33, pp. 1365–1367, 1997.
48. Bizheva K K, Siegel A M and Boas D A 1998 Phys. Rev. E 58 7664–7
49. Wax A, Yang C, Dasari R R and Feld M S 2001 Appl. Opt. 40 4222–7
50. Gandjbakhche A H, Bonner R F and Nossal R 1992 J. Stat. Phys. 69 35–53
51. Schmitt J M and Kumar G 1998a Appl. Opt. 37 2788–97
52. Vargas G, Chan E K, Barton J K, Rylander H G 3rd and Welch A J 1999 Lasers Surg. Med. 24 133–41
53. Tuchin V V, Xu X and Wang R K 2002 Appl. Opt. 41 258–71
54. Hodara H 1965 Proc. IEEE 53 696–704
55. Rollins A M and Izatt J A 1999 Opt. Lett. 24 1484–6
56. Podoleanu A G 2000 Appl. Opt. 39 173–82
57. B. Park, Mark C. Pierce, Barry Cense, Seok-Hyun Yun, Mircea Mujat, Guillermo Tearney, Brett Bouma, and Johannes de Boer, "Real-time fiber-based multi-functional spectral-domain optical coherence tomography at 1.3 µm," Opt. Express 13, 3931-3944 (2005)
58. Tearney G J, Bouma B E and Fujimoto J G 1997. High-speed phase- and group-delay scanning with a grating-based phase control delay line. Opt. Lett. 22 1811–13
59. Drexler W, Morgner U, Kartner F X, Pitris C, Boppart S A, Li X D, Ippen E P and Fujimoto J G 1999 Opt. Lett. 24: 1221–3.

60. Bouma B. E., Tearney G. J. 1999. “Power-efficient nonreciprocal interferometer and linear-scanning fiber-optic catheter for optical coherence tomography. Opt. Lett. . 24, 531–533.
61. E. A. Swanson, D. Huang, M. R. Hee, J. G. Fujimoto, C. P. Lin, and C. A. Puliafito, 1992. "High-speed optical coherence domain reflectometry," Opt. Lett. 17, 151-153.
62. A. Rollins, S. Yazdanfar, M. Kulkarni, R. Ung-Arunyawee, and J. Izatt, "In vivo video rate optical coherence tomography," Opt. Express 3, 219-229 (1998)
63. A. Fercher, C. Hitzenberger, G. Kamp and S. El-Zaiat, “Measurement of intraocular distances by backscattering spectral interferometry,” Opt. Comm. 117, 43-48, (1995).
64. G. Hausler, M. Lindner, 1998. “Coherence Radar” and “Spectral Radar”—New Tools for Dermatological Diagnosis,” J. Biomed. Opt. 3, 21-31.
65. M Wojtkowski, R Leitgeb, A Kowalczyk, T Bajraszewski, A Fercher, “In vivo human retinal imaging by Fourier domain optical coherence tomography,” J Biomed Opt. 7, 457-463 (2002).
66. S. R. Chinn, E. Swanson, J. G. Fujimoto, “Optical coherence tomography using a frequency-tunable optical source,” Opt. Lett. 22, 340-342 (1997)
67. B. Golubovic, B. E. Bouma, G. J. Tearney, and J. G. Fujimoto, “Optical frequency-domain reflectometry using rapid wavelength tuning of a Cr4+:forsterite laser,” Opt. Lett. 22, 1704-1706 (1997)
68. F. Lexer, C. K. Hitzenberger, A. F. Fercher, and M. Kulhavy, “Wavelength-tuning interferometry of intraocular distances,” Appl. Opt. 36, 6548-6553 (1997).
69. R. Leitgeb, C. Hitzenberger, and A. Fercher, "Performance of fourier domain vs. time domain optical coherence tomography," Optics Express 11, 889-894 (2003)
70. M. Choma, M. Sarunic, C. Yang, and J. Izatt, "Sensitivity advantage of swept source and Fourier domain optical coherence tomography," Optics Express 11, 2183-2189 (2003)
71. J. F. de Boer, B. Cense, B. H. Park, M. C. Pierce, G. J. Tearney, and B. E. Bouma, "Improved signal-to-noise ratio in spectral-domain compared with time-domain optical coherence tomography," Optics Letters 28, 2067-2069 (2003)
72. N. Nassif, B. Cense, B.H. Park, et al., 2004. "In vivo human retinal imaging by ultrahigh-speed spectral domain optical coherence tomography," Opt. Lett. 29, 480-482.
73. Hee M R, Huang D, Swanson EA and Fujimoto J G 1992 J. Opt. Soc. Am. B 9 903–8
74. de Boer J F, Milner T E, van Gemert M J C and Nelson J S 1997. Two-dimensional birefringence imaging in biological tissue by polarization-sensitive optical coherence tomography. Opt. Lett. 22 934–6

75. de Boer J F, Srinivas S M, Malekafzali A, Chen Z and Nelson J S 1998 Opt. Express. 3 212–18
76. Everett M J, Schoenenberger K, Colston B W Jr and Da Silva L B 1998. Birefringence characterization of biological tissue by use of optical coherence tomography. Opt. Lett. 23 228–30
77. Schoenenberger K, Colston B W Jr, Maitland D J, da Silva L B and Everett M J 1998 Appl. Opt 37 6026–36
78. Hitzenberger C K, Goetzinger E, Sticker M, Pircher M and Fercher A F 2001 Opt. Express. 9 780–90
79. R.C. Jones, J. Opt. Soc. Am. A 31(7), 488 (1941)
80. Jiao S and Wang L V 2002 Opt. Lett. 27 101–3
81. J.J. Gil, E. Bernabeu, Optik 76(2), 67 (1987)
82. Huard S 1996 Polarization of Light (Paris: Wiley)
83. Yao G and Wang L V 1999. Two-dimensional depth-resolved Mueller matrix characterization of biological tissue by optical coherence tomography. Opt. Lett. 24 537–9
84. Yasuno Y, Makita S, Sutoh Y, Itoh M and Yatagai T 2002. Birefringence imaging of human skin by polarization-sensitive spectral interferometric optical coherence tomography. Opt. Lett. 27 1803–5
85. de Boer J F, Milner T E and Nelson J S 1999. Determination of the depth-resolved Stokes parameters of light backscattered from turbid media by use of polarization-sensitive optical coherence tomography. Opt. Lett. 24 300–2
86. de Boer J F and Milner T E 2002 J. Biomed. Opt. 7 359–71
87. Saxer C E, de Boer J F, Hyle Park B, Zhao Y, Chen Z and Nelson J S 2000. High-speed fiber based polarization-sensitive optical coherence tomography of in vivo human skin. Opt. Lett. 25 1257–355
88. Roth J E, Kozak J A, Yazdanfar S, Rollins A M and Izatt J A 2001. Simplified method for polarization-sensitive optical coherence tomography. Opt. Lett. 26 1069–71
89. Izatt JA, Kulkarni MD, Yazdanfar S, Barton JK & Welch AJ (1997) In vivo bidirectional color Doppler flow imaging of picoliter blood volumes using optical coherence tomography. Opt Lett 22(18): 1439–1441.
90. B. A. Bower, M. Zhao, R. J. Zawadzki, and J. A. Izatt, "Real-time spectral domain Doppler optical coherence tomography and investigation of human retinal vessel autoregulation," J. Biomedical Opt. 12, 041214 (2007).
91. S. Yazdanfar, M. D. Kulkarni, and J. A. Izatt, 1997. High resolution imaging of in vivo cardiac dynamics using color Doppler optical coherence tomography. Opt. Exp. 1, 424-431.

92. MC Skala, A Fontanella, H Hendargo, MW Dewhirst, and JA Izatt. Combined Hyperspectral and Optical Coherence Tomography Microscope for Noninvasive Hemodynamic Imaging. Optics Letters 34, 289-291 (2009).
93. Yazdanfar S, Rollins A M and Izatt J A 2000. Imaging and velocimetry of the human retinal circulation with color Doppler optical coherence tomography. Opt. Lett. 25 1448–50
94. S. Yazdanfar, A. M. Rollins, J. A. Izatt, "In vivo imaging of human retinal flow dynamics by color Doppler optical coherence tomography," Arch. Ophthalmol. 121, 235-239 (2003).
95. Wang XJ, Milner TE & Nelson JS (1995) Characterization of fluid flow velocity by optical Doppler tomography. Opt Lett 20(11): 1337–1339.
96. X. J. Wang, T. E. Milner, and J. S. Nelson, 1995. Characterization of fluid flow velocity by optical Doppler tomography. Opt. Lett. 20, 1337.
97. Y. H. Zhao, Z. P. Chen, C. Saxer, S. H. Xiang, J. F. de Boer, J. S. Nelson, "Phase-resolved optical coherence tomography and optical Doppler tomography for imaging blood flow in human skin with fast scanning speed and high velocity sensitivity," Opt. Lett. 25, 114-116 (2000).
98. Chen Z, Milner TE, Dave D & Nelson JS (1997) Optical Doppler tomographic imaging of fluid flow velocity in highly scattering media. Opt Lett 22(1): 64–66.
99. Zhao Y, Chen Z, Saxer C, Xiang S, de Boer JF & Nelson JS (2000) Phase-resolved optical coherence tomography and optical Doppler tomography for imaging blood flow in human skin with fast scanning speed and high velocity sensitivity. Opt Lett 25(2): 114–116.
100. Z. H. Ding, Y. H. Zhao, H. W. Ren, J. S. Nelson, Z. P. Chen, "Real-time phase-resolved optical coherence tomography and optical Doppler tomography," Opt. Express 10, 236-245 (2002)
101. Leitgeb R, Schmetterer L, Wojtkowski M, Hitzenberger C K, Sticker M and Fercher A F 2002 Proc. SPIE 4619 16–21.
102. J. K. Barton and S. Stromski, 2005. Flow measurement without phase information in optical coherence tomography images. Opt. Express 13, 5234-5239.
103. A. H. Bachmann, M. L. Villiger, C. Blatter, T. Lasser, and R. A. Leitgeb, 2007. Resonant Doppler flow imaging and optical vivisection of retinal blood vessels. Opt. Express 15, 408-422.
104. J. Fingler, D. Schwartz, C. Yang, and S. E. Fraser, 2007. Mobility and transverse flow visualization using phase variance contrast with spectral domain optical coherence tomography Opt. Express 15, 12636-12653.

105. R. K. Wang, S. L. Jacques, Z. Ma, S. Hurst, S. R. Hanson, and A. Gruber, “Three Dimensional Optical Angiography,” Opt. Express 15(7), 4083–4097 (2007).

106. Z. Yuan, Z. C. Luo, H. G. Ren, C. W. Du, and Y. Pan, “A digital frequency ramping method for enhancing Doppler flow imaging in Fourier-domain optical coherence tomography,” Opt. Express17(5), 3951–3963 (2009).

107. Tao, YK; Davis, AM; Izatt, JA, Single-pass volumetric bidirectional blood flow imaging spectral domain optical coherence tomography using a modified Hilbert transform., Optics Express, vol 16 no. 16 (2008), pp. 12350-12361.

108. M. Szkulmowski, A. Szkulmowska, T. Bajraszewski, A. Kowalczyk, and M. Wojtkowski, “Flow velocity estimation using joint spectral and time-domain optical coherence tomography,” Opt. Express 16, 6008–6025 (2008).

109. E. Götzinger, M. Pircher, and C. K. Hitzenberger, "High speed spectral domain polarization sensitive optical coherence tomography of the human retina," Opt. Express 13, 10217-10229 (2005).

110. B. Baumann, E. Götzinger, M. Pircher, and C. K. Hitzenberger, "Single camera based spectral domain polarization sensitive optical coherence tomography," Opt. Express 15, 1054-1063 (2007).

111. B. Cense, M. Mujat, T. C. Chen, B. H. Park and J. F. de Boer, "Polarization-sensitive spectral-domain optical coherence tomography using a single line scan camera," Opt. Express 15, 2421-2431 (2007).

112. D. P. Davé, T. Akkin, and T. E. Milner, "Polarization-maintaining fiber-based optical low-coherence reflectometer for characterization and ranging of birefringence," Optics Letters 28, 1775-1777 (2003)

113. Al-Qaisi, M.K., Akkin, T., 2008. Polarization-sensitive optical coherence tomography based on polarizationmaintaining fibers and frequency multiplexing. Opt. Express 16, 13032-13041.

114. M. P. Varnham, D. N. Payne, R. D. Birch, E. J. Tarbox, “Single-polarization operation of highly birefringent bow-tie optical fibers,” Electron Lett., 19, 246-247, (1983).

115. J. R. Simpson, R. H. Stolen, F. M. Sears, W. Pleibel, J. B. MacChesney, R . E. Howard, “A single-polarization fiber,” J. Lightwave Technol., LT-1, 370-373, 1983.

116. K. Okamoto, T. Hosaka, J. Noda, “High-birefringence polarizing fiber with flat cladding,” J. Lightwave Technol., LT-3, 758-762, 1985.

117. T. Hosaka, Y. Sasaki, K. Okamoto, “3-km long single-polarization single-mode fiber,” Electron. Lett. 21, 1023-1024, 1985.

118. R. B. Dyott, J. R. Cozens, D. G. Morris, “Preservation of polarization in optical-fiber waveguides with elliptical cores,” Electron. Lett., 15, 380-382, 1979.

119. T. Katsuyama, H. Matsumura, T. Suganuma, “Low-loss single-polarization fibers,” Electron. Lett., 17, 473- 474, 1981.

120. N. Shibata, M. Tateda, S. Seikai, “Polarization-mode dispersion measurement in elliptical core single-mode fibers by a spatial technique,” IEEE J. Quhntum Electron., QE-18., 53-58, 1982.

121. T. Katsuyama, H. Matsumura, T. Suganuma, “Propagation characteristics of single polarization fibers,” Appl. Opt., 22, 1748-1753, 1983.

122. N. Shibata, M. Tateda, S. Seikai, N. Uchida, “Birefringence and polarization-mode dispersion caused by thermal stress in single mode fibers with various core ellipticities,” IEEE J. Quantum Electron., QE-19, 1223-1227, 1983.

123. S. C. Rashleigh M. J. Marrone, “Polarization holding in elliptical-core birefringent fibers,” IEEE J. Quantum Electron., QE-18, 1515-1523, 1982.

124. V. Ramaswamy, W. G. French, R. D. Standley, “Polarization characteristics of noncircular core single-mode fibers,” Appl. Opt., 17, 3014-3017, 1978.

125. K. Kitayama, S. Seikai, N. Uchida, M. Akiyama, “Polarization-maintaining single-mode fiber with azimuthally inhomogeneous index profile,” Electron. Lett., 17, 419-420, 1981.

126. T. Hosaka, K. Okamoto, Y. Sasaki, T. Edahiro, “Single-mode fibers with asymmetrical refractive-index pits on both sides of the core,” Electron. Lett., 17, 191-193, 1981.

127. Dorrer C, Belabas N, Likforman J P, and Joffre M. “Spectral resolution and sampling issues in Fouriertransform spectral interferometry.” J. Opt. Soc. Am. B 17(10), 1795–1802 (2000).

128. Cense B, Nassif N, Chen T, Pierce M, Yun S -H, Park B, Bouma B, Tearney G, and de Boer J. "Ultrahigh-resolution high-speed retinal imaging using spectral-domain optical coherence tomography." Opt. Express 12, 2435-2447 (2004).

129. Park B H, Pierce M C, Cense B, Yun S H, Mujat M, Tearney G J, Bouma B E and de Boer J F. “Real-time fiber-based multi-functional spectral-domain optical coherence tomography at 1.3 μm.” Opt. Exp. 13(11), 3931-3944 (2005).

130. C.K. Hitzenberger, A. Baumgartner, W. Drexler, A.F. Fercher, J. Biomed. Opt., 4(1), 144 (1999)

131. W. Drexler, U. Morgner, F.X. Kartner, C. Pitris, S.A. Boppart, X.D. Li, E.P. Ippen, J.G. Fujimoto, Opt. Lett. 24(17), 1221 (1999)

132. Fercher A F, Hitzenberger C K, Sticker M, Zawadzki R, Karamata B and Lasser T 2001 Opt. Express 9 610–15

133. Van Engen A G, Diddams S A and Clement T S 1998 Appl. Opt. 37 5679–86

134. C. Hitzenberger, E. Goetzinger, M. Sticker, M. Pircher, and A. Fercher, "Measurement and imaging of birefringence and optic axis orientation by phase resolved polarization sensitive optical coherence tomography," Opt. Express 9, 780-790 (2001).

135. E. Götzinger, B. Baumann, M. Pircher, and C. K. Hitzenberger, "Polarization maintaining fiber based ultra-high resolution spectral domain polarization sensitive optical coherence tomography," Opt. Express 17(25), 22704–22717 (2009)

136. Bürgel, U., Mecklenburg, I., Blohm, U., Zilles, K., 1997. Histological visualization of long fibre tracts in the white matter of adult human brains. J. Brain Res. 38, 397-404.

137. Burkhalter, A., Bernardo, K.L., Charles, V., 1993. Development of local circuits in human visual cortex. J. Neurosci. 13, 1916-1931.

138. Lanciego, J.L., Wouterlood, F.G., 2000. Neuroanatomical tract-tracing methods beyond 2000: what's now and next. J. Neurosci. Meth. 103, 1-2.

139. Basser, P.J., Mattiello, J., Le Bihan, D., 1994. Estimation of the effective self-diffusion tensor from the NMR spin-echo. J. Magn. Reson. B 103, 247-254.

140. Conturo, T.E., Lori, N.F., Cull, T.S., Akbudak, E., Snyder, A.Z., Shimony, J.S., McKinstry, R.C., Burton, H., Raichle, M.E., 1999. Tracking neuronal fiber pathways in the living human brain. Proc. Natl. Acad. Sci. U. S. A. 96, 10422-10427.

141. Tuch, D.S., Reese, T.G., Wiegell, M.R., Makris, N., Belliveau, J.W., Wedeen, V.J., 2002. High angular resolution diffusion imaging reveals intravoxel white matter fiber heterogeneity. Magn. Reson. Med. 48, 577-582.

142. Assaf, Y., Pasternak, O., 2008. Diffusion tensor imaging (DTI)-based white matter mapping in brain research: a review. J. Mol. Neurosci. 34, 51-61.

143. de Campos VB, Mello ML, Caseiro-Filho AC, Godo C. Anisotropic properties of the myelin sheath. Acta Histochem. 1980; 66: 32–39.

144. Oldenbourg R 1996 A new view on polarization microscopy. Nature 381, 811-812.

145. Axer, M., Amunts, K., Grässel, D., Palm, C., Dammers, J., Axer, H., Pietrzyk, U., Zilles, K., 2011. A novel approach to the human connectome: ultra-high resolution mapping of fiber tracts in the brain. NeuroImage 54, 1091-1101.

146. Nakaji, H., Kouyama, N., Muragaki, Y., Kawakami, Y., Iseki, H., 2008. Localization of nerve fiber bundles by polarization-sensitive optical coherence tomography. J. Neurosci. Methods 174, 82-90.

147. Larsen, L., Griffin, L.D., GrÄβel, D., Witte, O.W., Axer, H., 2007. Polarized light imaging of white matter architecture. Microsc. Res. Tech. 70, 851–863.

148. Hebeda, K.M., Menovsky, T., Beek, J.F., Wolbers, J.G., van Gemert, M.J.C., 1994. Light propagation in the brain depends on nerve fiber orientation. Neurosurgery 35, 720-724.

149. Canny, J., 1986. A computational approach to edge detection. IEEE Trans. Pattern Anal. Mach. Intell. 8, 679-698.

150. Stifter, D., Leiss-Holzinger, E., Major, Z., Baumann, B., Pircher, M., Götzinger, E., Hitzenberger, C.K., Heise, B., 2010. Dynamic optical studies in materials testing with spectral-domain polarization-sensitive optical coherence tomography. Opt. Express 18, 25712-25725.

151. Perona, P., Malik, J., 1990. Scale space and edge detection using anisotropic diffusion. IEEE Trans. Pattern Anal. Mach. Intell. 12, 629-639.

152. Catté, F., Lions, P.L., Morel, J.M., Coll, T., 1992. Image selective smoothing and edge detection by nonlinear diffusion. SIAM J. Numer. Anal. 29, 182-193.

153. Peng, H., Ruan, Z., Long, F., Simpson, J.H., Myers, E., 2010. V3D enables real-time 3D visualization and quantitative analysis of large-scale biological image data sets. Nat. Biotechnol. 28, 348-353.

154. Hegemark FB, Stone N, 2009. Towards automated classification of clinical optical coherence tomography data of dense tissues. Lasers Med. Sci. 24, 627–638.

155. Jørgenson TM, Tycho A, Mogensen M, Bjerring P, Jemec GBE (2008) Machine-learning classification of non-melanoma skin cancers from image features obtained by optical coherence tomography. Skin Res Technol 14: 364-369

156. Zysk AM, Boppart SA. Computational methods for analysis of human breast tumor tissue in optical coherence tomography images, J Biomed Opt 11(2006)

157. Ozcan, A., Bilenca, A., Desjardins, A.E., Bouma, B.E., Tearney, G.J., 2007. Speckle reduction in optical coherence tomography images using digital filtering. J. Opt. Soc. Am. A 24, 1901-1910.

158. Adler, D.C., Ko, T.H., Fujimoto, J.G, 2004. Speckle reduction in optical coherence tomography images by use of a spatially adaptive wavelet filter. Opt. Lett. 29, 2878-2880.

159. Jian, Z., Yu, L., Rao, B., Tromberg, B.J., Chen Z., 2010. Three-dimensional speckle suppression in optical coherence tomography based on the curvelet transform. Opt. Express 18, 1024-1032.

160. Al-Qaisi, M.K., Akkin, T., 2010. Swept-source polarization-sensitive optical coherence tomography based on polarization-maintaining fiber. Opt. Express 18, 3392-3403.

161. Guo, S., Zhang, J., Wang, L., Nelson, J.S., Chen, Z., 2004. Depth-resolved birefringence and differential optical axis orientation measurements with fiber-based polarization-sensitive optical coherence tomography. Opt. Lett. 29, 2025-2027.

162. Kemp, N.J., Zaatari, H.N., Park, J., Rylander, III H.G., Thomas, M., 2005. Depth-resolved optic axis orientation in multiple layered anisotropic tissues measured with enhanced polarization-sensitive optical coherence tomography (EPS-OCT). Opt. Express 13, 4507-4518.

163. Setterfield, H.E., Sutton, T.S., 1935. The use of polarized light in the study of myelin degeneration. Anat. Rec. 61, 397-411.

164. Miklossy, J., Van der Loos, H., 1991. The long-distance effects of brain lesions: visualization of myelinated pathways in the human brain using polarizing and fluorescence microscopy. J. Neuropath. Exp. Neur. 50, 1-15.

165. Ugryumova, N., Gangnus, S.V., Matcher, S.J., 2006. Three-dimensional optic axis determination using variable incidence-angle polarization-optical coherence tomography. Opt. Lett. 31, 2305-2307.

166. Paxinos, G., and Watson, C., 2007. The Rat Brain in Stereotaxic Coordinates, 6th edition. Elsevier Inc. (Academic Press).

167. Lichtman, J.W., Live, J., Sanes, J.R., 2008. A technicolour approach to the connectome. Nat. Rev. Neurosci. 9, 417-422.

168. Yushkevich, P.A., Avants, B.B., Ng, L., Hawrylycz, M., Burstein, P.D., Zhang, H., Gee, J.C., 2006. 3D Mouse Brain Reconstruction from Histology Using a Coarse-to-Fine Approach. Lecture Notes in Computer Science Volume 4057, 230-237.

169. Streicher J., Donat, M.A., Strauss, B., Spörle, R., Schughart, K., Müller, G.B., 2000. Computer-based three-dimensional visualization of developmental gene expression. Nat. Genet. 25, 147–152.

170. Huisken, J., Swoger, J., Del Bene, F., Wittbrodt, J., Stelzer, E.H., 2004. Optical sectioning deep inside live embryos by selective plane illumination microscopy. Science 305, 1007–1009.

171. Dodt, H.U., Leischner, U., Schierloh, A., Jährling, N., Mauch, C.P., Deininger, K., Deussing, J.M., Eder, M., Zieglgänsberger, W., Becker, K., 2007. Ultramicroscopy: three-dimensional visualization of neuronal networks in the whole mouse brain. Nat. Methods 4, 331–336.

172. Jährling, N., Becker, K., Dodt, H.U., 2009. 3D-reconstruction of blood vessels by ultramicroscopy. Organogenesis 5, 145–148.

173. Hama, H., Kurokawa, H., Kawano, H., Ando, R., Shimogori, T., Noda, H., Fukami, K., Sakaue-Sawano, A., Miyawaki, A., 2011. Scale: a chemical approach for fluorescence imaging and reconstruction of transparent mouse brain. Nat. Neurosci. 14, 1481–1488.

174. Chung, K., Wallace, J., Kiim, S.-Y., Kalyanasundaram, S., Andalman, A.S., Davidson, T.J., Mirzabekov, J.J., Zalocusky, K.A., Mattis, J., Denisin, A.K., Pak, S., Bernstein, H., Ramakrishnan, C., Grosenick, L., Gradinaru, V., Deisseroth, K., 2013. Strucutral and molecular interrogation of intact biological systems. Nature 497, 332-337.

175. Odgaard, A., Andersen, K., Melsen, F., Gundersen, H.J., 1990. J. Microsc. 159, 335–342.

176. Sands, G.B., Gerneke, D.A., Hooks, D.A., Green, C.R., Smaill, B.H., Legrice, I.J., 2005. Automated imaging of extended tissue volumes using confocal microscopy. Microsc. Res. Tech. 67, 227–239.

177. Tsai, P.S., Friedman, B., Ifarraguerri, A.I., Thompson, B.D., Lev-Ram, V., Schaffer, C.B., Xiong, Q., Tsien, R.Y., Squier, J.A., Kleinfeld, D., 2003. All-optical histology using ultrashort laser pulses. Neuron 39, 27–41.

178. Ragan, T., Kadiri, L.R., Venkataraju, K.U., Bahlmann, K., Sutin, J., Taranda, J., Arganda-Carreras, I., Kim, Y., Seung, S.H., Osten, P., 2012. Serial two-photon tomography for automated ex vivo mouse brain imaging. Nat. Methods 9, 255-258.

179. Bernardes, R., Cunha-Vaz, J.G. Optical coherence tomography a clinical and technical update. SpringerLink (Online service), Berlin; New York: Springer c2012.

180. Schuman, J.S. Optical coherence tomography of ocular diseases, 3rd ed. Thorofare, NJ: SLACK Inc. c2013.

181. Arous, B.J., Binding, J., Léger, J.F., Casado, M., Topilko, P., Gigan, S., Boccara, A.C., Bourdieu, L., 2011. Single myelin fiber imaging in living rodents without labeling by deep optical coherence microscopy. J Biomed Opt. 16, 116012.

182. Bizheva, K., Unterhuber, A., Hermann, B., Povazay, B., Sattmann, H., Drexler, W., Stingl, A., Le, T., Mei, M., Holzwarth, R., Reitsamer, H.A., Morgan, J.E., Cowey, A., 2004. Imaging ex vivo and in vitro brain morphology in animal models with ultrahigh resolution optical coherence tomography. J Biomed Opt. 9, 719-24.

183. Liang, C.P., Wierwille, J., Moreira, T., Schwartzbauer, G., Jafri, M.S., Tang, C.M., Chen, Y., 2011. A Forward-Imaging Needle-Type OCT Probe for Image Guided Stereotactic Procedures. Opt. Express 19, 26283-26294.

184. Wang, H., Al-Qaisi, M.K., Akkin, T., 2010. Polarization-maintaining fiber based polarization-sensitive optical coherence tomography in spectral domain. Opt. Lett. 35, 154-156.

185. Wang, H., Black, A.J., Zhu, J.F., Stigen, T.W., Al-Qaisi, M.K., Netoff, T.I., Abosch, A., Akkin, T., 2011. Reconstructing micrometer-scale fiber pathways in the brain: multi-contrast optical coherence tomography based tractography. Neuroimage 58, 984–992.

186. Preibisch, S., Saalfeld, S., Tomancak, P., 2009. Globally optimal stitching of tiled 3D microscopic image acquisitions. Bioinformatics 25, 1463-1465.

187. Budde, M.D., Frank, J.A., 2012. Examining brain microstructure using structure tensor analysis of histological sections. NeuroImage 63, 1-10.

188. Goergen, C.J., Radhakrishnan, H., Sakadzˇić, S., Mandeville, E.T., Lo, e.h., Sosnovik, D.E., Srinivasan, V.J., 2012. Optical coherence tractography using intrinsic contrast. Opt. Lett. 37, 3882-3884.

189. Wedeen, V.J., Rosene, D.L., Wang, R., Dai, G., Mortazavi, F., Hagmann, P., Kaas, J.H., Tseng, W.I., 2012. The Geometric Structure of the Brain Fiber Pathways Science 335, 1628-1634.

190. Augustinack, J.C., Helmer, K., Huber, K.E., Kakunoori, S., Zöllei, L., Fischl, B., 2010. Direct visualization of the perforant pathway in the human brain with ex vivo diffusion tensor imaging. Front. Hum. Neurosci. 4, 42.

191. Seehaus, A.K., Roebroeck, A., Chiry, O., Kim, D.S., Ronen, I., Bratzke, H., Goebel, R., Galuske, R.A.W., 2013. Histological Validation of DW-MRI Tractography in Human Postmortem Tissue. Cerebral Cortex 23, 442-450.

192. Jayaraman, V., Cole, G.D., Robertson, M., Burgner, C., John, D., Uddin, A., Cable, A., 2012. Rapidly swept, ultra-widely-tunable 1060 nm MEMS-VCSELs. Electron. Lett. 48, 1331-1333.

193. Jayaraman, V., Jiang, J., Potsaid, B., Cole, G., Fujimoto, J., and Cable, A., 2012. Design and performance of broadly tunable, narrow line-width, high repetition rate 1310 nm VCSELs for swept source optical coherence tomography. Proc. SPIE, 8276.

194. Jawerth, L.M., Mu¨nster, S., Vader, D.A., Fabry, B., Weitz, D.A., 2009. A Blind Spot in Confocal Reflection Microscopy: The Dependence of Fiber Brightness on Fiber Orientation in Imaging Biopolymer Networks. Biophysical Journal 98, L01–L03.

195. Chalut, K.J., Chen, S., Finan, J.D., Giacomelli, M.G., Guilak, F., Leong, K.W., Wax, A., 2008. Lable-free, high-throughput measurements of dynamic changes in cell nuclei using angle-resolved low coherence interferometry. Biophysical Journal 94, 4948-4956.

196. Yang, Y., Wang, T., Zhu, Q., 2012. Quantitative analysis of angle-resolved scattering properties of ovarian tissue using optical coherence tomography. J. Biomed. Opt. 17, 090503.

197. Lu, Z., Kasaragod, D.K., Matcher, S.J., 2011. Optic axis determination by fibre-based polarization-sensitive swept-source optical coherence tomography. Phys. Med. Biol. 56, 1105-1122.

198. Fan, C., Yao, G., 2013. Imaging myocardial fiber orientation using polarization sensitive optical coherence tomography, Biomed Opt Express 4, 460–465.

199. Mikula, S., Binding, J., Denk, W., 2012. Staining and embedding the whole mouse brain for electron microscopy. Nat. Methods 9, 1198-1201.

200. Srinivasan, V.J., Radhakrishnan, H., Jiang, J.Y., Barry, S., Cable, A.E., 2012. Optical coherence microscopy for deep tissue imaging of the cerebral cortex with intrinsic contrast. Opt Express. 20, 2220-2239.

201. Bolmont, T., Bouwens, A., Pache, C., Dimitrov, M., Berclaz, C., Villiger, M., Wegenast-Braun, B.M., Lasser, T., Fraering, P.C., 2012. Label-free imaging of cerebral ß-amyloidosis with extended-focus optical coherence microscopy. J Neurosci. 32, 14548-56.

202. R. Douglas Fields, 2008. White matter in learning, cognition and psychiatric disorders. Trends Neurosci. 31(7): 361–370

203. Thomason ME, Thompson PM., 2011. Diffusion imaging, white matter, and psychopathology. Annu Rev Clin Psychol 7:63-85. doi: 10.1146/annurev-clinpsy-032210-104507.

204. P. C. Sundgren, Q. Dong, D. Gómez-Hassan, S. K. Mukherji, P. Maly, R. Welsh, 2004. Diffusion tensor imaging of the brain: review of clinical applications. Neuroradiology, 46: 339-350.

205. Sandra Chanraud, Natalie Zahr, Edith V. Sullivan, Adolf Pfefferbaum, 2010. MR Diffusion Tensor Imaging: A Window into White Matter Integrity of the Working Brain. Neuropsychol Rev 20:209–225

206. Basser PJ., 1995. Inferring microstructural features and the physiological state of tissues from diffusion-weighted images. NMR Biomed. 8: 333-344.

207. Wedeen, V.J., Wang, R.P., Schmahmann, J.D., Benner, T., Tseng, W.Y.I., Dai, G., Pandya, D.N., Hagmann, P., D'Arceuil, H., de Crespigny, A.J., 2008. Diffusion spectrum magnetic resonance imaging (DSI) tractography of crossing fibers. NeuroImage, 41, 1267-1277.

208. Bock, A.S., Olavarria, J.F., Leigland, L.A., Taber, E.N., Jespersen, S.N., Kroenke, C.D., 2010. Diffusion tensor imaging detects early cerebral cortex abnormalities in neuronal architecture induced by bilateral neonatal enucleation: an experimental model in the ferret. Front. Syst. Neurosci. 4, 149.

209. Jespersen, S.N., Leigland, L.A., Cornea, A., Kroenke, C.D., 2012. Determination of axonal and dendritic orientation distributions within the developing cerebral cortex by diffusion tensor imaging. IEEE Trans. Med. Imaging 31, 16–32.

210. Budde, M.D., Janes, L., Gold, E., Turtzo, L.C., Frank, J.A., 2011. The contribution of gliosis to diffusion tensor anisotropy and tractography following traumatic brain injury: validation in the rat using Fourier analysis of stained tissue sections. Brain 134, 2248–2260.

211. Choe, A.S., Stepniewska, I., Colvin, D.C., Ding, Z., Anderson, A.W., 2012. Validation of diffusion tensor MRI in the central nervous system using light microscopy: quantitative comparison of fiber properties. NMR Biomed. 25, 900–908.

212. Bigun, J., Granlund, G., 1987. Optimal orientation detection of linear symmetry. Proceedings of the IEEE First International Conference on Computer Vision, London, pp. 433–438.

213. Brox, T., van den Boomgaard, R., Lauze, F., van de Weijer, J., Weickert, J., Mrázek, P., Kornprobst, P., 2006. Adaptive structure tensors and their applications. In: Weickert, J., Hagen, H. (Eds.), Visualization and Processing of Tensor Fields. Springer Berlin, Heidelberg, New York.

214. Haußecker, H., & Jähne, B. (1996). A tensor approach for local structure analysis in multidimensional images. Proceedings 3D Image Analysis and Synthesis' 96, Universität Erlangen-Nürnberg.

215. R. Rezakhaniha, A. Agianniotis, J. T. C. Schrauwen, A. Griffa, D. Sage, C. V. C. Bouten, F. N. van de Vosse, M. Unser, N. Stergiopulos, 2012. Experimental investigation of collagen waviness and orientation in the arterial adventitia using confocal laser scanning microscopy. Biomech Model Mechanobiol, 11(3-4):461-473.

216. M. Krause, J. M. Hausherr, B. Burgeth, C. Herrmann, W. Krenkel, 2010. Determination of the fibre orientation in composites using the structure tensor and local X-ray transform. J. Mater. Sci. 45: 888-896.

217. Schmitt, O., Birkholz, H., 2010. Improvement in cytoarchitectonic mapping by combining electrodynamic modeling with local orientation in high-resolution images of the cerebral cortex. Microsc. Res. Tech. 74, 225–243.

218. Schmitt, O., Pakura, M., Aach, T., Homke, L., Bohme, M., Bock, S., Preusse, S., 2004. Analysis of nerve fibers and their distribution in histologic sections of the human brain. Microsc. Res. Tech. 63, 220–243.

219. Kroon, D.-J., Slump, C.H., 2009. Coherence filtering to enhance the mandibular canal in cone-beam CT data. IEEE-EMBS Benelux Chapter, Enschede, The Netherlands.

220. Kleinnijenhuis, M; Barth, M; Alexander, DC; van Walsum, A-MVC; Norris, DG; (2012) Structure Tensor Informed Fiber Tractography (STIFT) by combining gradient echo MRI and diffusion weighted imaging. **NeuroImage**, 59 (4) 3941 - 3954.

221. Fischl B., 2012. FreeSurfer. NeuroImage 62: 774-781.

222. Wang R, Benner T, Sorensen AG, Wedeen VJ. Diffusion Toolkit: a software package for diffusion imaging data processing and tractography. Proc. Intl. Soc. Mag. Reson. Med. 2007; 15: 3720.

223. Mori, S., Crain, B.J., Chacko, V.P., van Zijl, P.C., 1999. Three-dimensional tracking of axonal projections in the brain by magnetic resonance imaging. Ann. Neurol. 45, 265–269.

224. Basser P, Pajevic S, Pierpaoli C, Duda J, Aldroubi A. In vivo fiber tractography using DT-MRI data. Magn ResonMed 2000; 44: 625–632.

225. Weinstein DM, Kindlmann GL, Lundberg EC. Tensorlines: advection diffusion based propagation through diffusion tensor fields. In: Proceedings of the IEEE Conference on Visualization, San Francisco, 1999. 249–254.

226. Wang, H., Zhu, J., Akkin, T., 2014. Serial optical coherence scanner for large-scale brain imaging at microscopic resolution. Neuroimage 84, 1007–1017.

227. Johnson, G.A., Ali-Sharief, A., Badea, A., Brandenburg, J., Cofer, G., Fubara, B., Gewalt, S., Hedlund, L., Upchurch, L., 2007. High-throughput morphologic phenotyping of the mouse brain with magnetic resonance histology. NeuroImage 37, 82–89.

228. Magnain C, Augustinack JC, Reuter M, Wachinger C, Frosch MP, Ragan T, Akkin T, Wedeen VJ, Boas DA, Fischl B, 2013. Blockface histology with optical coherence tomography: A comparison with Nissl staining. NeuroImage 84C:524-533.

229. Pyhtila JW, Graf RN, Wax A., 2003. Determining nuclear morphology using an improved angle-resolved low coherence interferometry system," Opt Express. 11:3473–3484.

230. M. G. Giacomelli and A. Wax, 2011. Imaging beyond the ballistic limit in coherence imaging using multiply scattered light, Opt. Express, 19: 1285 -1287.

231. Wang, K., Liang, M., Wang, L., Tian, L., Zhang, X., Li, K. & Jiang, T, 2007. Altered functional connectivity in early Alzheimer's disease: a resting-state fMRI study. Hum Brain Mapp 28, 967-978, doi:10.1002/hbm.20324.

232. Kitamura, S., Kiuchi, K., Taoka, T., Hashimoto, K., Ueda, S., Yasuno, F., Morikawa, M., Kichikawa, K. & Kishimoto, T. Longitudinal white matter changes in Alzheimer's disease: a tractography-based analysis study. Brain Res 1515, 12-18, doi:10.1016/j.brainres.2013.03.052 (2013).

233. Schmitt, A., Hasan, A., Gruber, O. & Falkai, P., 2011. Schizophrenia as a disorder of disconnectivity. Eur Arch Psychiatry Clin Neurosci 261 Suppl 2, S150-154, doi:10.1007/s00406-011-0242-2.

234. Rosenberger, G., Nestor, P. G., Oh, J. S., Levitt, J. J., Kindleman, G., Bouix, S., Fitzsimmons, J., Niznikiewicz, M., Westin, C. F., Kikinis, R., McCarley, R. W., Shenton, M. E. & Kubicki, M., 2012. Anterior limb of the internal capsule in schizophrenia: a diffusion tensor tractography study. Brain Imaging Behav 6, 417-425, doi:10.1007/s11682-012-9152-9.

235. Miyata, J., Hirao, K., Namiki, C., Fukuyama, H., Okada, T., Miki, Y., Hayashi, T. & Murai, T., 2007. Interfrontal commissural abnormality in schizophrenia: tractography-assisted callosal parcellation. Schizophr Res 97, 236-241, doi:10.1016/j.schres.2007.07.032.

236. Voineskos, A.N., Lobaugh, N.J., Bouix, S., Rajji, T.K.,Miranda, D., Kennedy, J.L., Mulsant, B.H., Pollock, B.G., Shenton, M.E., 2010. Diffusion tensor tractography findings in schizophrenia across the adult lifespan. Brain 133, 1494–1504

237. Nair, A., Treiber, J. M., Shukla, D. K., Shih, P. & Muller, R. A., 2013. Impaired thalamocortical connectivity in autism spectrum disorder: a study of functional and anatomical connectivity. Brain 136, 1942-1955, doi:10.1093/brain/awt079.

238. Pollonini, L., Patidar, U., Situ, N., Rezaie, R., Papanicolaou, A. C. & Zouridakis, G., 2010. Functional connectivity networks in the autistic and healthy brain assessed using Granger causality. Conf Proc IEEE Eng Med Biol Soc 2010, 1730-1733, doi:10.1109/iembs.2010.5626702.

239. Tham MW, Woon PS, Sum MY, Lee TS, Sim K. 2010. White matter abnormalities in major depression: evidence from post-mortem, neuroimaging and genetic studies. J Affect Disord. 132:26--36.

240. Pugh, K. R., Mencl, W. E., Shaywitz, B. A., Shaywitz, S. E., Fulbright, R. K., Constable, R. T., Skudlarski, P., Marchione, K. E., Jenner, A. R., Fletcher, J. M., Liberman, A. M., Shankweiler, D. P., Katz, L., Lacadie, C. & Gore, J. C., 2000. The angular gyrus in developmental dyslexia: task-specific differences in functional connectivity within posterior cortex. Psychol Sci 11, 51-56.

241. Koyama, M. S., Di Martino, A., Kelly, C., Jutagir, D. R., Sunshine, J., Schwartz, S. J., Castellanos, F. X. & Milham, M. P., 2013. Cortical signatures of dyslexia and remediation: an intrinsic functional connectivity approach. Plos One 8, e55454.

242. Vandermosten, M., Boets, B., Poelmans, H., Sunaert, S., Wouters, J. & Ghesquiere, P., 2012. A tractography study in dyslexia: neuroanatomic correlates of orthographic, phonological and speech processing. Brain 135, 935-948, doi:10.1093/brain/awr363.

243. Seehaus A, Roebroeck A, Chiry O, Kim DS, Ronen I, Bratzke H, Goebel R, Galuske RAW, 2012. Histological validation of DW-MRI tractography in human postmortem tissue. Cerebral cortex [Epub ahead of print].

244. Caminiti, R., Carducci, F., Piervincenzi, C., Battaglia-Mayer, A., Confalone, G., Visco-Comandini, F., Pantano, P., Innocenti, G. M., 2013. Diameter, Length, Speed, and Conduction Delay of Callosal Axons in Macaque Monkeys and Humans: Comparing Data from Histology and Magnetic Resonance Imaging Diffusion Tractography. J. Neurosci .33: 14501 - 14511.

245. Harsan, L.-A., Dávid, C., Reisert, M., Schnell, S., Hennig, J., von Elverfeldt, D., Staiger, J.F., 2013. Mapping remodeling of thalamocortical projections in the living reeler mouse brain by diffusion tractography, Proc Natl Acad Sci USA 110: E1797–E1806.

246. Leergaard, T.B., White, N.S., de Crespigny, A., Bolstad, I., D'Arceuil, H., Bjaalie, J.G., Dale, A.M., 2010. Quantitative histological validation of diffusion MRI fiber orientation distributions in the rat brain. PLoS One 5, e8595.

247. Hansen, B., Flint, J.J., Heon-Lee, C., Fey, M., Vincent, F., King, M.A., Vestergaard-Poulsen, P., Blackband, S.J., 2011. Diffusion tensor microscopy in human nervous tissue with quantitative correlation based on direct histological comparison. NeuroImage 57, 1458–1465.

248. Dauguet J, Peled S, Berezovskii V, Delzescaux T, Warfield SK, Born R, Westin C. 2007. Comparison of fiber tracts derived from in-vivo DTI tractography with 3D histological neural tract tracer reconstruction on a macaque brain. Neuroimage. 37:530--538.

249. Jbabdi, S., Lehman, J.F., Haber, S.N., and Behrens, T.E. (2013). Human and Monkey Ventral Prefrontal Fibers Use the Same Organizational Principles to Reach Their Targets: Tracing versus Tractography. J. Neuroscience 33, 3190-3201.

250. M. Reuter, H.D. Rosas, B. Fischl, 2010. Highly Accurate Inverse Consistent Registration: A Robust Approach. NeuroImage 53(4):1181-1196.

251. Fillard, P., Descoteaux, M., Goh, A., Gouttard, S., Jeurissen, B., Malcolm, J., Ramirez-Manzanares, A., Reisert, M., Sakaie, K., Tensaouti, F., Yo, T., Mangin, J.F., Poupon, C., 2011. Quantitative evaluation of 10 tractography algorithms on a realistic diffusion MR phantom. NeuroImage 56, 220–234.

252. Alexander, A.L., Hasan, K.M., Lazar, M., Tsuruda, J.S., Parker, D.L., 2001. Analysis of partial volume effects in diffusion-tensor MRI. Magn. Reson. Med. 45 (5), 770–780.

253. Tuch, D.S., 2004. Q-ball imaging. Magn. Reson. Med. 52, 1358-1372.

254. Conor Leahy, Harsha Radhakrishnan, and Vivek J. Srinivasan, 2013. Volumetric imaging and quantification of cytoarchitecture and myeloarchitecture with intrinsic scattering contrast. Biomed. Opt. Express 4(10): 1978-1990.

255. Götzinger E., Pircher M., Geitzenauer W., Ahlers C., Baumann B., Michels S., Schmidt-Erfurth U., Hitzenberger C. K., "Retinal pigment epithelium segmentation by polarization sensitive optical coherence tomography," Opt. Express 16(21), 16410–16422 (2008).

256. Assayag, O., Grieve, K., Devaux, B., Harms, F., Pallud, J., Chretien, F., Boccara, C., Varlet, P., 2013. Imaging of non-tumorous and tumorous human brain tissues with full-field optical coherence tomography. NeuroImage Clin. 2, 549–557

257. Insel TR, Landis SC, Collins FS. Research priorities. The NIH BRAIN Initiative. Science. 2013; 340: 687 – 688.

258. A. G. Podoleanu, G. M. Dobre, R. G. Cucu, R. Rosen, P. Garcia, J. Nieto, D. Will, R. Gentile, T. Muldoon, J. Walsh, L. A. Yannuzzi, Y. Fisher, D. Orlock, R. Weitz, J. A. Rogers, S. Dune, and A. Boxer, 2004. Combined multiplanar optical coherence tomography and confocal scanning ophthalmoscopy. J. Biomed. Opt. 9, 86-93 (2004).

259. N. Iftimia, R. D. Ferguson, M. Mujat, A. H. Patel, E. Z. Zhang, W. Fox, and M. Rajadhyaksha, "Combined reflectance confocal microscopy/optical coherence tomography imaging for skin burn assessment," Biomed. Opt. Express 4(5), 680–695 (2013).

260. M. Gaertner, P. Cimalla, S. Meissner, W. M. Kuebler, and E. Koch, "Three-dimensional simultaneous optical coherence tomography and confocal fluorescence microscopy for investigation of lung tissue," Journal of Biomedical Optics, vol. 17, Jul (2012).

261. Jeong B., Lee B., Jang M.S., Nam H., Yoon S.J., Wang T., Doh J., Yang B.G., Jang M.H., Kim K.H., 2011. Combined two-photon microscopy and optical coherence tomography using individually optimized sources. Opt. Express 19, 13089–13096.

262. C. Joo, K. H. Kim, and J. F. de Boer, "Spectral-domain optical coherence phase and multi-photon microscopy," Opt. Lett. 32, 623-625 (2007).

263. S. P. Chong, T. Lai, Y. Zhou, S. Tang, "Tri-modal microscopy with multiphoton and optical coherence microscopy/tomography for multi-scale and multi-contrast imaging," Biomed. Opt. Express 4, 1584–1594 (2013).

264. A. Alex, J. Weingast, M. Weinigel, M. Kellner-Höfer, R. Nemecek, M. Binder, H. Pehamberger, K. König, and W. Drexler, "Three-dimensional multiphoton/optical coherence tomography for diagnostic applications in dermatology," J Biophotonics 6, 352–362 (2013).

265. A.F. Fercher, W. Drexler, C.K. Hitzenberger and T. Lasser, "Optical coherence tomography - principles and applications," Rep. Prog. Phys. 66, 239-303 (2003).

# PUBLICATION LIST

## Book Chapter

- **Wang H,** Akkin T. Brain imaging and mapping with multi-contrast optical coherence tomography. In *The Textbook of Advanced Neurophotonics and Brain Mapping*, Kateb B, Chen Y, eds. (Taylor & Francis). (*in preparation*)

## Papers

1. **Wang H**, Zhu J, Reuter M, Vinke LN, Yendiki A, Boas D, Fischl B, Akkin T. Cross-validation of serial optical coherence scanner and diffusion tensor imaging: A study on neural fiber maps in human medulla oblongata. (*accepted*)
2. **Wang H**, Lenglet C, Akkin T. Structure tensor analysis of serial optical coherence scanner images for mapping 3D fiber orientation and tractography in the brain. (*to be submitted*)
3. Akkin T, **Wang H** (2014). Serial optical coherence scanner for brain imaging and mapping. The Conference on Lasers and Electro-Optics, San Jose (*invited*).
4. **Wang H,** Zhu J, Akkin T (2014). Serial optical coherence scanner for large-scale brain imaging at microscopic resolution. *NeuroImage* 84, 1007-1017.
5. **Wang H**, Black AJ, Zhu J, Stigen T, Netoff TI, Abosch A, and Akkin T (2011). Reconstructing micrometer-scale fiber pathways in the brain: multi-contrast optical coherence tomography based tractography. *NeuroImage* 58, 984-992.
6. **Wang H**, Al-Qaisi MK and Akkin T (2010). Polarization-maintaining fiber based polarization-sensitive optical coherence tomography in spectral domain. *Opt. Lett.* 35, 154-156.
7. Al-Qaisi MK, **Wang H**, and Akkin T (2009). Measurement of Faraday rotation using phase-sensitive low-coherence interferometry. *Applied Optics* 48, 5829-5833.

## Conference Presentations / Posters

1. **Wang H**, Zhu J, Akkin T (2013). Serial optical coherence scanner for large-scale brain imaging at microscopic resolution. Poster presentation at IEM Conference and Retreat, Minneapolis.
2. **Wang H**, Zhu J, Reuter M, Yendiki A, Fischl B, Boas D, Akkin T (2012). Cross-validation of multi-contrast optical coherence tomography and diffusion tensor imaging. Poster presentation at IEM Innovation Showcase, Minneapolis.
3. **Wang H** (2012). Multi-contrast optical coherence tomography for neuroimaging. Poster presentation at Doctorial Research Showcase, University of Minnesota.
4. **Wang H**, Black AJ, Zhu J, Stigen T, Netoff TI, Abosch A, and Akkin T (2012). Multi-contrast optical coherence tomography for brain imaging. Poster presentation at Annual Symposium on Neuroengineering, Minneapolis.

5. **Wang H**, Fischl B, Boas D, Akkin T (2012). Optical tractography of human brain. Oral presentation at SPIE Photonics West, San Francisco.
6. **Wang H**, Zhu J, Stigen T, Netoff TI, Abosch A, and Akkin T (2011). Multi-contrast optical coherence tomography for brain imaging. Poster presentation at IEM Innovation Showcase, Minneapolis.
7. **Wang H**, Akkin T (2011). Multi-functional optical coherence tomography for brain imaging. Oral presentation at SPIE Photonics West, San Francisco.
8. **Wang H**, Black AJ, Akkin T (2010). Multi-functional optical coherence tomography for retinal imaging. Poster presentation at Vision research symposium, Minneapolis.
9. **Wang H**, Akkin T (2009). Spectral domain polarization-sensitive OCT based on polarization-maintaining fibers. Poster presentation at LifeScience Alley Annual Conference & Expo, Minneapolis.